Fracture of Automotive High Strength Steels

By:

Nurrasyidah Izzati Rohaizat

A thesis submitted in partial fulfilment of the requirements for the degree of
Doctor of Philosophy

The University of Sheffield
Faculty of Engineering
Department of Mechanical Engineering

Submission Date

9th March 2018

This research is done under the supervision of

Dr Christophe Pinna

in the Department of Mechanical Engineering

Abstract

This research is focused on the study of local deformation damage initiation and propagation in DP1000 steels which are good candidate for future generation of cars. The potential of DP1000 for applications in next generation of cars relies on a better understanding of the relationship between its overall mechanical properties and the deformation and damage of its microstructure. Such understanding will in turn favours the advancement in the development of future steels.

Damage development and plastic deformation have been studied in a statistically meaningful way by performing a DIC procedure conducted at two different scales simultaneously. Plastic deformation in both ferrite and martensite phase analysed over a large representative microstructure are statistically measured up to the UTS point revealing that the martensite phase in the DP1000 is deforms plastically at very large strain values and showing a very similar strain heterogeneity as observed in the ferrite.

A new experimental procedure to study crack propagation in DP1000 steel has been designed for the development of a laboratory scale punch test that generate loading conditions representative of industrial forming operations for the study of damage. Cracks were observed to form from the top outer surface and propagating towards the mid thickness. Void formation is found to take place near the ferrite-martensite boundaries in the ferrite phase. Crack paths are observed to propagate only in the ferrite phase and preferably goes around the martensite phase without crossing or breaking the martensite island.

Effect of processing conditions on the macroscopic mechanical properties of DP1000 will also be investigated using the newly developed experimental procedures.

I dedicate this thesis to the one strong woman figure in my life, my mother.

Acknowledgements

This journey to complete PhD and thesis write-up has been very challenging, with countless of obstacles faced that makes the finishing line seemed too far and almost impossible to reach if it. However, even after the worst storms, the sun will shine again. This work is certainly not done single-handedly. First of foremost, I would like to thank my mother, Mrs Zuraida Din who has been unfailingly supportive, providing persistent encouragements and understanding since the very beginning of my studies. There were times when I reached dead end for my work, when I feel lost and hopeless when I was dealing with relationship-friendship problems or when I have my funding was suddenly cut which left me in fear of getting deported back; she would always find the way to help me overcome these problems. Without my mother, it would not be possible for me to reach this far.

I dedicate this work to the memory of my late grandparents, who have helped my single mother to raise me. I had an amazing childhood with warm affection and great joy. With their persevere guidance I managed to successfully passed exams from my primary school and to boarding school, and was selected to further my studies in the United Kingdom from Masters to PhD. The beginning of PhD years was very tormenting, as my grandfather passed away and then followed by my grandmother a year later. They were so close to me that I could not imagine my life without them, and I was blaming myself for not being able to there for them. Mentally, I was suffering but I need to keep my promises that I have to complete my PhD and make them proud. I would thank my beloved grandmother, Mrs Hajah Rahmahjan Akhbar Khan and dear grandfather, Mr Din for inspiring me to become a better person in life.

This research would not have been possible without the guidance and persistence help from my PhD supervisor, which is a senior lecturer in the Mechanical Engineering Department, Dr Christophe Pinna. I was very lucky and grateful to be accepted as his student, and have always interested with the research topic offered to me. His respectable expertise covering vast topics in Solid Mechanics and Materials have provided me valuable insight, feedback and advice which have made this research and thesis writing possible. Furthermore, with Dr Pinna's supervision, I have also learned many qualities towards becoming a competent researcher. His continuous encouragement to discover new method or knowledge as well as to be analytical and curious in learning process, were very beneficial to me. I would also like to thank the other lecturers and staffs from The University of Sheffield s for their precious advice/recommendation and generous help: Professor Stephen Beck, Dr Hassan Ghadbeigi, Dr Peter Korgul, Mr Mike Rennison and Mr Richard Kay.

My deepest thanks to the Tata Steel Ijmuiden, The Netherland for supplying the materials for this research and the process was made possible by Dr David Hanlon. Dr Hanlon has provided useful information on the material and his opinions from the industrial perspective has been very helpful and truly appreciated.

A huge appreciation to my sponsors, the Government of Malaysia (MARA) and University Kuala Lumpur (UniKL) for investing in me by funding my studies abroad hence, allowing me to fulfil my dreams in the pursuit of achieving doctorate. Finally, I would like to thank the Deputy Foreign Minister Datuk Seri Reezal Merican Naina Merican and his assistant Mr Syamsul Erwin, and not forgetting Datuk Zaharin Mohd Yasin for their generous assistance in supporting me to get my fourth year PhD funding that helped me to manage through the final year, hence completing my PhD.

Table of Contents

List of Figures

List of Tables

List of Equations

Abbreviations

AHSS	Advanced High Strength Steels
DP	Dual Phase
UTS	Ultimate Tensile Strength
SEM	Scanning Electron Microscope
DIC	Digital Image Correlation
F	Ferrite
M	Martensite
TTT	time-temperature-transformation
M_s	Martensite start temperature
A	Austenite
C_M	Carbon content of martensite
V_M	Martensite phase volume fraction
YS	Yield strength
TS	Tensile strength
RD	Rolling direction
TD	Transverse direction
SD	Standard deviation

Nomenclatures

σ	Stress
ε	Strain
K	strength constant
ε_p	True plastic strain
ε_{UTS}	Strain at UTS
ε_f	Strain at fracture
E	Young's Modulus
σ_{UTS}	Ultimate tensile strength
ε_{max}	Maximum elongation to fracture
E_{xx}	Strain component in x-direction
E_{yy}	Strain component in y-direction
E_{xy}	Shear strain
F_{msx}	Force, maximum
W_{max}	Out-of-plane displacement, maximum
e1	Maximum principal strain
e2	Minimum principal strain

Chapter 1

Introduction

Steels are a very popular choice in the automotive industry due to their high strength to weight ratio and excellent formability. These properties are therefore ideal to enable the forming of complex geometries, reduction of weight for fuel efficiency and high strength for passenger's safety. The global demand for safer cars and the introduction of government regulations for low emissions have pushed the development of the so-called Advanced High-Strength Steels, AHSS (Balliger and Gladman, 1981).

Vehicles that use components made of AHSS are found to be much safer due to the high strength of AHSS which gives excellent rigidity and better crashworthiness in terms of energy absorption capacity due to the high elongation-to-fracture of AHSS. In terms of improvement in fuel consumption, AHSS components are also designed using smaller gauges with optimised material properties to remove unnecessary weight, therefore, improving fuel consumption compared to cars made with conventional steels.

Figure 1-1 shows an example of a commercial car that utilizes combination of the steels from the AHSS group which is aimed towards weight reduction whilst maintaining passengers' safety. Development of future cars incorporates the utilisation of the AHSS depending on the steel grades. Stronger steels with high yield strength are used for the body panels of passenger compartments to prevent deformation or intrusion during crash impact. While in the car crumple zone, steels with high work hardening, good ductility and good strength are used for a better crashworthiness due to high energy absorption over a distance during collision (Keeler and Kimchi, 2015).

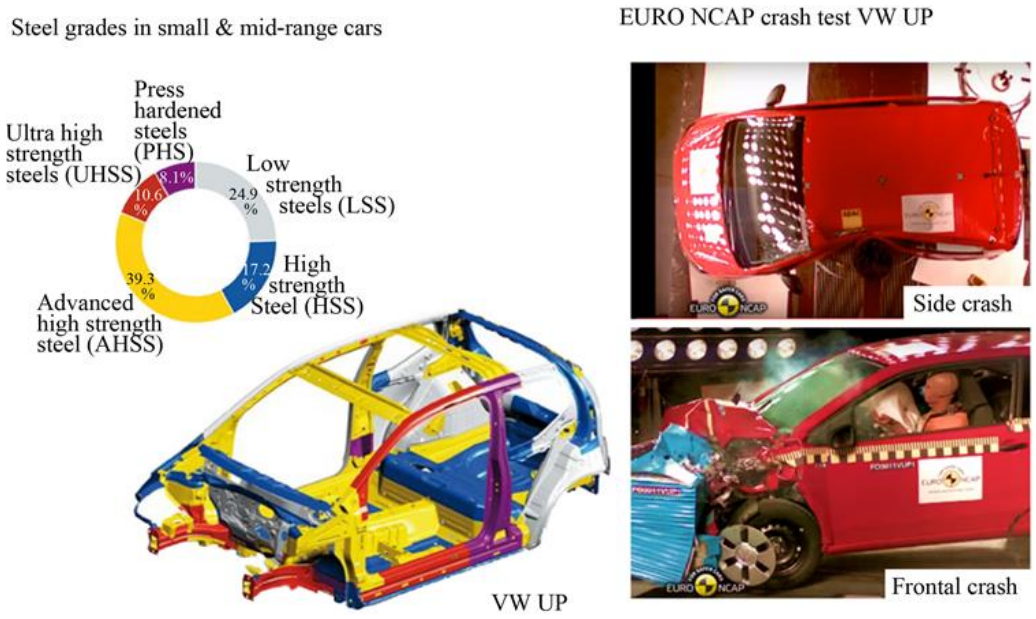

Figure 1-1 (Left) An example of a city car which utilises the various grades of AHSS aiming at lighter and safer cars (Euro NCAP, 2011). *(Top right) Crash test showing a collision impact from the side affecting the passenger compartment and (bottom right) is an example of impact collision to test the car frontal crumple zone* (Wagner et al., 2016).

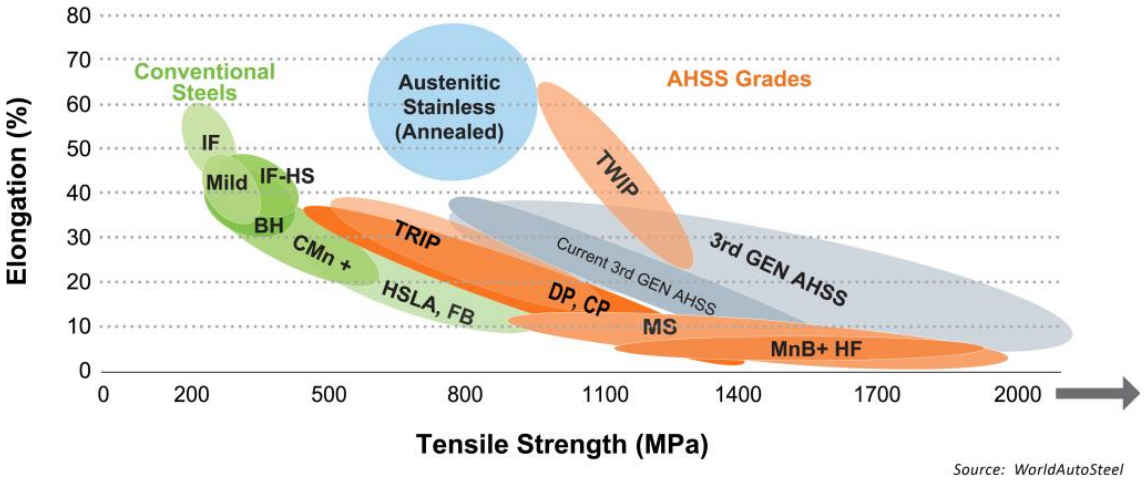

Figure 1-2 Global formability diagram showing variation of AHSS grades, including several different types of commercial steels (Keeler and Kimchi, 2015).

There is a wide range of steel types within the AHSS family. These types of steels are produced through various selections of chemical compositions and consist of different kinds of microstructural phases forming as a result of carefully designed heat treatments. Some of the steels categorized under AHSS family are Dual Phase (DP), Transformation –Induced Plasticity (TRIP), and Complex Phase (CP). They are grouped according to their unique multi-phase microstructures that makes them different in terms of ductility, strength toughness and fatigue properties as shown in Figure 1-2.

Among the many alternatives of steels in the AHSS group, DP steels is the ideal choice for the production of lighter and stronger automobile components. This due to the excellent mechanical properties for having low yielding point, high tensile strength with excellent ductility, as well as showing high work-hardening rates during the early stage of plastic deformation(Sarwar and Priestner, 1996).

The dual phase steels excellent capabilities for its strength and ductility are attributable to the two major phase components that make up the microstructure, which are ferrite and martensite. In general, the dual phase microstructure can be described as a combination of soft ferrite matrix with a uniformly distributed hard martensite islands. The strength of the dual phase steel is closely related to the microstructure, particularly the volume fraction of martensite and ferrite grain size. In comparison to HSLA steel grades of the similar tensile strength, the ductility of the dual phase steels is far more superior (Davies, 1978).

Controlled heat treatments are important in the processing of dual phase steels in order to obtain strength variations by altering ferrite-martensite phase compositions in the microstructure through modifying the quenching temperature after the intercritical annealing procedure. Tempering process also plays an important role in improving the

ductility of dual phase steels while slightly compromising strength. However the effect of tempering on the plastic deformation incompatibility of the two phases (hard martensite and soft ferrite phases) needs to be further studied (Hayashi et al., 2013). Previous research findings also revealed that dual phase steels mechanical properties, particularly the tensile strength and yield strength have high dependencies on the tempering temperatures applied (Davies, 1981).

In the effort for the improvement of the dual phase steels, various studies have been published especially on the deformation and damage behaviour at the scale of microstructure. However, in certain studies, results obtained are limited to very little examples of damage evidence and areas of analysis are small (localized). The observations reported are limited to the region of investigation and are affected by the surrounding phase morphology. Therefore, there is a need to generate more statistically meaningful results for the study of deformation and damage in dual phase steels as well as using samples that are representative to the morphology of the studied microstructures. These statistically meaningful experimental results in return can help modellers for the development of physically based multi-scale models.

The most popular mechanical testing technique being used in studying deformation or damage nucleation in dual phase steels is by running a tensile test inside a scanning electron microscope and combine it with a digital image correlation technique. The downside of this technique relates to the fact that damage initiates below the observed surface in the SEM and therefore can hardly be seen in the microstructure on the top surface of the specimen. It is therefore necessary to develop a new experimental procedure that can assist the study of damage development in dual phase steels, especially for investigating damage propagation of DP steels. Due to the complexity in capturing damage propagation, there very few articles published on investigating damage

propagation of DP steels. The key novelty of this work lies in the new understanding of damage development in DP steels through the development of a new experimental procedure to study damage initiation and propagation at the microstructural scale with statistically meaningful analysis and deformation conditions representative of a forming test.

Certain DP steels grades, e.g. DP600, DP800 especially, have found their applications in the car-making industries. However, the new generation DP1000 (DP steels with higher strength, of Ultimate Tensile Strength (UTS) of 1000MPa, are still under studied and further research is required before they can become commercially viable. The optimisation of their mechanical properties, very much dependent on their microstructures, consisting of two phases, ductile ferrite phase and hard martensite phase, and their distributions following various heat treatments during their processing, is still a topic of active research.

The potential of DP1000 for applications in next generation cars relies on a better understanding of the relationship between its overall mechanical properties and the deformation and damage of its microstructure. Such understanding will in turn favours the advancement in future steel developments.

1.1. Aim and Objectives

The aim of this project is focused on understanding the effect of tempering on the mechanical properties of DP1000 by investigating microstructural deformation, damage nucleation and propagation and to provide recommendations for optimal process conditions.

Particular attention is paid on formability, relevant to the automotive industry, and the ability of the material to sustain long elongation to failure. Given the lack of understanding from the literature on damage development in DP1000, but also more generally in AHSS, specific focus will be put on studying the mechanisms for damage nucleation and propagation under conditions representative of forming operations. Research will be also conducted in an effort to generate statistically meaningful results of both micro-scale deformation and damage in DP1000 for future implementation into multi-scale models predicting the macroscopic response of the material.

Several objectives have been identified towards achieving the aim in this study. Firstly, investigation is focused on the study of local deformation and damage development in the a commercial DP1000 provided by TATA Steel, Ijmuiden by conducting mechanical testing inside a Scanning Electron Microscope (SEM) for different material microstructures resulting from controlled heat treatments carried out by the industrial partner. Full-field strain measurements at the scale of the microstructure are carried out using Digital Image Correlation (DIC) to characterise local plastic deformation and analyse damage development. An original procedure is developed to analyse results in a statistically meaningful way using a two-scale DIC procedure. Both tensile and vertical bending tests are conducted to study both damage initiation and propagation.

A second objective is to study deformation and damage development under conditions more representative of industrial forming operations. A new punch test has therefore been designed and manufactured in enabling the material to be deformed under conditions closer to bi-axial loading. The test has also been designed to accommodate 3D optical DIC for strain measurements during the test and to analyse conditions for material

failure. Post-mortem damage analysis is conducted by sectioning the failed specimen after the test for visualisation inside a SEM.

A third objective is to analyse the effect of various heat treatments on the deformability and damage development in DP1000 with a view at recommending optimal process conditions for improved mechanical properties. This has been conducted using steels with different controlled post-tempering treatments carried out at Tata Steel Europe and conducting both in-situ mechanical testing inside the SEM and punch testing.

1.2. Thesis Structure

This thesis concentrates on the understanding of the damage mechanisms and plastic deformation behaviours at microstructure scale in DP steels with several different heat-treatment conditions by developing novel experimental methods with Digital Image Correlation technique (DIC) hence, aiming towards the development future DP steels with improved properties. This thesis has been structured into seven chapters:

Chapter 2 presents the current knowledge on the DP steels material as well as reviewing the damage assessments methods and experimental techniques being utilised in the literatures.

Chapter 3 introduces the material used for this research and is the beginning of the result section, which compromises of the stress-strain response obtained from conducting standard tests on the research materials; DP1000 steels with five different heat-treatment conditions. This chapter will later explain on the experimental procedures which have been adopted in this research for the investigation of damage and deformation in DP steels such as conducting conventional testing to micromechanical testing, using

various DIC techniques from optical 2D and 3D-DIC to microscale-DIC and finally the laboratory scale biaxial punch test method.

Chapter 4 is the main result chapter in this research work. Results are obtained from performing a micro-tensile test in SEM and being analysed using DIC method. Earliest damage initiation sites are identified and monitored to their overall stress-strain state and heterogeneity in the plastic strain deformation are critically analysed to compare the material's tempering condition effect on ferrite-martensite phase difference. Damage in the mid-thickness of materials are also revealed by doing a cross-section analysis of the broken samples which have been tested.

Chapter 5 is another main result section which is from performing a novel technique, a formability test which resembles the forming process in automotive industry that enables to study of DP materials formability and assessing the crack propagation in the tested samples. For this test, results are shown in two sections: firstly, is the mechanical response and the 3D-DIC analysis from testing all the DP materials. Secondly is the dissection of the tested broken specimen to allow the study of crack propagation leading complete fail which are observed at the microstructure scale.

Chapter 6 provides a detailed discussion on the obtained results thus, aiming to draw a relation between the different tempering temperatures condition to overall mechanical material response, damage and deformation behaviour especially on micro-scale strain heterogeneity in ferrite-martensite phases, identifying common damage mechanisms found from the statistical damage initiation study, void formation and crack propagations.

Finally, Chapter 7 finalizes the whole research by highlighting the key findings from the conducted studies and provide some recommendation for future works needed.

Chapter 2

Literature Review

The start of this chapter discusses the background of dual phase steels beginning with the early development of the materials, the production involving thermomechanical procedures and known processing methods leading to microstructural evolution of the ferrite-martensite microstructure.

The second part of this chapter will highlight the key results collected from past to the present-day investigations conducted by the researchers studying the deformation mechanisms as well as the damage behaviour of the dual phase steels.

2.1. Dual Phase Steels

Dual phase steels are distinguished by their unique homogenous microstructure consisting a uniformly distributed martensite with fine-grained ferrite matrix as two major phase components with traces of lower bainite and retained austenite, and sometimes the phase composition may also include residues of pearlite, carbides and acicular ferrite that varies according to the processing route. (Davies, 1978; Rashid, 1981; Tasan et al., 2015).

The development of dual phase steels has begun since the mid of 1960's, where it started with the production of ferrite-martensite steels produced for the making of tinplate through rapid quenching low carbon steels from high temperatures which are close to the critical temperature. These early approaches were intended for producing steels with quenched martensite phase however were first aimed to improve strength rather than formability. However, towards the mid 1970's, there have been an increase in the development of dual phase steels towards improving the formability due to demands in

the automotive industry regulations for low emissions through weight reduction whilst maintaining the safety standards (Rashid, 1981). The development towards improving the dual phase steels for higher strength-to-weight ratios and improved formability makes these materials as a potential candidate to tackle these challenges in order to fulfil the global demands for economical and lighter transport.

2.1.1. Microstructure of Dual Phase Steels

The excellent mechanical properties of the dual phase steels for their high strength-to weight ratios and good ductility are closely linked to the two-phase microstructure. The combination of hard martensite phase embedded in soft, fine-grained ferrite matrix gives the material with useful properties such as high ultimate tensile strength (UTS) which is enabled by the hard martensite phase while the ductile ferrite phase promotes the material an increase in elongation-to fracture. In addition to that, the low proof stress (low initial yielding stress) due to the ductile ferrite phase allows the material to exhibit high strain-hardening rate near the start of the plastic deformation and good macroscopically homogeneous plastic deformation without the presence of Lüders bands. These excellent properties of the dual phase steels in turns, makes them ideal to be used for forming process in the automotive industry (Karlsson and Sundström, 1974; Sarwar and Priestner, 1996; Tasan et al., 2015). Figure 2-1 shows an example of a dual phase steels microstructure captured by Ghadbeigi et al., 2010 using a scanning electron microscope revealing the dark ferrite phase (labelled as F) and well-dispersed white martensite islands (labelled as M) as annotated in the micrograph.

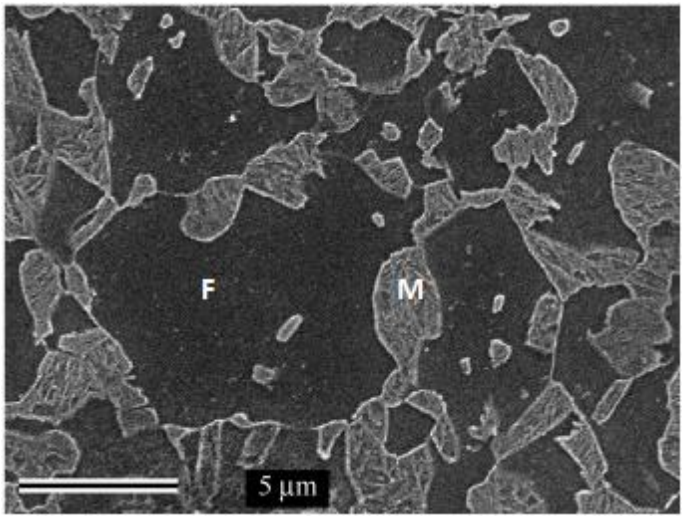

Figure 2-1 The microstructure of DP1000 steels consisting of dark ferrite phase and well-dispersed white martensite islands which is captured using scanning electron microscope showing (Ghadbeigi et al. 2010)

2.2. Microstructural Evolution and Processing Methods of Dual Phase Steels.

The dual phase steel was first among the steels varieties in the Advanced High Strength Steels (AHSS) family to be incorporated into the automotive industry for the making of lightweight and reinforced structural components for automobiles. The components made from the dual phase steels have outstandingly high tensile strength and good drawability due to dual phase microstructure. This section will explain the formation ferrite and martensite phases as well as the processing methods for the production of dual phase steels.

2.2.1. Phase Transformation Mechanisms

The formation of the two-phase microstructure of dual phase steels take place through phase transformation enabled by annealing (a process that alters physical and sometimes chemical properties of steels through heat treatments usually to improve ductility and decrease brittleness). This annealing process is conducted on a “starting steel” which is a

high strength micro-alloyed steels that is made up of fine-grained ferritic matrix with iron carbides found to form in the grain boundary and small islands of pearlite phase (Rashid, 1981). Phase transformation can be defined as changes happening within a system; while phase is characterized as the components that makes up part of the system of which the composition and properties are homogenous but is physically different from other part of the systems. When the initial state of the system is unstable relative to the final state, transformation will take place. Thus, phase transformation happens when one or more phases develop into new phases or forms into a mixture of phases within the material (Porter and Easterling, 1992). Which in this case by performing the annealing process, phase transformation will take place and resulting in a microstructure comprises of two or more phases such as ferrite, martensite and perhaps traces of retained austenite that makes up the dual phase steel system.

Phase transformation happening in the production of ferrite-martensite microstructure in the dual phase steels as a result from several heat treatment procedures, can be explained through TTT (time-temperature-transformation) diagram along with an iron-carbon (Fe-C) equilibrium diagram as shown in Figure 2-2. In the TTT diagram, two routes are shown in order to obtain the ferrite-martensite microstructure. The first route involved quenching the material to a temperature below martensite start (M_s) after a short holding period at high temperature in the austenite, A and ferrite, F (intercritical) regime. This method allows the unstable portion of austenite phase to transform in martensite. Usually this method takes place during the final annealing procedure in the making of dual phase steels. The second route shows that the material is quenched from a higher temperature than the first route mentioned earlier. The material which is in a fully austenite regime is then quenched to the temperature below M_s and resulting in the

formation of ferrite phase from undercooled austenite phase and the remainder transforms completely in martensite (Tasan et al., 2015).

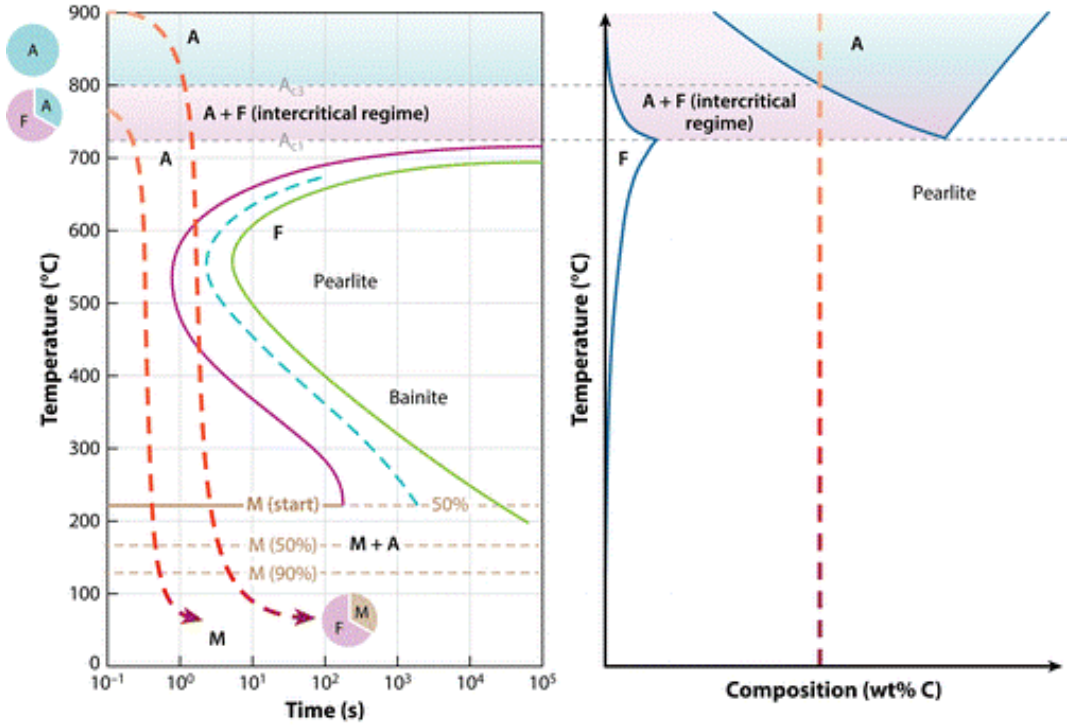

Figure 2-2 The schematic diagram show the heat treatments procedure to obtain the dual-phase microstructure. On the left shows the TTT (time-temperature-transformation) diagram and on the right is the iron-carbon equilibrium diagram. (Abbreviation used are A: austenite phase, F: ferrite phase and M: martensite phase). (Tasan et al., 2015)

2.2.2. Processing Methods

The unique microstructure of dual phase steels consisting both hard martensitic phase embedded in soft ferrite matrix can be acquired by performing several processing methods on low or medium carbon steels. The processing method that is widely used and highly researched is continuous annealing. Continuous annealing process can be encapsulated into three simple steps which begin with rapid annealing (heating) to the austenitic region or it reaches above critical temperature A_1, then the temperature is hold over a brief period and subsequently quenching (cooling) below the martensite start (M_s) temperature. Another method to produce the dual phase microstructure is through hot rolling. The process is usually performed at high temperatures that the material reaches

the austenite range (according to the temperature-composition, Fe-C phase diagram). Near the end of the rolling process, the temperature would drop to the intercritical regime, where at this point only 80-90% of austenite will transform into ferrite and the remainder would transform once the material reached the slow cooling in the coil resulting in the transformation products of martensite and retained austenite. The dual phase steels can also be produced through batch annealing method; researchers are less interested in this method compared to continuous annealing and as-rolled method. In batch annealing, it is slightly different from continuous annealing, as the procedures require materials to be heated up to intercritical temperature range and instead of rapid cooling, this technique requires a least a few days to allow material cools down to room temperature (very slow cooling rate). This approach would require steels with high alloying elements such as Mn and Mo and high hardenability (Rashid, 1981).

2.3. Digital Imaging Correlation Technique

Before going into details on the investigation of dual phase steel, it is best to introduce the Digital Image Correlation technique first. This technique has garnered a lot of attention from researchers especially in the attempt to understand the damage mechanisms and deformation of the dual phase steels. The Digital Image Correlation technique or also known as the DIC technique enables the researchers to quantify displacements and deformations on objects surface, allowing researchers to further implementing this technique on micro-scale and nano-scale mechanical testing applications.

In the field of experimental solid mechanics, there are various optical methods which are available that can be used especially in experimental solid mechanics and can be applied for the investigation in the mechanics of fracture as well as mechanical deformation of solids. Among the many optical methods available (such as holographic

interferometry, moiré interferometry and speckle pattern interferometry), the digital image correlation technique has found application in many fields of study and increasingly popular due to its advantages which does not require complex optical system set-ups in order to measure deformation of a surface (Bruck et al., 1989; Yoneyama and Murasawa, 2009).

2.3.1. Surface Preparation and Experimental Set-Up for DIC

The concept of DIC technique is shown in Figure 2-3. Generally, the DIC technique acquires images of the investigated object over time before storing the images in digital form. The patterned surface of the analysed objects which the random pattern may include grids, dots, lines and random arrays; enables digital image registration (matching) to compare sub-regions (also known as subsets) of the entire image to make full-field measurements possible. These full-field measurements are obtained by analysing the captured digital images using algorithms, where the approach is automated during the entire process (Sutton et al., 2009).

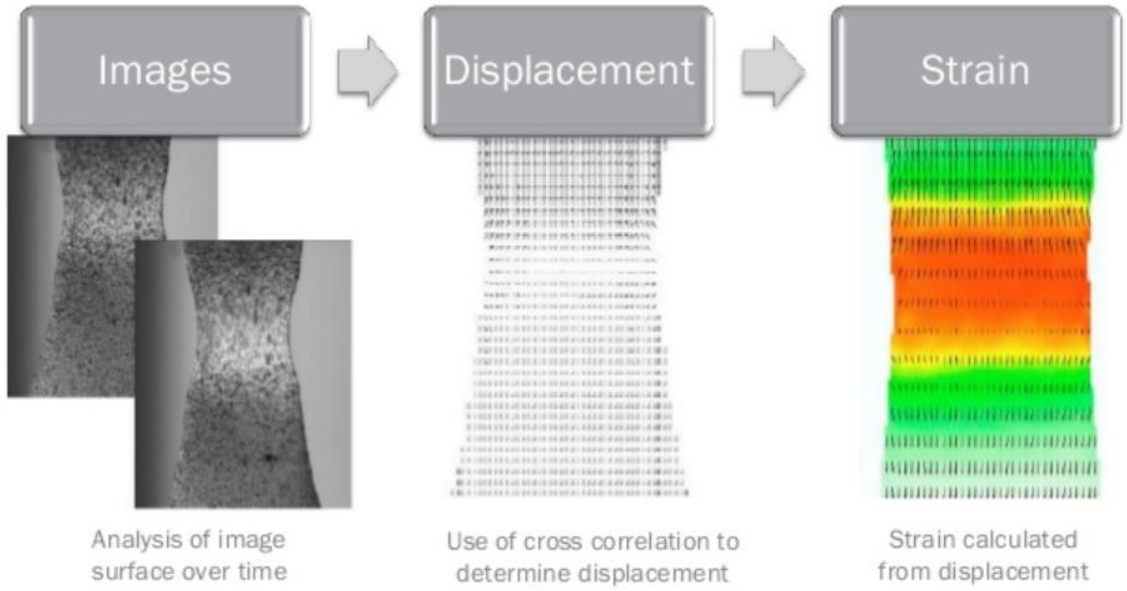

Figure 2-3 Flow steps of DIC technique to provide a full-field measurement of an inspected surface. (Instron, 2015)

The DIC technique begin with the surface preparation of the studied object. The plane surface of the studied specimen should have speckle pattern of different grey levels as the quality of speckle can highly affect the accuracy of DIC correlation (Haddadi and Belhabib, 2008). Depending on the studied materials, some materials surface may already be naturally textured with good contrast thus allowing the material ready to be studied using DIC. However, for the materials with plain surface without texture; the region of interest (ROI) must undergo surface preparation create a random speckle pattern using black and white paint. This speckle pattern can be achieved simply by applying a thin layer white matte paint and followed by creating a uniformly distributed contrasting black speckles on top of the white layer base paint (Haddadi and Belhabib, 2008). There are many methods available to generate the speckle pattern, such as by using standard spray aerosol, airbrush, brush-flickering, transferable stickers and rubber stamp (Instron, 2015).Figure 2-4 shows some examples of different speckles patterns which are used in experiments that implemented the DIC technique.

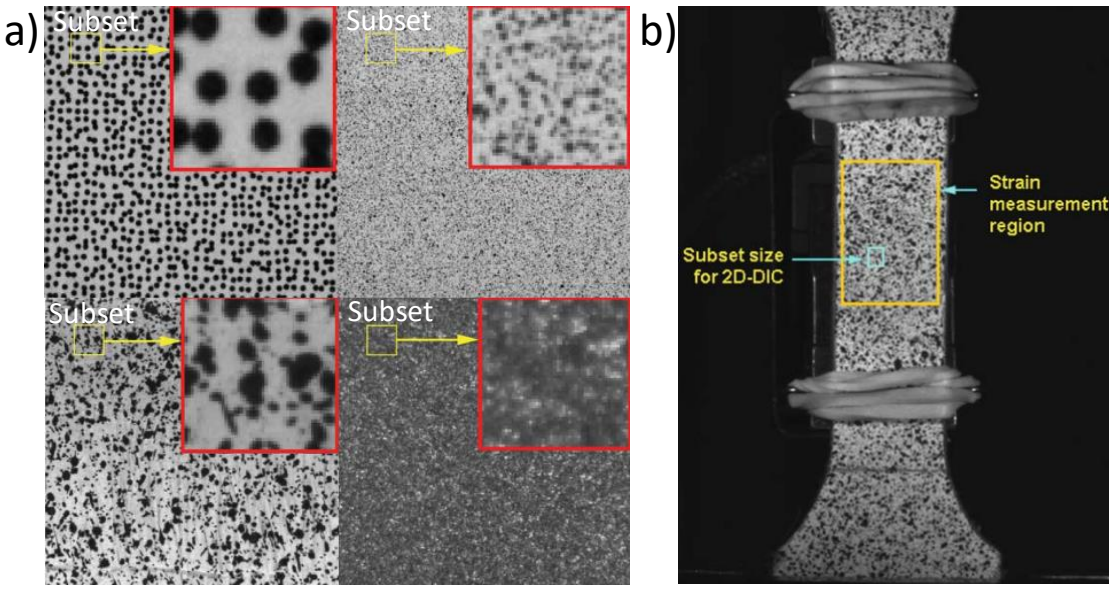

Figure 2-4 Examples of typical speckle patterns in (a) which have been used for DIC and the sub-regions or subsets with unique grey value intensity to allow the digital image registration/matching (Su et al., 2016). *Example of a tensile specimen prepared for DIC in (b)* (Sutton et al., 2009).

2.3.2. Micro-scale DIC

Apart from the widely used optical DIC methods which include 2D DIC for in-plane deformation and 3D DIC stereovision for out-of-plane measurements, there is another DIC technique which that is based on dynamic SEM observation/imaging or also known as micro-scale DIC (μDIC) which is highly used for studying the microscopic strain distribution and damage in dual phase steels.

SEM investigation on DP steels has begun as early as 1986 where Shen et. al, 1986 studied the deformation behaviour dual phase steels of different treatments using a scanning microscope equipped with a tensile straining stage. Advance in technology later leads to the application of DIC in SEM investigation enabling microscopic strains to be quantified at the scale of microstructure in DP steels.

In the investigation of deformation and damage behaviour of DP steels that uses the μ-DIC technique, it is found that the procedures being used the researchers are almost similar in general. This technique was first developed by J Kang, 2005 where they carried out an in-situ tensile test on an aluminium alloy inside a Hitachi S-4800 field-emission scanning electron microscope (FE-SEM). Various specimen geometries were designed using ABAQUS software and they found that geometry as shown in Figure 2-5 is suitable for the test. This is due to the uniform strain distribution along the middle region within the 2mm length found according to the results from the Finite Element Analysis (FEA).

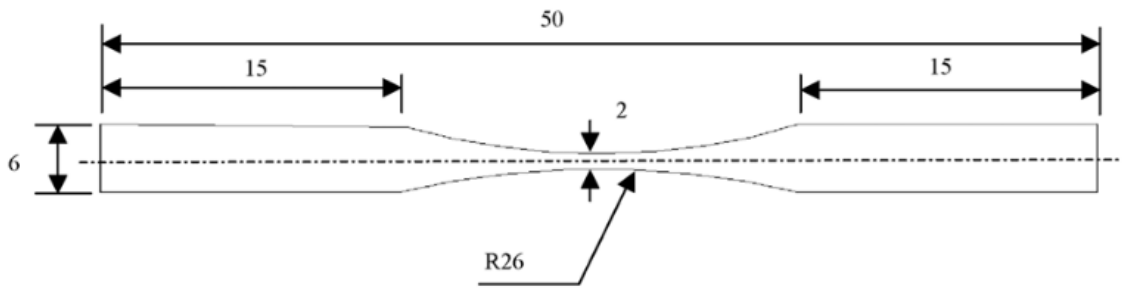

Figure 2-5 In-situ tensile geometry.

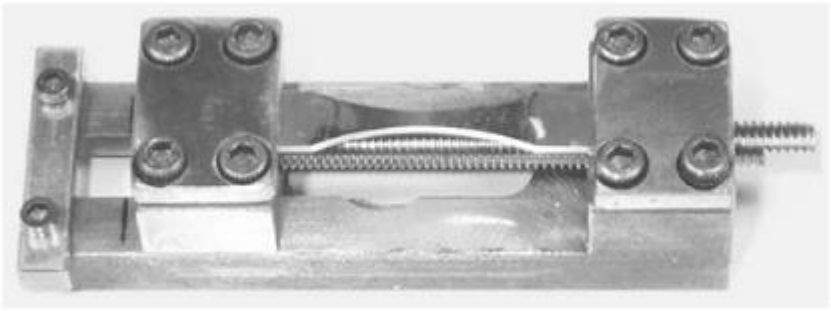

Figure 2-6 Tensile jig used for testing inside SEM, also called in-situ tensile stage.

Prior to testing, tensile specimens are polished to 1µm and etched for 15 seconds using a 2% Nital solution to reveal the grain boundaries of the DP microstructure (J Kang, et. al., 2007). In their papers, it is also mentioned that the reduction of specimen thickness may be needed depending on the loading limitation of tensile stage being used. Image/ micrographs are then captured in series and taken at different tensile strains using the FE-SEM. Once the tests are completed, the series of SEM images captures are processed using a commercial software, e.g. ARAMIS to be correlated using DIC method. The microscopic strain mapping using SEM topography image correlation, or µ-DIC procedure shows a good agreement to the strain results obtained using conventional strain measurements which was done by applying rows on indents on the surface (Kang et al., 2007, 2005).

2.4. Deformation Behaviours of Dual Phase Steels

Numerous investigation has been carried out to understand the deformation behaviour of the dual phase steels in the effort for the development of steels with improved properties. The two-phase microstructure consisting of hard martensite and soft ferrite phase leads to the complex micro-mechanical behaviour and affects the resulting mechanical properties.

In most metals particularly plain carbon steels, the deformation behaviour can be described using the relationship obtained from stress strain data of a tensile test as given in Equation 1 or Equation 2 (Dieter and Bacon, 1986).

$$\sigma = K\varepsilon_p^n$$

Equation 1

Or

$$\log \sigma = \log \mathrm{K} + \mathrm{n}\log \varepsilon_{\mathrm{p}}$$

Equation 2

Where σ is the true stress, *K* (the strength constant) is the stress when the ε_p (true plastic strain) reaches 1.0 and *n* is the strain-hardening exponent. Thus, for a true uniform plastic deformation behaviour, the plot of $\log \sigma$ and $\log \varepsilon_p$ will yield a straight line with *n* as the gradient; when $\sigma = K\varepsilon_p^n$ is thus satisfied. (Rashid, 1981). However, Rashid and Cprek, 1978 found that dual phase steel does not satisfies $\sigma = K\varepsilon_p^n$, where the plot $\log \sigma$ and $\log \varepsilon_p$ is found to stray from non-linearity. The dual phase steel exhibits several deformation behaviours confirmed by the multi-stages strain hardening happening during deformation. Korzekwa et al. 1984 who also observed the multi-stage strain hardening in the dual phase steels, highlights that there is a high dislocation density happening close to the interfaces of ferrite and martensite.

2.4.1. Effect of Microstructure Morphology on DP Steels Deformation Behaviours.

Many studies have assessed and observed that the complex deformation and failure behaviours of dual phase steels are related to the high difference in terms of strain accommodation in ferrite and martensite phase. Macroscopically, deformation of dual

phase steels may be homogenous however; if the deformation is assessed at microstructural level, the deformation is highly heterogenous with high strains in the ductile ferrite phase and low strain in the hard martensite phase. This observed phenomenon is referred at strain localization in many studies.

The inhomogeneous strain distributions in the ferrite and martensite phase was observed in the 1986, though performing tensile testing inside SEM on dual phase steels of various heat treatments (Shen et al., 1986). In their study, the effect of microstructural parameters such as C_M (carbon content of martensite) and V_M (martensite phase volume fraction) was also studied. Increment of both C_M and V_M increase the strain difference ratios between ferrite and martensite. High carbon content in martensite, C_M is known for the increase of hardness. In addition, they witnessed that tempering reduced the micro-hardness difference between ferrite and martensite and this results to an improved strain ratio. The tempering treatments was done at 400°C and 600°C. Another study also observed the strain partitioning in the ferrite and martensite phase through a method which coupled tensile testing in SEM with Digital Image Correlation method (Kang et al., 2007). Their results also found that the effect of heat treatments on the dual phase steels significantly reduces the strain difference in ferrite and martensite that leads to the increase of ductility. In their study, they compared the responses of material heat treated to 750°C and 450°C.

Depending on processing routes, microstructure of DP steels may exhibit a banded microstructure. In an investigation studying the effect of microstructural banding, it is found that the overall global properties (such as yield strength, ultimate tensile strength, etc.) of DP steel is strongly depending on band morphology such as thickness, geometry and specially the continuity of the bands (Tasan et al., 2010). The study highlights that continuous microstructure banding with high hardness caused harmful effects to the DP

steels. Damage initiates earlier in continuous bands microstructure due to the obstructed development of shear bands during deformation causing the shear bands developed through the banded region. Eventually this causes the banded microstructure to deform surpassing the plastic domain. It was recommended in the study to develop DP steels with discontinuous banded microstructure as early damage initiation can be prevented due to the flow of shear strain through the breaches within the discontinuous banding.

Heterogeneity in strain distribution is also greatly affected by parameters such as grain size, martensite phase volume fraction and martensite distribution as reported in investigation conducted on DP600 and DP 800 (Tasan et al., 2014). From the study, it is revealed that DP microstructure with larger martensite islands leads to earlier strain localisation to take place which begin at low applied loads. This is in contrast with microstructure consisting a well-distributed smaller martensite island which allows the surrounding ferrite phase to accommodate strain better. In terms of grain size, the study observes that larger ferrite grains deform plastically earlier compared to the finer ones. The deformation happening in the larger ferrite phase then developed into deformation nodes or “hot spots” of the microstructural strain network. In order to improve the DP overall mechanical properties, the report suggested to produce a microstructure with finer grain size and homogenously distributed martensite phase that will reduce the strain heterogeneity in the microstructure. The effect of grain refinement is also extensively studied in another study by Calcagnotto et al. 2010, where it is reported that grain refinement in DP steels induces ductile failure mechanisms as observed in tensile and impact tests. They also mentioned that in a finer grain microstructure, the well-dispersed and almost spherical-shaped martensite islands benefits inhibiting the development of cracking in martensite and cleavage fracture happening in ferrite. It is also found in the

study that grain refinement improves the tensile strength and yield strength. However, there is no effect in enhancing the material total elongation and uniform elongation.

The strength and hardness within the ferrite phase are heterogenous in an as-received continually annealed DP steels which found through a study using nanoindentation and micropillar compression tests (Ghassemi-Armaki et al., 2014). For the nanoindentation, a maximum force of around 2500 μN was applied with the resulting indentation size being smaller than the grain size of ferrite and martensite. For each specimen, 400 nanoindentations were made with a spacing of around 6 μm. Meanwhile, for the micropillar compression test, micropillars specimens were fabricated separately from individual ferrite and martensite phases obtained from a deformed tensile as-received DP specimen. The respective diameters of micropillars specimens for ferrite were around 2 μm and for martensite at around 1.0–1.5 μm. Compression tests were then conducted at a strain rate of 10^{-3} s^{-1}. It is reported that behaviour of the ferrite grains is affected by the distance of the grain to the neighbouring ferrite-martensite interface. The hardness and strength of ferrite phase increases when it is near to the interface of ferrite and martensite. The heterogenous behaviour within the ferrite grain is observed up to the 7% of global strain during a tensile deformation; when work hardening takes place in the interior ferrite grain however, the ferrite in the region close to the interface softens. Through micropillars compression tests, it is found that the ferrite phase begins to yield at around 395MPa while the onset of yielding in the martensite phase is at around 1GPa. From the subsequent yielding, the martensite phase undergoes a fast hardening up to 1.5GPa then from 2.3GPa – 2.5GPa, the hardening gradually increases. The yielding and work hardening of martensite phase is said to begin earlier before the DP steels reaches UTS.

2.4.2. Heterogeneity in Plastic Deformation at the Scale of Microstructure Studied using Micro-scale DIC and Other Methods

Many studies have utilise the procedure of coupling the tensile testing inside SEM and μ-scale DIC (microscale- Digital Image Correlation) to study the deformation behaviour happening at the scale of microstructure of dual phase steel. The μ-scale DIC technique provides strain measurements as well as strain distribution on a deforming microstructure enabled by tracking the vector changes in displacement of the "unique random pattern" of the surface. The clear contrast between dual phase microstructure consisting well-dispersed white (light-grey) martensite islands surrounded by black (dark) ferrite as seen in the SEM micrographs serves as the "unique random pattern" and is effective for the μ-scale DIC procedure.

A study conducted on DP600 steels employing the similar μ-scale DIC technique quantified the strain increment within the phases and found that local strain values reaches up to 120% in the ferrite phase but very near to the ferrite-martensite interface as the tensile specimen is at the end of necking regime at 42% applied strain (Ghadbeigi et al., 2010). The development of high strain intensities within the deformation bands are shown in Figure 2-7. In their investigation, strain partitioning is also studied by assessing strains in ferrite and martensite separately; and they found that the martensite phase has slightly lower deformation than ferrite. Strain heterogeneity seemed more apparent after 22% applied strain and deformation bands are found to form in the ferrite phase orientating at 45° to the loading direction.

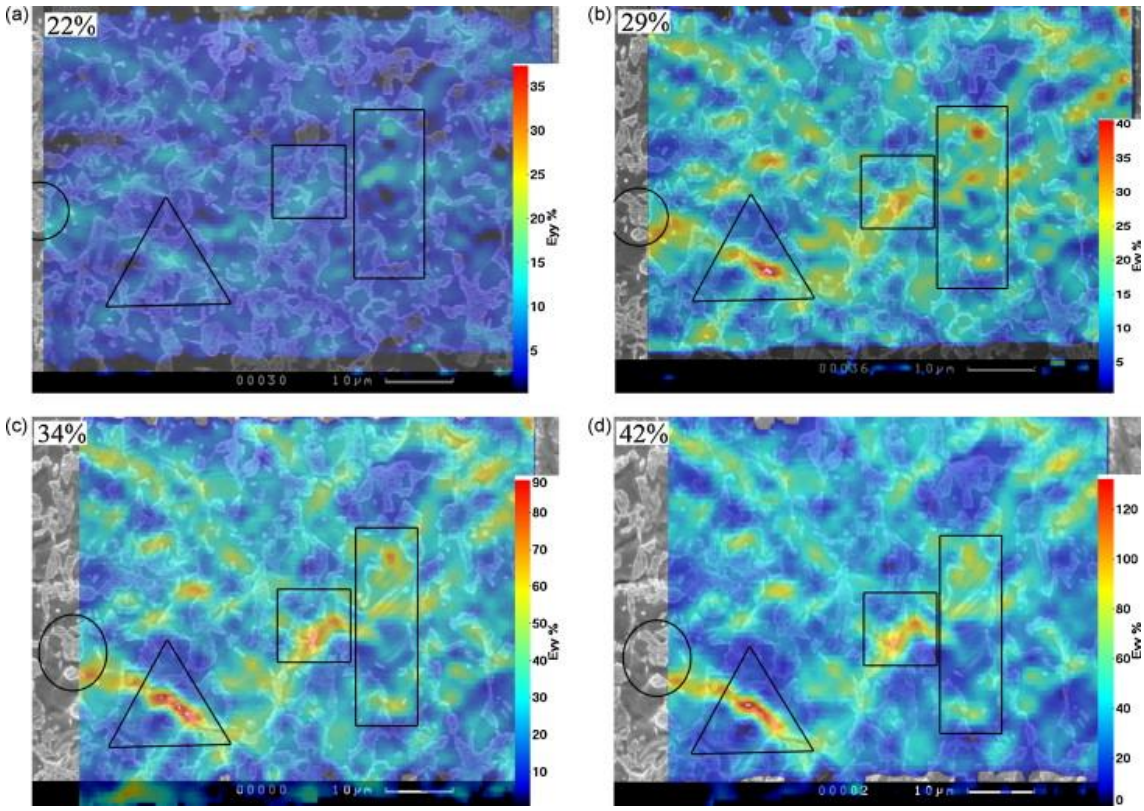

Figure 2-7 Development of high strain intensities within deformation bands. In the highlighted triangle, reveals that strain value has increased up to120% (H Ghadbeigi et al., 2010).

In another study which uses the similar µ-scale DIC technique on DP1000 steels, a critical strain heterogeneity was observed earlier, before the uniform elongation takes place and with increasing global deformation the strain heterogeneity increases (Kapp et al., 2011). The study also reported that, strain distribution maps show a network-like deformation pattern and the region of highest strains or "hot spots" are identified as the primary sites of damage initiation after being observed in the cross-section.

Another method which applied the similar concept of µ-scale DIC technique, uses an Ag nanodots patterning instead of using the DP microstructure itself to measure local strain at nanoscale (Joo et al., 2013). Through the nanodots deposition method, they found that without the presence of martensite islands in the shear stress directions, the ductile ferrite phase can be subject to a higher deformation. In agreement with Ghadbeigi et al. 2010 observation, this nanodots patterning technique also found that the plastic

deformation of martensite phase is very much smaller compared to the ferrite with increasing global applied strain.

An alternative method to perform the μ-scale DIC is by employing the micro-lithography method which uses the gold deposition method to create gold grid overlay on the surface of microstructure. This method is applied on DP600 and DP800 steels where the behaviour of ferrite and martensite deformation is studied at grain scale (Marteau et al., 2013). Heterogeneity in the strain distribution is also reported in this study, and it was found that although the strain values may be higher in ferrite, martensite too undergoes more or less large deformation and the deformation levels exceeds the elasticity domains. The strain values in both phases linearly increase with the applied strain. It is also reported that, the orientation, shape and size of grain does not affect strain heterogeneity after doing microstructure characterisation using Electron Back Scattered Diffraction (EBSD). This result is also aligned with the finding by Han et al. 2013 where it was found that strain heterogeneity is not affected by the orientation of ferrite phase, or the nature of ferrite-martensite interface but is highly depending on the morphology of neighbouring microstructure.

2.5. Damage Mechanisms in Dual Phase Steels.

It is identified that early damage forms in the dual phase steels begin as microcracks due to incompatibility of strain accommodations of the ductile ferrite phase and hard martensite phase. However, upon loading the microcracks development would eventually stopped as the growth is arrested due to the hardening and localized deformation in the ferrite phase. The cause of damage leading to final failure need to be understand and in this section; key information on the damage mechanisms happening in the microstructure of dual phase steels identified through numerous studies which based on various experimental techniques of different loading conditions as well as modelling.

2.5.1. Failure Mechanisms and Void Formation

Formation of void in a tensile test has been investigated as early since the 1988, where Steinbrunner et al. has reported three main void initiation mechanisms in the DP600 steels studied. The identified mechanisms are ferrite-martensite interface decohesion, cracking of martensite and lastly the deformation and ductile fracture of the martensite phase.

The initiation and growth of damage in a DP steel has been investigated using X-ray tomography during in-situ (micro-scale) tensile test (Maire et al., 2008). The sections of tensile specimens at necking and at the onset of fracture regimes inspected using X-ray tomography revealed a high density of voids nucleation, growth and coalescence, as shown in Figure 2-8. From damage quantification of void fractions, they found that when the tensile strain is homogenous, the void fraction is almost constant. However, when necking takes place, there is a locally high increment of void fraction observed. Voids formation is heterogenous and the highest void fraction is found to be at the centre of specimen. It is explained that the high density of void fraction at the centre of specimen is due to the outer shape of specimen after necking, which induces a high stress triaxiality at the centre of the specimen.

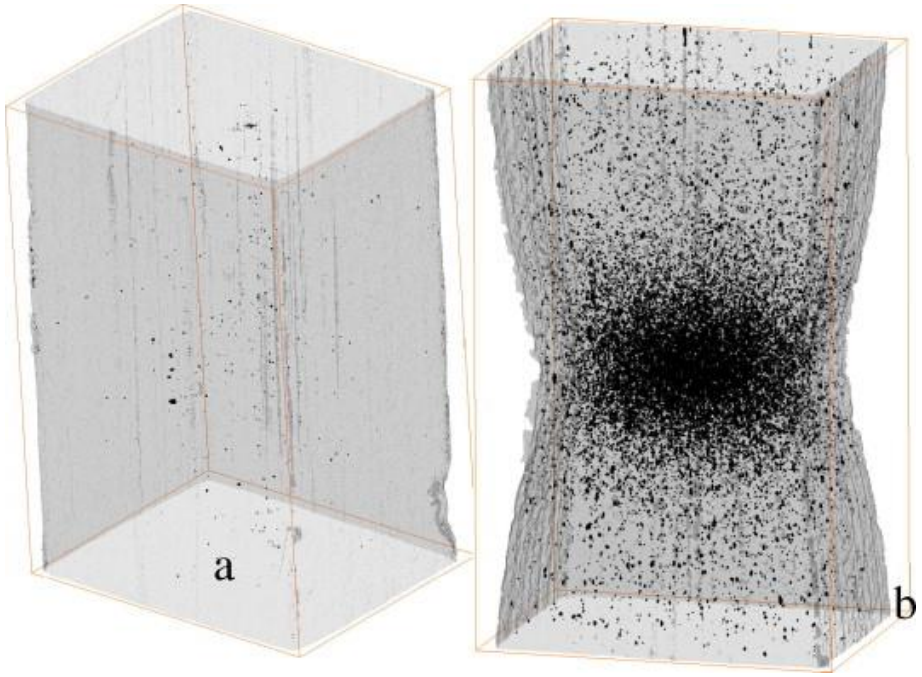

Figure 2-8 An X-ray tomography 3D representation of void formation during a tensile test where (a) is the state just after necking and (b) is at the onset of fracture (Maire et al., 2008).

A study involving the application of in-situ tensile testing in a SEM on a DP600 steel has successfully captured crack propagation during the onset of fracture by interrupting the micro-tensile test during necking. (Ghadbeigi et al., 2013). Example of crack propagation presented in the paper is shown in Figure 2-9. These specimens are then tested until they reach different strain levels of post-uniform deformation, after necking starts and up to final fracture, to allow crack development below the surface at mid-thickness and to prevent the specimen from entirely breaking. These specimens whose deformation was stopped at different stages, are then sectioned in the mid-thickness and are inspected for the formation of damage. Crack development is shown in Figure 2-9 (c), with initiation at the centre where the voids volume fraction and stress triaxiality are the highest. In terms of crack propagation path, microstructural observations showed that the crack propagated mainly in the ferrite phase with occasional deflection when martensite was in the way. The crack also propagated occasionally

through some martensite islands when there was no possible alternative path through the ferrite phase.

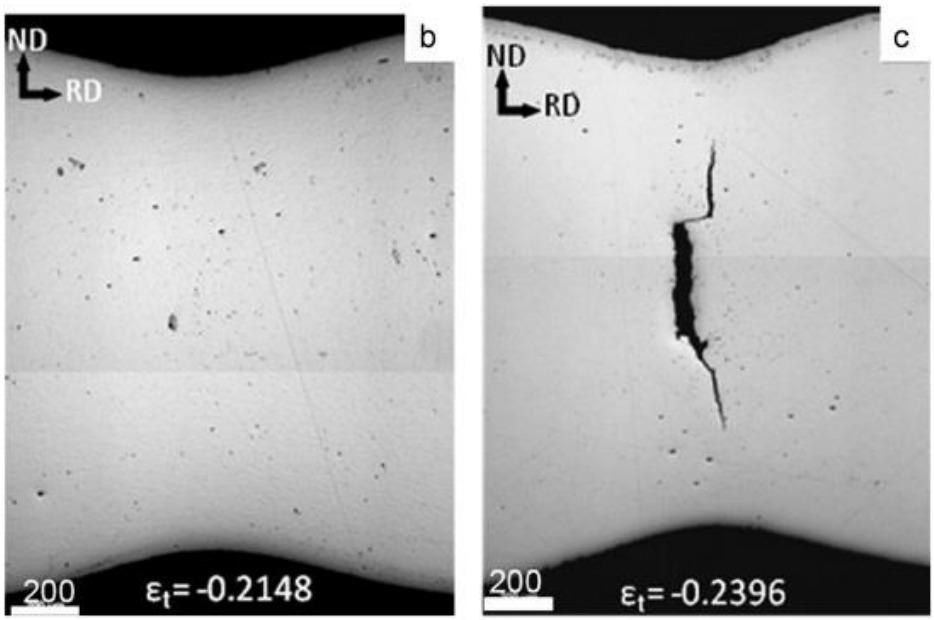

Figure 2-9 Crack propagation happening in a DP600 specimen captured just before final fracture of specimen (H Ghadbeigi et al., 2010).

Ahmad et al. 2000 performed intercritical heat treatments on DP steels and investigated the effect of micro void formation on DP steels properties. Their study revealed that the void formation behaviour in microstructure with low martensite percentage is due to ferrite-martensite interfacial decohesion; where both ferrite and martensite phase plastically deform and elongated along the tensile axis leading to the final fracture by ductile mode. In the microstructure of high martensite percentage, behaviour of void formation changes from decohesion at interface into transgranular microcracks forming at an orientation 90° to the tensile axis; where plastic deformation of the microstructure is very low causing brittle mode type of failure. The micro void behaviour in the high V_M specimen may be due to high carbon content in the material that consequently increases the tensile strength however reduces the ductility of the material.

In another study which conducted investigation on the effect of martensite morphology and distribution on the DP steels mechanical properties and damage mechanisms has revealed that the main mechanisms of void formation can be a transition from martensite cracking to the ferrite-martensite interface decohesion (He et al., 1984). From their observation, the damage mechanism on the DP with coarse microstructure begin with the cracking of martensite at low applied strain leading to the formation of void; and later is followed by secondary void formation due to the ferrite-martensite phase decohesion. In the paper, they also reported another damage mechanism that is happening in the subsurface at the localized necking region where there is a high density of voids forming under continuous tensile straining. These voids in the necking region subsequently begin to coalesce and resulting into a large cavity; which is a ductile fracture process. The rapid formation of large cavity due to void coalescence later exerts a sudden high stress level in the neighbouring region forcing the cavity to grow and propagate as brittle, cleavage fracture. Conversely, DP steels with fine microstructure and well-dispersed martensite is able to prevent the cracking of martensite during the low straining stages. This is due to the ferrite grains that can freely deform without any constraints from the neighbouring martensite. Thus, majority of void formations are nucleated due to ferrite-martensite interface decohesion and resulting in ductile damage process from the continuous increment in voids formation (ductile "cup-and-cone" process) with increasing strain until specimen total failure.

An investigation is carried out by Ghadbeigi et al. 2013 on DP600 steels and they develop the mechanisms for deformation and damage evolution leading to final fracture. From their study, it is revealed that the failure mechanism of martensite phase is by the formation of microcracks due to large deformation through tensile and bending mode; however, no ferrite-martensite interfacial decohesion was observed even after the

martensite phase has deformed plastically up to 50% strain. It was also observed that necking which begins on each sides of the phase, happening at the narrow middle region causing the development of microcracks and propagates through the centre region causing martensite to fail. The explained fracture mechanism is shown in Figure 2-10. Later, with increasing plastic deformation in the surrounding ferrite phase, the broken martensite island is then progressively displaced within the microstructure.

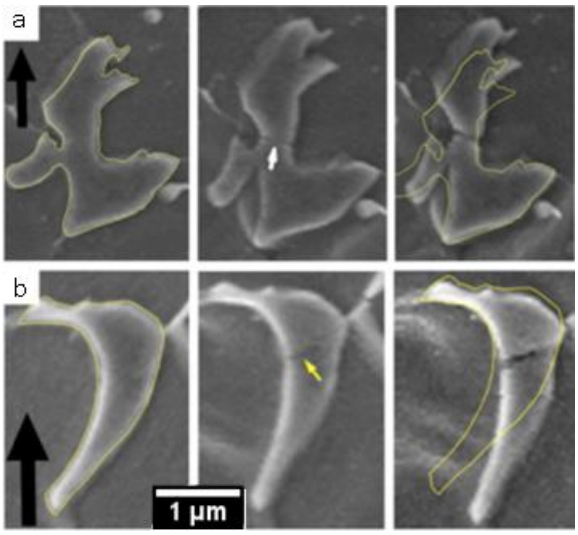

Figure 2-10 Progressive images showing the development of micro-cracks occurring in martensite phase where (a) is martensite fracture due local tensile deformation where necking took place in the narrow centre region and (b) local bending mode (Ghadbeigi et al., 2013).

Avramovic-Cingara et al. 2009 investigated the effect of martensite morphology and distribution on the damage and fracture behaviour of DP600 steels. They reported that in DP steels with a uniform martensite phase distribution, the damage growth happens at slower constant rate and void nucleation process is more uniform leading to a higher density of void formation before fracture. In contrast with the microstructure consisting a martensite band (banded microstructure), at the necking region of specimen; void growth is more accelerated happening at the martensite banding and the coalescence

occurs along the transverse direction to the applied load. Figure 2-11 shows the formation of damage is different depending on the martensite distribution. The effect of higher carbon content in the martensite phase is observed in higher void nucleating at the interfaces. In their study, four damage mechanisms were identified in the specimen with banded microstructure. These identified mechanisms are martensite cracking, martensite particles separation, ferrite-martensite phase decohesions and nucleation of void on inclusions.

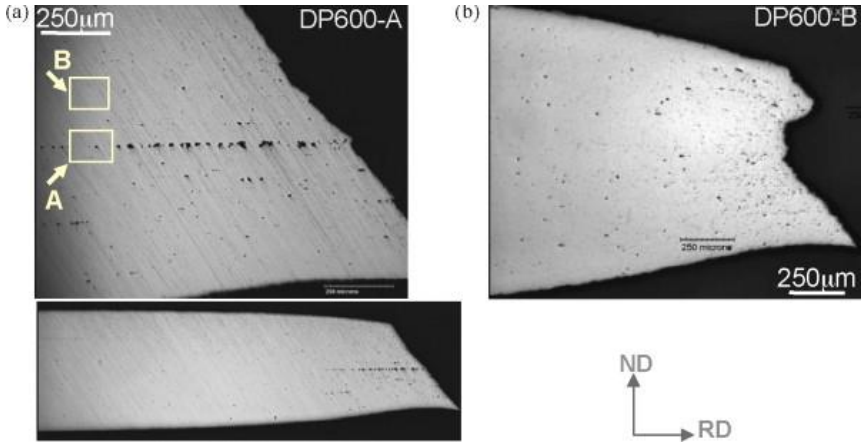

Figure 2-11 Formations of voids in the through thickness cross-sections of DP600 steels. (a) shows the formation on cracks along the centre-line where the banded microstructure is located in DP600-A (specimen with a banded martensite) while (b distribution of void is uniform and is higher in density forming at the necking region (Avramovic-Cingara et al., 2009a).

Numerous amount of studies was conducted to study the damage mechanisms in the DP steels, and the common observation in most studies are through martensite cracking, martensite-ferrite decohesion and the combination of both. In 2015, Tasan *et al.* compiled the result obtained on the damage mechanisms concluded the relation between the martensite volume fraction and ferrite grain size. The type of damage mechanisms relation to V_M, martensite volume fraction and ferrite grain size is shown in Figure 2-12.

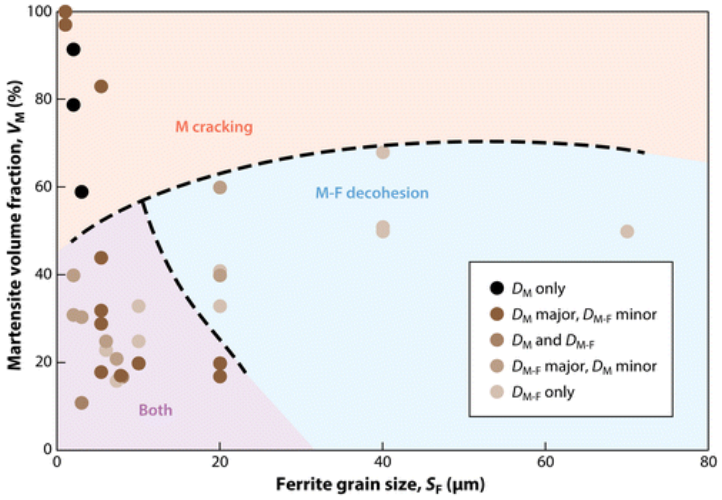

Figure 2-12 Effect of martensite volume fraction and ferrite grain size on the damage mechanisms of DP steels based on the various conducted studies(Tasan et al., 2015)

2.6. Computational Modelling on Mechanical Behaviour of DP Steels

The study on predicting the mechanical behaviour of Dual Phase steels using analytical concepts and numerical methods has begun since 1974 (Karlsson and Sundström, 1974). Apart from predicting the material's behaviour, computer simulation are also essential in providing important information which cannot be obtained directly from running experiments; such as stress distribution, dislocation densities as well as early-stage damage initiation (Tasan et al., 2015).

DIC technique can be combined with Finite Element (FE) modelling to generate information on stress distributions in a deforming specimen thus allowing deformation and damage mechanism to be further elucidated. A study has been carried out on DP800 steels which combine experimental observations and simulations. Two void initiation models have been proposed. The first model explains the void formation at ferrite-ferrite interfaces. In this case, elongated voids are prone to appear at locations where long grain boundaries are surrounded by martensite decohesion of ferrite-ferrite interfaces. The phenomenon is explained by the high stress concentration caused by high strain

incompatibility. The second model regards void formation at ferrite-martensite interphase boundaries. Here spherical voids form where small ferrite grains separate martensite islands. The decohesion of ferrite-martensite interfaces happens due to high hydrostatic pressure (Kadkhodapour et al., 2011). Sun *et al.*, 2009 studied how, in DP steels, the failure mechanism is affected by different volume fractions of martensite. For DP microstructures with less than 15% martensite volume fraction, the dominant cause of damage is associated with the growth and coalescence of pre-existing micro voids in the ferrite grains. Once the martensite volume fraction is more than 40%, strain incompatibility between ferrite and martensite phases becomes the dominant factor influencing damage.

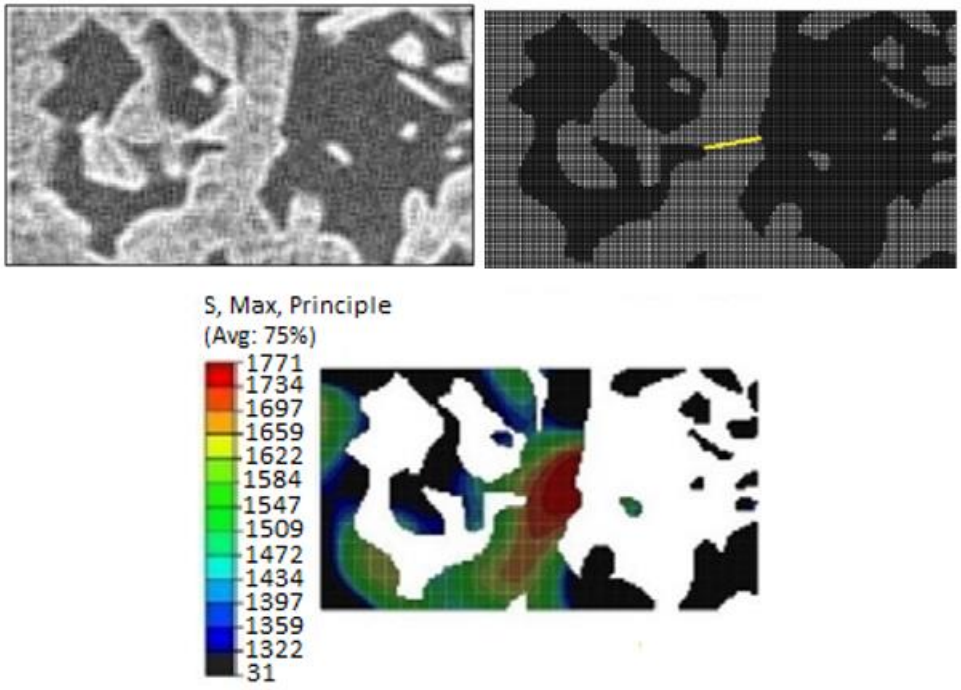

Figure 2-13 Simulating stress field happening at the area where crack initiated in the martensite phase. SEM image of microstructure is meshed and later combined with DIC results obtained experimentally for the boundary condition for the model (Alharbi et al., 2015).

Recently, Alharbi *et al.*, 2015 built a microstructure based model to follow the evolution of damage in DP1000 steel. The strain distribution obtained by DIC is imported as boundary conditions in the FE model to allow the stress state in the ferrite and

martensite phase at a stage near to failure to be studied. From their work, it is found that at the early stage of deformation, void nucleation is seen at specimen strains as low as 2%. In addition, a principal stress threshold value of around 1700MPa is predicted to be necessary to initiate damage in martensite that is close to the interface with ferrite as shown in figure 2.3. This gives a new insight into the study of damage mechanism in DP steels, which the methodology can be applied in this further research of describing damage in DP1000 steels with variation in microstructure.

2.7. Formability Tests

2.7.1. Motivation for the Development of an Improved Test Procedure

Section 2.5.1 showed that most procedures used to study the damage mechanisms in dual phase steels are either through micro-tensile testing inside a SEM or through post-mortem investigation on broken specimens. Although tensile testing inside a SEM provides useful insight into the deformation of phases leading to damage initation, the extent of damage at the surface of the specimen is very limited as most damage development takes place below the surface

There is therefore need to develop an improved and controlled test procedure to allow crack propagation to be investigated. Moreover the conditions for damage development should be more representative of industrial forming operations, i.e. involving bi-axial or out-of-plane deformation of the specimen. In addition, a forming process allows for a higher degree of deformation of the specimen, thus promoting a higher degree of damage nucleation. This is the reason why a forming test has been developed in this research with the primary focus of this test being on studying damage development in the microstructure of DP steels.

2.7.2. Review of Relevant Forming tests

In this section, the concept and methodology of existing formability tests is discussed in order to make comparison for finding of the most suitable method in testing the DP1000.

In forming or metalworking, usually the material undergoes a few processes in order to obtain the desired final shape without damage, while in formability testing, specimens are tested to their limit so that failure occurs through fracture or tearing. The scope of this review is narrowed down to formability tests conducted on sheet materials, since the specimens received from Tata Steel are in the form of sheets.

There are many available options for formability testing of sheet metals. With different types of materials, the relative amount of stretching and drawing will change according to the type of formability test being run (Hosford and Caddell, 2011).

Listed below are the tests that have been thoroughly studied and the metal forming concepts were referred to and are applied during the design of a formability test for this project.

OSU Formability Test

The OSU (Ohio State University) Formability Test simulates the typical sheet forming operations and the punch-height-to failure has been proved to correlate well in industrial press performance. Usually the OSU Formability and Friction tests would be run together to obtain the correlation of how materials and lubricants behave during forming process. Figure 2-14 shows the OSU formability tests using two different types of punches.

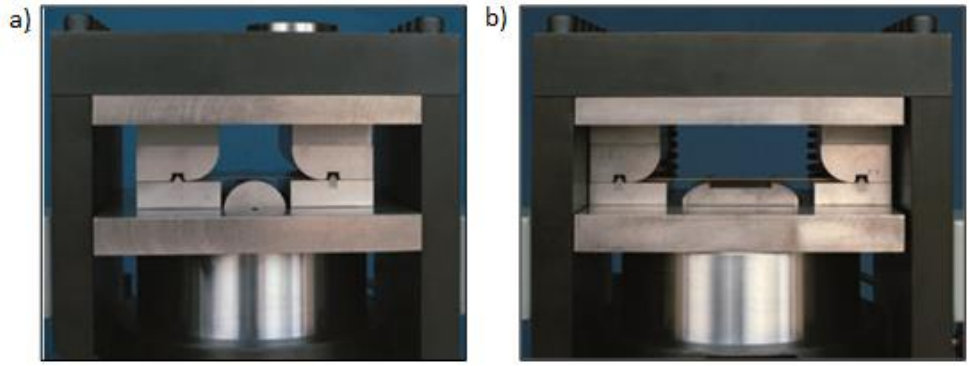

Figure 2-14 OSU formability die set (left) and friction die set (right), (Wagoner et al., 1994).

LDH (Limiting Dome Height) and Nakajima Testing

The LDH test uses a 4-inch (101.6mm) punch tool and can be used to determine forming limit diagram. The die has a bead feature to prevent material draw-in, thus enabling the maximum depth of cup formed with flanges are clamped. Due to minor variations affected by the way of specimen clamping, the LDH test faced a major problem in reproducibility within a laboratory and between laboratories (Hosford and Caddell, 2011). The procedure of LDH test and Nakajima test are very similar which uses the same punch tooling except for the specimen geometries being used, which circular blanks for LDH and rectangular blanks for Nakajima test. Example of these tests are shown in Figure 2-15.

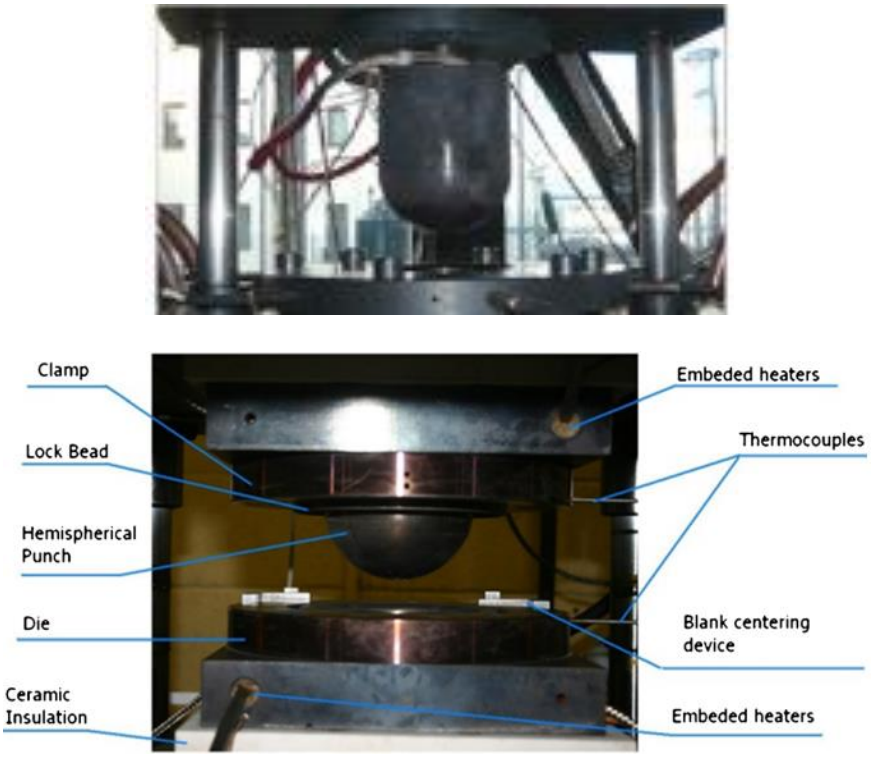

Figure 2-15 (Top) Example of Nakajima tests on a 1000kN electric machine (Bariani et al., 2008) *and (Bottom) LDH testing set up which is conducted at elevated temperature* (Bagheriasl and Worswick, 2015).

Cupping Test

There are many types of cupping test available, discussed in this section are the three chosen Swift cup test, Erichsen and Olsen test and Fukui Conical cup test. Figure 2-16 shows the schematic diagram of a Swift cup test. The test is used to determine the drawing ratio for flat-bottom cups by using a flat punch tool. While the Erichsen and Olsen tests Figure 2-17 use a hemispherical tool to stretch material. The result obtained from this test is affected more on stretch-ability rather than drawability of material. Due to large flanges, drawing occurrence is small. The Erichsen is usually used in Europe, while the Olsen test is used in America. The Fukui conical cup test uses a ball as a forming too but similar to the other tests (Swift cup and Erichsen/Olsen test), it also involves stretching and drawing of material. Figure 2-18 shows the setup up of Fukui conical cup

test. Comparison among the three tests on material drawing and stretching can be seen on Figure 2-19. Compared to LDH test, the cupping test is less favourable since it has been identified with the disability to control the inadvertent drawing in of flange and lubrication inconsistency due to the smaller size of penetrator used (Hosford and Caddell, 2011).

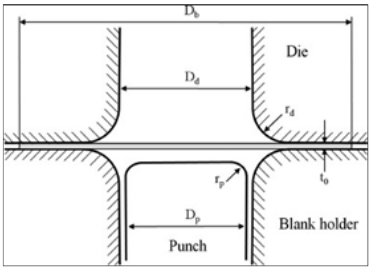

Figure 2-16 Swift Cup-Drawing Test for Testing Flat-Bottom Cups (Yoon et al., 2010).

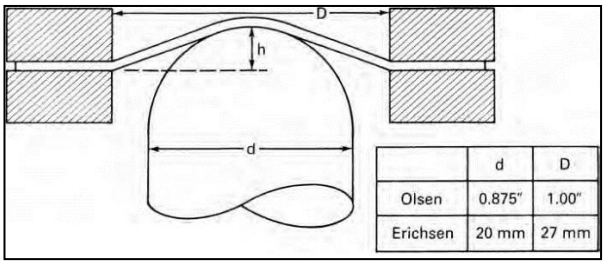

Figure 2-17 Schematic view Olsen and Erichsen tests using a hemispherical tool (Hosford and Caddell, 2011)

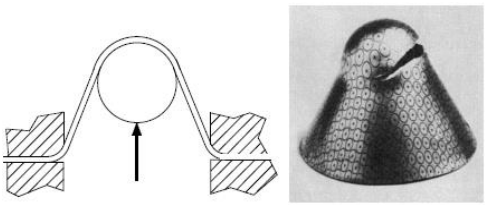

Figure 2-18 Schematic view of Fukui Test (left) and a failed Fukui cup (right) (Hosford and Caddell, 2011).

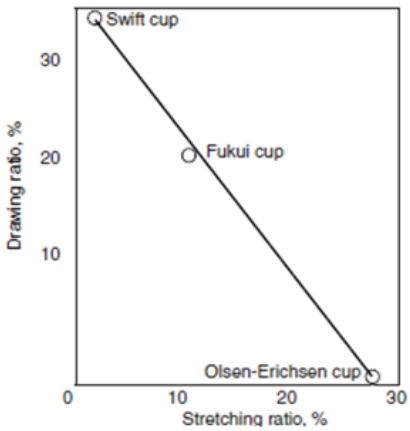

Figure 2-19 Comparison of drawing and stretching ratios of several cupping tests (Hosford and Caddell, 2011).

2.8. Summary and Novelty of this Study

The literature review has demonstrated the complexity of AHSS microstructures following thermo-mechanical processing conditions and the effect of phase distributions on local deformation and damage formation. Few recent studies have used advanced full-field strain measurement techniques, such as DIC, to characterise the local deformation and damage of AHSS microstructures, especially in DP steels. Although new insight has been generated from these studies, results have usually been reported on relatively small areas of microstructures and with few damage sites analysed. Published studies on DP1000 steels reveal early damage initiation in martensite but with hardly any strain value reported for the onset of damage. Most studies have focused on tensile testing with results obtained from the surface of the specimen and therefore limited to very few damage nucleation events. Only one study has provided insight into damage propagation at the scale of the microstructure in DP600 but results were limited to tensile testing which might not be representative of industrial forming operations, and without local strain measurements as far as propagation was concerned.

This study will therefore focus on developing new understanding of local deformation, damage initiation and propagation in DP1000 steels with the aim of generating statistically-meaningful results of strain distributions and damage development in representative areas of the microstructures. New testing geometries will be developed to generate loading conditions more representative of industrial forming operations and to offer new possibilities for the study of damage propagation in relation to local strain measurements. Furthermore, the effect of processing conditions on the macroscopic mechanical properties of DP1000 will be investigated using the newly developed experimental procedures.

Chapter 3

Methodology

This chapter elaborately explains on the experimental procedures that have been employed towards this investigation in understanding damage in DP materials. Various kinds of experiments were conducted in this study. These conducted experiments can be categorized into laboratory scale mechanical testing and in-situ tensile testing conducted in a Scanning Electron Microscope (SEM). Experiments in both categories incorporate the use of Digital Image Correlation (DIC) technique that provides useful strain distribution information for the tested DP steels specimens. In this study, three types of DIC technique has been utilized which are Optical 2D DIC, Optical 3D DIC and micro-scale (μ-scale) DIC. The 2D DIC provides an in-plane strain measurement while conducting the ASTM standard tensile test which later is also useful in obtaining the stress-strain response. The 3D DIC has been used for a small-scale laboratory punch test and it provides the out-of-plane strain distribution of a deforming specimen. Lastly, the micro-scale DIC is later being used for in-situ testing in the SEM providing the strain information based on the DP steels unique microstructural morphology. Every step of procedures carried out in this investigation will be thoroughly discussed in this chapter.

3.1. Motivation for Using Tempered DP Steels

As explained in the literature, failure of DP steels is closely related to the strain heterogeneity happening at the scale of microstructure. This microscopically inhomogenous strain distribution due to the incompatibility of deformation between hard martensite phase and soft ferrite matrix (Avramovic-Cingara et al., 2009a; Sun et al., 2009). Studies found that is it possible to reduce the strain mismatch gaps between ferrite and martensite phase through tempering process. This is because, in DP steels, tempering soften the martensite thus reducing the partitioning of strain to the soft ferrite (Han et al., 2013; Nakada et al., 2014). Compared to a quenched martensite that shows very little deformation, a tempered martensite attains deformation from the very beginning. Regarding to damage, the softening of martensite through tempering leads to better ductility because a substantially larger strain is required to initiate damage(Kang et al., 2007). It has been reported by various other researchers that tempering improves ductility (Rashid, 1981) although it may reduce the tensile strength with increasing tempering temperature , while not affecting the work hardening behaviour significantly (Kang et al., 2007; Speich et al., 1983).

In this research, for the study of understanding the damage initiation and propagation, the effect of tempering will also be taken into account by using DP steels that have been tempered at different temperatures. The effect of tempering that can reduce the strain difference of ferrite and martensite, as well as improving the ductility shows an opportunity to study to maximise the potential of DP steels. By the end of this research, it is expected that the effect of different tempering conditions on the deformation and damage mechanism of DP steel will be fully understood. Alongside the main objectives, by studying the DP steels of different heat treatments, this study expects to find the optimum tempering temperatures that can bring out the best DP steels performance.

3.2. Selecting Tempering Temperatures

The two parameters that can influence the degree of tempering (softening) are through controlling temperature and time (Olsen and Cohen, 1972). In a study conducted by Kamp et al., 2012 , it is found that the properties of DP steel are noticeably changed after applying a few seconds of tempering. In their studies, the effects of tempering on DP steels are assessed through several tests such as uni-axial tensile test, Erichsen cupping height test, bendability and hole expansivity. For the DP steels which are tempered between 200°C to 450°C for a short duration of 0 to 10 minutes, they observed that improvements in hole-expansivity as well as bendability; despite the decrease for tensile elongation (Kamp et al., 2012). From their results, DP steels tempered at 200°C to 450°C shows improvements several aspects of DP steels properties.

In this research, the investigated materials, DP1000 steels will be tempered according to the range of tempering temperatures between 200°C to 450°C, as referred to the aforementioned study above. Investigation will be carried out at the scale of microstructure as well as through running conventional laboratory scale mechanical tests; alongside with the application of micro-scale DIC (μ-DIC) and optical DIC, which will be explained later in this chapter.

3.3. Materials: DP1000 of Different Tempering Conditions

For this research, the material used for investigation is dual phase steels with the UTS of 1000MPa provided by the TATA Steel, Ijmuiden. The received materials are cold rolled DP1000 sheet steels with a production thickness of 1.6mm. The same DP1000 steels are then tempered at five different time-temperature combinations corresponding with the Holloman-Jaffe (HJ) parameters which are done by the TATA Steel as well.

Table 3-1 shows the parameters of the five different heat treatments on DP1000. The Holloman-Jaffe parameter gives the relationship of the tempering effect dependency on both temperature and time (Jordan et al., 2009). With increasing HJ, material have a deeper temper.

Table 3-1 Time and temperature combination corresponds to Holloman-Jaffe (HJ) parameters

Temperature (°C)	Time (s)	HJ Parameter
As-quenched	-	-
185°C	600	8.8
240°C	600	9.9
290°C	600	10.8
340°C	600	11.8
365°C	600	12.3

The variations of tempering condition provide this investigation six different conditions of DP1000 steels to be studied and see how these heat-treatments affect damage formation in the microstructure under loading. The first condition or the reference condition is the as-quenched DP1000 steels. These as-quenched steels are not further tempered and will be referred as material As-Quenched (AQ) for this study. The other five conditions will be the DP1000 steels which are later undergone a post-tempering process at different temperatures and will be referred using their tempering temperatures that are 185°C, 240°C, 290°C, 340°C and 365°C. These ranges of temperature chosen are expected to show effects on the mechanical properties of DP1000 steels without allowing phase transformation to take place, hence retaining the original microstructure.

For each condition, four pieces of DP1000 sheet steel samples are supplied with their width and length measuring 120mm by 550mm, respectively. Figure 3-1 shows several DP1000 steels sheet where they are cut shorter (width) in the transverse direction and the longer (length) side is following the rolling direction during the material's

processing. The mechanical properties, as well as the chemical composition for this standard as-quenched DP1000 steel, are shown in Table 3-2 and Table 3-3, respectively. The stress-strain responses of these materials will be later shown in the result section. The obtained sheet steels are then machined using the EDM into suitable geometries that meet the experimental set up requirements.

Figure 3-1 DP1000 sheet steels which are being used as research material in this study. Samples for every tempering conditions samples are received in sets of four with an approximate size of 120mm x 550mm x 1.6mm (width x length x thickness).

Table 3-2 Mechanical properties of an as-quenched (without any further heat-treatments) DP1000 steels.

	Galvanize	**$YS_{0.2\%}$ (Mpa)**	**TS (MPa)**	**Gauge (mm)**
DP1000	No	729	1051	1.6

Table 3-3 Chemical composition of the DP1000 steels.

C	**Mn**	**Si**	**N**	**P**	**S**	**Nb**	**V**
0.148	0.147	0.051	-	4 ppm	0.001	0.013	0.001

3.4. Digital Image Correlation Technique

3.4.1. Principle of DIC

Captured images are evaluated through correlation by dividing the complete image into smaller interrogation windows as shown in Figure 3-2. Depending on the correlation mode chosen, the correlation function passes through the complete image and works on the intensities inside each interrogation window. From this, each interrogation window will obtain one deformation vector field.

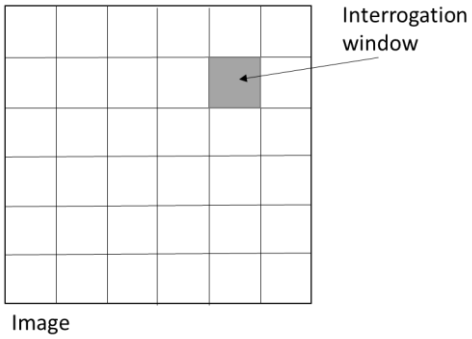

Figure 3-2 Image is divided into smaller interrogation windows depending on the chosen window size.

Using a correlation algorithm, displacements are obtained by comparing the image pattern within the window/subset to another. Interrogation window size and overlap should be carefully chosen to obtain the best result. Usually, multi pass with decreasing subset is used to calculate vector field by an arbitrary number of iterations. Firstly, a reference vector field is calculated by evaluating the first pass with the initial interrogation subset. For the next pass will be half the size of the previous pass, allowing vectors to be computed in the next pass to be more accurately. With smaller final interrogation window size, spatial resolution of the vector field is improved with less inaccurate vectors. Figure 3-3 shows the schematic diagram of the strain evaluation of DIC technique.

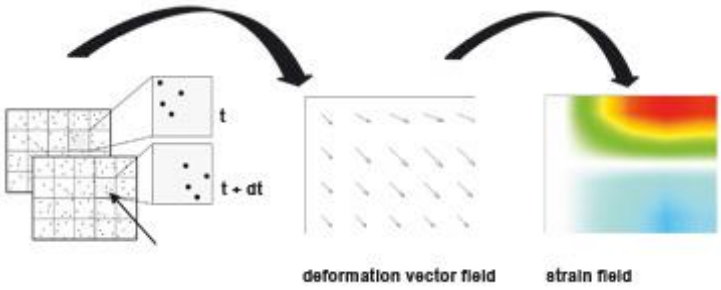

Figure 3-3 Strain evaluation process in DIC (Davis, 2004).

Following equation shows the cross-correlation algorithm used to calculate vectors that uses intensity index of the pattern in the two-analysed subset:

$$c(dx, dy) = \sum_{x=0,y=0}^{x<n,y<n} I_1(x, y) I_2(x + dx, y + dy), -\frac{n}{2} < dx, dy < \frac{n}{2}$$

Equation 3

Equation 3 is an example of correlation used called the standard cyclic FFT-based algorithm. Image intensities are denoted as I_1 and I_2 that represents the 1st and 2nd interrogation window while C is the correlation strength for all integer displacements (*dx, dy*) between the two interrogation windows. While *n* is the size of the interrogation windows (Davis, 2004).

3.4.2. Strain measurements within a phase using DIC

Figure 3-4 shows two different types of grey–scale patterns that can be used for DIC. Regardless the types of patterns being used, the basic principle for obtaining strain and displacements remains the same.

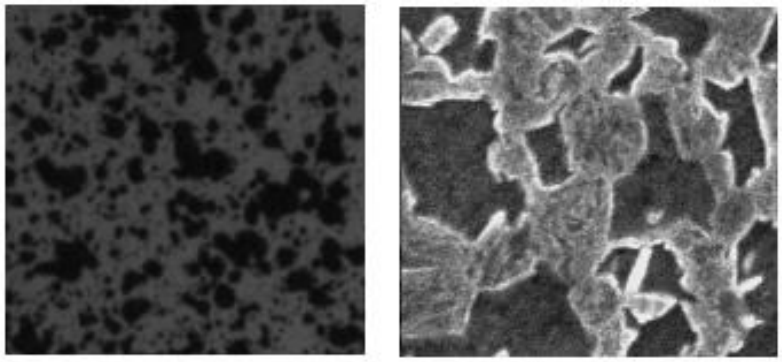

Figure 3-4 (Left) Speckles made using spray paint for optical DIC. (Right) Natural pattern of a microstructure used for SEM DIC.

As previously explained, this method divides images into smaller interrogation windows, which are also known as subsets. These subsets (displacement components of a local area) are unique from each other due to the different grey-scale pixel distribution within the subset area. These unique subsets are being used for the displacement detection throughout the entire analysed region. Displacements are determined by seeking through the whole analysed area for the same subsets in the two images taken before and after deformation as shown in Figure 3-5 (Yoneyama, 2016). Thus, it is important to choose the correct subset size according to the speckle or grain size of microstructure in order to make the correlation work.

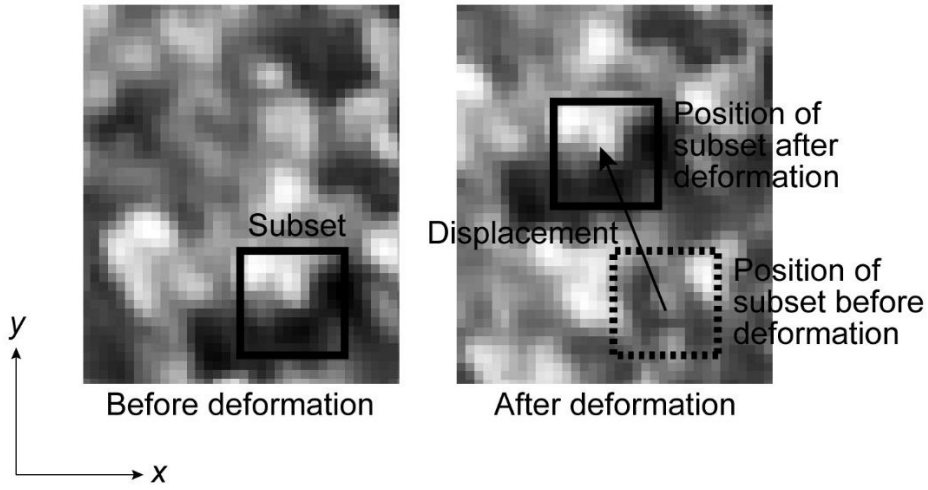

Figure 3-5 Basic principle of digital image correlation (Yoneyama, 2016).

3.4.3. Source of Errors in DIC technique

It is important to ensure the reliability of the measured data when using the DIC system. Identifying the source of errors before running the DIC system can be useful to ensure the errors throughout using the DIC technique can be controlled from the beginning as setting up the system to the end when analysing DIC results.

In DIC, one of the error sources are classified into correlation. The correlation errors can be further divided into statistical and systematical errors. There are several influence from the hardware system and environment conditions such as noise from cameras, different illumination conditions for the cameras, photon shot noise, contrast in image intensity and stochastic pattern of the specimen surface. The main statistical errors are usually due to the noise in camera image. By using changing different types of cameras, the reduction of camera noise can greatly reduce the resulting correlation errors (Siebert et al., 2007).

It is important to consider the errors within DIC system itself that are due to the image processing parameters and resulting in errors in the calculated displacement and strains. There are several studies conducted to assess the accuracy of measured field

displacements by DIC. Quantitative error assessment in DIC pattern matching has shown that errors in the measured displacements and strains are affected by the interpolation method, sub-pixel-motion, intensity noise, contrast, level of applied strain and subset size (Wang et al., 2009). In one of the studies, a comparative analysis has been carried out to compare the measurements obtained using DIC technique and validate using measurements obtained using microgrid technique independently (Ghadbeigi et al., 2012). It is reported from the study that an average error of 16% within the strain values measured using DIC despite the investigated microstructure has gone through a large deformation of over 73% strain, hence showing the reliability of DIC technique to be used on natural pattern of DP microstructure. The results obtained by Ghadbeigi et al. which are based on independent technique provides confidence in the way the correlation parameters are controlled for DIC at the micro-scale. These errors are acknowledged later in this investigation for the experiments involving micro-scale tensile tests in SEM using μ-DIC technique.

3.4.4. Optical Digital Image Correlation (DIC)

In this thesis, mechanical testing such as tensile test and bending test are conducted along with the use of the Optical Digital Image Correlation (DIC) to obtain full field displacement and strain distributions of the tested specimen. The DIC enables the measuring of surface deformation of test samples, regardless the resulting deformation is 2D, in-plane deformation of planar specimen or 3D, out of plane deformation (Pan et al., 2009). Figure 3-7 shows two different experiments with different set up of 3D DIC, which is using two cameras for the stereovision thus permitting 3D information (e.g. strain and displacements) to be obtained from the captured images. Standard 2D DIC would only require one camera. Materials may undergo reduction in area at the cross

section (necking) when it is close to fracture. For ductile steels, the amount of cross section area reduction is close to 50%. Depending on the types of specimen used, if the out-of-plane deformation is very low, then it is good to use the 2D DIC as it can be easily set up and saves time.

In order for the DIC to work, region of interest on the specimen need to be first painted with a random black speckle pattern on a white matte background. To do that, specimen firstly painted by using a white matte paint covering the entire gauge length surface while leaving the grip section covered (to avoid slipping of specimen at the grip during testing due to the peeling of paint). Paint need to be uniform and not too thick, so that paint will stick to the specimen regardless the intensity of deformation it is undergoing. Once the paint is dry, using a black spray paint (or an airbrush) to speckle the specimen with random pattern evenly spread-out and maintained a good contrast between the white background and black speckle for the DIC analysis to work optimally. Final look of a speckled specimen can be seen in Figure 3-6.

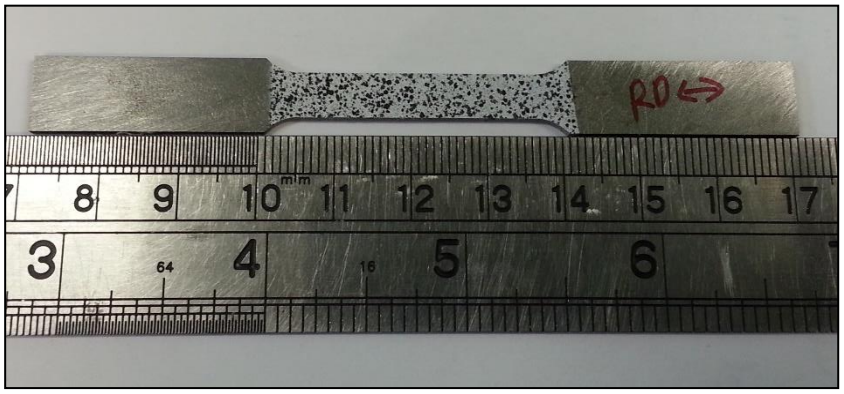

Figure 3-6 Speckled standard 12.5mm tensile specimen.

Figure 3-7 3D DIC set up for standard tensile test (left) and 3D DIC set up for a forming/punch test (right).

3.5. Standard Tensile Tests using Optical 2D DIC

In this section, the received DP1000 steels samples of different applied post-tempering treatments are tested through a laboratory scale tensile test designed following a standard test method. The experimental data collected from conducting this test on all six different condition samples will return stress-strain responses which is significantly useful in this investigation. The collected experimental stress-strain responses for each DP material condition allow the comparisons on how the heat-treatments affects the overall DP steels mechanical response, besides these stress-strain responses will be needed to relate the damage formation in the specimen to their overall loading states.

3.5.1. Design of Experiment

In order to obtain the stress-strain response for the DP steels under investigation, the tensile test has to be carefully designed so that it fulfil the standard requirements as well as feasible to carried out in the laboratory whilst using available machines and facilities. The first goal by the end of conducting this experiment is to compare if the DP1000 as-quenched material behaves differently if it is tested in the rolling direction (RD), transverse direction (TD) and at along the 45°. Secondly, is to compare the responses among the six different tempering conditions to compare the heat treatment effect on obtained mechanical response.

As explained earlier in the material section, the receive DP material has a 1.6 mm thickness. The most suitable way to test this DP sheet-type steels is by referring the ASTM Standard E8/E8M Standard Test Methods for Tension Testing of Metallic Materials (ASTM Standard, 2011). Crucial information on the material properties such as the Ultimate Tensile Strength (UTS), strain corresponding at UTS (ε_{UTS}), strain at fracture (ε_f), Young's Modulus (E) can be obtained from performing this standard method. Preferably, it is chosen the 12.5mm nominal width tensile specimen geometry for all tests conducted to standardize this investigation. However, the total length required for a 12.5mm width standard geometry can only be tested in rolling directions due to the as-received sheet steels samples size limitation. 12.5mm width specimen geometry has an overall length which exceeded the as-received sheet steels width of 120mm. To overcome this problem, a smaller 6mm width subsize specimen geometry is chosen for testing the DP1000 materials in all three directions (RD, TD, 45°) and this is done for the as-quenched type only. An example of a 6mm subsize specimen and 12.5mm standard is shown in Figure 3-8 and their geometries are presented in Figure 3-9. The 12.5mm width standard geometry will be used on all material types, but only in the rolling directions.

Triplicate tests were performed for each direction or DP1000 tempering conditions. Summary of the tests to be performed are in Table 3-4. The DP steel samples are then sent for EDM wire cut to produce the tensile coupon test according to the selected specimen geometries.

Figure 3-8 Example of two tensile specimen geometries after being cut using the EDM. At the bottom is the 12.5mm width standard specimen and the top (smaller) one is the 6mm wide subsize specimen.

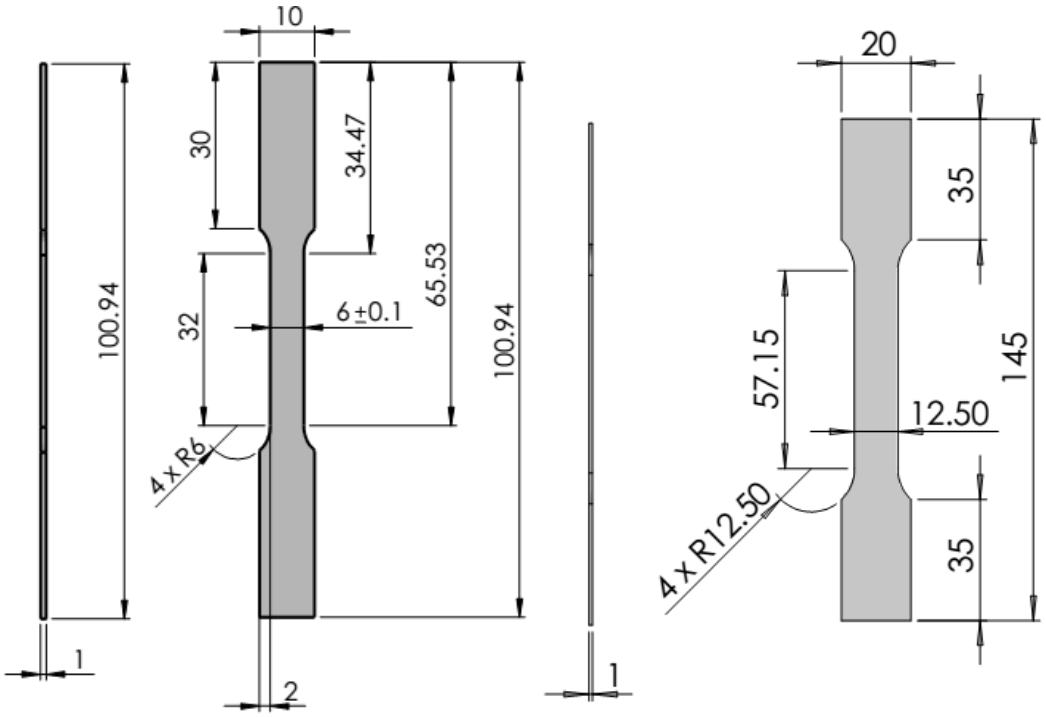

Figure 3-9 Tensile specimen geometries for standard sub-sized specimen, 6mm width (left) and standard specimen, 12.5mm width (right).

Table 3-4 Summary of the results required to be obtained after conducting the standard tensile test. Tests are categorized into the two different specimen geometries.

Specimen Geometry	**ASTM 6mm wide (standard subsize specimen)**	**ASTM 12.5mm wide (standard specimen)**
Materials	As-quenched DP	All (As-quenched, 185°C, 240°C, 290°C, 340°C and 365°C)
Directions	Longitudinal (RD) Transverse (TD) 45°	Longitudinal (RD)
Experimental data	1x material 3x directions 3x test repetitions	6 materials 1x direction x 3 test repetitions
Total expected results	6 curves	18 curves

3.5.2. Experimental Set Up of Tensile Test and Optical 2D DIC

Tensile tests are conducted on a 25kN Tinius Olsen (electric) machine along with the use of optical 2D DIC to track the deformation on the gauge length of tensile specimens from the start of deformation until failure. The DIC technique is an alternative method to replace devices such as extensometers and strain gauges. The DIC method is used to measure the longitudinal strain that allows the elongation happening along the specimen's gauge length, which is within 50mm or 25mm (for standard geometry 12.5mm width or subsize geometry 6mm width, respectively). The experimental data obtained from running this tension test will be later used to construct stress-strain curves derived from force-displacement data from each separate test. Specimens are then painted for DIC purpose. Example of painted specimen is shown in Figure 3-10.

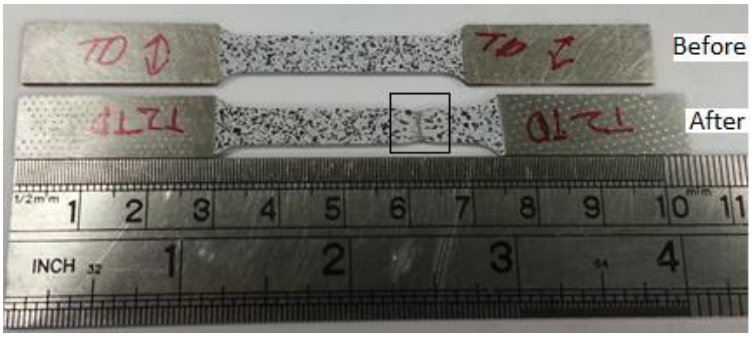

Figure 3-10 Example of DP1000 6mm width subsized specimen before and after testing. Highlighted box shows the failed region of specimen.

A pair of wedge-type grips is then equipped to the 25kN Tinius Olsen electric machine, which is suitable for flat specimens. The machine's crosshead speed is set to 2mm/min. For the optical 2D DIC, the rate of image capture is set at 1 image per second. The output signal from the Tinius Olsen machine is connected to DIC encoder so that the force and displacement obtained from the machine are synchronized with the DIC data capturing. Figure 3-11 shows the experimental set up of the conducted tensile testing.

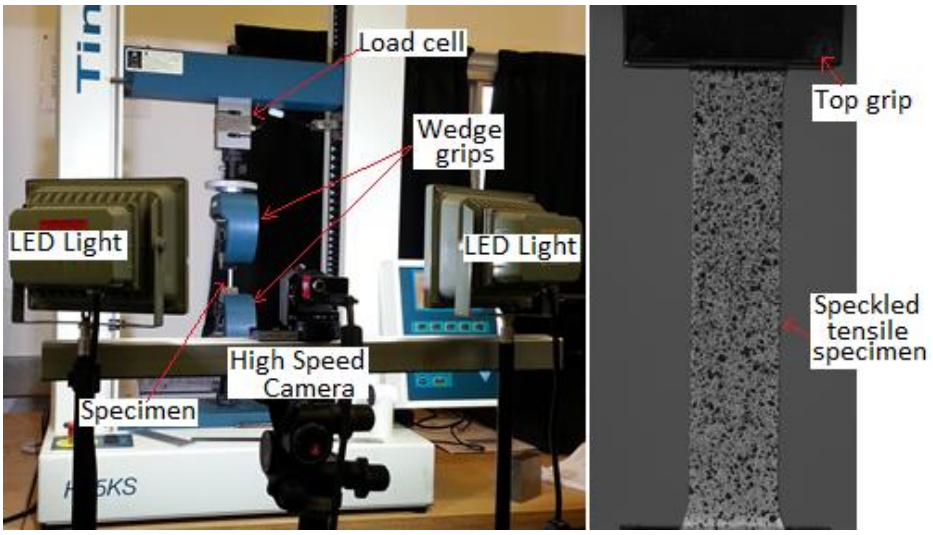

Figure 3-11 Experimental set up of a standard tension test on a 25kN Tinius Olsen electric machine (left). Tensile specimen fixed in a wedge-type grip with surface painted with random speckles for DIC purpose (right).

3.5.3. Optical 2D DIC to Measure Longitudinal Strain

Once all experimental data has been collected after finishing the tensile testing, next step is to construct the stress strain curves. The experimental data obtained from the tension testing need to be corrected due to effect of machine stiffness. According to (Hockett and Gillis, 1971), machines stiffness in mechanical testing is identified as ratio of the applied load to the deflection of all of the elements of the load train except the specimen gauge length. It is important to remove the effect of machine stiffness during the elastic interaction between specimen and testing machine to produce a correct result from conducting mechanical testing.

In the tensile testing, extracting strain happening in the specimen gauge length is possible with the use of optical DIC method. Common practice is by attaching strain gauges to the specimen gauge length or by using LDVT (Linear Variable Differential Transformer) device to measure the extension in the specimen gauge length. However, the optical DIC technique is relatively less complicated and provide additional information as necking begin in the specimen as well as useful strain distributions during the tensile testing.

Figure 3-12 shows the procedure to obtain strain happening in the specimen gauge length during the tensile testing. Force-displacement results obtained from the electric Tinius Olsen machine is synchronize to the DIC data capturing, which will later allow, the force and specimen gauge length extension to be plotted and therefore allowing a correct stress-strain data to be obtained. An example of image showing the virtual strain gauge using DIC method is shown in Figure 3-13.

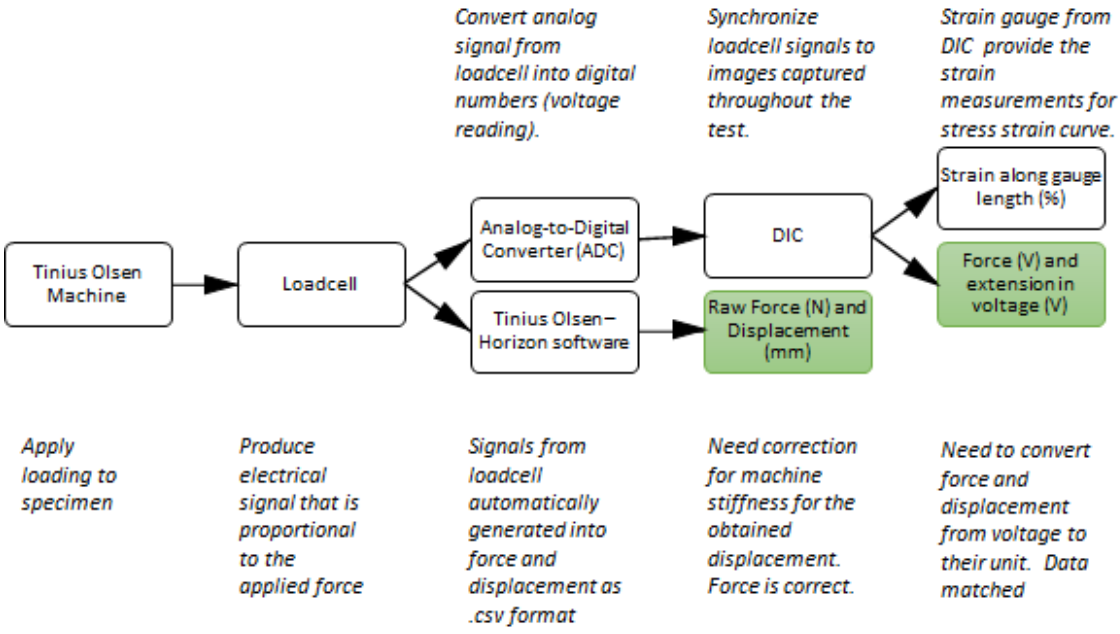

Figure 3-12 Flowchart explaining the procedure to obtain strain in tensile specimen gauge length.

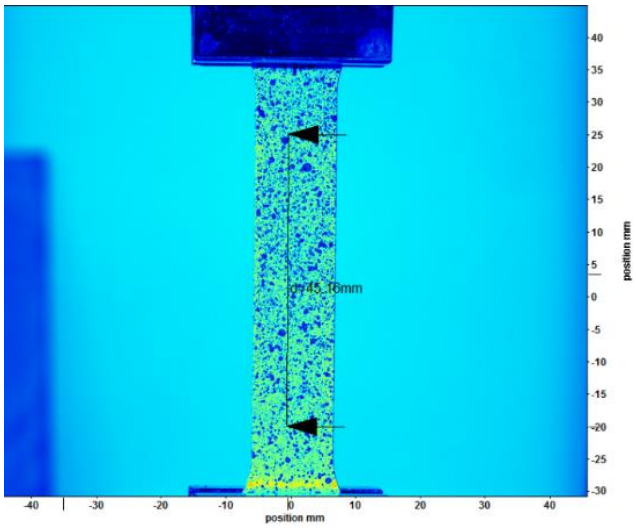

Figure 3-13 Example of applying virtual strain gauge using DIC technique.

3.6. Microscale Tensile Test in SEM using μ-DIC

3.6.1. Specimen Surface Preparation for SEM

Sectioning Process of DP Steel Sheets

Starting with the sectioning of DP steel sheets to produce the desired size and geometries of specimen, the rolling directions are first identified to allow the preferred orientation for specimen to be chosen. The specimens used for tensile test in SEM are chosen to be tested in their rolling direction. The most commonly used device for section is the abrasive cut-off saws machine, which is suitable to produce coarse-sized blocks of specimens. This machine cuts specimens faster, however the finishing surface after cutting must be removed for the true microstructure to be examined. Smaller and delicate specimens may require the use of precision cutting machines. The time taken for sectioning may be longer but provides better and precise finishing. However, when it comes to specimens with complex geometries it is preferably to use electrical discharge machining (EDM).

In this experiment, the received DP materials are cut into the 2mm-width micro tensile testing geometry as shown in Figure 3-14 (left) using Electrical Discharge Machining, EDM wire cut along the rolling direction of the DP steel sheet. This geometry is referred from Ghadbeigi et al. 2010 work as it is compatible with the micro-tensile stage in SEM which have been used previously.

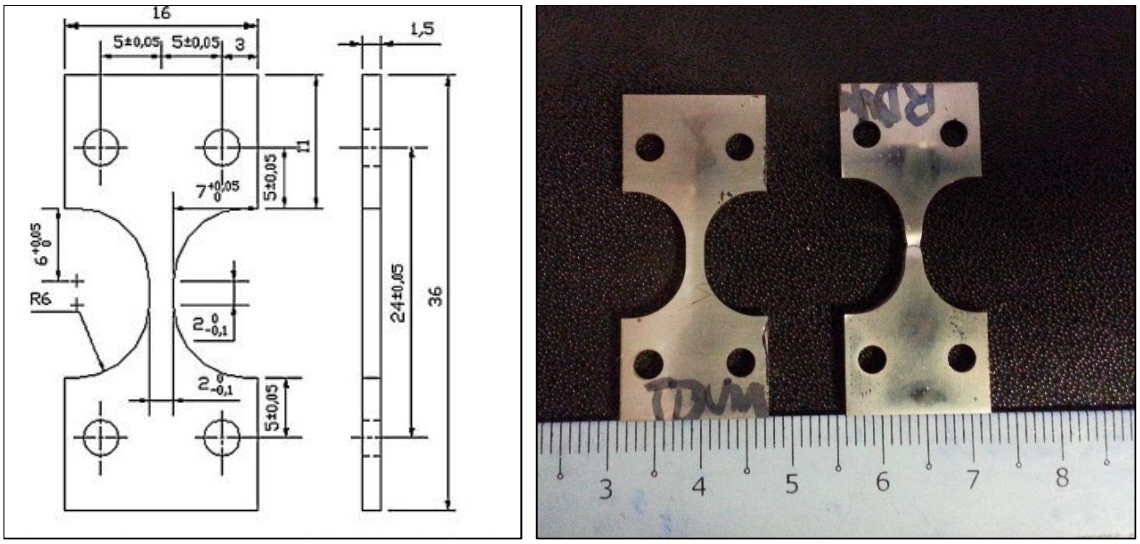

Figure 3-14(Left) Mini tensile specimen geometry with gauge width of 2mm by Ghadbeigi et al. 2010. *Dimensions are in millimetres, (Right) A picture showing polished and etched micro tensile specimen before and after testing.*

Grinding and Polishing Process of Specimen

In order to conduct the micro-tensile test in SEM, DP steel specimens under studied must be properly prepared to reveal the microstructures. Especially when the test results are going to be analysed using DIC technique, it is important to ensure the grain boundaries of the microstructure to be clearly observed; so that the SEM micrographs captured have excellent resolution with high contrast.

For the microstructure to be observed under SEM, the surface of the micro-tensile specimens has to go through a manual surface grinding and polishing process to achieve a flat surface and remove scratches. Usually, automated process is more preferable as it is time-saving, produces a uniform flatness and allow a better control for the removal of material during grinding. However, the current micro-tensile geometry being used is too big to fit the automatic grinding-polishing machine. Therefore, the grinding-polishing process is carried out manually.

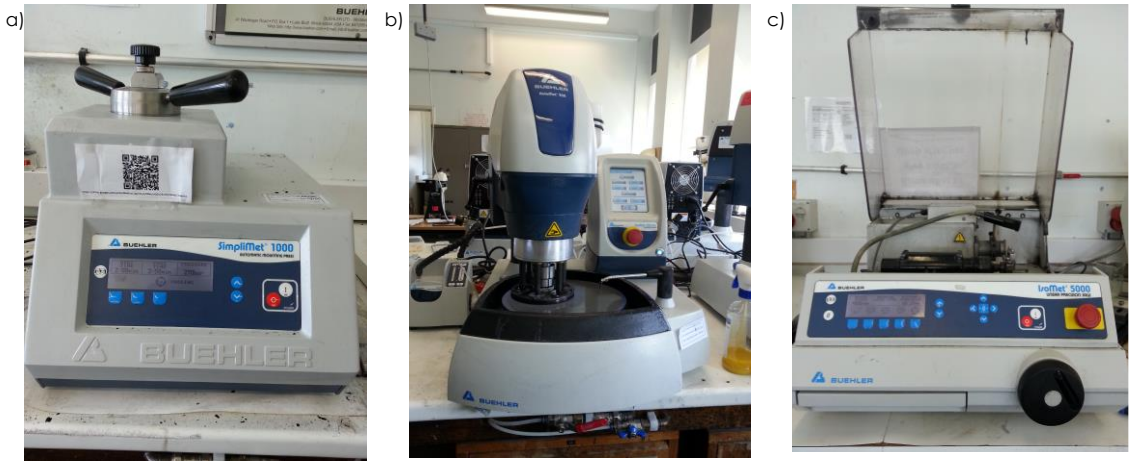

Figure 3-15Examples of the machines which are used for the surface preparation on specimens. (a) Hot-mounting machine to mount specimen for gripping the specimen during polishing. (b)An Automet machine that allows polishing to be carried out automated or manually. (c) A precision cutting machine.

For this experiment, the grinding process follows a six-step procedure of material removal using different grades/roughness of abrasive silicon carbide (SiC) papers. The start of the process begins by using the SiC papers with the coarsest grade that is P180. Coarser SiC papers like grade P180 allow faster rate for material removal compared to grade P1200. The sequence for the grades of SiC papers used are P180, P280, P400, P800 and lastly P1200. Duration for grinding during each steps depends on the rotation speed of the machine use. For a speed of 250-300rpm, the grinding process using SiC papers P400 and above is around 3 to 4 minutes. After the grinding process, the next procedure is polishing that is the finishing process for the removal of micro scratches (cannot be seen with naked eyes). There are two steps for the polishing process, which are polishing using 6μm then 1μm diamond suspensions. Once the specimens are polished to a very fine mirror-like finish, they are then inspected under an optical microscope to ensure the surface is scratch free and either ready for etching or need to be grind/ polish. Figure 3-15 shows the machines that are used for the sample surface preparation.

Etching Process- Revealing Microstructure

In order to reveal the microstructure features of DP steels at microscopic level, the ready polished specimens need to be etched using chemical technique of metallographic etching. There are various etchants used to reveal the microstructures of steels. Enchants make the observation of specimen microstructure possible by revealing grain boundaries, inclusions, different metallic phases, and cracks. Among the common etching techniques being used are chemical, electrolytic, thermal, molten salt, magnetic and plasma (Voort, 2018). The commonly used by researchers are through chemical and electrochemical etching.

For DP steels, the commonly used technique is through chemical technique using Nital with a 2% concentration. In low carbon steels, Nital is highly effective for revealing the ferrite grain boundaries as well as the martensite phase (Voort, 2018). The 2% concentration Nital solution can be prepared by diluting 2ml nitric acid into a 100ml industrial methylated spirits (IMS). The polished specimens are then etched in the Nital solution for 2 to 4 seconds until the mirror-like surface turned grey (foggy/ no longer shiny). The sample should be quickly cleaned /rinsed with isopropanol to avoid over etching before it is checked under microscope to determine whether the specimen needs more etching or ready to be observed in SEM. Etchant dissolves (bites) the metal exposed on the surface and leaving the microscopic grain features beneath to be observed. Over-etching will damage the specimen microstructure and prevent features to be clearly observed.

Micro-Tensile Test in SEM

Tensile testing are then carried on these polished micro tensile specimens out using the Deben MICROTEST tensile stage as shown in Figure 3-16 which will take place inside a CAMSCAN SEM. The tensile stage module is capable of loads up to 5kN

(500kg). The module can also be used as a bending stage by changing the grips provided by the manufacturer. The module can be controlled using acquisition software, which also gives the real-time display of force-extension curve for further use in analysing the result. Further details on the procesure to carry out the micro-tensile test in SEM is throroughly discussed in the next section, Section 3.6.2 Interrupted Micro-Tensile Testing with Micro-Scale DIC at Different Magnifications Simultaneously .

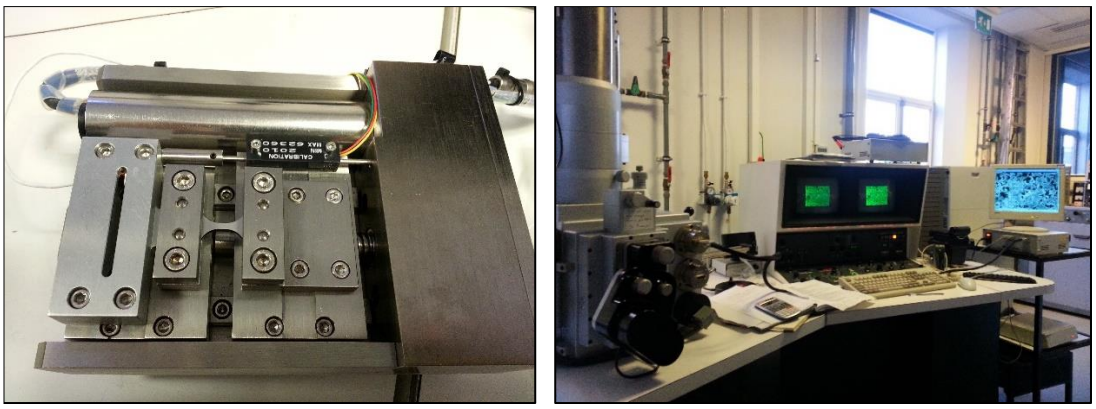

Figure 3-16 (Right) 5kN Deben MICROTEST tensile stage with tensile specimen, (Left) CAMSCAN, SEM used for micrograph acquisition.

3.6.2. Interrupted Micro-Tensile Testing with Micro-Scale DIC at Different Magnifications Simultaneously

For the micro-tensile test, the testing will be interrupted (stopped) at several times instead of running a continuous test from beginning of loading to final fracture of specimen. The higher frequency of interruptions will facilitate the µ-DIC analysis and benefits towards the investigation of damage in the microstructure. Throughout the test,

during each stages of interruptions (when test is stopped at every 0.05mm) the microstructure of the area of interest is captured at two magnifications using the SEM.

At the end of the test, two sets of different magnification images are acquired where the total of images for each set can vary from 27 to 30 images which depending on the tested materials and the numbers of interruption stages. The different magnifications are intended for the post-processing of the result. The set of images with low magnification provide a larger field of view of the investigated area of the microstructure. Micrographs with larger field of view gives information of representative microstructures of the different tempering condition materials, for example the martensite to ferrite volume fraction, martensite-ferrite distribution (microstructural morphology) and describing the deformation in the microstructure. To describe the plastic deformation that is taking place in the microstructure before specimen failure (break), the set of images captured earlier are analysed using Digital Image Correlation (DIC) technique to provide strain distribution in the representative microstructure. Utilising the DIC in this study is intended for the comparison for each specimens of their plastic deformation in the representative microstructure before complete failure happen. Example of strain distribution obtained from μ-scale DIC analysis performed are shown in Figure 3-17.

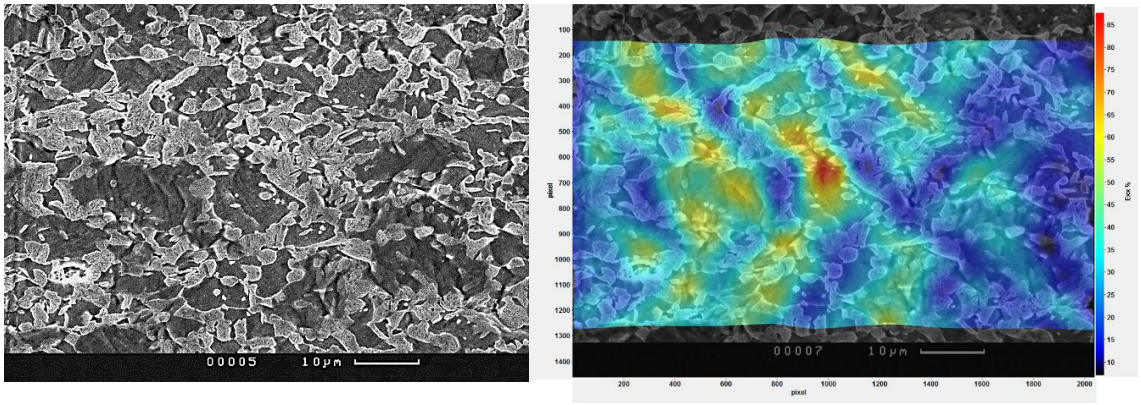

Figure 3-17 Deformed specimen from tensile test on the onset of specimen fracture (left) and strain maps superimposed on the deformed specimen micrograph using the commercial StrainMaster software from LaVision (right).

The second set of images which are taken at high magnification, thus giving a much lower field of view. The location area of analysis for high magnification images are within the low magnification image. Basically, the high magnification image is a small section of the low magnification image which is magnified (zoomed-in) and then captured thus producing images with a closer view at the microstructure. Higher magnification or close-up view of the microstructure allows damage nucleation sites to be captured and will be further analysed to see the maximum plastic deformation in the martensite phase before they break. This method will be using DIC as well so that strain values before martensite failures can be quantified and these values will be compared with damage nucleation sites happening in among all six different tempering condition materials. For this damage nucleation study, damage is identified in several sites (six or more locations) in the microstructure of the low magnification image to provide statistically meaningful result of the strain analysis on the damage sites. Figure 3-18 shows a simplified experimental procedure in the form of a flowchart summarising the steps being taken to carry out the in-situ tensile test to ease the understanding of the experimental procedures section.

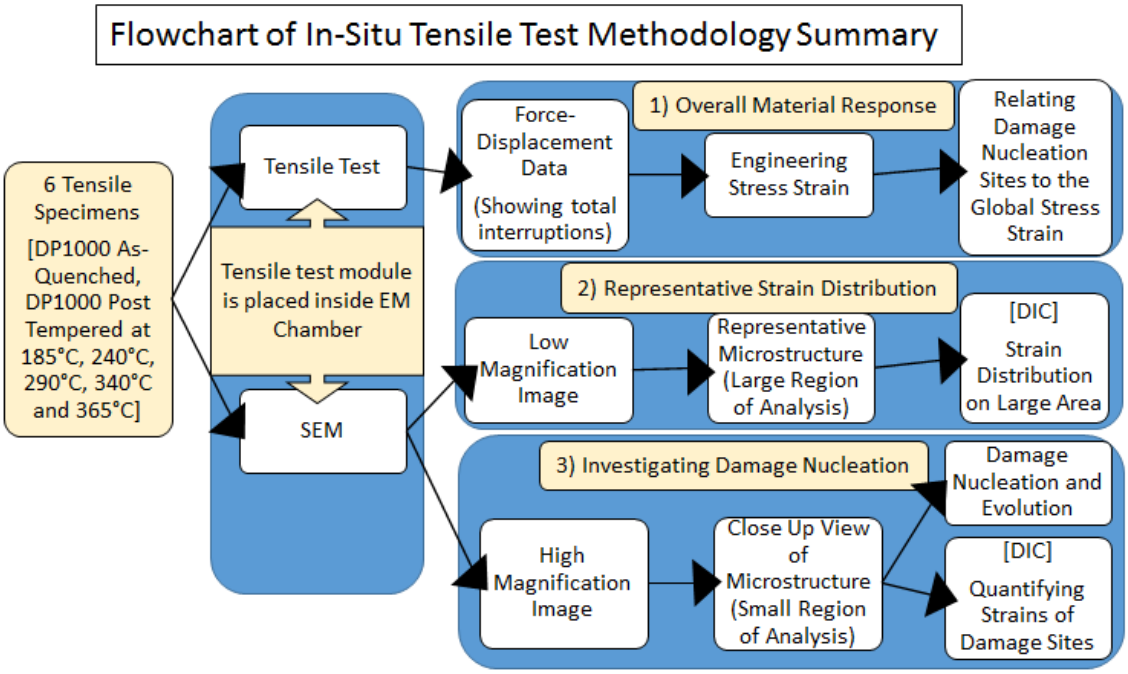

Figure 3-18 Experimental procedures being used to conduct the in-situ tensile test that is summarized in a flowchart.

3.6.3. Procedure to Obtain Average Strain for Ferrite and Martensite from DIC Strain Map

Strain maps from DIC results provide information on strain distribution happening in the analysed microstructure. However, problems arise when there is a need to inspect the average deformation taking place in the ferrite and martensite separately when the specimen reaches UTS during tensile loading. This is because, the DIC software is unable to distinguish the strain fields in ferrite and martensite so the software can only extraction of strain fields in both ferrite and martensite phases as a whole. This section will explain the procedure to extract the average strain values of ferrite and martensite from a DIC strain map (obtained from running a micro-scale tensile test).

As explained in the literature review section, it is known that these strain maps, or strain fields are obtained by the discretisation of an image into smaller interrogation

windows which will later produce deformation vector fields within each of these interrogation windows. For this particular analysis, an interrogation window size measuring 24 x 24 pixels is chosen for this microstructure. For the correlation, an overlap of 50% was chosen to increase the vector fields which yields one deformation vector per 12 x 12 pixels interrogation window. Strain fields are then evaluated from the obtained vector fields per each interrogation windows, which yields the strain maps as shown in Figure 3-20 (A).

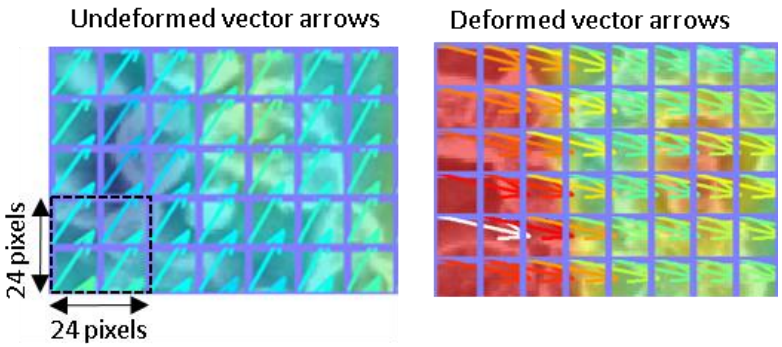

Figure 3-19 A section of a magnified area of a strain map. Arrows represents the vector arrows which the magnitudes and orientations change according to the deformation of microstructure. Grid overlays represents the interrogation window size.

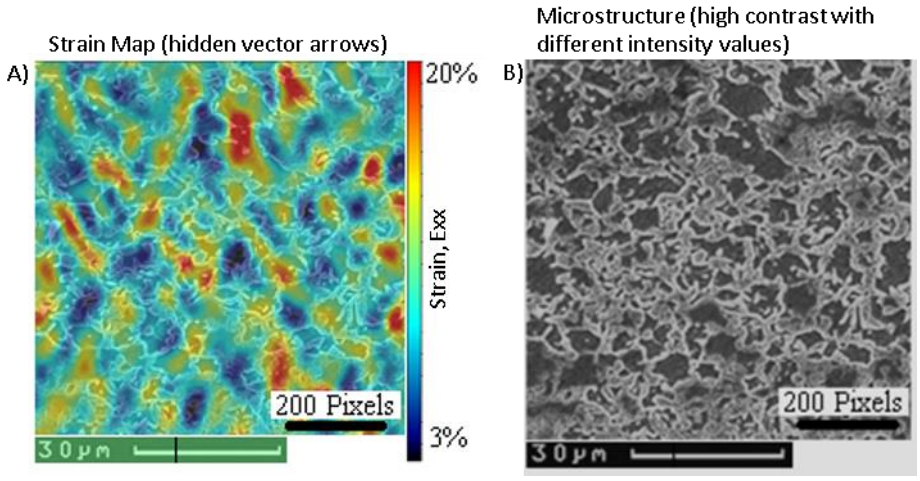

Figure 3-20 Strain map at UTS (A) and the grey scale image of microstructure without strain map overlay (B).

Figure 3-20 shows the two main results required in order to obtain the mean strain in ferrite and martensite. A strain map (Figure 3-20 A) with successful correlation, is

required for the extraction of strain fields measurements and a grey-scale microstructure image with good contrast (Figure 3-20 B) is needed for distinguishing between ferrite and martensite phases. In order to this, the image intensity values (pixel values) that represents the brightness of the pixel is extracted from the microstructure image. For a grey scale image, intensity values range from 0 to 255; where 0 is black and 255 is white. A threshold between this intensity range is chosen to segregate the values for dark phase ferrite and bright phase martensite. The strain values from DIC result (within the 12 x 12 pixels) and the intensity values obtained from the grey-scale image needs to be matched, so that the strain fields coordinates are synchronized to the coordinated of the intensity values.

To match the coordinates between strain vectors from DIC and intensity values of a grey-scale image cannot be done directly. This is because, strain vectors are extracted for every 12 by 12 pixels but the grey-scale intensity data is obtained for every pixel in the images. The extracted strain vectors data yields to a grid of 123 x 170 (20910 data counts) while data obtained from intensity values is 1476 x 2040 (3011040 data counts). Grey-scale image needs to be compressed by 12 times where an area of 12 by 12 pixel intensity is averaged to 1 mean pixel value, and the total 1476 x 2040 pixels is reduced to 123 x 170 pixels that finally matches the strain vectors.

Once the intensity values are matched to strain vectors from DIC, each strain vectors are now correctly positioned to each mean intensity values of the grey-scale image. Now, the data can be extracted into Excel spreadsheet in order to separate the strain values of ferrite and martensite according to the range of intensity values. The extracted data are tabulated according to their positions as shown in Figure 3-21 (a). Strain values in ferrite and martensite are still mixed in one column. So, to separate the strain values for ferrite and martensite, column for mean intensity values need to be sorted in ascending order (ensuring the strain values follows the sorted intensity value). A

threshold value, *X* is chosen to separate the intensity values for ferrite (dark region) and martensite (bright region). Any values that falls between 0 to *X* has dark intensity, so they are categorize into strains for ferrite; while for the rest of the strain values that fall between the range (*X*-1) to 255 will be the strain for martensite. The tabulation of this data is shown in Figure 3-21 (b).

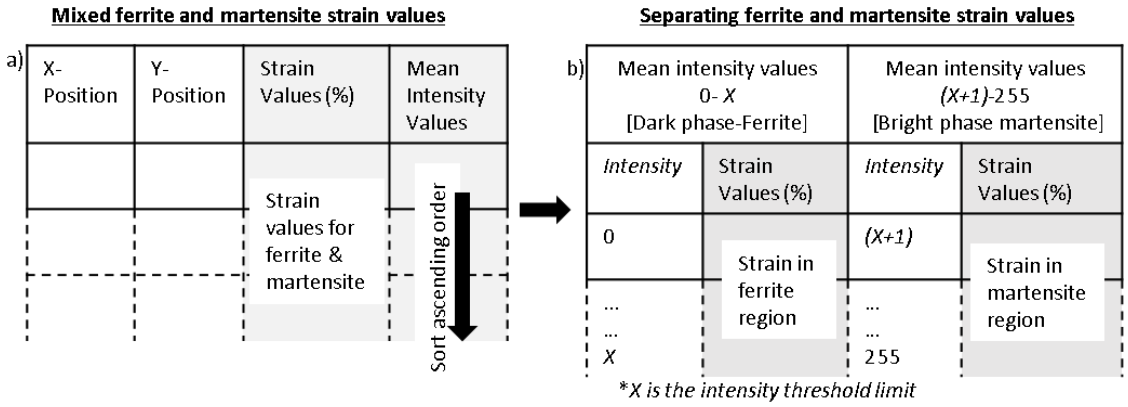

Figure 3-21 Tabulating data for the extracted strain values and intensity values according to their position (a) and the final table for separating the strain values in ferrite phase and strain values in martensite phase.

Once the strain values for ferrite and martensite are segregated, the average strain values for ferrite and martensite can finally be calculated by plotting a frequency distribution plot. This is shown in Figure 3-22, where the vectors from DIC strain map are extracted and processed to allow the average strain of ferrite and martensite to be assessed from the frequency distribution plot.

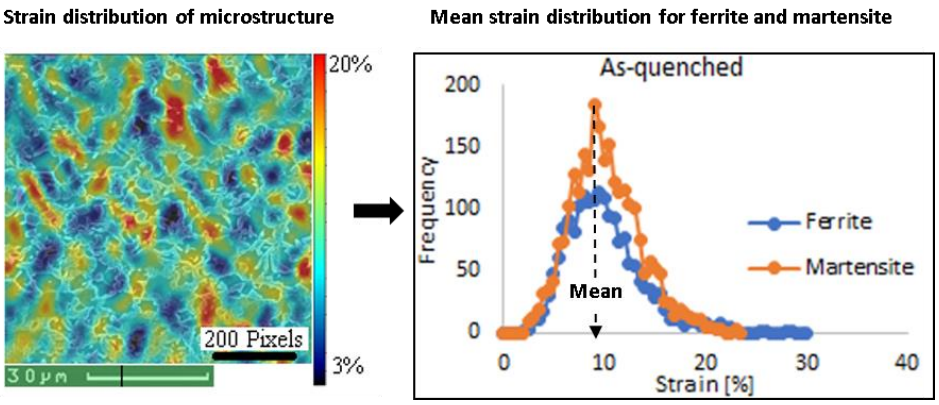

Figure 3-22 DIC strain map (left) provides the strain distribution for the analysed microstructure and frequency distribution plot (right) shows the average strain values in ferrite phase and martensite phase separately.

3.7. Punch Test using Optical 3D DIC

3.7.1. Overview

Several experiments have been conducted in order to study crack propagation such as micro-scale bending test, laboratory scale bending test and using pre-strained specimens to be tested in bending tests; however, results obtained were not convincing thus leading to the development of a laboratory-scale punch test.

Guided with concept of OSU test, a few other suitable testing options are also found and studied to find the most suitable test for this project. In fulfilling the main objectives of this project, the experiment should be designed in way that the test could initiate cracking in the materials and allowing damage development and crack propagation to be studied for enabling the advancement of understanding the DP steel damage behaviour.

The development of this punch test for the study of damage seems to be more beneficial in terms that the exerted biaxial loading on the DP specimens will replicate the forming process in the automotive industry.

3.7.2. Designing Process

There are two main criteria which must be considered prior the designing the experiment. Firstly, the conducted test should be to initiate crack in the studied DP steel specimens. Secondly, the rig of the experiment should be designed to be compatible with the attachments for the 3D-DIC equipment and should be fit enough to be placed on the Mayes Machine. Apart from that, it is very crucial that the rig to give a maximum exposure of the specimen surface that the DIC cameras views on the specimen's top surface area is large and not obstructed.

The rig should also allow enough light to reach the surface and the distance between specimen's surface and DIC cameras could be adjusted until enough focal length is achieved. This is an important feature of rig, as the cameras may need to be positioned at a specific distance from the surface to allow effective and continuous correlation while also avoiding blurred images due to high out of place deformation in specimens. The cameras positioning to the sample is shown in Figure 3-23.

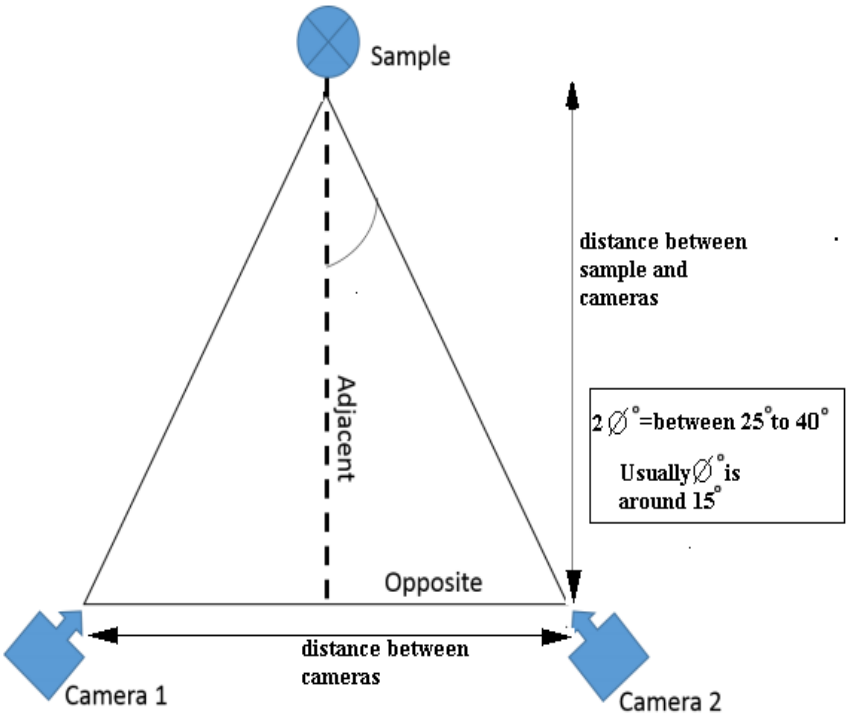

Figure 3-23 Schematic diagram of 3D DIC cameras set up which require the cameras to be placed at a certain angle and distance.

After considering several designs, the decision has finally come down to a small laboratory-scale punch test method as shown in Figure 3-24. The punch method will be an improvement made to a readily available formability test concept i.e. Hecker's LDH formability test. Among most of the existed tests, this concept seemed to be the best one that could provide relatively high amount of deformation. This concept is chosen as it is expected to exert very large deformation on the DP specimens to allow the development of damage to grow extensively hence, making the study of damage possible.

This laboratory scale punch test seems to be an ideal representative of real forming operation condition and it is expected to provide biaxial loading on the studied DP materials which in turn provide the similar type of damage happening during a forming process.

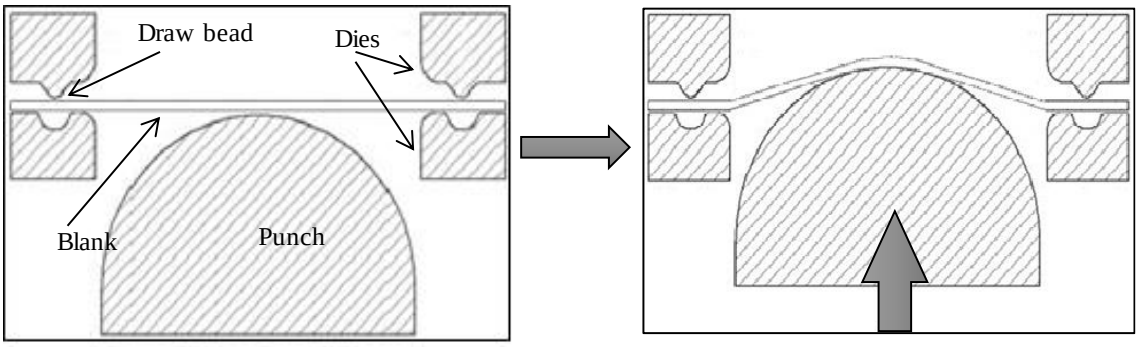

Figure 3-24 Schematical concept of punch test to be used to study damage in DP steels for this project.

This punch test almost similar concept to the stretch forming method. After considering other forming test examples, it is found that many of the formability concepts involves stretch forming. The stretch forming testing concept is found to be the most suitable for this project as it has been widely used for testing the autobody components in the automotive industry. In stretch forming process, the tested material will be subjected to out of plane stretching and biaxial tensile stresses which are regularly found in the manufacturing of autobody parts e.g. door panels, trunk lid, truck cab roof and etc (Panda and Kumar, 2010).

In designing the punch test, the procedure is mostly referred from the previously chosen method by Hecker, which is the LDH test and some from the cupping tests method. This method will be utilizing a hemispherical punch being placed on a hydraulic press machine (for this project is the 100kN electric Mayes machine) together with a die set to hold the specimen. A complete technical drawing of this test punch tool and dies is shown in Figure 3-25.

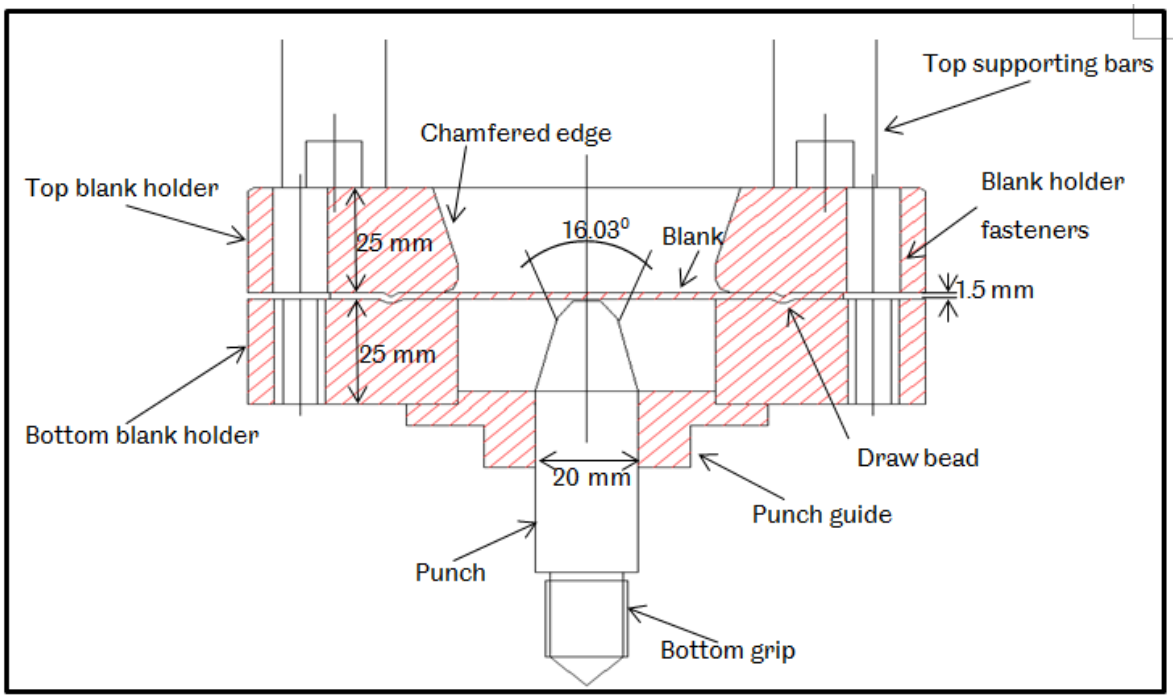

Figure 3-25 Laboratory scale punch test set up using a 90mm diameter blanks.

3.7.3. The Punch Test Components

90mm Diameter Specimen Blanks

This punch test will require the use of 90mm diameter circular blanks. The geometry is smaller than other standard forming tests, as long as the deformation-to-failure is sufficient for further inspection inside the SEM. This simple laboratory-scale punch test is aimed at exerting large deformation on specimens to allow damage formation. Figure 3-26 (left) shows an example of the 90mm diameter of DP 1000 steel blanks. For conducting punch test using 3D DIC, the surface of specimens has to be speckled.

First, a matte white paint is sprayed evenly until it covered the entire surface as shown in Figure 3-26 (right). Then, soon as it dries, the black spray paint is used to make a uniformly distribute speckle pattern on the white matte layer. The speckling should be done cautiously to avoid the blotchiness from effecting the strain analysis by DIC later.

It is important that the speckles background to be non-reflective and highly contrasting colour with the speckles

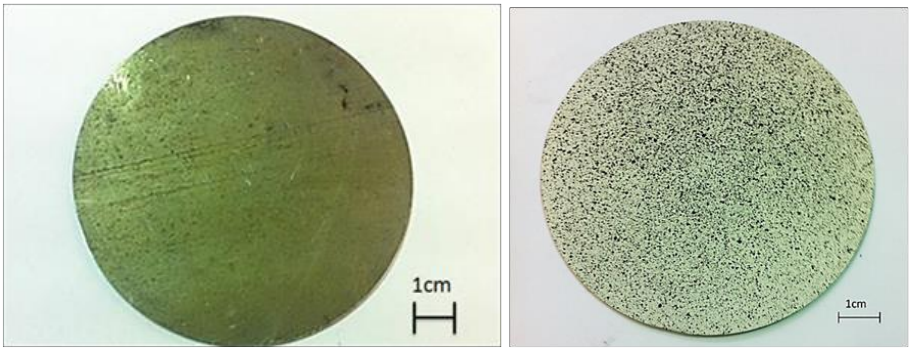

Figure 3-26 Specimen blank with 90mm diameter

Die Set

In order to securely constraint the whole peripheral of the blank during testing, a special die set, as shown in Figure 3-27 is manufactured with circular draw bead feature to secure the blank flanges from being drawn in thus, sufficiently gives the required hold-down force during punching and without actually causing damage to the blank itself. This will only let the area of materials within the die opening to be deformed during stretch forming. The dies will be tightened with six bolts around it giving enough force to ensure the blank is in a secured position.

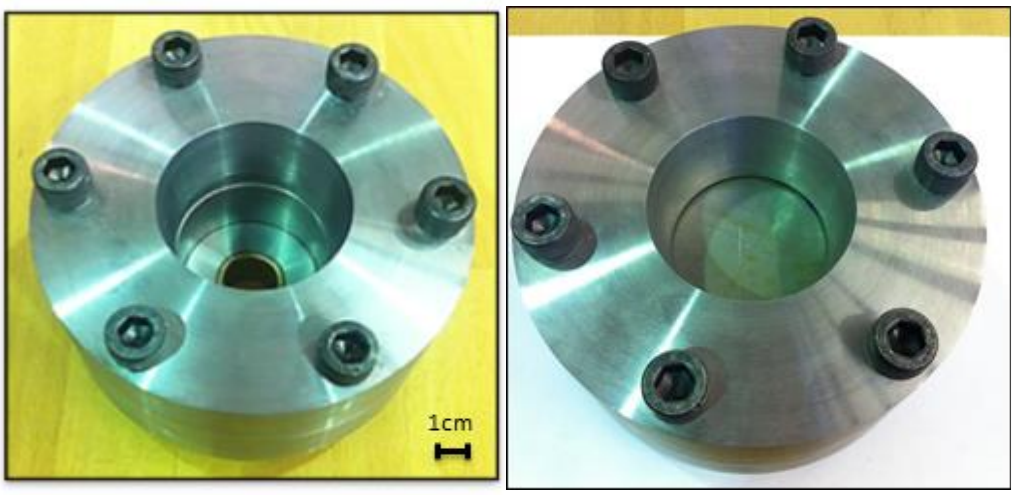

Figure 3-27 Empty die set (left) and die set with specimen fixed in between the die set(right).

Punch Tool

The punch played a very important role in this testing. It is expected that the punch should exert large deformation on specimen. Without a proper design, the desired result could not be achieved. Thus, a round headed conical punch as shown in Figure 3-28 is manufactured with several properties which needed to be prior acknowledged. A few problems regarding the punch that needed to be foreseen are the friction conditions at the tip. When friction is too high, failure of specimen will not be due to pure stretching from the punch. Instead, it will tear up due to the material cohesion at the tip which would happen when sharp asperities at the punch tip begin to pull the material in contact as the punch moves upwards (at a microstructural level). Hence, the punch tip is smoothened to remove any microscopic sharp asperities and hardened to ensure the punch tip is hard enough and there will be no material flow and wear when it is in contact with the sample. For this project, for all the four experiments conducted during the real testing, graphite grease is used for lubrication. With the lubrication, there will be less resistance between the interface of punch tip and material due to the low coefficient of friction of graphite thus inducing sliding.

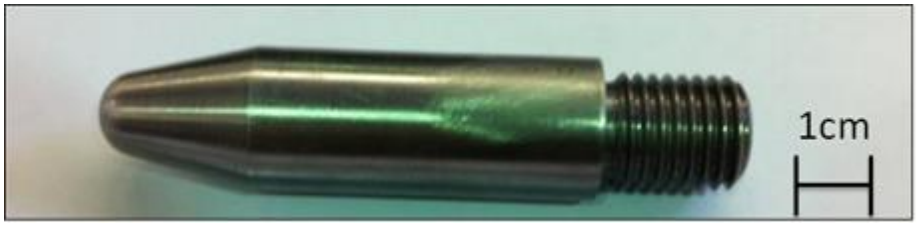

Figure 3-28 Conical Head Punch Tool

Punch Test Complete Set Up with 3D DIC

The punch test rig is set up as on a 100kN Electric Mayes machine as shown in Figure 3-29. The general method of assembling the whole rig is started with the clamping of the blanks. The blank is secured in between the dies and tightened before being put on the punch. The die set will be supported with a pair of stands from the bottom for a little clearance between the punch tip and the specimen to avoid the punch from damaging the specimen before the start of the experiment. Supporting bars are then placed on top of the die set to provide a hold down force during the test and is tightly bolted at the connection which secures the position of both top supporting bar and bottom supporting bar of the Mayes machine to secure the die set.

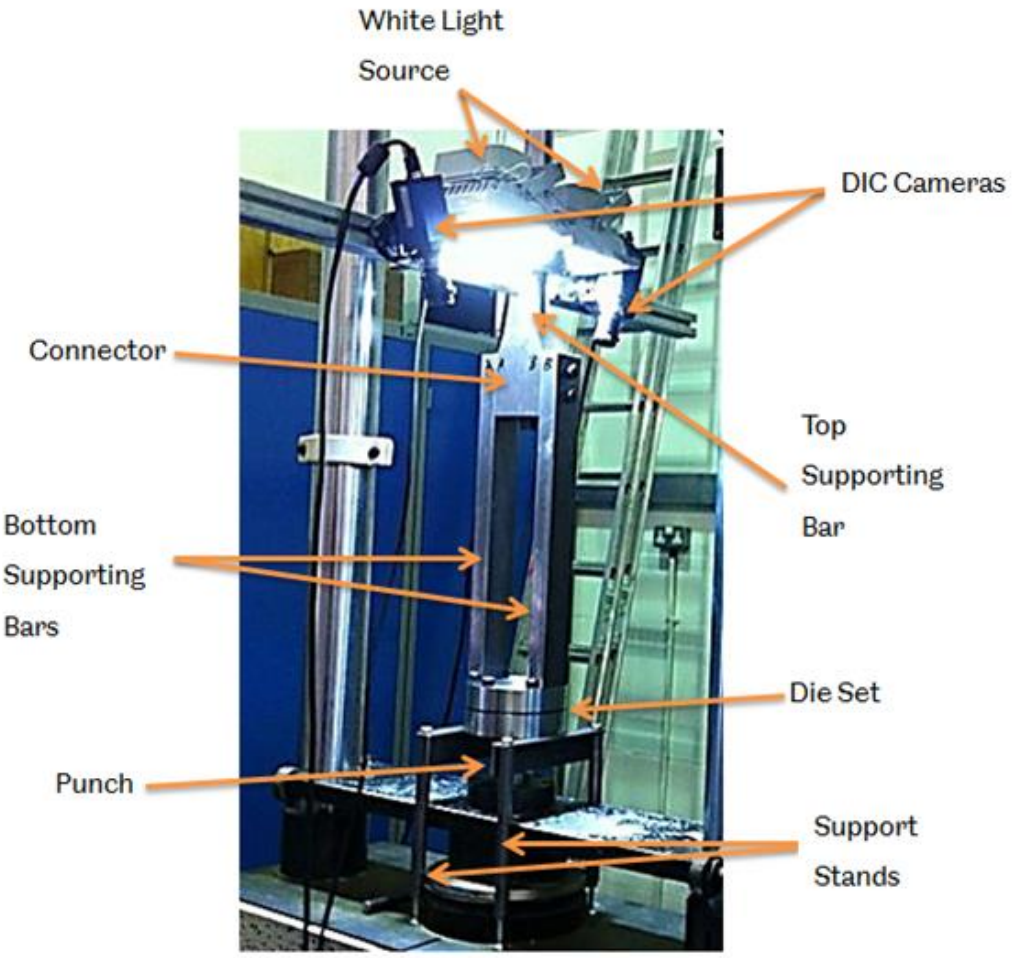

Figure 3-29 A complete set of punch test using 3D DIC technique

The 3D DIC set up is done by mounting cameras on the boom at the top of the test rig and connecting both of the cameras to the computer to view the area of interest on the specimen. On the computer, the software being used for the pattern recognition based on the principles of digital image correlation is the VIC-3D by Correlated Solution. Every pair of images continuously captured by both of the cameras will be processed into stereo images. Both of the cameras orientation is adjusted until the area of interest is at the centre of camera views, then the best focal length is found by adjusting the lenses. Figure 3-30 shows the measurements of cameras set up relative to the specimen. Cameras are adjusted until they are in focused at the same location on the specimen preferably at the centre region. Examples of speckles images with a good focus are shown in Figure 3-31.

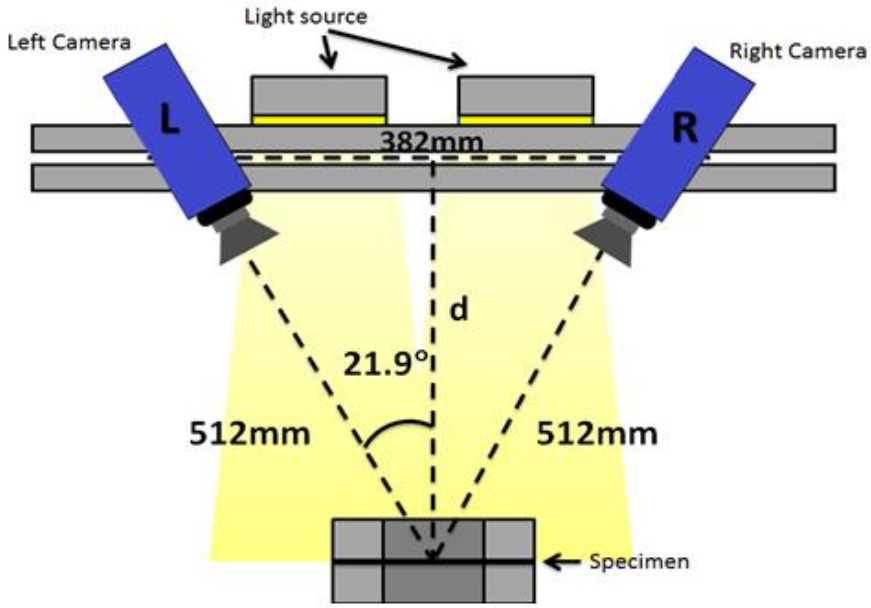

Figure 3-30 3D DIC (stereo vision) cameras set up at a measured distance relative to the position of specimen.

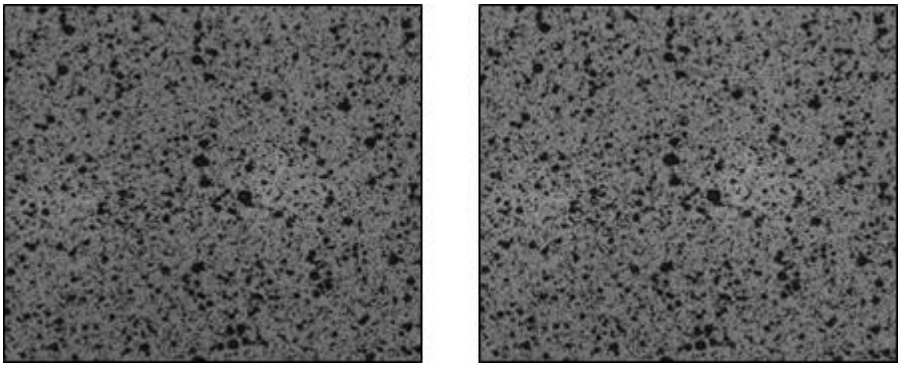

Figure 3-31 View from both cameras which should be focus on the same location on the sample, preferably at the centre.

Once both cameras are in focused, calibration process is carried out by using a pre-determined dot-pattern calibration plate as shown in Figure 3-32. At least 25 images are capture for the calibration process which later only 15 images with good calibration score are chosen to make sure the calibration error between the two cameras is below 0.03. During the capturing of calibration images, the calibration plate is move under the cameras view to produce images involving translation, rotation and in- and -out-of-plane movements. Punch test can be started as soon as 3D DIC set up is ready.

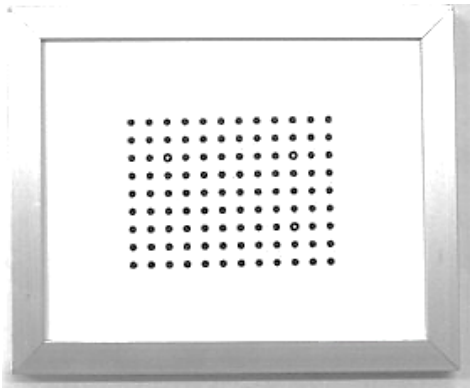

Figure 3-32 Example of calibration plate for 3D DIC which are available in different pitch sizes between the dots and dots counts.

Chapter 4

Damage Development in DP1000 Steels with Different Heat Treatments.

This chapter will present the result obtained from the mechanical testing conducted on the tempered DP1000 steels. The effects of tempering on the mechanical behaviour of DP1000 steel are observed by comparing the obtained tensile response from the standard tensile test. In another test which uses a micro-scale tensile test conducted inside SEM, deformation happening at the microstructure are analysed using micro-DIC and presented to understand the effect of tempering on reducing the strain partitioning of the two phases, ferrite and martensite (the softening of martensite or hardening in ferrite). Apart from understanding the deformation behaviour by observing the strain accumulation in the microstructures, results obtained from studying the earliest damage mechanism happening on the surface of DP1000 steels are also presented. Result collected on the earliest martensite cracking found are presented. From the results, the required strain values to initiate crack in martensite phase through tensile testing inside SEM are identified as well as, successfully determine two damage mechanisms of cracking of martensite. Lastly, this chapter also presents the post-mortem results of broken micro-tensile samples for the analysis of damage initiation in the cross-section.

4.1. Investigation Flow Process

In this investigation, two experiments have been conducted and repeated on all the DP steels specimens of different tempering conditions. The flow process of investigation on damage development of the DP steels is shown in Figure 4-1.

The first part of this investigation is to obtain mechanical response the of all the DP1000 steels under studied by running a standard tensile test (grey box in the flowchart is labelled as number 1). The result obtained will highlight the comparison between each material of different tempering conditions based on the obtained stress-strain curves.

The second experiment involves the use of micro-tensile testing inside SEM that allows damage development in the DP steels to be studied at microstructure scale. Results from this experiment are then categorized into three main sections as in highlighted grey boxes (number 2, 3 and 4) in the flowchart.

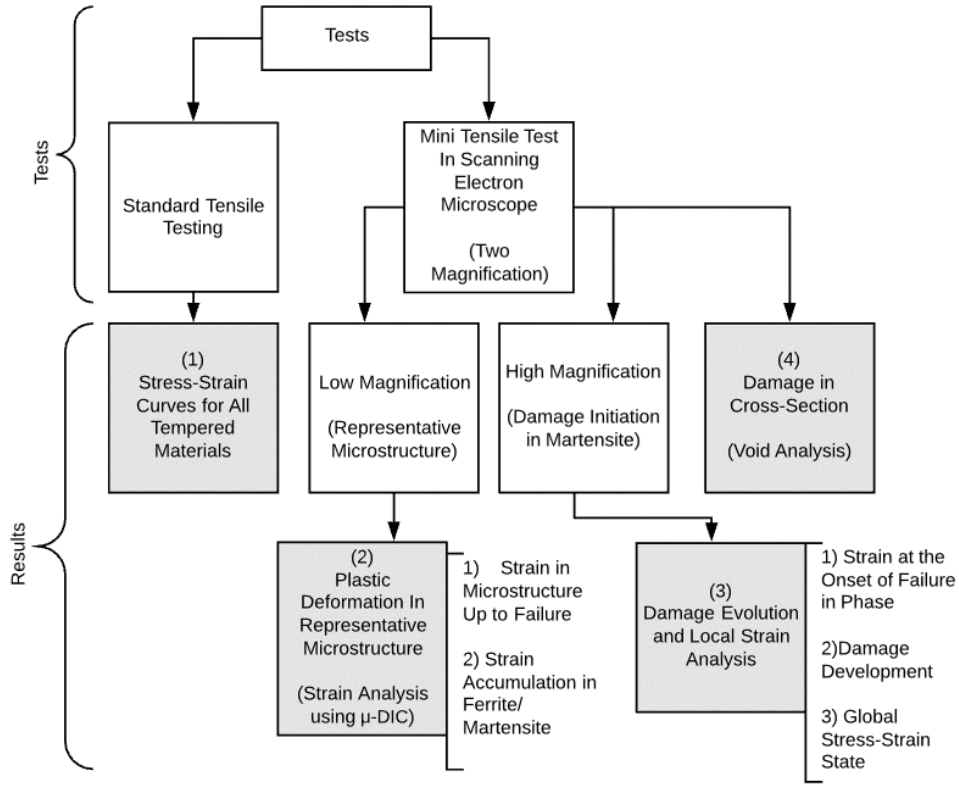

Figure 4-1 The flowchart shows the structure of results which are presented in this chapter.

4.2. Tensile Testing

A standard tensile testing procedure has been carried out on all different tempering conditions DP1000 specimens. The experimental procedure for this tensile testing has been explained previously in **Section 3.5-Standard Tensile Tests using Optical 2D DIC**.

4.2.1. Preliminary Testing

The as-quenched (not-tempered) DP steels are first tested in different orientations to determine whether the material is anisotropic. As previously explained in the methodology sections, this test will be using a standard subsize 6mm width tensile specimen due to provided material size limitation (as-received materials provided at first were too short in length for 12.5mm tensile specimens to be machined in transverse direction). In Figure 4-2, results from the three orientation shows the same behaviour in the elastic region, yielding and UTS. For the elongation to failure, the difference is at approximately 0.7%. Since the result show a very small difference from directionality effect, all DP1000 materials of different tempering conditions will be tested along the longitudinal direction.

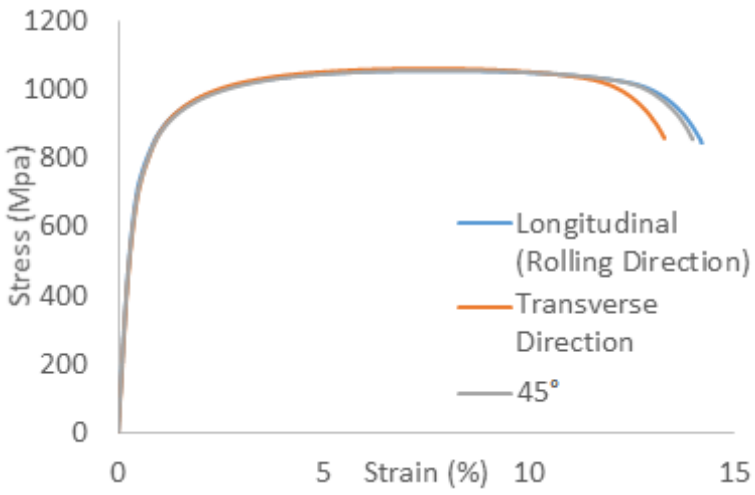

Figure 4-2 Stress-strain curves of as-quenched DP1000 specimen tested with varying orientations.

The result obtained for this experiment is validated by comparing against the result obtained from the industry, Tata Steel. Stress-strain responses from a 6mm width specimen and 12.5mm width specimen is plotted against a "reference" curve obtained by the industry which using a 25mm width tensile specimen geometry. The stress-strain curves in Figure 4-3 shows that the tensile testing results using a 12.5mm width are in good agreement compared to the results obtained in the industry, with a UTS at around 1050MPa and maximum elongation to failure of 14%. The specimen of 6mm width geometry shows a drop-in stress near failure, but the overall behaviour in elastic and plastic region up to UTS matches the reference curve, nevertheless. It is important to do this check, to ensure correct data acquisition obtained from the machine. With this, it is confirmed that for later tests (in obtaining stress-strain curves comparison on DP1000 with different heat treatment), 12.5mm width geometry will be used and should be machined along the in the longitudinal direction of the steels.

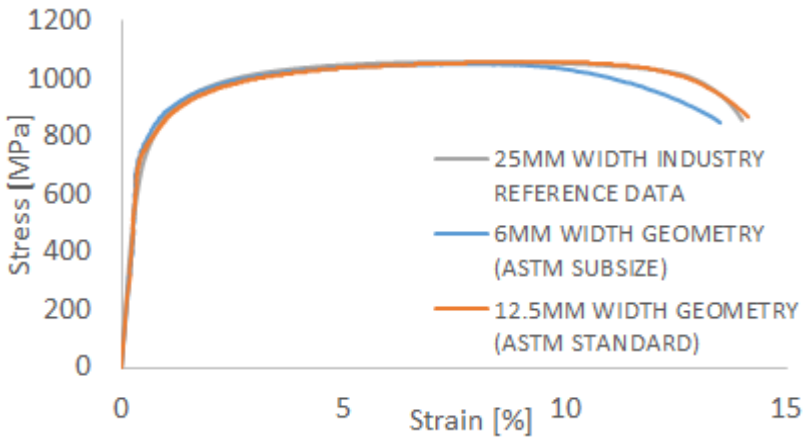

Figure 4-3 Stress-strain curves of as-quenched DP1000 comparing tensile specimens of different geometries responses.

The tensile testing conducted earlier provide confidence in choosing the right specimen geometry as well as allowing this study to focus the material response only in the longitudinal direction.

4.2.2. Stress-Strain Curves for DP1000 Steels with the Effect of Tempering

This section will present the representative stress-strain curve for the investigated DP1000 steels. An ASTM standard tensile testing procedure has been performed on all the studied materials which are DP1000 as-quenched (without any tempering) and the five sets of DP1000 steels with different tempering temperatures at 185°C, 240°C, 290°C, 340°C and 365°C. All six conditions of DP1000 materials are cut according to the 12.5mm width geometry standard tensile testing coupons and in the longitudinal direction (rolling direction, RD) and are put to test.

Tensile specimens are prepared in three batches. Each batch involves the testing for all six DP1000 materials of different tempering conditions. Once the tensile testing is completed on all the three batches, stress-strain curves are generated from the force-displacement data obtained from the electric machine and specimen elongation measured using optical DIC. The method being used to obtain the stress-strain curve has been explained previously in section 3.3.3-Optical 2D DIC to Measure Longitudinal Strain.

Figure 4-4 shows the complete result of the stress-strain curves obtained for all six materials presented separately according to their tempering conditions. Each plot comprises of three curves from the three batches of testing. Scatter plot for each material show that results are consistent for all three batches, which means tensile testing method is reliable and has good repeatability. The elastic region, yielding point and the UTS maintains approximately the same for each material except for the maximum elongation before fracture. In the as-quenched (AQ) material, curve is smooth without any presence of Lüders bands (secondary yielding). However, with the increase in tempering temperatures, the Lüders bands appears to be more prominent in the curves.

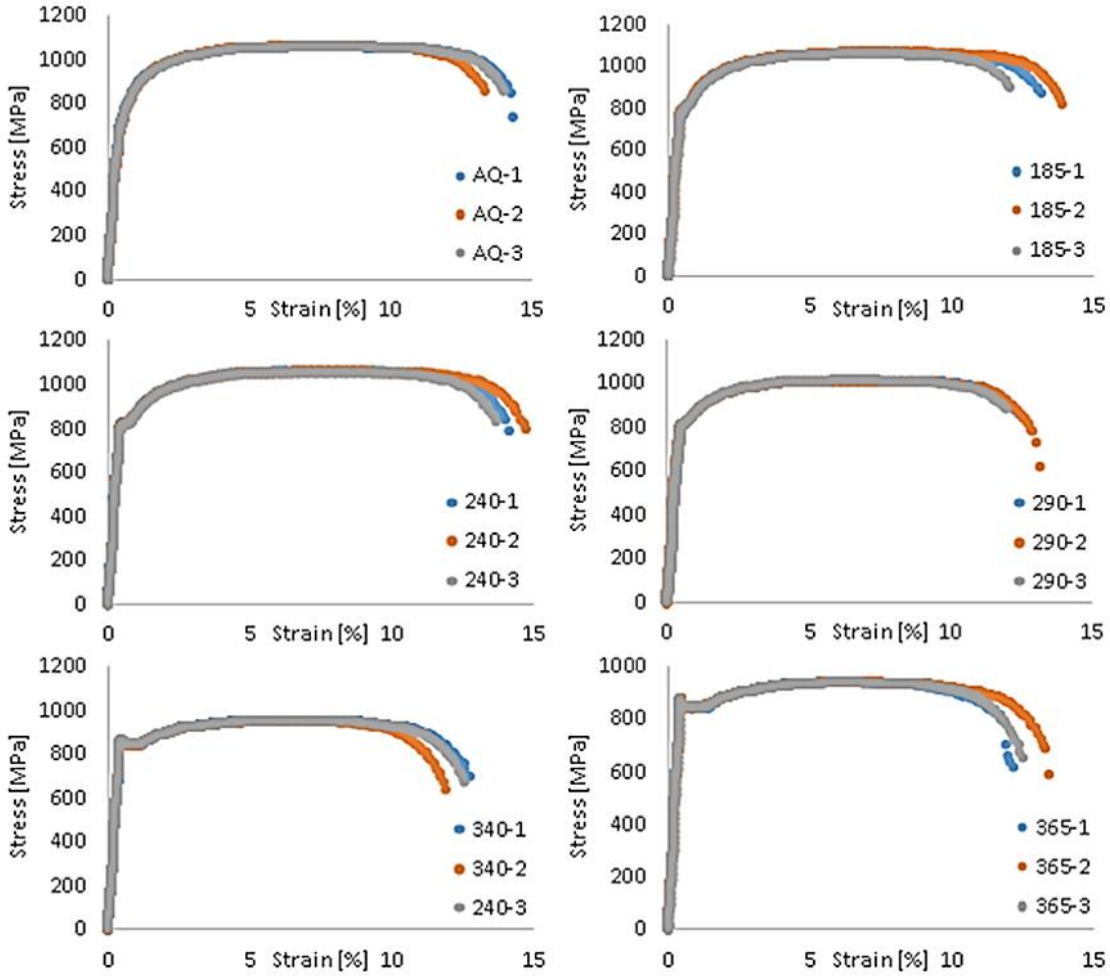

Figure 4-4 Stress-strain curves obtained from standard tensile test using an ASTM standard 12.5mm-width tensile geometry.

Table 4-1 Mean result for the stress-strain curves obtained using ASTM standard 12.5mm-width tensile geometry.

	Batch 1		Batch 2		Batch 3		σ_{UTS} [MPa]		ε_{max} [%]	
	σ_{UTS} [MPa]	ε_{max} [%]	σ_{UTS} [MPa]	ε_{max} [%]	σ_{UTS} [MPa]	ε_{max} [%]	Mean	SD	Mean	SD
AQ	1060.50	14.28	1063.70	13.30	1061.10	13.97	1061.77	1.70	13.85	0.50
185°C	1067.10	13.11	1069.60	13.87	1063.10	12.04	1066.60	3.28	13.01	0.92
240°C	1062.90	14.16	1060.20	14.72	1057.90	13.66	1060.33	2.50	14.18	0.53
290°C	1041.30	14.16	1013.40	13.14	1015.40	12.67	1023.37	15.56	13.32	0.76
340°C	955.30	12.73	952.40	11.90	953.90	12.58	953.87	1.45	12.40	0.44
365°C	941.60	12.12	941.00	13.37	939.80	12.46	940.80	0.92	12.65	0.64

**σ_{UTS}: Ultimate tensile strength (MPa)

ε_{max}: Maximum elongation to failure (%)

SD: Standard deviation

The values for UTS, σ_{UTS} and maximum elongation to failure, ε_{max} taken from the standard tensile testing results on all three batches of specimens are gathered and presented in Table 4-1. The mean values and standard deviation are calculated based on the data from all three batches. The calculated mean UTS, σ_{UTS} and maximum elongation to fracture, ε_{max} are then plotted in Figure 4-5 for an evident comparison to be made between the materials. The standard deviations evaluated for each mean value are plotted as error bars in the figure. Highest UTS value is recorded from material 185°C measuring at 1067MPa, where it is 0.45% slightly higher than reference material AQ. The UTS for material 365°C highly affected by highest tempering temperature where the UTS dropped to 941MPa, which decreased by 11.4% compared to the reference material AQ. Despite the huge drop in UTS, the maximum elongation to failure of material 365°C is also severely affected and dropped by 8.4% below reference material AQ. Material 240ºC shows an interesting improvement in maximum elongation to failure, ε_{max} with a 2.4% increment higher than ε_{max} of material AQ. Also, the UTS of material 240°C dropped by 0.14% reduction from material AQ.

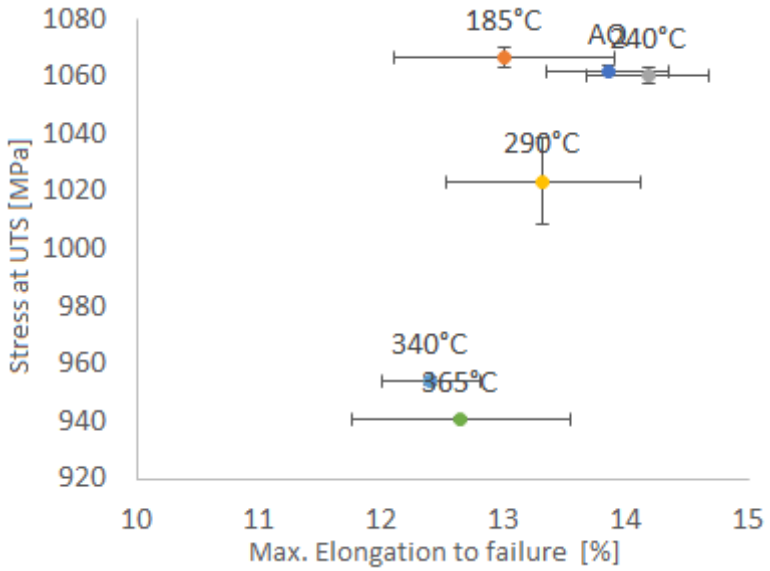

Figure 4-5 Result comparison for DP1000 material of the effect of different tempering condition plot based on UTS and maximum elongation.

From the triplicate stress-strain curves presented earlier in Figure 4-4, one median curve is chosen for each material and then, these curves of different materials are plotted in one graph to observe the effect of tempering on the tensile test response. Figure 4-6 shows the stress-strain curves of all six DP1000 steels with different tempering conditions. From the graph, the trend shows that the stress and elongation to fracture reduces with increasing tempering temperatures for DP steels tempered at 185°C, 290°C, 340°C and 365°C. DP steels tempered at 240°C however, does not follow the pattern and shows that the curve is almost similar to reference material AQ.

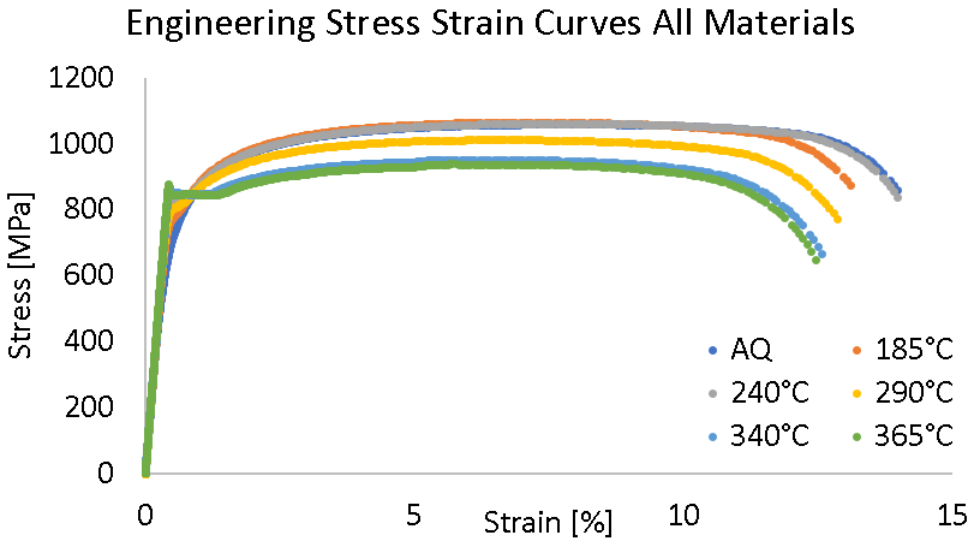

Figure 4-6 Stress-strain curves comparison for all DP1000 steels with the effect of tempering.

The reason behind the obtained stress-strain responses from these six DP1000 steels of different tempering conditions need to be further explained by acquiring more information on the damage and deformation behaviour happening at the microstructural scale of DP1000 steels. The unique microstructure comprises of two distinctive phases, ferrite and martensite that are affected by the tempering may affect the damage behaviour in DP steels thus influencing the overall stress-strain response. In the next section, investigation is proceeded to studying damage at microstructure scale.

4.3. Micro tensile test in SEM: Damage Development in DP1000 Steels

Different behaviours of the stress-strain curves have been observed in each DP materials of different tempering conditions. To understand how the tempering process is affecting the overall material's mechanical response, investigation then move on to understanding the damage behaviour happening in the DP material at microstructure level.

This section will present the results obtained from testing a set of DP1000 steels of different tempering conditions using a micro tensile testing machine, the 5kN Deben's In-Situ Tensile Testing module that is taking place inside a Scanning Electron Microscope. Results from this experiment are analysed at several different aspects comprising the study of plastic deformation behaviour happening in the ferrite and martensite phases, the stress-strain state as well as local strains measurement for the earliest damage nucleation on the surface microstructure and lastly, assessing damage development in the mid-thickness and near the fracture surface of tested specimens.

4.3.1. Tensile Testing Inside SEM

A set of DP1000 steels 2mm-width specimens of different tempering conditions are tested under a scanning electron microscope until failure. The experimental procedure of this in-situ testing method has been explained previously in **Section 3.6 Microscale Tensile Test in SEM using μ-DIC**

Figure 4-7 shows a micro tensile specimen subjected to loading inside and SEM. This in-situ tensile testing is repeated on all the DP steels of different conditions. For every specimen, the test is stopped at every 0.05mm extension for image acquisition of the deforming microstructure under loading. The sets of successive images captured will be later used for strain analysis using DIC technique

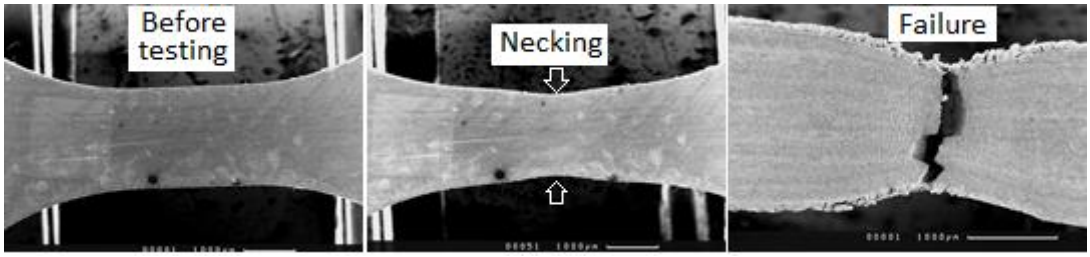

Figure 4-7 Three sequential images of 2mm-width micro tensile specimen captured using an SEM at the lowest magnification showing the entire gauge length. From left is the undeformed specimen, then middle image reveals the necking happening at the middle gauge section region and image on the right is when specimen is completely broken.

.

The results from running the tensile testing are shown in stress-strain graphs plotted in Figure 4-8. The stress-strain curves are shown separately according to the materials. As observed in the graph, the plotted curve is not smooth. The frequent drops in the stress values are due to the interruption when test is stopped of image acquisition. These stress-strain curves are derived from force-extension data acquired from the tensile-testing modules.

In each stress-strain plot, certain stages of interruption are circled and labelled using numbers and letter (A to G). The numbers correspond to the interruption stages and letters (A to G) refers to the sites of the earliest damage found to initiate in the microstructure of the investigated materials. This study on damage formation in the microstructure will be thoroughly explained later in Section 4.3.4.

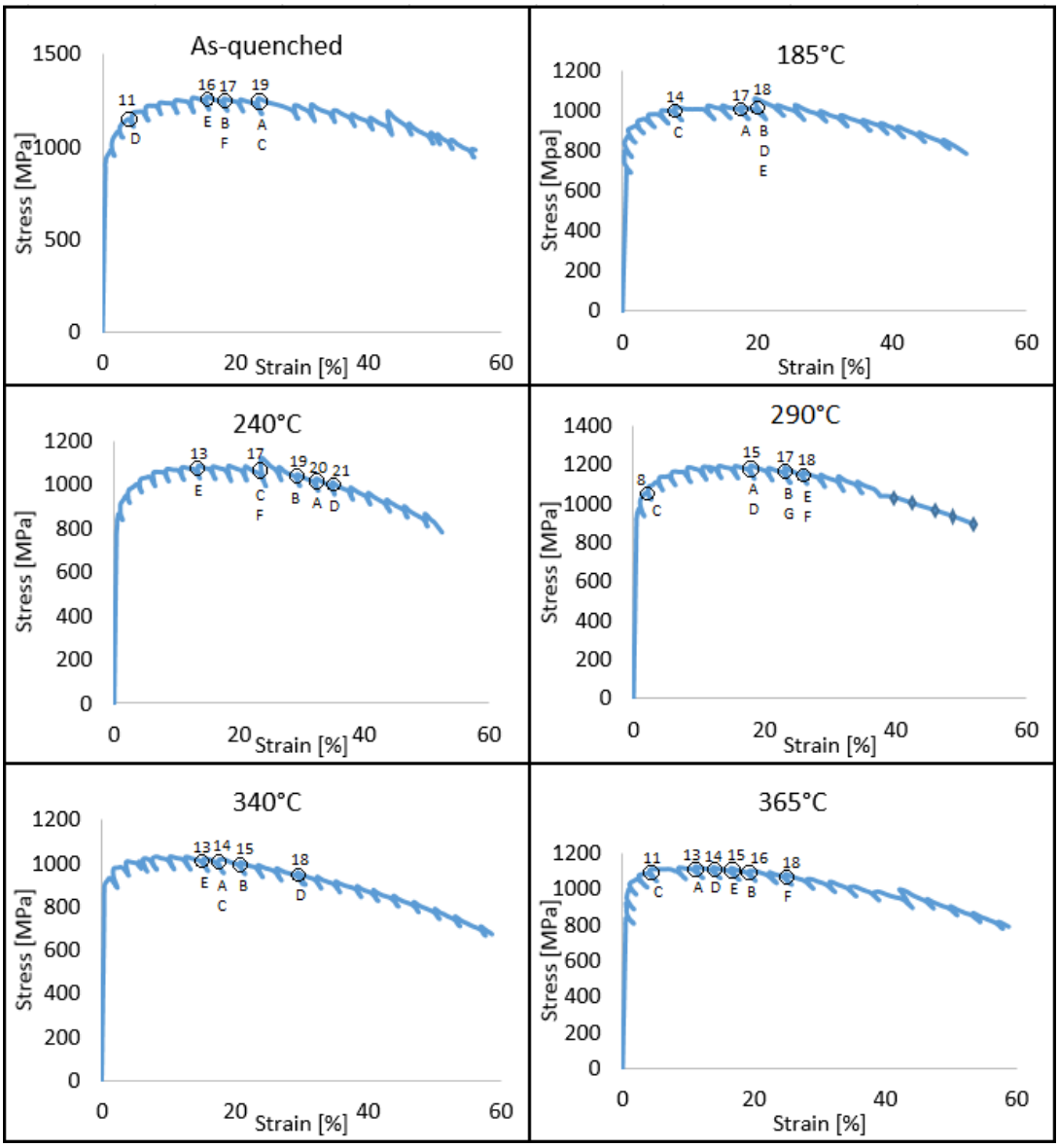

Figure 4-8 Stress-strain curves obtained from micro tensile test in SEM using 2mm-width tensile geometry. In each plot, certain interruptions are labelled with numbers and letters (A to G) denoting the onset of martensite phase cracking during the test. Numbers indicate the stage of interruptions and letters (A to G) are referring to the sites of the earliest martensite cracking happening in the investigated microstructures.

Table 4-2 Collected data from the 2mm-width micro tensile test stress-strain result.

	Specimen thickness	At maximum stress (at UTS)			At maximum elongation to fracture [ε_{max}]	
		σ_{UTS}	ε_{UTS}	Interruption stage at σ_{UTS}	ε_{max}	Total interruption stages
	[mm]	[MPa]	[%]		[%]	
AQ	1.5	1271	15.8	16th	56	30th
185°C	1.46	1060	19.7	18th	51.1	28th
240°C	1.4	1088	13.7	13th	52.5	27th
290°C	1.4	1195	18	15th	52.1	27th
340°C	1.5	1035	10.3	12th	58.7	28th
365°C	1.5	1126	11.1	13th	58.8	27th

Table 4-2 is the result summary of stress-strain curves from the testing the 2mm-width specimens. The table presents the stress and strain values as the tested specimens reaches the UTS (σ_{UTS} and ε_{UTS}) and also the maximum elongation to fracture, ε_{Max}. Specimen as-quenched has the highest UTS values among all specimens of 1271MPa happening at 15.8% strain with a maximum elongation to fracture, ε_{Max} of 56%. In terms of specimen elongation to fracture, specimen material 365°C recorded the highest elongation where ε_{Max} is 58.8% and the UTS is the second highest after material AQ where σ_{UTS}= 1126MPa and ε_{UTS}= 11.1%. The UTS for all materials are within the range of 1035MPa to 1271MPa, where lowest is material 185°C and highest is material AQ. While the values for maximum elongation to fracture between the specimens are range between 51.1% to 58.8%. The specimen for material 340°C has the shortest strain to reach UTS which ε_{UTS} is 10.3% and the corresponding UTS is the lowest for all materials of 1035MPa. The low UTS value for specimen 340°C is compensated with its second highest maximum elongation to fracture, where the ε_{Max} is 58.7%, which is only 0.1% difference lower than the material 365°C which have the highest elongation to fracture.

Results obtained from standard tensile test shown in Table 4-1 and results from micro-tensile test shown in Table 4-2 are found to have a big difference in terms of strain. Standard tensile test reveals that the maximum strain before fracture is at around 12-14%, however for the micro-tensile in SEM; the strain values are very high at around 50-58%. This large difference found is due to the effect of the tensile specimen geometries being used where the standard has 50mm gauge length while the micro specimen is only 2mm long. Standard tension test is useful to allow comparisons between materials as this method had been widely used in research and industry. Although the results obtained from the micro-tensile test does not follow standard, the stress-strain response is important to determine the elastic stage, yielding point, the UTS and the elongation to

fracture of the micro-tensile specimen. These information is necessary for investigation to relate the damage happening in the microstructure to the specimen's global state of loading (stress and strain).

As seen on these in-situ tensile testing stress-strain curves in Figure 4-8, in all materials; DP1000 steels as-quenched to the highest tempering of 365°C, it is observed that certain interruption stages on each curves are circled which indicates the initiation of damage in the specimens microstructure. Stress-strain curves for all materials shows that damages formation in the tested specimens begin as the tensile specimen reaches UTS or very near to the UTS region. In the later section, these earliest damage developments observed to form in the microstructure will be presented and explained in detail. Figure 4-9 shows the formation of damage in relation to the stress-strain state of the tested specimens. This figure is obtained by plotting the recorded stress-values for each damage formation sites are recorded, and it is found that the onset of the earliest form of damage (which happens to begin in martensite for all cases) will start as when the specimen stress (global stress) state reaches above 1000MPa.

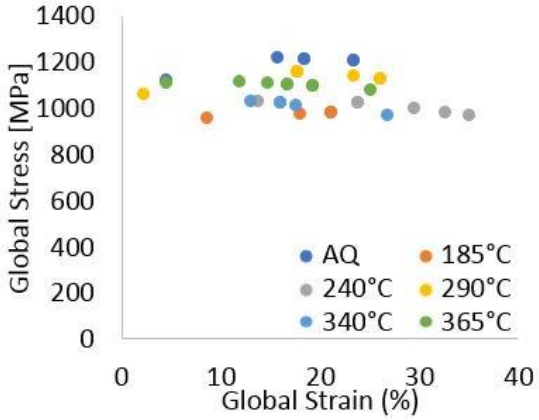

Figure 4-9 The stress-strain state for the onset of earliest damage formation on the surface of specimen under tensile loading microstructure.

4.3.2. Representative Microstructure

As previously explained, the conducted micro tensile testing in SEM is stopped at every 0.05mm extensions on all tested materials. During these interruptions (when test is halted briefly), images are captured at two chosen magnifications which large field image taken at very low magnification (around 300 times magnification) and a small field image but showing a detailed up-close image of the microstructure (at around 600 times magnification). The magnification is chosen to be very low to cover as much area of the microstructure, so that the representative microstructure (including ferrite-martensite distribution) for DP1000 as-quench can be captured and most importantly is that the grain boundaries between the two phases can be clearly seen in the image. Large field images provide information of the studied material morphology such as microstructural phase distributions, banded phases, volume fraction of phases and etc.

These images of the representative microstructure are taken just before the test begin, for capturing the undeformed microstructure of each specimens. Before the start of the test, region of interest (ROI) is first identified in the microstructure. The region of interest is chosen to be in the middle of the specimen gauge section where the location of total specimen failure is expected to happen. Once a suitable magnification is chosen, the magnification will be kept constant for the acquisition of a series of images (corresponding to the interruption stages) throughout the test.

The representative images of the undeformed microstructures of each DP steels with different tempering conditions are shown in Figure 4-10. These images are taken at 300 times magnification with an image field size of 0.25 x 0.25 mm. It is necessary to capture images that covers a large area however still maintaining a good contrast of grain boundaries in the microstructure. Table 4-3 provides the information on the image magnification, image field size, and the estimated martensite volume fraction (V_M). An

image processing software, ImageJ is used to measure the ferrite-martensite volume fraction of the representative image by utilising the intensity threshold tools to distinguish the two main phases. According to the table, the studied DP1000 specimens are found to have a relatively high martensite volume fraction (V_M). For the six different tempered specimens, the V_M across the materials range from 60.7% to 67.2%. Thus, these changes are not due to the tempering process however it is rather dependant of the local microstructure. This range of +/- 6.5% difference of the V_M found across the studied specimens can be reduce by zooming out and then capture using a much lower magnification. Images captures with sufficiently large field size are better for obtaining the representative microstructure, as the calculated V_M will remain closely similar when is measure at different ROI in the microstructure. However, it is more important to clearly see and maintain a good contrast of the microstructure in this test. So, these captured images are sufficient to be a representative image with a known error range between 6.5%.

Table 4-3 Martensite phase volume fraction of the DP1000 specimens.

	Magnification	**Image Field Size (mm)**	**Phase Volume Fraction (%)**	
			Ferrite, V_F	**Martensite, V_M**
AQ	300x	0.25 x 0.25	32.8	67.2
185°C			35.9	64.1
240°C			37.7	62.3
290°C			38.1	61.9
340°C			35.8	64.2
365°C			39.3	60.7

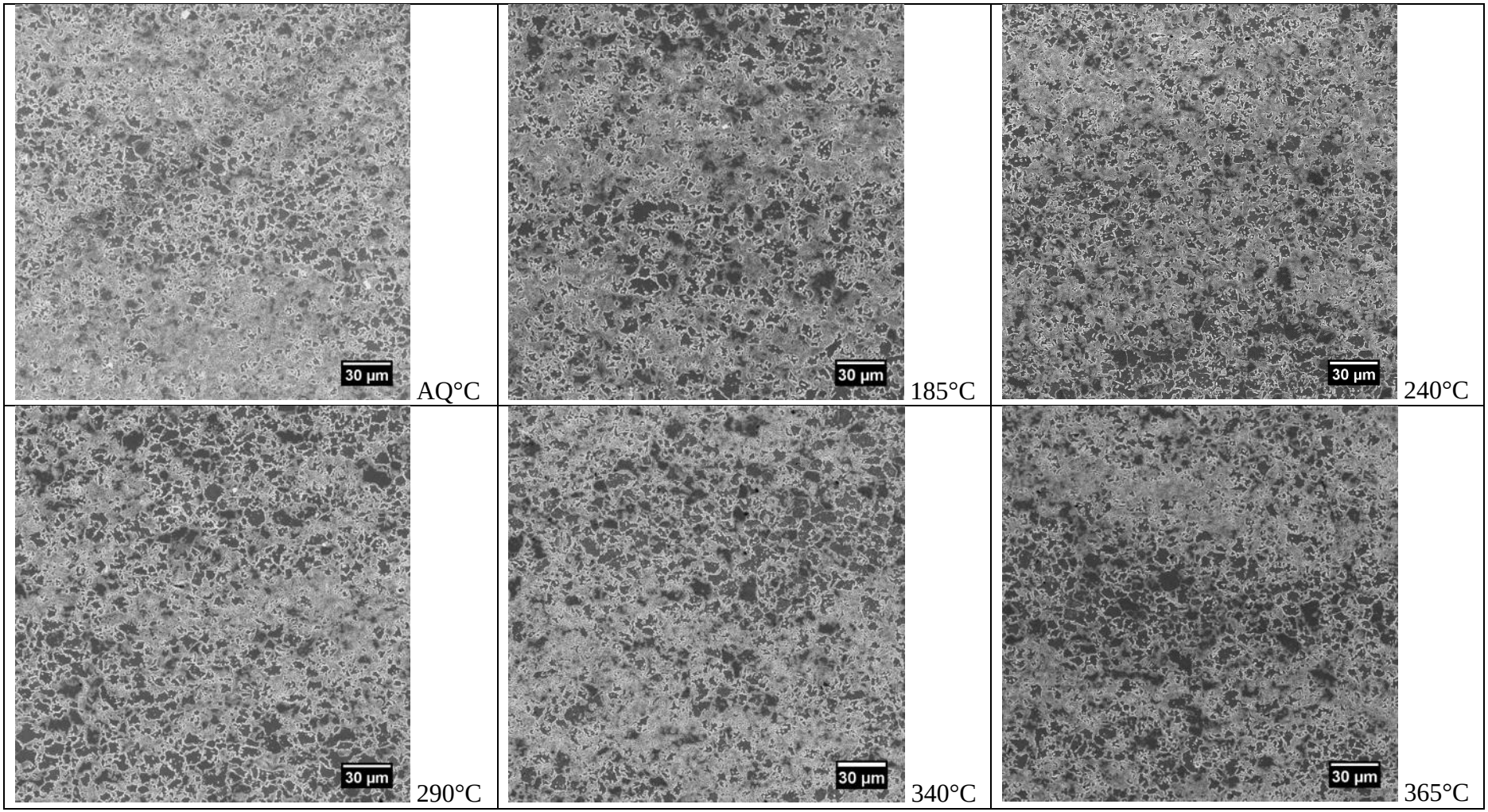

Figure 4-10 Representative microstructures of DP1000 steels of different tempering conditions captured at 300 times magnification.

As shown in Figure 4-11 it is observed that in the surface of the microstructure, the phase distribution is slightly heterogeneous. *"Martensite bands"* are seen to be present in repeatedly parallel to the rolling directions of the material and exists throughout the whole length of the DP steel sheets.

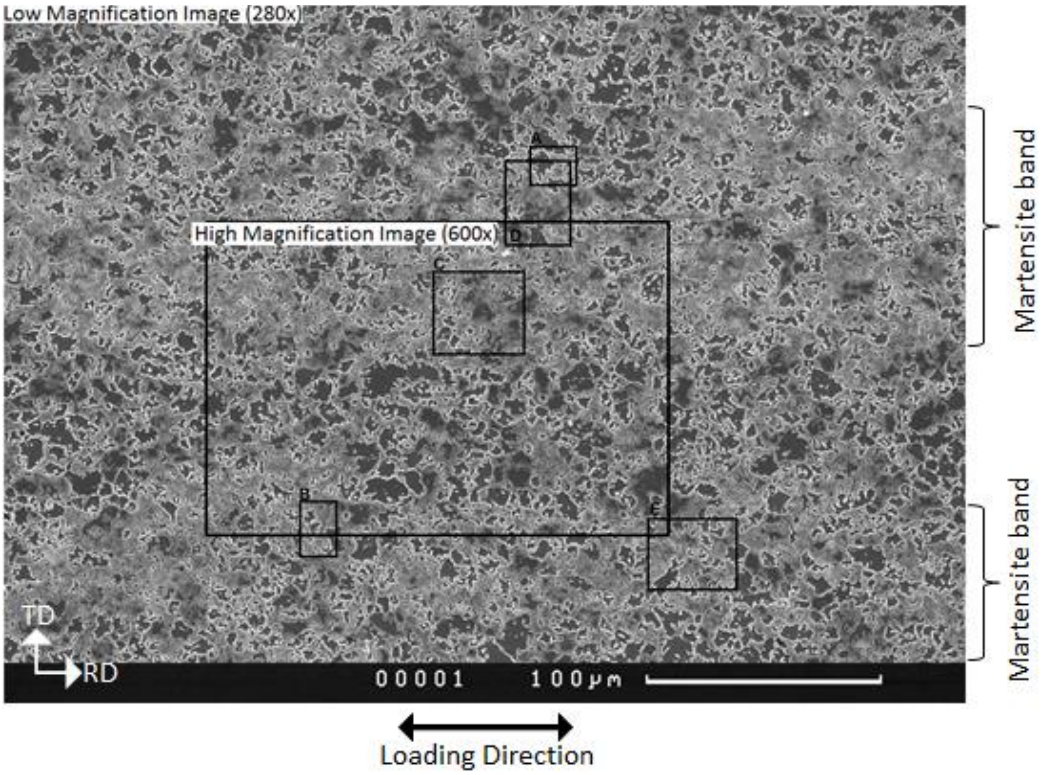

Figure 4-11 An example of representative microstructure of DP1000 steels post-tempered at 185°C captured at 280x magnification (large field image). The second largest rectangle highlighted in this figure is the region of analysis for high magnification images. Smaller rectangles labelled with A to E are the sites where damage initiation in the microstructure are first spotted. Rolling direction of material is horizontal. Same procedure is applied for all six materials.

These martensite bands are large clusters of martensite islands which are closely connected together with relatively very small ferrite islands forming in between the gaps. The presence of these martensite bands is seen in all six DP materials studied.

From the same image in Figure 4-11 shown the location of the high magnification image captured as well as the five sites where earliest damage formation was observed. These five damage sites (A to E) are the ones which have been mentioned in the in-situ

stress-strain curves for specimen 185°C, Figure 4-8 with their corresponding stress-strain values. This same procedure has been repeated on all six materials.

4.3.3. Plastic Deformation in DP1000 Steels Microstructure Analysed using Micro-Scale DIC

In this section, the investigation is continued on the effect of the heat-treatments on the strain accumulation in the ferrite-martensite phase of all six materials. The comparison of strain accumulation in each separate ferrite and martensite phase will be shown to see if these applied heat-treatments affect strain difference of the martensite and ferrite phase. Apart from that, the comparison between strain in the martensite bands region and large ferrite phase will also be studied by observing the strain distribution of the overall region of investigation (ROI) of the microstructures.

Figure 4-12 shows an example of a deformed microstructure of DP1000 steels as-quenched during a micro tensile testing which is analysed using DIC. By comparing the undeform microstructure and microstructure-at-UTS (at σ=1167MPa ε=30%), it is observed that the both ferrite and martensite phases has elongated (stretched) along the direction of tensile loading. The amount of strain undertaken by the microstructure is shown by DIC analysis done on the microstructure surface as shown in the strain distribution plot.

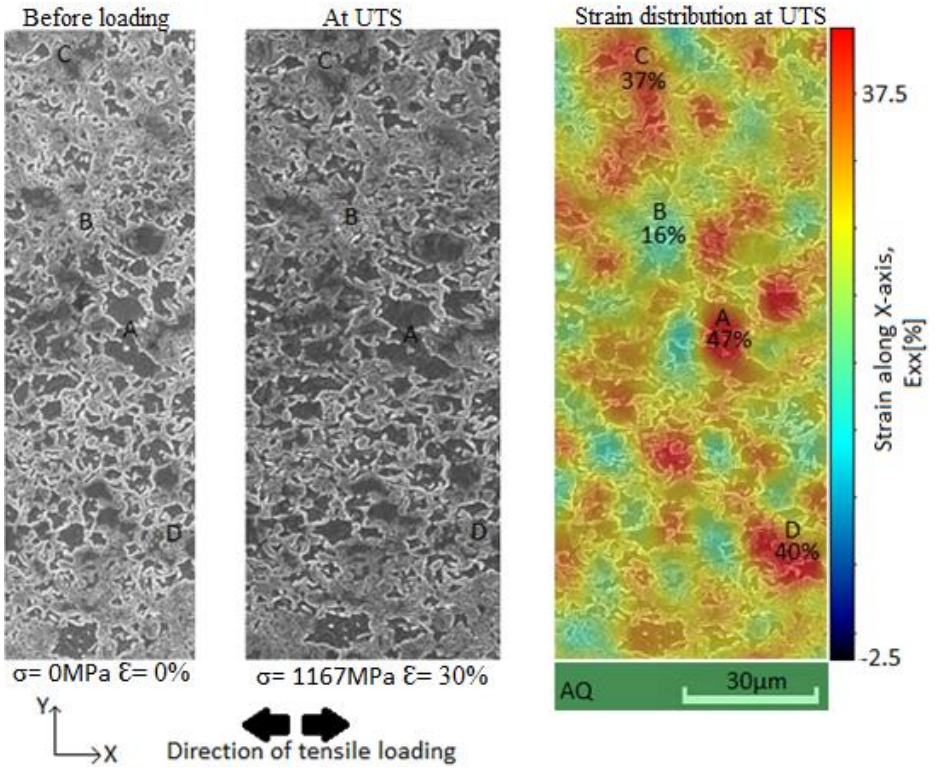

Figure 4-12 An example of deformation in DP1000 as-quenched microstructure taken from a section of high magnification image, 600xM (small field). The deformed image is captured when specimen is at UTS showing the microstructure has elongated according to the direction of tensile loading. On the right-hand side is the strain distribution graph which is during the instance of UTS. On all three images, four letters are indicated on the images, which two located in the martensite band (C and D) and another two in large ferrite phase region (A and B).

In the strain distribution plot from a high magnification image, it is observed that the hot spots formation (areas of high strain values) are aligned at 45° angle to the direction of tensile loading. For all three images, the undeformed, at UTS and strain distribution plot, four points labelled A, B, C and D are positioned at certain area of the microstructure. Points A and B are in the large ferrite region which is in between the large martensite strips region (martensite bands) where both points C and D are located. Point A shows that a large ferrite phase in the large-ferrite-phase-region has reached the highest local strain (strain at the microstructure obtained from DIC analysis) of 47% as the tensile specimen reached UTS. While strain in the C and D which are in the martensite bands are 37% and 40% respectively. The region of low strain values is at around 16% as shown in B which is located in martensite phase and is in the intermediate region of large ferrite

phase and martensite band. However, the example being shown here from the high magnification image is too small to provide confidence in the obtained result. So, analysis is conducted on a large field image as the strain distribution over a large area which include the region of large ferrite in between two region of banded martensite as shown in Figure 4-13 .

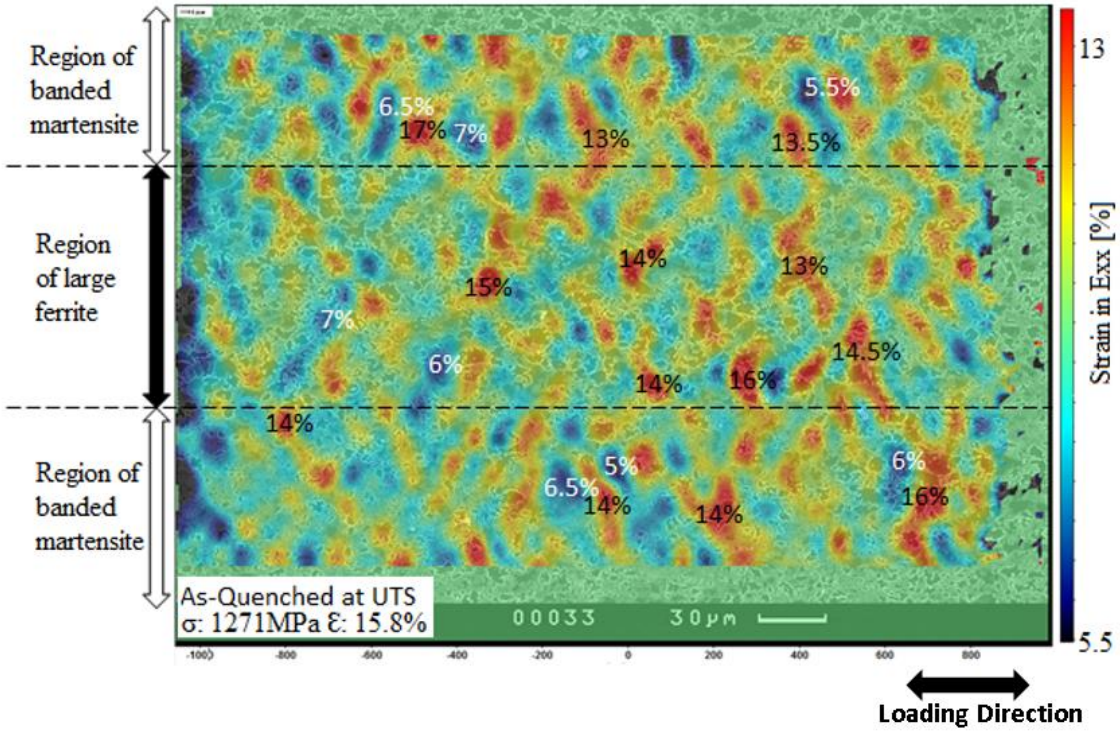

Figure 4-13 An example of large field image taken at 300x magnification of an as-quenched specimen when it reached UTS.

First observation is in agreement with the result obtained in Figure 4-12, where the orientation of the strain distribution are 45° to the tensile loading direction. In the region of large ferrite phase, high local strains in the hotspots reaches up to the range of 14% to 16%. In the regions of banded martensite at both top and bottom sides of the large ferrite region, high local strains at several hot spot areas seems to be at almost similar to the result obtained in the large ferrite region, that the values range from 14% to 17%.

Thus, it concludes that strain accumulation in both ferrite and martensite are almost uniform up to the stage where the tensile specimen reaches UTS.

An effective method to analyse the strain accumulation in the ferrite and martensite phase is by plotting a frequency distribution graph for the strain values obtained in both phases separately. For all materials, the strain distribution results are extracted at the stage where specimen reaches the UTS. The local strain values obtained from DIC at the UTS stage are then categorized according to the phases either ferrite or martensite, as shown in Figure 4-14.

The aforementioned strain accumulations are the amount of deformation taking place of the phases in the microstructure. Mean and maximum values from the frequency distribution plots are obtained and summarized in Table 4-4. The plastic deformation in ferrite phase are slightly higher than plastic deformation in martensite for all materials as the specimen are loaded until UTS. This is shown in the mean strain values of ferrite which is slightly higher than mean values in martensite for all materials as shown in the table. Material 365°C shows that the ferrite phase has the highest plastic deformation of 39% as shown in the maximum strain in ferrite. While material 240°C has the highest plastic deformation in martensite of 33%. Specimen that has the highest difference in plastic deformation of ferrite and martensite phase is specimen 365°C, with a highest strain difference of 42.3%. This high strain difference shows that the material has a hardness difference between the phases which may lead to high strain partitioning in the materials. Material 290°C shows an opposite trend where martensite is 7.7% higher than the ferrite phase and the strain difference is at 2.3%.

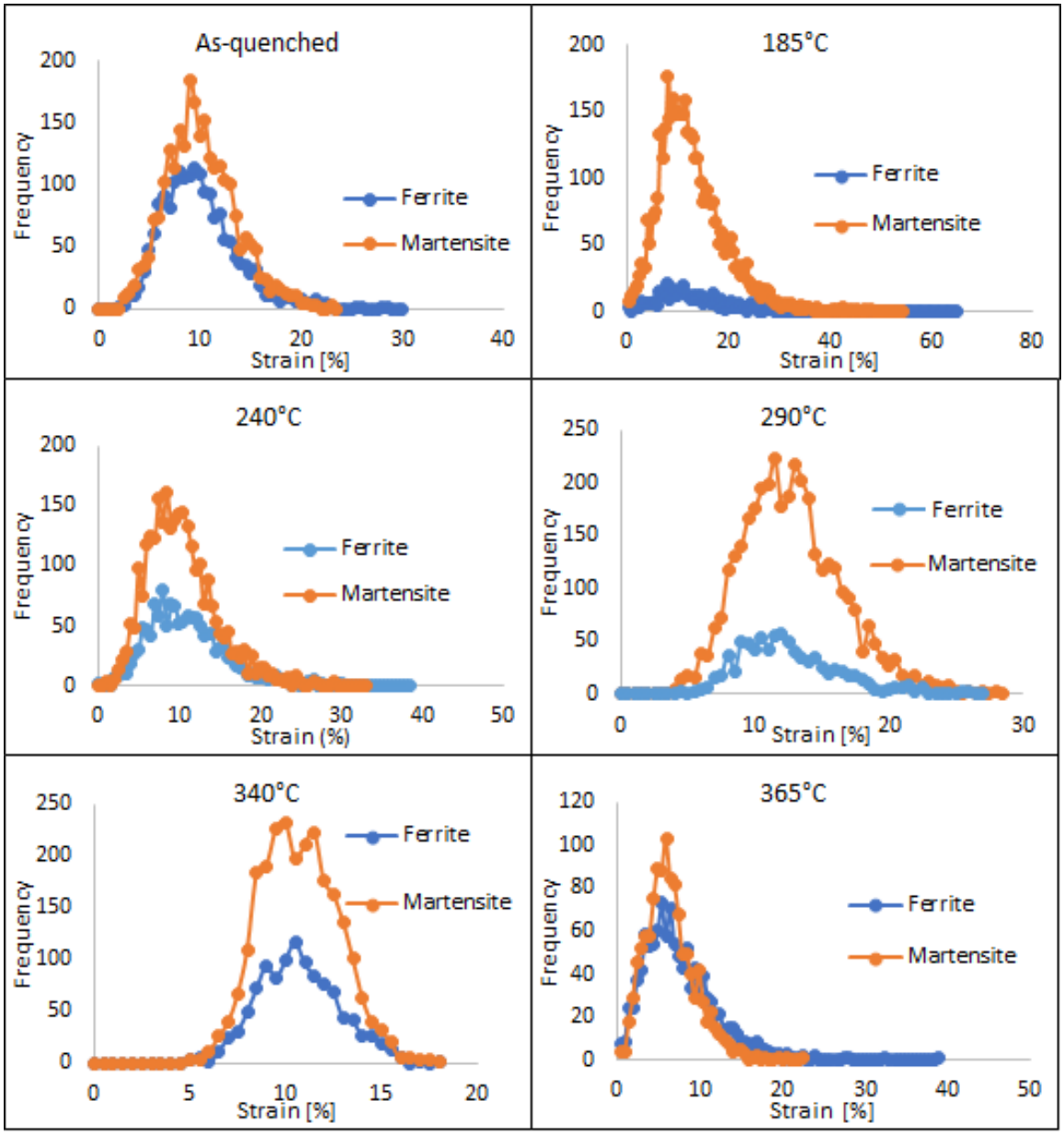

Figure 4-14 Frequency distribution plot of local strain accumulation in ferrite and martensite phases for all six DP1000 steels of different tempering conditions as tensile specimen reaches UTS.

Table 4-4 Mean, maximum and difference in maximum strain values result from the obtained frequency distribution of ferrite and martensite as specimen reached UTS.

	Mean Strain (%)		Max. Strain (%)		Max. Strain Difference (%)
	Ferrite	**Martensite**	**Ferrite**	**Martensite**	
AQ	10	9	28.5	23	19.3
185°C	11.5	8	65	54.5	16.2
240°C	8	7.5	38.5	33	14.3
290°C	12.5	11.5	26	28	-7.7
340°C	10.5	9.5	17.99	17.57	2.3
365°C	6.5	6	39	22.5	42.3

4.3.4. Analysing Earliest Microcracks Nucleation on the Surface of Tensile Test Specimens.

The sets of high magnification images captured during the micro tensile testing are inspected for formation of microcracks in the microstructures of all six DP steels specimens. The earliest formation of microcracks in the specimens are then tracked in each steps of loading stages to understand the crack development behaviour. The microcrack developments are then relate to the overall micro tensile specimen stress-strain state (global stress-strain state) to understand if the tempering process affects the behaviour of crack formation.

In order to obtain statistically representative results, for every specimen; it is aimed to capture microcrack formation instances as many as possible within the ROI of high magnification image taken. These instances of microcracks formation or damage sites are found to be in range of five to eight. There are 37 damage sites in total found in all six specimens. These 37 microcracks are the earliest formation of damage found to form in the inspected ROI when conducting the micro tensile testing and these are presented in APPENDIX I.

These earliest formations of microcracks in the DP steels studied are mostly found in the martensite phase. Several damage behaviours or damage mechanisms have been identified in relation to the formation of microcracks in the martensite. The most frequently observed damage mechanism found in most damage sites is – the formation of crack that begin within the martensite phase. In few other damage sites, another behaviour is observed where crack which form due to the decohesion of ferrite-martensite interface (F-M decohesion) propagates and leads to cracking of the nearest martensite phase. It is also found that cracking in martensite started when there is high deformation in the

surrounding ferrite phase. Table 4-5 shows the observed damage sites in all six specimens categorized according to their identified damage mechanisms.

Table 4-5 Damage sites of microcracks categorized into the damage mechanisms identified.

Damage Mechanisms	AQ	185°C	240°C	290°C	340°C	365°C
Cracking within martensite phase	A B C D E F	A B C E	A B F	B C D E G	C E	A B C D E F
Cracks near M-F interface and propagates into martensite phase			C D E	A F	B	
Others		D			A D	

An example of cracking that begins within the martensite phase is shown in Figure 4-15. Only in this figure, the images are labelled to show the way the results are presented. This example is taken from damage events found in specimen 290°C in area E (290°C-E). At interruption step 18th, the martensite island in this figure shows that it has deformed up to 18% local strain (obtained using DIC) where the overall specimen is loaded up to (Ɛ= 26%, σ= 1129MPa) before a crack is seen to begin to grow in the middle of the martensite phase. At interruption step 22nd (Ɛ= 37.6%, σ= 1039MPa), a crack is observed in the martensite phase at area labelled (i). With further increased in loading at the 25th step (Ɛ= 46%, σ= 969MPa), crack which started at region (i) has propagated through the path where martensite is the narrowest and grew into ferrite as labelled in area (ii).

This type of mechanism where martensite cracking develop from within the centre of the phase are also commonly observed in the rest of DP materials studied. Several examples from other materials that shows the same mechanism as mentioned in 290°C-E are shown in Figure 4-16.

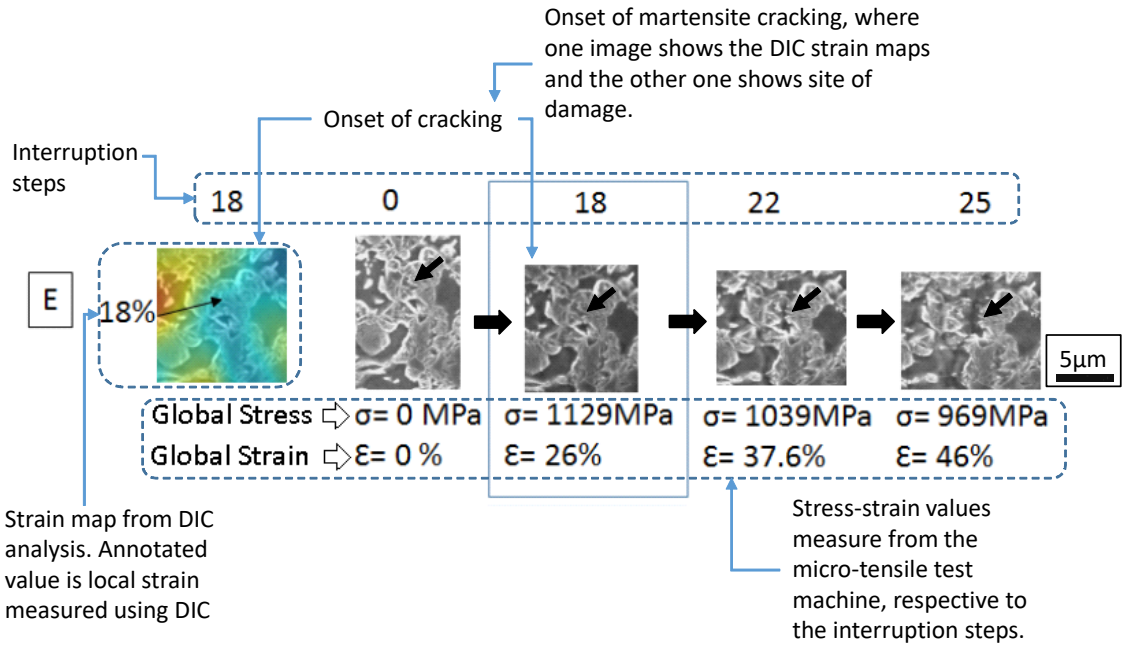

Figure 4-15 An example of crack initiated within the martensite phase in specimen 290°C. From left, is the strain distribution obtained using DIC. Series of images in greyscale are the sequence of crack formation from the start of the test until the end.

Each examples from the six materials are chosen and shown in Figure 4-16. They show that crack begin in the martensite phase and after further loading increment, the crack grows throughout the martensite phase and break apart the martensite phase in half. Clear examples are for specimen AQ-C, 290°C-G and 340°C- C. The strain values show that for these presented examples, the local strain values needed for the onset of martensite cracking is within the range 11% to 22.5%. The global loading stage for the cracking to start within the martensite phase is in the range where the tensile specimen reaches around the UTS. Most cracks are also observed to be along the 45° angle to the loading direction. Among all the 37 damage sites identified, it is found that 26 of them are the cracks which nucleated inside of martensite.

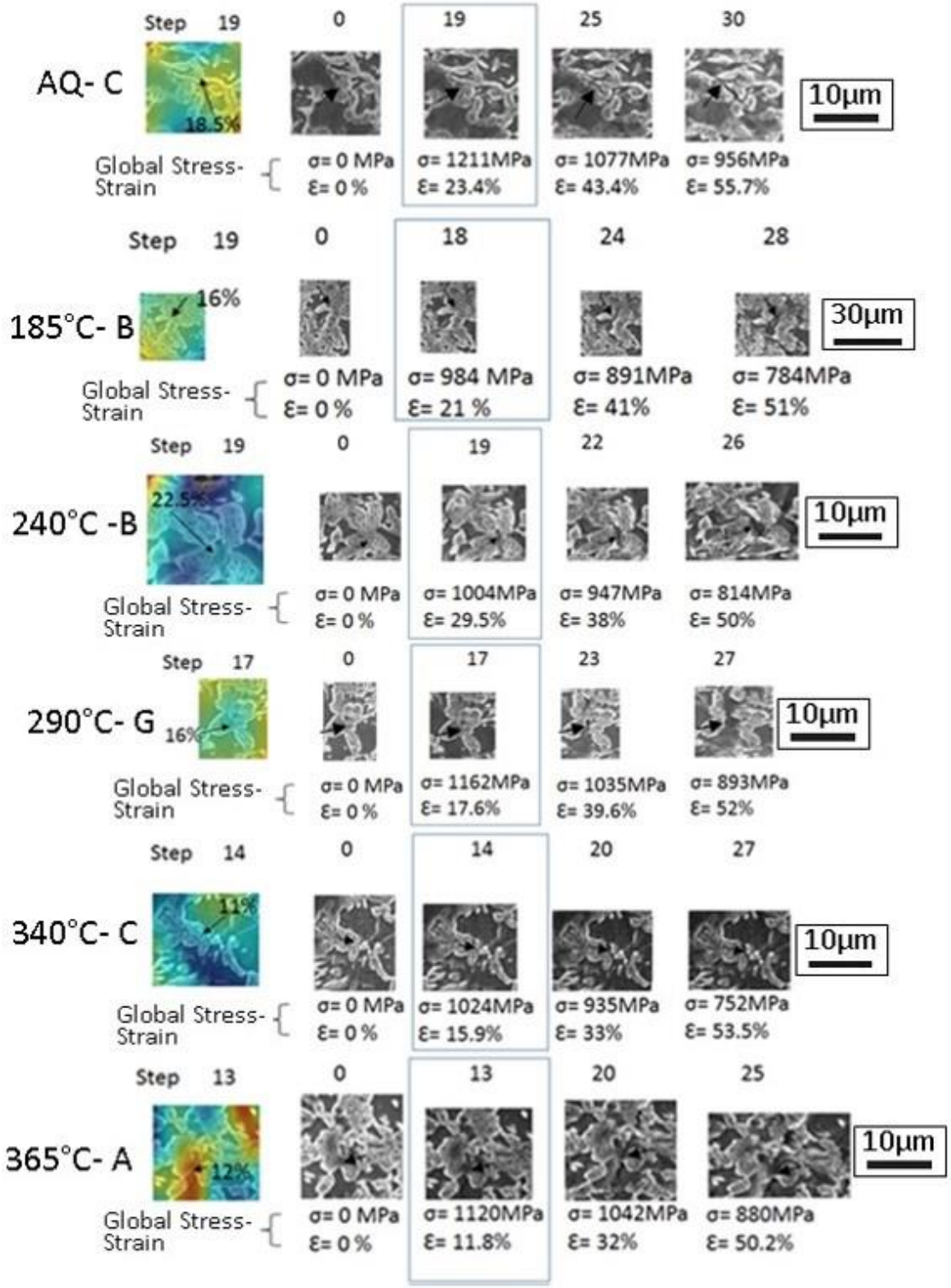

Figure 4-16 Examples of damage mechanism caused by cracks which nucleates within the martensite phase. Each examples are chosen from one of the damage sites found in each different materials.

The second damage behaviour found is martensite cracking due to the de-cohesion near the interface of ferrite and martensite. The increase of loading on specimen caused the crack to propagate into the martensite phase and following the de-cohesion path initially and later causing the martensite to fully break into two segments. An example of this case is shown in Figure 4-17, where damage site is identified in specimen 240°C-D. At zero load, the image shows an intact microstructure of the identified damage site. At interruption step 21st (where the tensile specimen loading state is ε= 35%, σ= 969MPa), as pointed using the yellow arrow; a shallow plunge (dip) formed near the F-M (ferrite-martensite) interface due to a high plastic deformation in the ferrite phase. At this stage, the martensite phase has plastically deformed up to 31% of local strain measured using DIC. This is the final interruption step before crack begin to develop inside the martensite phase, or similarly is called the onset of fracture in martensite. In step 29th (ε= 50%, σ= 814MPa), the global stress value falls from 969MPa to 814MPa. This is due to the thinning of the specimen gauge thickness (necking in the tested tensile specimen); the ferrite phase shows an increment in deformation and the crack which formed along the de-cohesion region (as pointed using yellow arrow) near the F-M interface has propagated into the martensite phase. At step 27th, the martensite has fully broken into two separate segments and crack from point (i) has developed through the martensite phase and out into point (ii) causing crack in smaller nearby martensite phase. This mechanism however is less likely to be seen as compared to the type of damage where crack initiated within the martensite phase, as there are only 6 damages sites that has similar mechanisms to this among 37 damage sites found in all six materials. Further example of these damage sites representing this type of mechanism is shown in Figure 4-18.

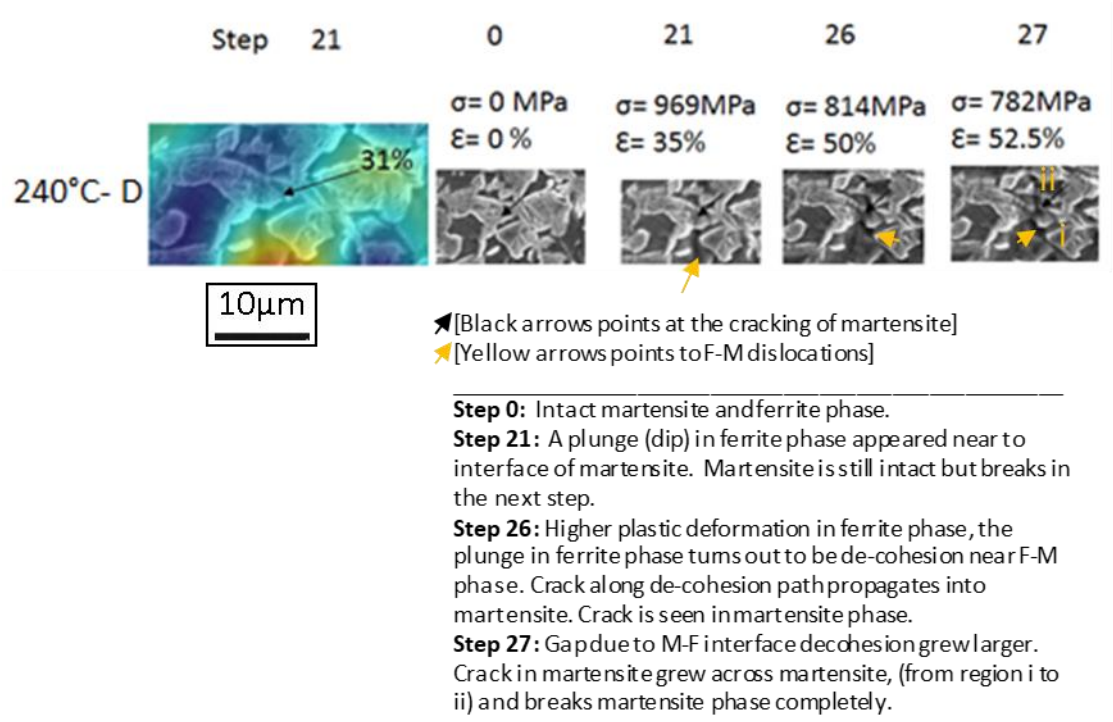

Figure 4-17 An example of de-cohesion near ferrite-martensite interface that propagates into the martensite phase observed in specimen 240°C.

In Figure 4-18, in order to categorize damage sites into this damage mechanism of which crack begin by the de-cohesion near the F-M interface then grows into ferrite; the observation made was there should be an appearance of de-cohesion in near the F-M interface before there is any cracks develop in the nearby martensite island. As directed by the yellow arrows in the figure, the martensite phase failed (crack developed into the martensite phase) after the de-cohesion emerges in the inspected damage site. The strain distribution result shown is the maximum amount of plastic deformation in the inspected martensite island before it fails (which is not to be mistaken for the F-M de-cohesion to begin). In several damage sites such as 240°C-E, 290°C-A and 290°C-F it is obvious that the crack development is along 45° to the loading direction, as observed in several cases in Figure 4-16 presented earlier on crack formation within the martensite phase.

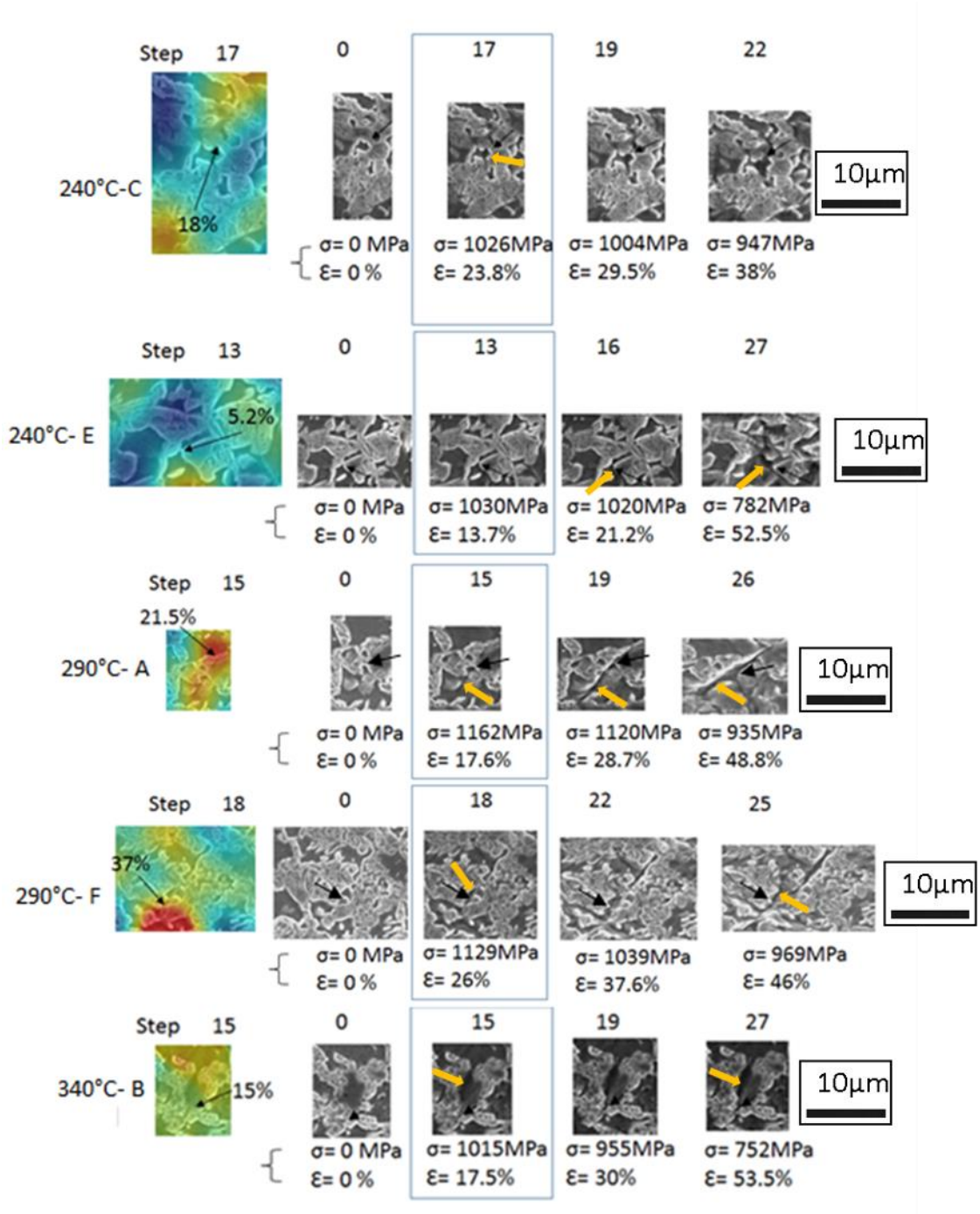

Figure 4-18 Damage sites of which cracks initiate in the form of de-cohesion near F-M interface which with the increment in loading. Crack propagate into martensite island and cause the martensite island to break. Black arrow is pointing at the location of crack initiation, while yellow arrow is the pointing towards the formation of F-M de-cohesion due to large deformation in the ferrite phase. Damage sites shown are taken from several specimens and are differentiated using the labels on the left-hand-side e.g. 240°C- C is material 240°C at damage site C.

In Figure 4-19, an uncommon damage behaviour is found in the form of vertical cracks perpendicular (90° angle) to the loading direction of the specimen 340°C-A. Compared to the undeformed microstructure in step 0, step 14th (Ɛ= 15.9%, σ= 1024MPa) is showing the start of the formation of the said vertical crack as pointed using yellow arrow and at this stage martensite is at its onset on fracture where damage developed through the pointed (using black arrow) martensite island in the next loading stage. At step 19th (Ɛ= 30%, σ= 955MPa), it shows that the vertical crack has propagated at both sides of the vertical directions which are labelled as (i) and (ii). The end of the crack with propagates in the (ii) direction passes through the martensite island and splits the martensite into two separate segments. At step 27th (Ɛ= 53.5%, σ= 752MPa), despite the very high tensile loading, the vertical cracks show a very small growth which is safe to say the cracks are impeded from propagating.

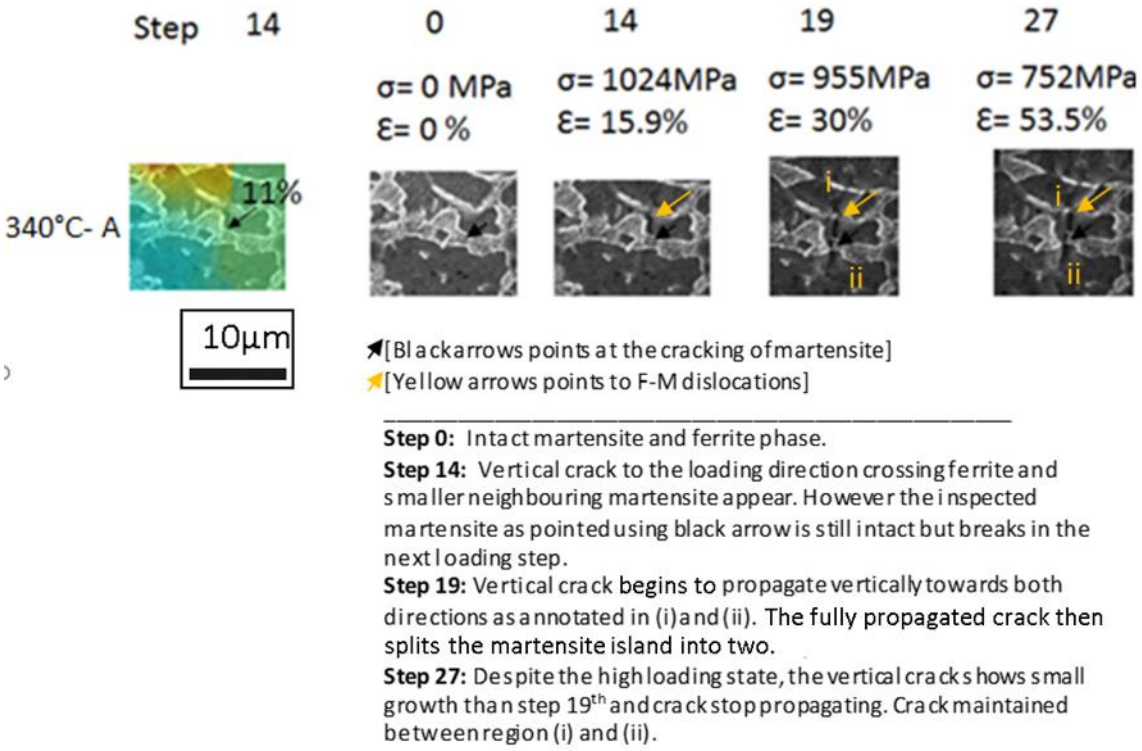

Figure 4-19 Formation of vertical cracks which is first seen in the ferrite phase near the F-M interface which with the increment of tensile loading the crack propagates across the martensite and breaks the martensite following the narrowest martensite path. The shown example is taken from specimen 340°C in damage site A, 340°C- A.

Overall, the investigation carried out in this section is the observation being made on the microstructure of the surface of tensile testing specimens. In all cases of the damage sites identified, the earliest damage begins as micro-cracks formation in the martensite phase. These micro-cracks happening on the surface however, do not lead to final failure of specimen as this is due to the initiation of damage happening in the subsurface of a tensile specimen.

The local strain of the martensite islands at the development of crack (onset of fracture) are recorded and is plotted against the global stress state of the specimen in Figure 4-20. In the Figure 4-20 (left-hand-side) where the measured local strain in martensite during the onset of crack development in the martensite phase is plotted against the global stress, it is found that all 37 identified martensite cracking begin once the global stress state reaches above the value of around 1000MPa, more specifically 957MPa. Most initiation of martensite cracking took place when they are near the UTS region in most cases. In Figure 4-20 (right-hand-side), shows that the local strain measured in martensite during the onset of failure is linearly increase with the increment in the global strain (strain exerted on tensile specimen).

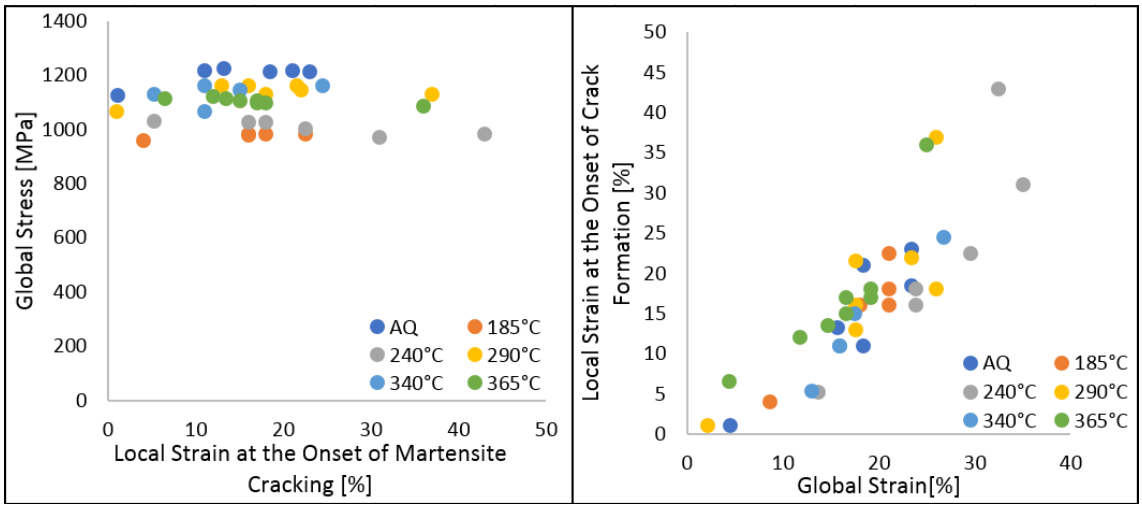

Figure 4-20 Graph showing the relationship of the strain during the onset of crack development in martensite and their overall specimens' stress-strain states.

4.4. Metallographic Cross-section Analysis of Tested Tensile Specimens

As discovered in the previous section, the earliest forms of damage begin in on the surface of DP steels specimens under tension loading are initiated in the martensite phase or near the interface of (ferrite-martensite) F-M grain boundaries. In the total of 37 damage sites studied, which damage initiation on the surface are all related to martensite cracking, none of them leads to the final failure. In order to understand how the tempering treatments affects the damage behaviour for each tempered specimen leading total specimen failure, damage is further inspected in the cross-section of specimens.

Broken specimens from the tensile testing are collected and prepared to allow for inspection in the cross-section to be carried out. As shown in Figure 4-21, in (a) is the example of two halves of broken micro tensile specimen which later in (b), the broken tensile specimen is cut near the centreline from the tip of the fracture surface to the bottom of specimen. The cut is made with an offset (0.5mm) from the centreline to allow the material reduction as they are subjected to cross-section surface preparation i.e. grinding, polishing and etching for SEM. The sectioned specimen is shown in (c). Figure (d) shows the sectioned specimen mounted using a hot-mounting conductive bakelite revealing the cross-section surface.

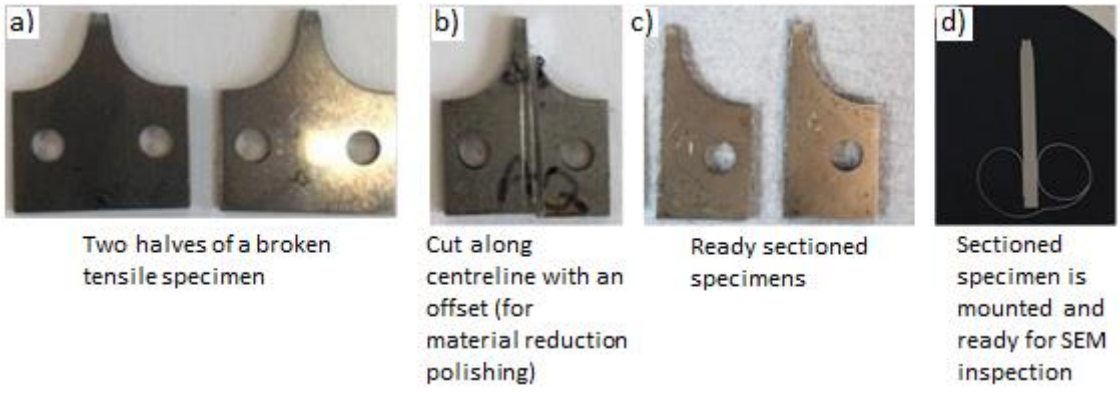

Figure 4-21 Example of a broken tensile specimens prepared for damage inspection in the cross-section.

Figure 4-22 shows the plane where damage in the cross-section will be assessed. As shown in the figure, the X-Y plane is the top surface of specimens where the analysis of micro-cracks in martensite were observed. Now after sectioning the broken micro-tensile specimens in half, this study will now be observing damage in the Z-Y plane as shown in the figure. As highlighted in the box "inspected fracture surface" in the figure, using SEM, micrographs acquisition will be focused at the fracture surface and local regions beneath the fracture surface in the through-thickness cross-section.

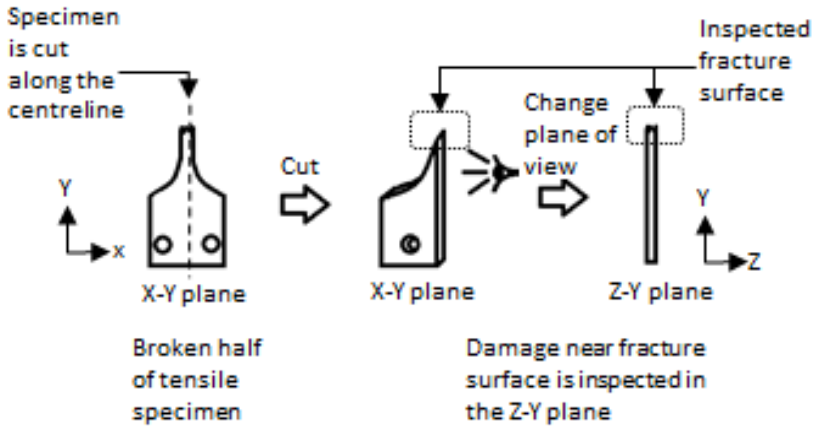

Figure 4-22 Schematic diagram showing the plane where damage is inspected (Z-Y plane).

4.4.1. Localized Necking and Through Thickness Cross-Section Profile

Figure 4-23 shows the fracture surface of broken micro-tensile testing specimens captured in the cross-section of Z-Y plane. From the fracture surface profiles, it is observed that there is a distinct difference in each specimens of different tempering treatments. The fracture surface for material as-quenched is rather relatively flat and smooth compared to the rest of other specimens. While the middle region for part material 185°C and 240°C are rather fibrous with relatively small sharp fracture surfaces at an angle. Among all specimens, specimen of material 290°C and 340°C shows ductile shear fracture which are relatively larger than those seen in material 185°C and 240°C. In specimen 365°C, the specimen shows a combination of fibrous in the middle as seen in

material 185°C and 240°C and large shear fracture on each side as seen in 290°C and 340°C.

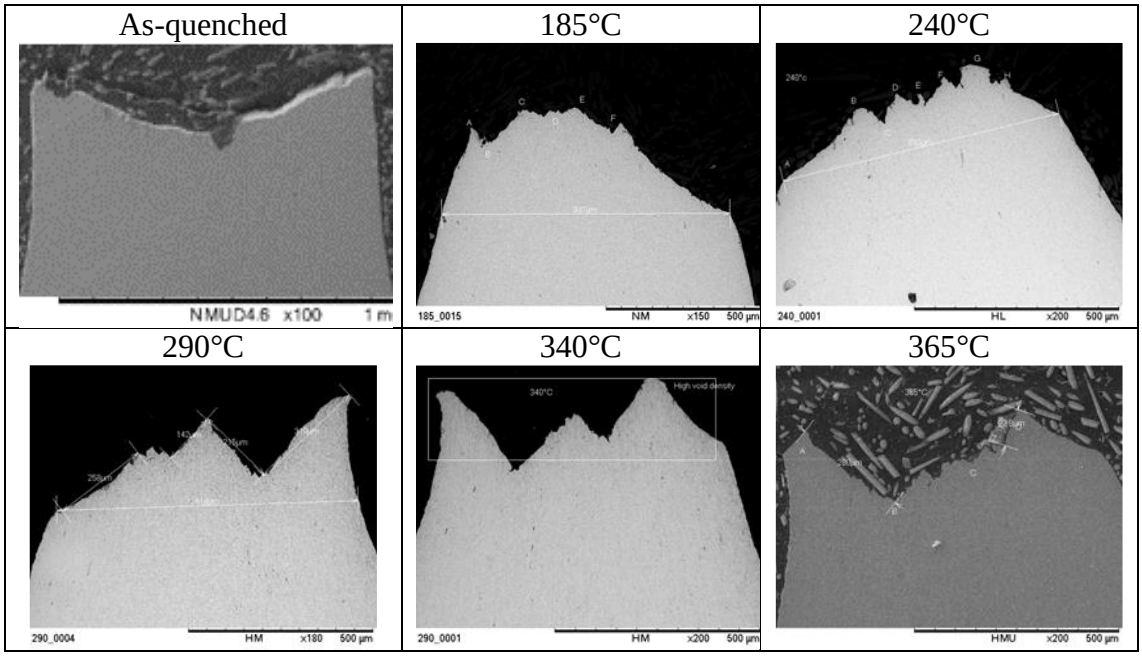

Figure 4-23 Fracture surface of broken tensile specimens observed in the cross-section or in plane Z-Y.

Table 4-6 Reduction of specimens thicknesses at fracture surface from their original thicknesses before the start of testing.

Specimen	Thickness (mm)		
	Before test	After test	Thinning (%)
As-Quenched	1.5	0.98	34.5
185°C	1.46	0.94	35.6
240°C	1.4	0.69	50.7
290°C	1.4	0.81	42.1
340°C	1.5	0.70	53.3
365°C	1.5	0.77	48.7

Table 4-6 shows the thickness measured before and after the test, and the thinning reduction of the fracture surface along the z-axis (cross-section) is calculated. Among all specimens, material as-quenched shows that it has the lowest thickness reduction value of only 34.5%. Specimen that has the largest thinning is specimen 340°C and followed by specimen 240°C with their reduction amount of 53.3% and 50.7% respectively. Specimen of the highest temper, specimen 365°C has the third highest reduction of 48.7%

4.4.2. Crack Propagation and Void Formation near Fracture Surface

Specimen As-Quenched

Fracture surface of the as-quenched tensile specimen is carefully inspected to understand the damage behaviour happening in the through thickness. Figure 4-24 shows five images captured at several magnifications that reveals the damage formation around the centre of specimen through thickness.

Figure 4-24 (A) is a combination of three images captured at 1000x magnification to form a montage covering a large area of the centre region of the fracture surface, hence explaining the changes of contrast though the thickness. The image is labelled with (a1), (a2), and (a3) where region (a1) at the centre shows an evident shear fracture with a fracture profile occurring at a shear angle; while at region (a2) and (a3), the fracture profile is rather flat compared to (a1) without any large shear fracture. Location of the large montage fracture surface (A) on the specimen through thickness is shown in image (AA).

Figure 4-24 (a1), (a2) and (a3) provide a closer observation at the microstructure just below the fracture surfaces. It is clear in image (a1), crack propagation at the shear fracture region is observed to follow just outside the martensite boundaries. The martensite phase are still intact as pointed in the image (a1). Crack propagates in the ferrite phase and propagation path seems follows around the martensite boundaries but maintained in the ferrite phase. Void sizes are larger in this region compared to the voids found at the flat fracture surface. However, this is crack propagation behaviour is only seen in the centre region (a1) where shear fracture is observed. In the region where fracture surface is flat, (a2) and (a3) which is observed at the either sides of centre regions

(a1); crack propagation seems to cross both ferrite and martensite phase with the presence of smaller voids which are mainly found near the interface.

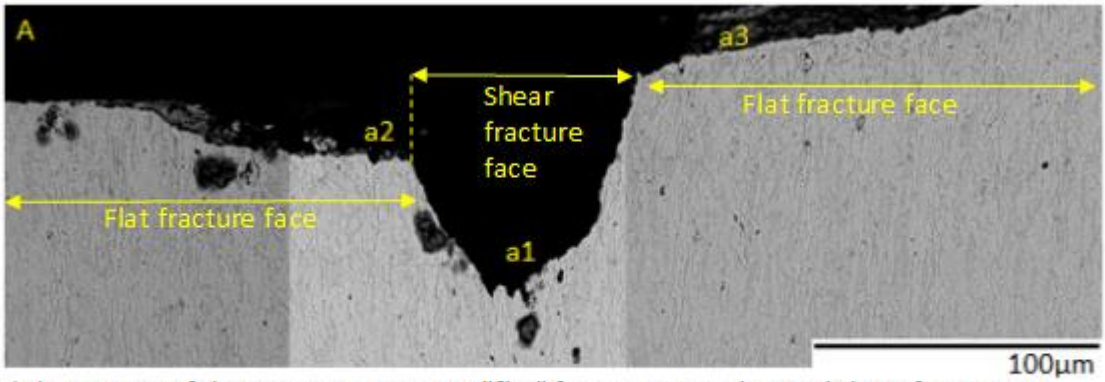

(A) Montage of three images covering "flat" fracture, a2 and a3 and shear fracture, a1 surface profiles taken at the centre of specimen through thickness cross-section.

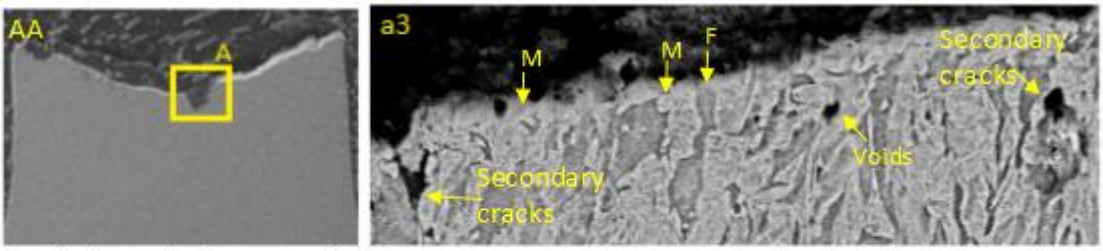

(AA) Shows the location of where image montage A is situated in the whole through thickness cross-section.

(a3) Shows flat fracture surface where crack propagation is at 90° to the applied load crosses both ferrite and martensite phase

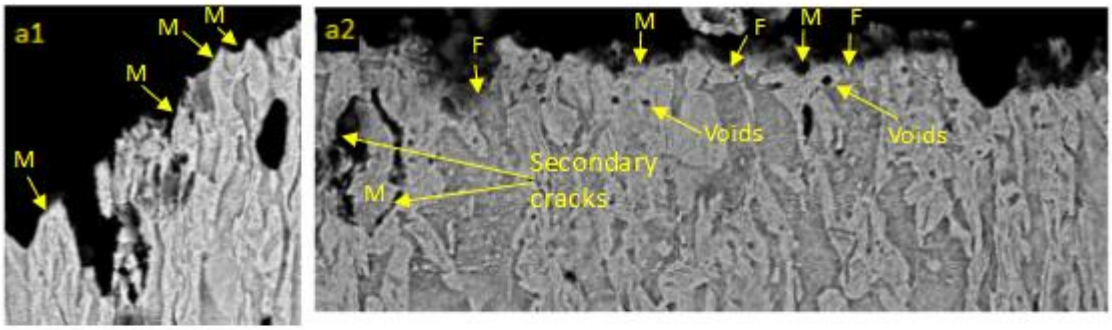

(a1) Crack path along the shear fracture region reveals that crack propagates around the martensite phase boundaries. Image showing martensite phase are still intact.

(a2) Flat fracture surface on the left-hand-side showing crack propagation that crosses both ferrite and martensite phase, along 90° to the direction of the applied load. Secondary cracks near main fracture surface reveals crack forms around the martensite phase.

Figure 4-24 Damage in the through thickness cross-section of DP1000 as-quenched.

The secondary cracks happening in Figure 4-24 (a2) and (a3) provides another information of the damage behaviour at the flat fracture surface. Large secondary cracks

in image (a2) showing an obvious crack along each sides of the martensite island without crossing the martensite.

Specimen 185°C

The fracture surface of tensile specimen 185°C is shown in Figure 4-25 (B). Fracture occurred at the localized necking region and it is observed that the region near centre shows an irregular fibrous fracture and at the outer perimeter of the necking, fracture occurred through shear deformation at approximately 45° angle to the loading direction.

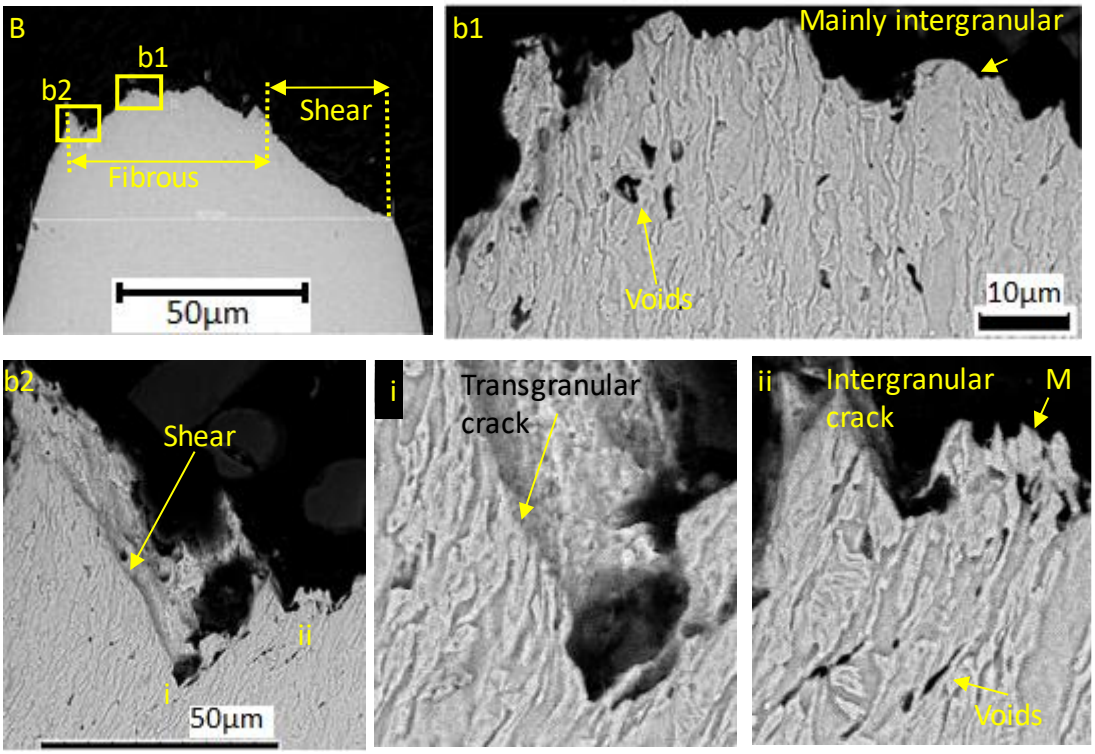

Figure 4-25 Fracture surface of DP1000 heat-treated at 180°C.

At the fibrous fracture region, crack path is observed at a higher magnification as shown in Figure 4-25 (b1) revealing a rather intergranular crack propagation which mainly follows along the outside of martensite boundaries and martensite island are still intact. However, for a shear fracture angled at 45° to the loading direction, crack tends to

propagate through both ferrite and martensite phase as shown in (b2)-I. Nearby region which is not in the high shear stress regime maintained the intergranular crack propagation by moving around the martensite island as shown in (b2)-ii.

Several examples of voids found near region (b1) just beneath the fracture surface are shown in Figure 4-26. Majority of voids formation are found to be orientated at 45° to the loading direction. Image (b1)-i are some of the large size voids are found near region (b1) where is near to the central region. Image (b1)-iv reveals smaller spherical voids formed and orientated at 45° which have not yet coalesced.

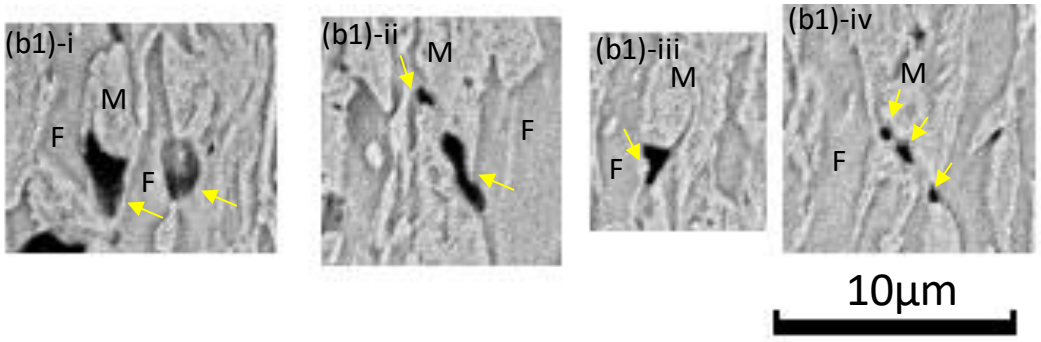

Figure 4-26 Void formation just outside the martensite islands and are elongated at 45° to loading directions. Void in image (b1)-i to iv are the voids forming near region (b1) which are just beneath the fracture surface.

Specimen 240°C

The fracture surface of specimen 240°C as shown in Figure 4-27 (C) shows a ductile fracture that resembles the "cone-shaped" fracture profile. Specimen 240°C fracture surface consists of fibrous fracture region in the centre and the shear fractures on both sides of the outer perimeter of the necking; where compared to specimen 185°C, large shear fracture is observed at only on one side.

Upon closer look at the microstructure just beneath the fracture surface in Figure 4-27 (c1), (c2) and (c3); fracture paths are mainly intergranular type where the fracture

edges followed the martensite island boundaries. However, throughout the whole specimen thickness, transgranular type propagation is only observed at a small region at (C-i) where fracture surface is flat.

Distribution of void formation is uniform and increased in density at the localized necking region, close to the fracture surface. (C-ii) shows the largest void compared to the other observed voids, which is located next to fracture edge. Most developed voids near the necking region are similar to the void shown in (C-iii), which forms at around the martensite islands and orientated at 45° to the tensile direction.

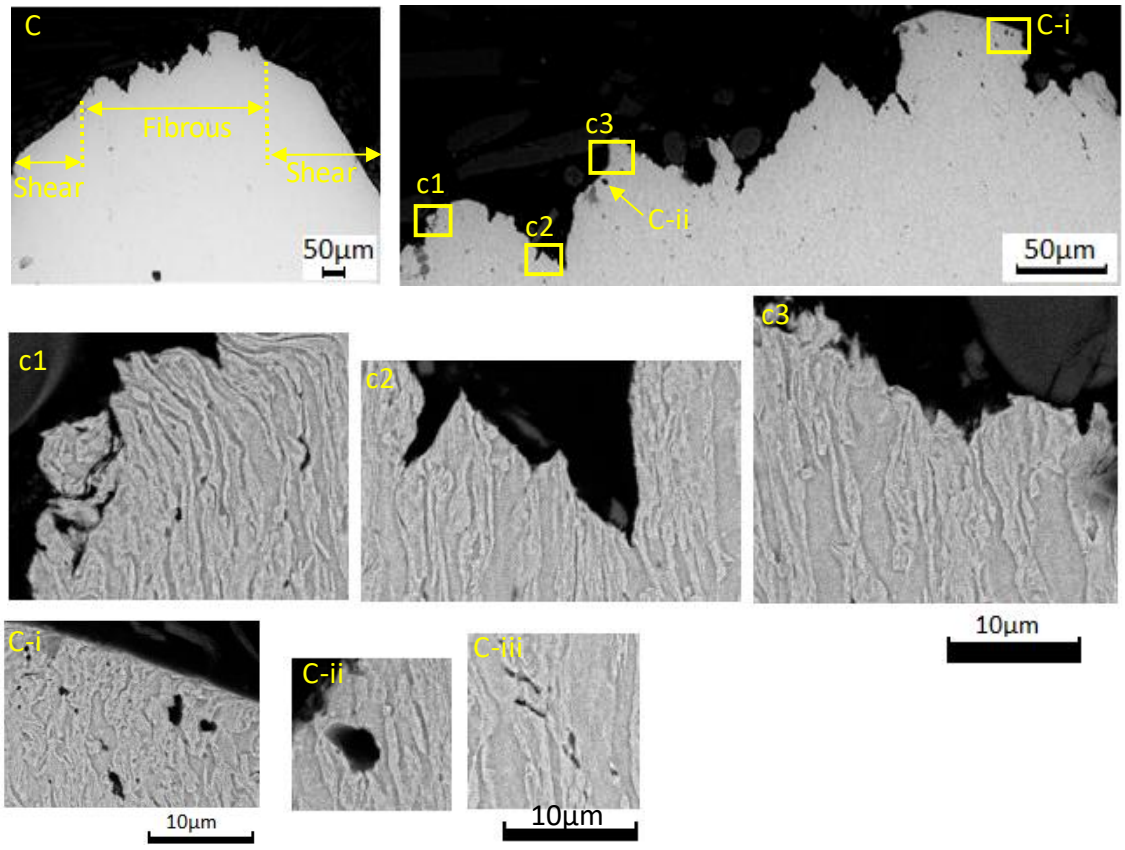

Figure 4-27 Fracture surface of specimen 240°C

Specimen 290°C, 340°C and 365°C

The fracture surface of specimen 290°C and 340°C has large prominent shear fracture profiles compared to other specimens; while the fracture surface in specimen 365°C has a profile of fibrous and shear fracture as observed in specimens 185°C and 240°C. Figure 4-28 (D), (E) and (F) are the fracture surfaces for specimen 290°C, 340°C and 365°C, respectively.

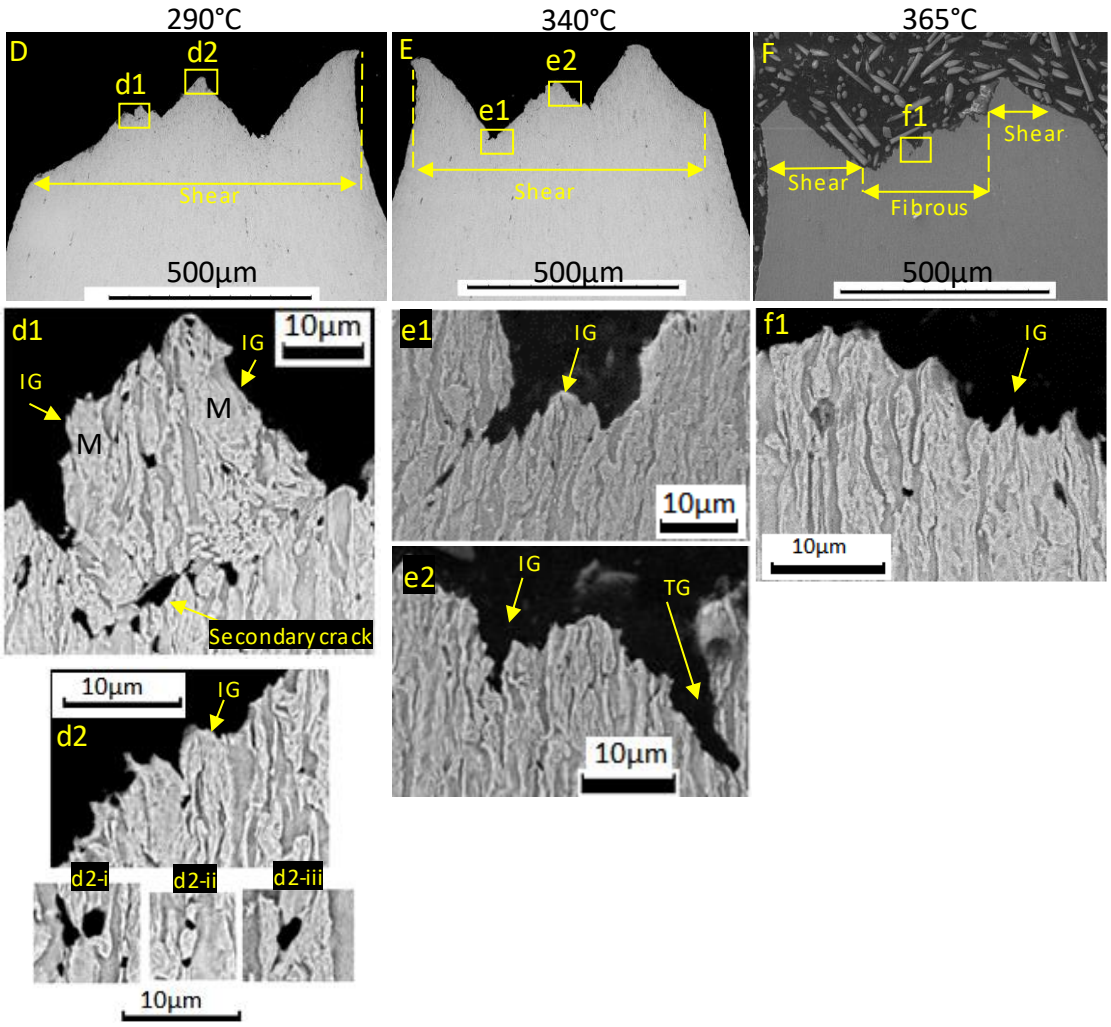

Figure 4-28 Fracture surface of specimens 290°C, 340°C and 365°C.

The fracture path in the three specimens shows mainly intergranular crack path as shown in Figure 4-28 (d1) for specimen 290°, (e1) for specimen 340°C and (f1) for

specimen 365°C and are labelled with “IG” for intergranular crack. A transgranular type of fracture is seen at one region on specimen 340°C and is shown in image (e1). Void nucleation observed in the three specimens are similar to those seen in the previously due to ductile fracture, with voids nucleating adjacent to the martensite grain which is in the ferrite phase. Examples of the observed voids are shown in image (d2-i), (d2-ii) and (d2-iii) which corresponds with the observed void in specimens AQ, 185°C and 240°C presented previously.

Void Analysis near Fracture Surface

Void analysis is performed on all specimens to obtain their average sizes of voids forming just beneath the fracture surfaces. Location for void analysis is chosen at the centre region of the through thickness cross-section for measuring the void fraction amount and their average sizes. SEM images of the centre regions are then captured at 1000x magnification at three local regions, adjacent to each other. At 1000x magnification, image field size is at 168μm by 126μm. Hence, with the total of three micrographs, the total area analysed for void fraction is 1008μm by 123μm. The measured void fraction is shown in Table 4-7.

Void fraction for the as-quenched DP1000 specimen is lowest at compared to the rest of the materials with deeper tempering. While void formation in specimen 365°C it is found is found to be the highest.

Table 4-7 Void fraction measured at the centre of the through thickness region, just beneath the fracture surface

Material	Measured Void Fraction (%)
AQ	0.18
185°C	0.24
240°C	0.37
290°C	0.44
340°C	0.38
365°C	0.53

Chapter 5

Formability Test using 3D DIC to Investigate Crack Propagation in the Sub-Surface of DP1000 Steels

5.1. Introduction

This chapter presents the results obtained from conducting punch test using three-dimensional (3D) optical Digital Image Correlation (DIC) on the investigated DP1000 materials with the effect of different heat-treatments. In this investigation, a laboratory scale punch test has been developed which resembles the forming process in automotive industry that enables to study the effect of post-tempering treatments of DP materials on its formability and most importantly, this procedure is aimed to generate crack at the surface to allow crack propagation to be studied at microstructural scale.

5.2. Preliminary Tests

Results from tensile test only reveals martensite cracking which does not lead to final failure of specimen. Crack propagation of DP1000 steels need to be understood and to do that, different kind of testing need to be developed which can exert higher deformation on the studied material. Before the punch test is developed, several alternative tests have been conducted in the attempt to capture crack propagation happening in the DP specimens.

A micro-scale bending test with μ-scale DIC has been conducted inside an SEM on a 5kN Deben's vertical bending machine as shown in Figure 5-1 (left). Compared to the in-situ tensile test, results from the in-situ bending test are less satisfying due to machine limitation which could only allow deformation of less than 6mm on a thin

specimens. The maximum strain values obtained from DIC analysis on the bending test could only yield up to 12.2% in the ferrite phase with slight deformation in the martensite phase.

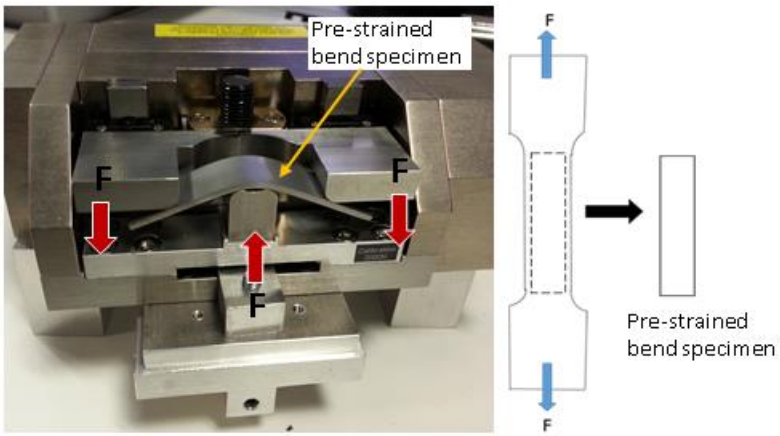

Figure 5-1 A specimen is bent to the maximum using the Deben Microtest Vertical Bending machine outside the SEM chamber (left) and schematic diagram showing the extraction of pre-strained bending specimen form a standard tensile specimen (right).

Another initiative is taken by pre-straining a 12.5mm width standard tensile specimen near to UTS before machining out the elongated gauge section and test it again using the micro-scale bending test inside SEM. Despite using a pre-strained bending specimen, the maximum strain values are still too small for failure to initiate. Since from the tensile test, it was observed that damage starts to appear once strain values exceed 80%. At 12.2%, specimens undergo plastic deformation, and microstructures become deformed, but no damage is observed.

In a desperate attempt to observe damage formation in the studied material, the pre-strained and slightly bent specimen from the previous step is then further loaded under compression using a 25kN electric machine and later is inspected under optical and SEM microscope for damage. Figure 5-2 shows the formation of vertical crack perpendicular to the loading direction on the surface.

Damage has been observed, however this testing method is not a controlled loading which makes the analysis hard to be analyse. So, since damage is hard to be observed in a tensile and bending test. The final option is to produce a test which can exert out-of-plane deformation such as forming test. This then leads to the development of the small scaled punch test to study damage formation in the DP1000 steels.

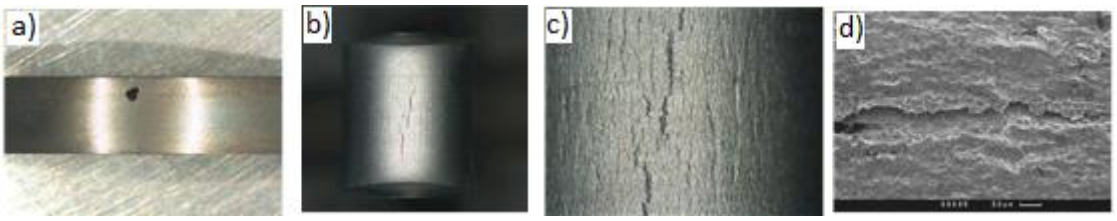

Figure 5-2 A set of images of DP1000 steel specimen pre-strained and bended which (a)-(c) are taken using optical microscope while (d) using an SEM. (a) Half-bended specimen, where there are no sign of damage yet only high plastic deformation (b) Fully-bended specimen taken at low magnification (c) Fully-bended specimen taken at high magnification showing formation of cracks. (d) SEM images showing up close view of crack formation.

5.3. Punch Test using 3D DIC

In this investigation, the received 1.5mm thickness DP1000 steel sheets of different tempering conditions are machined into 90mm diameter blanks and tested until specimen fails. From running this punch test, it is expected to observe crack formation on the surface of specimen which later will be inspected in the mid-thickness to provide information on the damage mechanisms occurring in a condition similar to the forming process in the industry. In conjunction with that, the effect of different heat treatments applied on the formability of the studied DP1000 steels can also be compared.

The 90mm diameter specimens are produced in sets of three for each material. Table 5-1 shows that the punch tests are done in three batches. The first batch of DP steels samples are tested using the non-contacting optical method, 3D-DIC coupled with the

punch test to allow deformation and strains to be measured. The second and third batch is intended to validate the obtained results which will prove the developed punch test has good repeatability and the collected data from the tests are statistically reliable.

Table 5-1 The total of punch tests conducted on the studied DP1000 materials of different heat treatments.

Materials	**Punch tests Conducted**			**Total Tests**
	Batch 1 (using 3D DIC)	Batch 2 (without 3D DIC)	Batch 3 (without 3D DIC)	
As-Quenched	✓	✓	✓	3
185°C	✓	✓	✓	3
240°C	✓	✓	✓	3
290°C	✓	✓	✓	3
340°C	✓	✓	✗	2
365°C	✓	✓	✓	3

5.3.1. Force-Displacement Response

In this experiment, the punch test rig along with stereo vision DIC cameras are securely fixed on a MAYES 100kN electric machine. For each test, the machine is set to load the specimens at constant position rate of 2.5mm per minute in compression mode. Before testing begin, it is ensured that there is no contact between the specimen and the tip of punch. The DIC system will begin the stereo image capturing soon as Mayes machine is set to run. Data acquisition device of the machine will display real-time force-displacement response of the loading state during the test. Test is stopped once the force response drops abruptly which can also be heard from the loud sound produced by the broken sample. Figure 5-3 shows broken samples after tested using punch test.

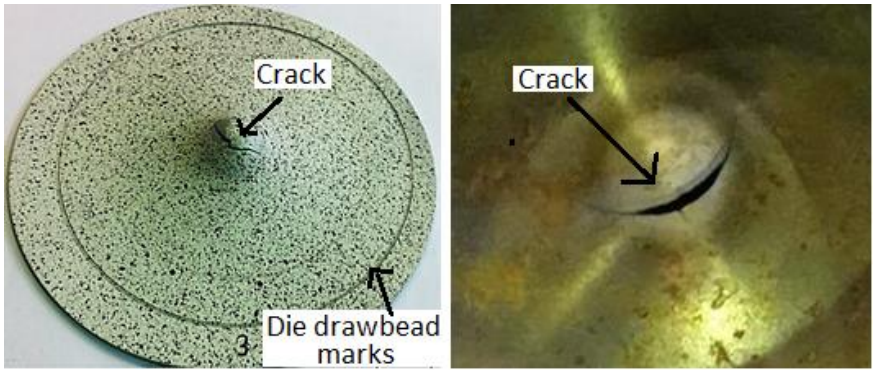

Figure 5-3: Examples of broken punch test specimens. Image on the left is the broken specimen coated in paint for DIC and image on the right is the revealed crack after the speckled coating is removed from specimen surface.

Experimental data from all three batches have been successfully collected for all studied DP materials except for DP1000 post-tempered at 240°C, where the data from the third batch is missing due to some problems faced during the test. The force-displacement results are shown in Figure 5-4. In these plots, the displacement is re-aligned to 0, when the load is at 1 kN. This is because it is difficult to identify the start point of contact between punch and specimen due to low noise in machine reading below 1kN. Increment in load reading becomes stable as it gets close to 1kN for all tests.

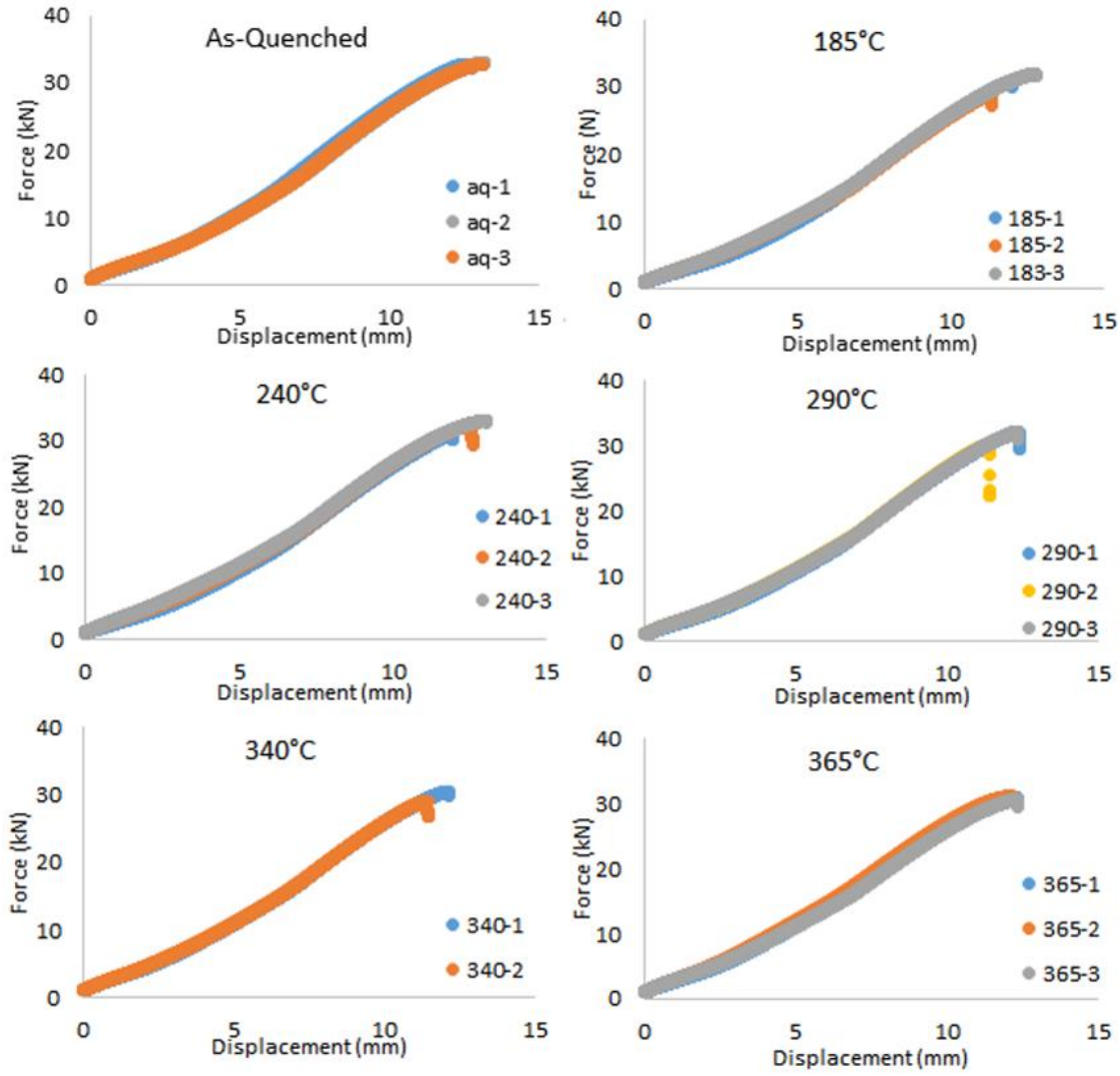

Figure 5-4 Force-displacement response obtained from conducting punch test plotted according the tempering conditions.

The maximum values for both force and displacement for all of the obtained results are shown in Table 5-2. Mean values with standard deviation are calculated based on the data from the three batches, then these values are plotted in Figure 5-5. The plot shows that DP post tempered at 240°C has the highest mean max. displacement that is 13.68mm

Table 5-2: Results obtained from conducting punch test on all three batches of specimens. Maximum force-displacement values are gathered from collected data and their mean values are calculated and shown in the table.

Materials	**Batch 1**		**Batch 2**		**Batch 3**		**Mean, μ**		**St. Dev., σ**	
	F_{max} [kN]	W_{max} [mm]	F_{max} [kN]	W_{max} [mm]	F_{max} [kN]	W_{max} [mm]	F_{max} [kN]	W_{max} [mm]	F_{msx}	W_{max}
As-Quenched	32.8	13.1	32.8	12.8	33.1	13.2	32.91	13.03	0.14	0.2
185°C	30.7	12.0	28.5	11.3	31.9	12.8	30.36	12.05	1.4	0.59
240°C	30.8	15.3	32.2	12.6	33.0	13.1	31.99	13.68	0.91	1.18
290°C	32.1	12.4	30.0	11.4	32.0	12.4	31.36	12.05	0.96	0.49
340°C	30.4	12.1	28.9	11.9	-	-	29.65	12.01	0.78	0.14
365°C	31.0	12.3	31.0	12.2	30.6	12.3	30.87	12.28	0.19	0.07

F_{max}: Maximum force, W_{max}: Maximum out-of-plane displacement
St. Dev: Standard deviation

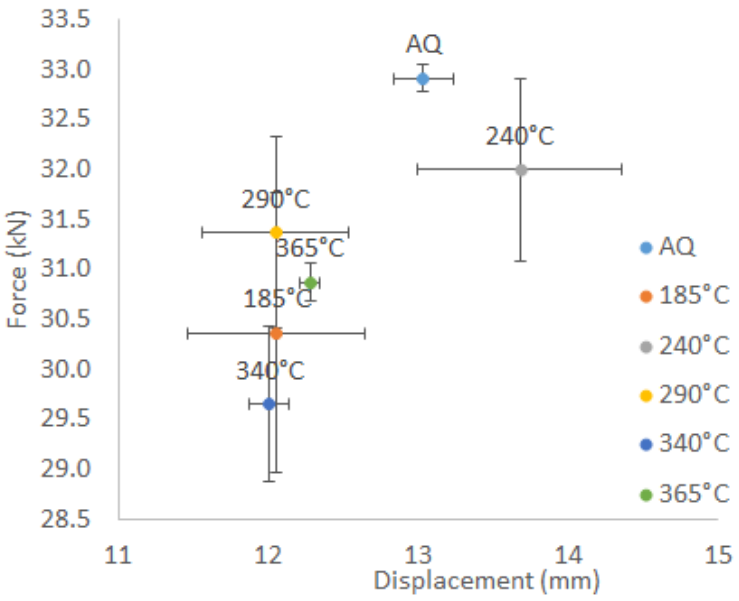

Figure 5-5: Mean values for the obtained for the maximum force-displacement are plotted with error bars based on data spread among the three batches.

5.3.2. 3D Strain Distribution in Punch Test

The optical 3D DIC method being used alongside in this test provides further information on the out of plane deformation happening on the surface of specimen. After the test, the captured images from the DIC device are processed in order to provide information on the strain localisation and deformation of the specimen.

For the optical 3D DIC method to work, two cameras are attached to the punch test rig and are focused on the centre of a well-lit specimen. Hence, allowing the 3D DIC system to analyse out-of-plane deformation of the specimen. The image captured by the DIC system is shown in Figure 5-6, where image (A) is the undeform specimen taken before test begin and image (B) is the failed specimen taken after test is stopped.

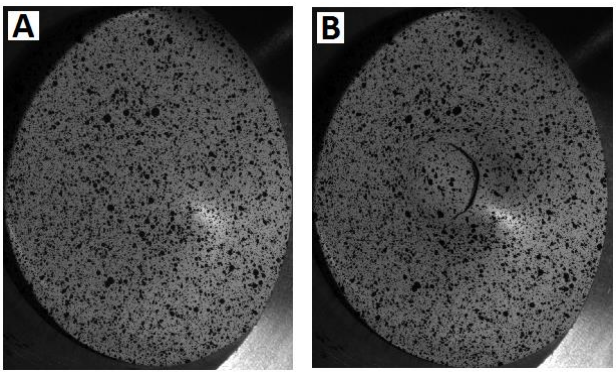

Figure 5-6 Example of punch test specimen before and after testing.

Once experiments are completed, the captured images are processed using a DIC commercial software, Correlated Solutions VIC-3D to extract deformation and strain results. The full deformation development happening when the punch test took place can be observed in the series of images in Figure 5-7. In the figure, there are six images in series showing the deformation development on the surface of tested DP steel specimen blanks from the start of test until the onset of specimen failure. Each images (IMG 1 to IMG 596) in Figure 5-7 are showing the strain distribution map of the increment of strain, Exx happening on the surface of tested specimen. These sequence of images are explained in details in Table 5-3.

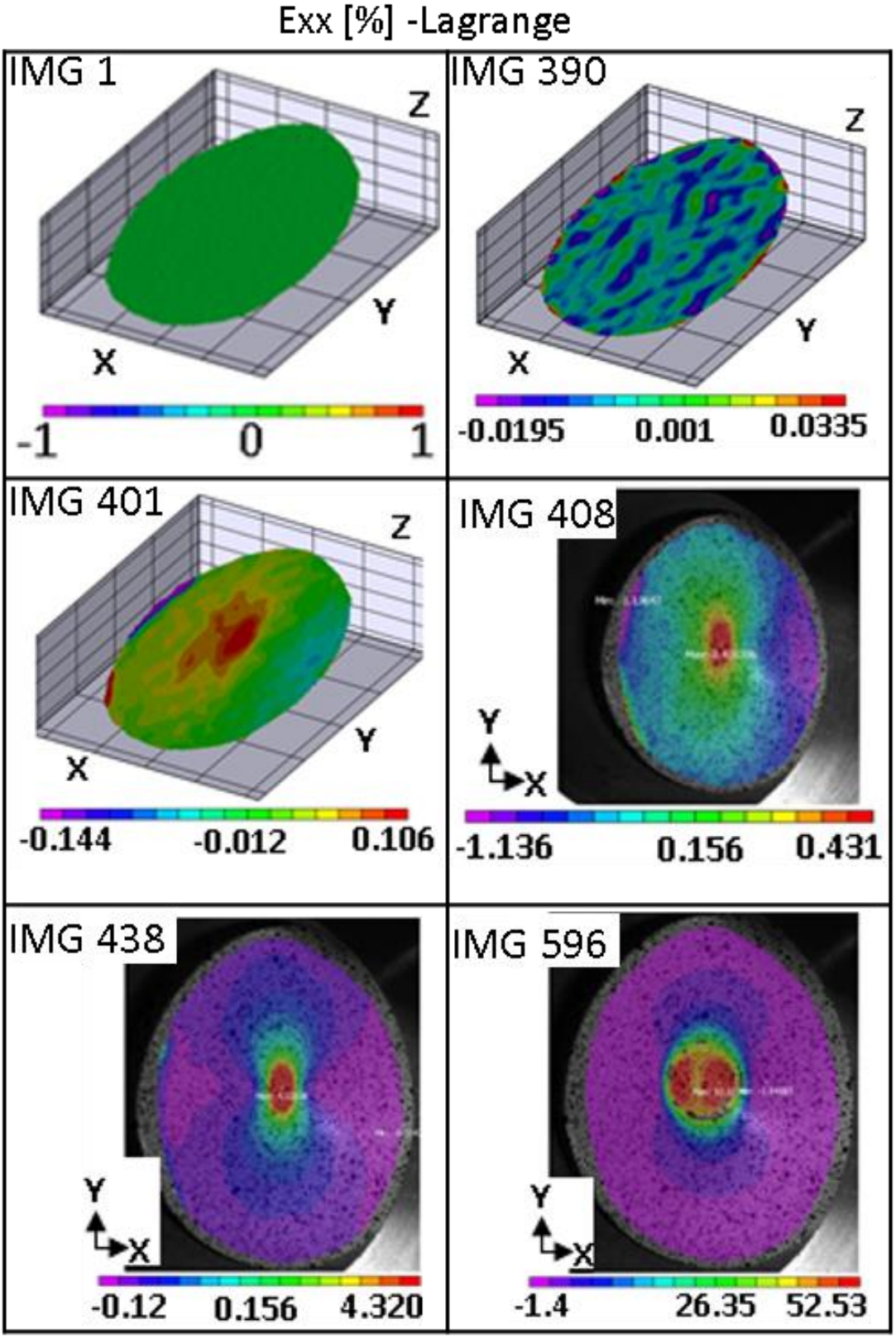

Figure 5-7 Development of strain, Exx happening on as-quenched punch test specimen from the beginning to the onset of fracture. These images are explained in Table 5-3.

Table 5-3 Deformation development of punch test in Figure 5-7 explained according to the respective images.

IMG1	**Exx = 0%.** During the start of the test, the first image captured will show a uniform green distribution which states that the current strain is at 0%. At this point, the punch tool is still far away from being in contact with the punch blank. (3D-view)
IMG 390	**Exx = +/- 0.03%.** At this point of the test, the punch tool has not reached the specimen yet. Result observed on the strain distribution is due to the noise created due to the DIC correlation. The punch blank is still intact from any deformation. (3D-view)
IMG 401	**Exx = 0.1%.** Punch tool has reached the specimen and deformation begin to take place. Plastic deformation begins to form at the centre of punch blanks and is still not visible with naked eye. With DIC analysis, the start of deformation is easily to catch and controlled if the test has to be stopped at certain level of deformation. (3D-view)
IMG 408	**Exx = 0.4%.** Strain hot spot, the largest deformation is growing at the point of contact between punch tool and specimen. (View is changed to 2D-view for a better view on the strain map).
IMG 438	**Exx = 4.3%.** From deformation of 0.4% to 4.3%, with increasing load, strain distribution is becoming more localized, with larger increment at punch tool contact and very little deformation /no changes at the surrounding area. (2D-view)
IMG 596	**Exx = 53%.** Towards near fracture, necking occurs around the side on the deformed dome. As observed in the strain map, hot spot that was initially in the centre has now moved to each sides of the dome. Specimen broke once strain values reaches above 52.3%. (2D-view)

Figure 5-8 shows the out-of-plane deformation development of the surface of as-quench specimen as it is being loaded by the punch. The result is displayed on the side of a 3D plot, in an XZ axis to show the amount of deformation took place in the specimen. In image (4), the result shows the maximum out-of-plane or z-axis displacement before crack appear, or specimen fail, and test is stopped. To obtain the maximum displacement

in the z direction, the result is presented in a 2D plot as shown in Figure 5-9 to observe the maximum values of out-of-plane displacement. Same method is repeated for all specimens in Batch 1 that have been tested using the 3D DIC system and the result are then presented in a table for comparison.

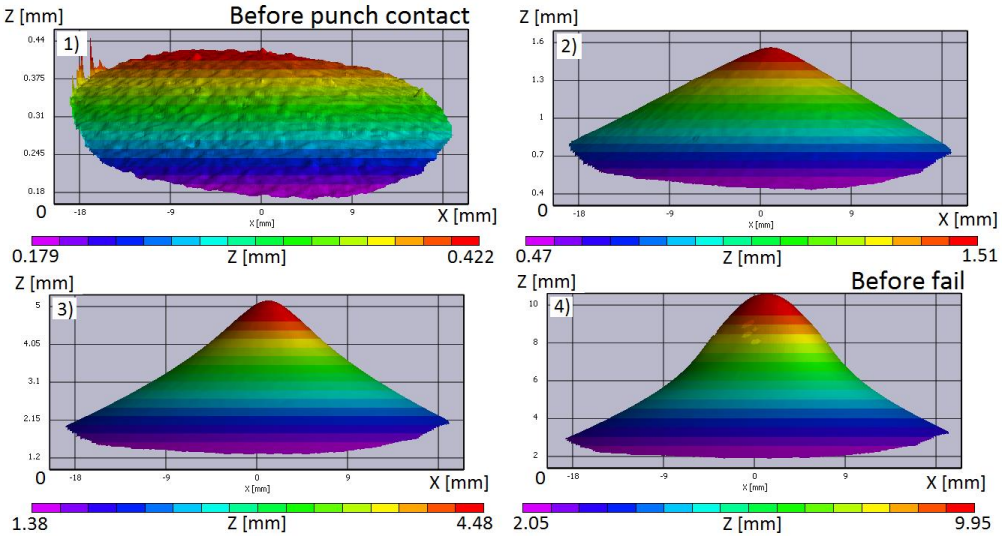

Figure 5-8 Images 1 to 4 are a series of 3D-DIC results showing the out of plane deformation of an as-quenched specimen during punch test.

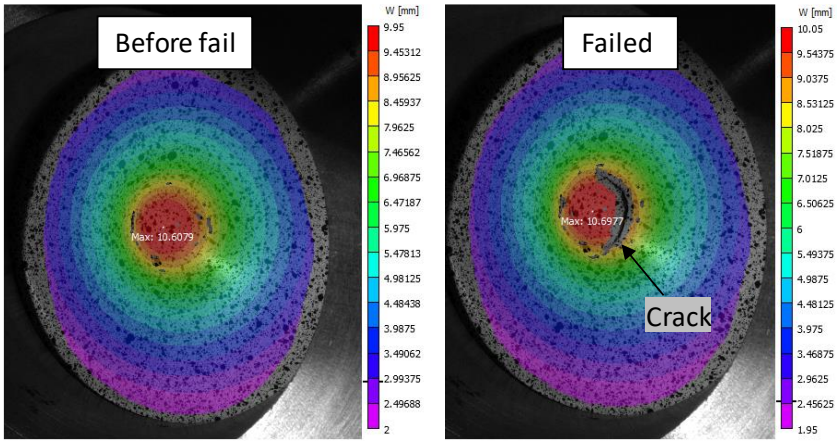

Figure 5-9 The out-of-plane displacement plot of as-quenched specimen displayed in 2D plot. Image before fail (left) is the maximum z-displacement obtained before crack developed which can be seen in the failed image (right).

Table 5-4: Maximum out-of-plane displacement of all specimens obtained using DIC in comparison with maximum displacement obtained from the machine.

Materials	Out-of-plane Displacement, Z-axis (mm)		Differences	
	3D DIC	Machine	(mm)	(%)
As-Quenched	10.6	13.1	2.5	19.1
185°C	10.76	12.0	1.24	10.3
240°C	9.84	15.3	5.46	35.7
290°C	10.3	12.4	2.1	16.9
340°C	9.93	12.1	2.17	17.9
365°C	10.52	12.3	1.78	14.5

Table 5-4 shows the maximum out-of-plane displacement result obtained using DIC including the maximum values taken from the machine. It is found that the displacement in z-axis obtained from the machine is higher than the values obtained using DIC. Differences found between the measured values are in between the range of 10% to 19%, except for specimen 240°C. For specimen 240°C, there is a high difference in the displacement between results from DIC and machine result which is due to a failed DIC correlation towards the end of the test. Correlation failed because the large deformation happening on the specimen caused the speckled coating to peel off/ damaged. Thus, the maximum values obtained from DIC, for specimen 240°C is not the final or the maximum ones.

From the DIC, deformation of tested specimens can be analysed in terms of their strain distributions. Referring to Figure 5-10, the series of four images; (1 to 4) shows the strain development in the as-quenched specimen from the beginning of the test to the maximum loading state before specimen failed. In image (1), specimen is still intact and there is no contact yet between the punch and specimen. Hence, result from the strain plot before punch contact is the noise from the correlation with a maximum value of 0.03%.

From image (2) to (3), strain begin to grow most noticeably at the centre region from 1.72% to 10.80%. Approaching the final stage of test before specimen failed as shown in image (4), deformation in the sample seemed to localise around the outside of the centre region as indicated by the arrow with a high strain concentration with an average value of 19.7%. Similar pattern of result is observed in all other specimens where strain first accumulate at the centre and later with increasing loading, strain increment begins to localise around the outside of centre region (resulting from the large surface contact between punch and specimen).

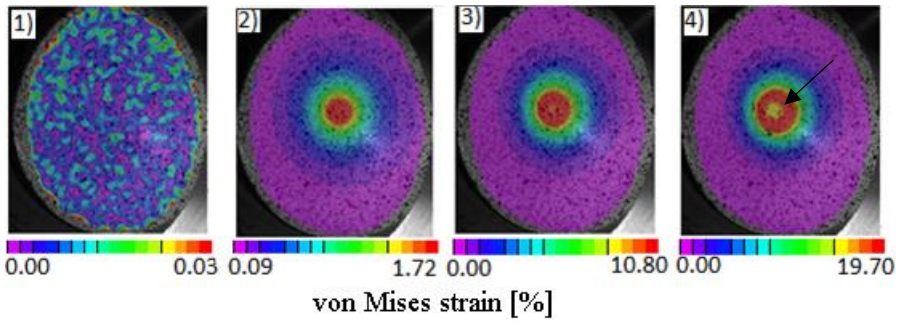

Figure 5-10 Plots showing the increment in von Mises strain distribution of as-quenched specimen being loaded during the punch test. High strain of localized necking is as indicated in (4).

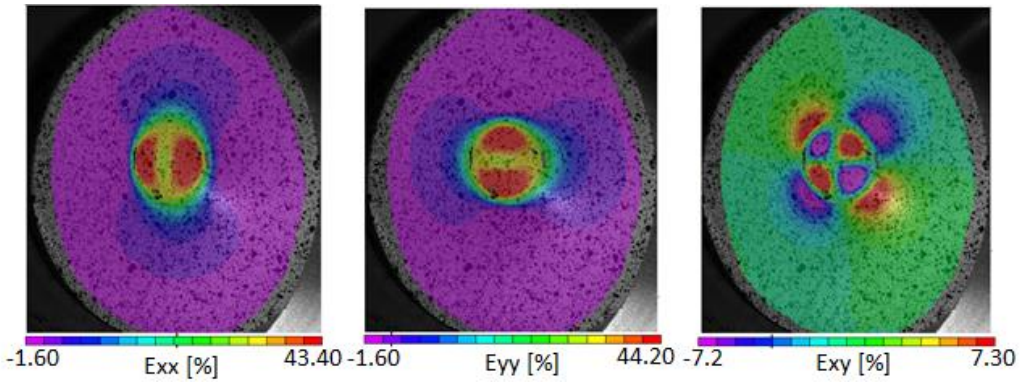

Figure 5-11 Results showing strain plots in Exx, Eyy and Exy of specimen as-quenched at the onset of failure.

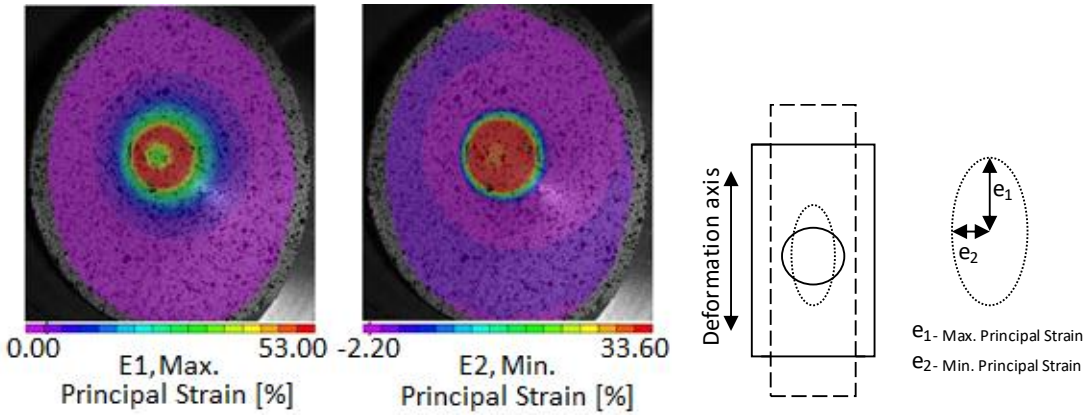

Figure 5-12 Maximum, e_1 and minimum, e_2 principal strain of as-quenched at the onset of failure.

Since the strain distribution maps for all specimens are similar in terms of strain localization pattern or map shape as shown in Figure 5-11 and Figure 5-12, results from all materials are presented in a table rather than using strain distribution plot. This will make comparing the results among the different materials to be simpler and thus, allowing results of several other strain variables can be included and compared together at the same time. DIC correlation generates a wide range of useful output data during the post-processing and the data extracted in this result section are as listed below:

- E1: Maximum Principal (major) strain
- E2: Minimum Principal (minor) strain
- Exx: Strain along x-axis
- Eyy: Strain along y-axis
- Exy: Shear Strain
- The von Mises criterion: Surface strain calculation using principal strain. Equation being used is as follows:

$$\epsilon_v = \sqrt{\epsilon_1^2 - \epsilon_1\epsilon_2 + \epsilon_2^2}$$

Equation 4

Where $\in_v$ is the von Mises strain, $\in_1$ is Maximum principal strain and $\in_2$ is Minimum Principal strain. It is worth to note that, the 3D DIC technique can only calculate strain on the surface, and does not include the deformation happening in the through thickness. (Correlated Solutions, 2017)

Strain values from the DIC correlation are extracted once specimen reaches their maximum out-of-plane deformation which during the onset of specimen to be broken. Table 5-5 shows all tested materials tabulated with their corresponding strain results. By comparing the set of strain variables, as-quenched specimen has the highest strain values among other materials with a von Mises strain, $\in_v$ of 26.1%. The second and third highest strain values recorded before specimens are broken are specimens 365°C and 185°C, respectively; with $\in_v$ values of 9% and 11.9% lower than the as-quenched.

However, it is important to refer to the previously highlighted issue for material 240°C in Table 5-4. For material 240°C, the result obtained using DIC is only reliable up to certain stage during the test. Towards the end before specimen breaks, specimen 240°C has immensely deformed leading to speckle paint peeling which caused DIC failed to correlate and unable to yield the strain measurements. Therefore, another method for strain analysis is chosen to investigate the effect of heat treatment on the formability on DP material.

Table 5-5 Comparing the maximum strain measurements extracted from processing the 3D-DIC results on all specimens.

Materials	Strain [%] – Taken at maximum point before specimen fail					
	von Mises	**E1**	**E2**	**E_{XX}**	**E_{YY}**	**E_{XY}**
As-Quenched	26.1	60.2	35.0	55.9	60.1	12.1
185°C	23.0	53.2	30.9	49.2	53.7	9.53
240°C	17.2	38.7	28.6	33.9	38.6	9.6
290°C	20.4	46.8	31.3	45.8	46.3	11.2
340°C	20.9	47.9	28.8	47.7	46.5	8.7
365°C	23.7	54.5	32.2	49.6	53.7	10.65

Since DIC correlation is likely to fail towards the end on the punch test, which in this case happened to specimen 240°C; thus, the best way to compare the strain state of each material is to measure the maximum strain values at a specific state of deformation of the specimens. The state in which, strain measurements to be carried out is chosen to be when specimen reached 6mm displacement in the z-axis (out-of-plane displacement). At this point, results from all materials have been carefully confirmed so that there is no loss of correlation in the strain distribution plot to avoid any errors.

Strain measurements are immediately recorded as specimens reached 6mm out-of-plane displacement. The results are the presented in Table 5-6. From this table, it is shown that specimen 240°C has the highest strain (in all strain variables) among all materials with an $\in_v$ higher than 2.9% of the reference as-quenched material with a $\in_v$ of 7.56%. While the material with the third highest $\in_v$ is 365°C that is 2.5% lower than as-quenched.

Table 5-6 Comparing the strain measurements which are extracted as specimens reaches 6mm out-of-plane displacement.

Materials	Strain [%] – Taken at Z-displacement of 6mm					
	von Mises	**E1**	**E2**	**E_{XX}**	**E_{YY}**	**E_{XY} (max/min)**
As-Quenched	7.65	16.0	15.0	15.5	15.9	3.4/-3.5
185°C	6.75	13.7	13.3	13.3	13.7	2.9/-3.0
240°C	7.87	16.6	15.04	16.2	16.5	3.5/-3.5
290°C	6.98	14.3	13.9	14.0	14.2	3.1/-3.1
340°C	7.32	15.1	14.3	14.9	15.1	3.2/-3.3
365°C	7.46	15.7	14.4	15.1	15.6	3.3/-3.3

Results obtained from the punch test shows good repeatability after being repeated at several times and on different materials. If tensile test provides a uniaxial loading on the tested specimens, the punch test provides a biaxial loading as shown in Figure 5-13. The mode of loading can be identified by plotting the maximum principal strain, e_1 against the minimum principal strain, $e_{2;}$ which reveal the increment of e_1 is approximately proportional to e_2. Thus, with the $e_1 \approx e_2$ reveals that specimens are under equi-biaxial loading through the conducted punch tests.

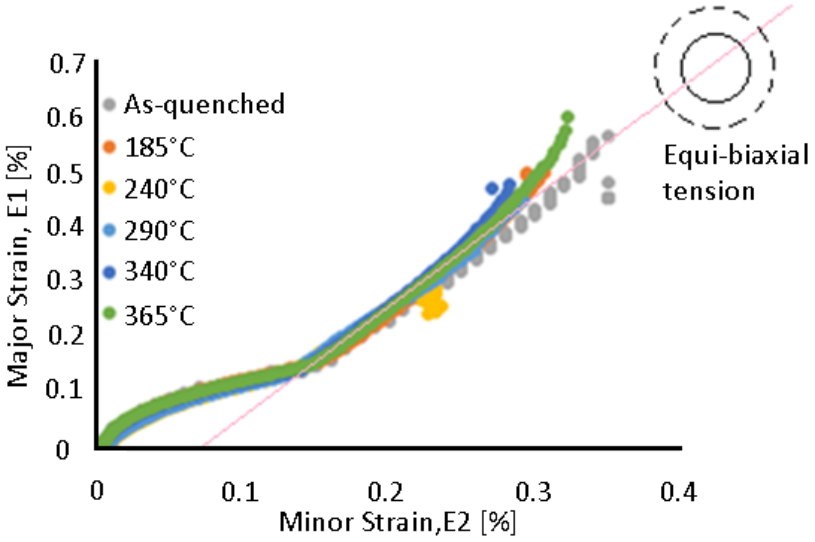

Figure 5-13 Plot of max. principal strain, e_1 against min, principal strain e_2 of all materials (left). Trend line in pink showing that punch tests exerts almost equi-biaxial stretching on tested specimens.

5.3.3. Crack Propagation Analysis on Punch Tests Fractured Specimens.

In order to study the damage in the fractured regions of punch test specimens, the large 90mm diameter specimens from all tested materials need to be cut and undergone a surface preparation for SEM. The tested specimens which are still covered with paint are cleaned using isopropanol solution to reveal the metallic surface. A segment of specimen at the middle region, measuring 20mm by 20mm where crack formed is extracted by using EDM wire cutting machine. The square segment of the fracture sample is then, sectioned again at the centreline to produce a 20mm by 10mm fracture sample. Figure -5-14 shows the process of extracting the fractured segments from the large circular blanks after the punch tests. The extracted segments are then mounted using conductive bakelite before the surfaces are polished and etched for SEM inspection. The chosen plane for damage observation is at the specimens through thickness cross-section

where damage sites is expected to be at the localized necking region of the specimens; which will also be the sites where crack propagation will be studied.

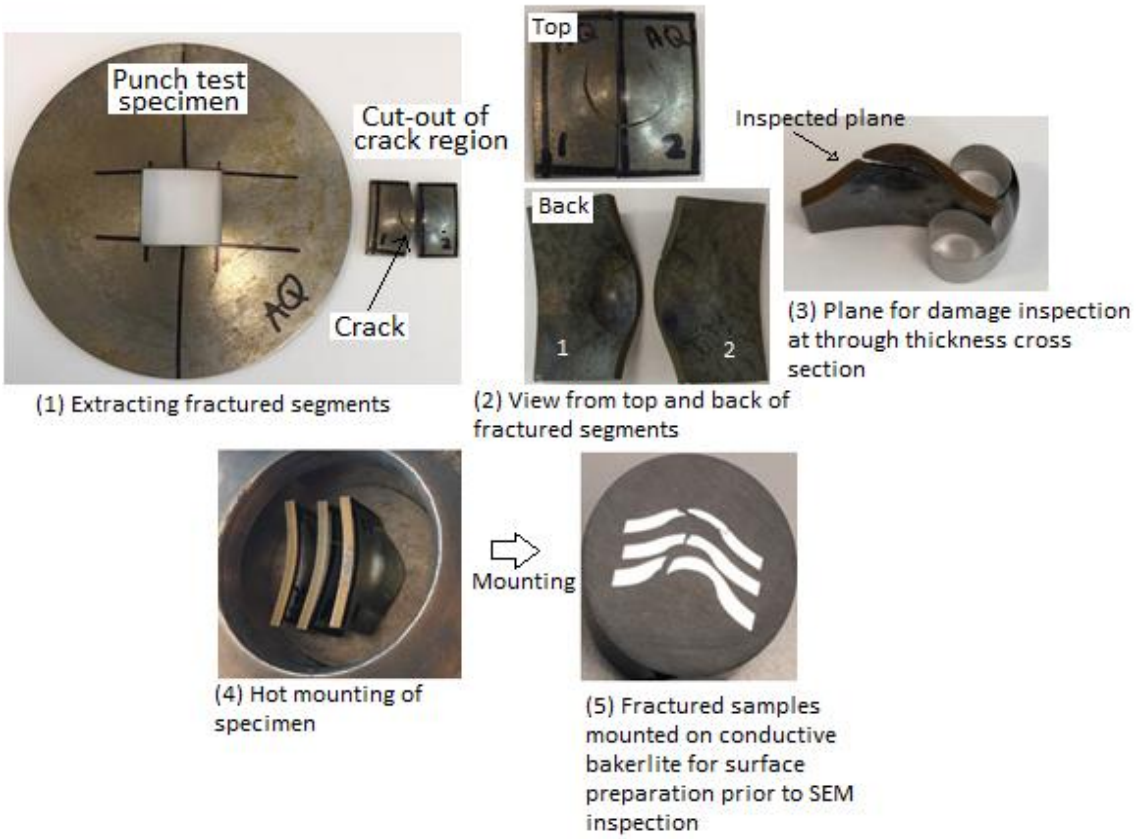

Figure -5-14 Centre region of a failed punch test specimen is extracted out and later is cut in half to reveal the cross-section profile of a failed punch test specimen.

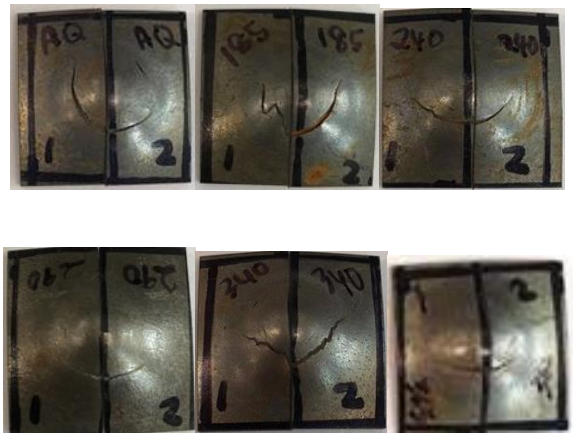

Figure 5-15 Top view of crack forming in the punch from all tested materials. From top left to bottom right are specimens AQ, 185°C, 240°C, 290°C,340°C and 365°C.

Crack formation on the surface of specimen is shown in Figure 5-15. These are the 20mm by 20mm segments after being extracted from the 90mm diameter punch specimens. As observed in the images of each specimen, crack developed in a “crescent-shape” along the localised necking region in every specimen. During the test, it is important to immediately stop the loading just after specimen failed. Specimen fails when the force reading drops abruptly. If loading is exerted for too long on specimen after it failed, the fractured region will deform in a catastrophic manner and preventing post-punch test analysis for damage in the though thickness to be done. Example of a good fracture specimen for the post-test microstructural damage inspection is shown in Figure 5-16.

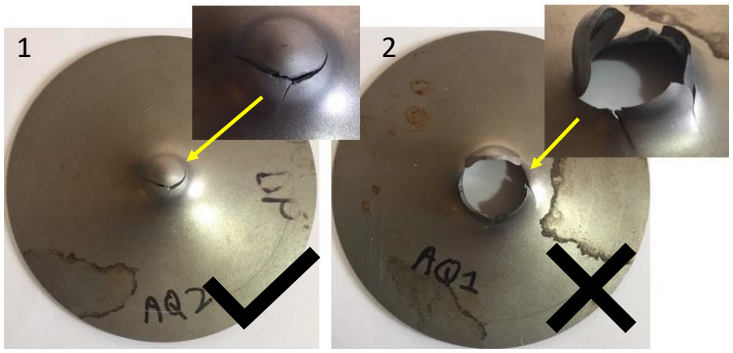

Figure 5-16 Example of the recommended size of fracture in (1) with a smaller and controlled fracture and a large catastrophic fracture in (2) which should be prevented for the post-punch test microstructural damage inspection.

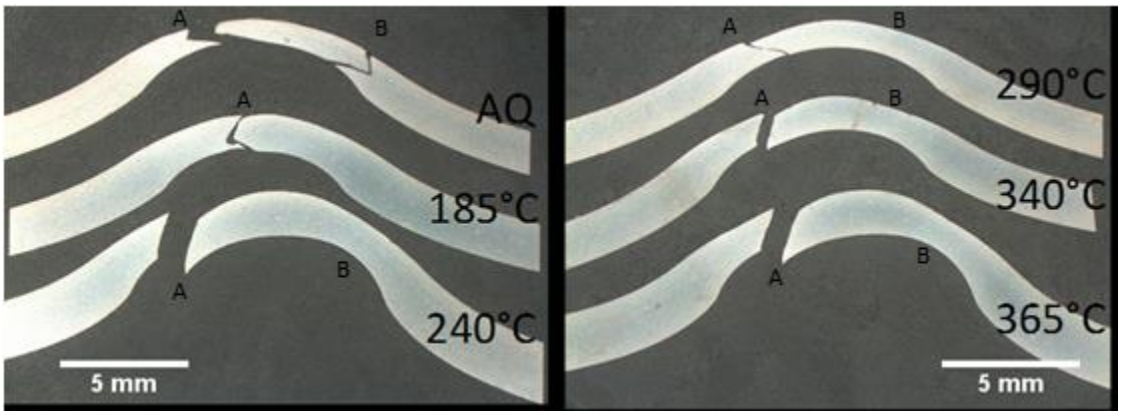

Figure 5-17 The through thickness cross section surfaces of punch test samples captured using optical microscope. Necking region labelled with A and B in the figures are measured and presented in Table 5-7.

The polished and etched fracture samples are then inspected under an optical microscope to have a closer view on the fractured region. Figure 5-17 shows the through thickness cross-section of all six tested DP materials revealing the fracture profiles as well as significant thickness reduction at the localized regions. It is observed that fracture profiles in specimen AQ and 185°C has the combination of shear and fibrous fractures, while specimen 240°C, 290°C,340°C and 365°C, the fracture profile are complete shear fracture which are orientated at around 45° to the longitudinal direction.

At the beginning of the test, the thickness of all 90mm diameter punch blanks are at 1.6mm which are maintained from their original as-received thickness. At the end of the text, after specimen fracture, it is found that due to high out of plane deformation, plastic deformation is localised at the contact region between the sides of punch and material, which are also shown with DIC strain distribution result previously in Figure 5-10. This reduction of thickness at the fractured region is measured and presented in the Table 5-7. Specimen AQ has the largest reduction of 42%, specimen 290°C has the second largest reduction of 40%, while specimen 240°C has the smallest reduction of only 17%.

Table 5-7 Thickness reduction at the necking region. A and B are the locations where necking is measured as shown in Figure 5-17. Where region (A) is the location of fracture.

Specimen	Thickness at Necking (mm)		Reduction from 1.6mm (%)	
	A	**B**	**A**	**B**
AQ	0.93	1.21	41.9	24.4
185°C	1.25	-	21.9	-
240°C	1.33	1.32	16.9	17.5
290°C	0.96	1.01	40.0	36.9
340°C	1.08	1.16	32.5	27.5
365°C	1.25	1.19	21.9	25.6

Specimen As-Quenched

In the as-quenched, AQ sample, fracture surface is observed on both sides of the localized necking region, as shown in Figure 5-18 (A1) and (A2). Fracture surfaces in (A1) and (A2) are a combination of fibrous and shear fracture. Main cracks in (A1) and (A2) are orientated at 45°, along the maximum shear stress. The void density at the necking region of the AQ punch test specimen is less present compared to the high density void formation in AQ tensile specimens. In region (A1a) along the main crack, there is a large broken fragment which is still attached to the specimen fracture surface. In the region near this attached fragment, large voids are observed in enlarged image (A1a-ii). These voids formation may be due to high plastic deformation and large void has coalesced beneath the observed surface (which could also be part of the main crack).

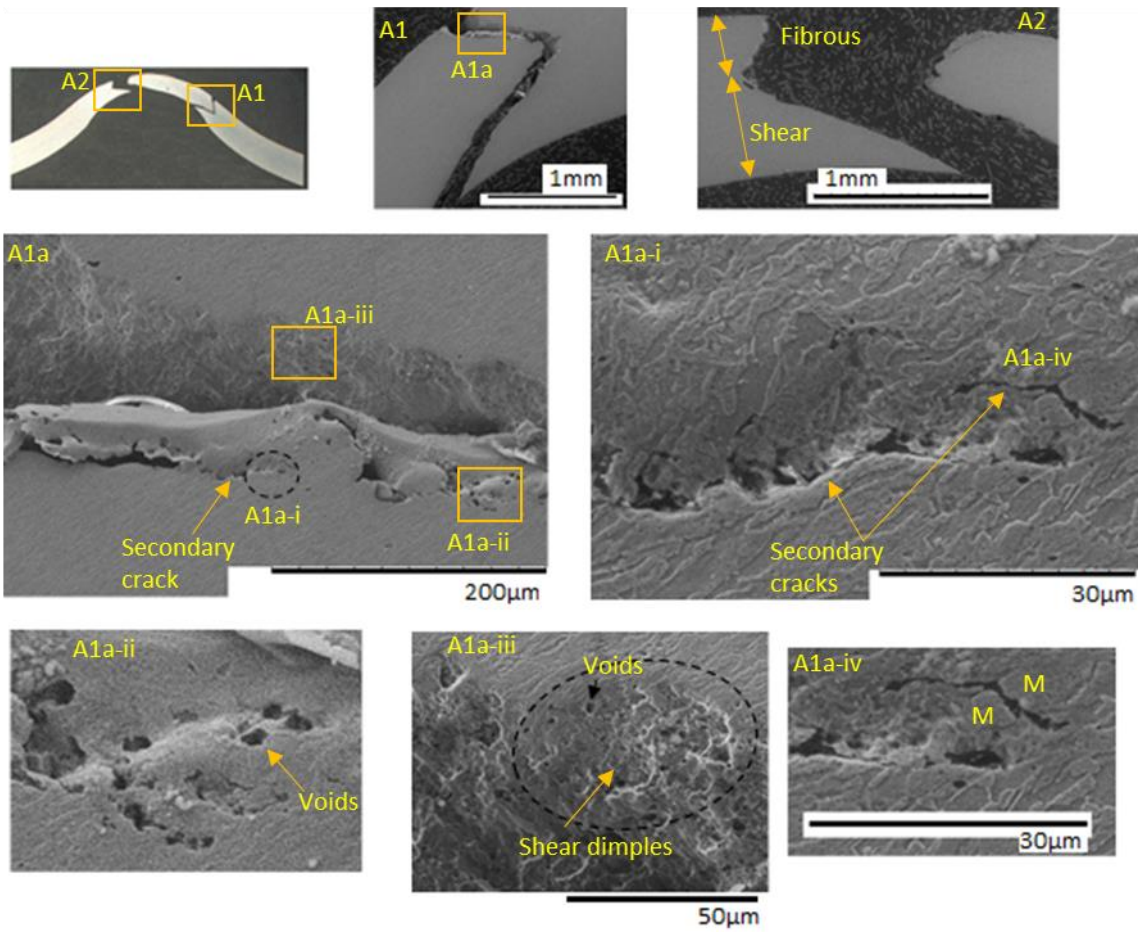

Figure 5-18 Damage at the fracture surface of as-quenched punch test specimen.

On the fracture surface at (A1a-iii) shows that specimen fails due to ductile fracture with the formation of shear dimples and spherical voids in the cross-section. Secondary cracks provide information on the crack propagation path of the as-quenched sample; where crack is observed to cross a large martensite island (labelled with M) in (A1a-iv).

Specimen 185°C

The fracture profile of specimen 185°C shows a combination of fibrous in the center and shear fracture in the outer perimeter of the through thickness cross-section. This observation is almost similar as seen in specimen AQ. Compared to specimen AQ where there is very low void formation observed on the inspected surface, specimen 185°C has a very high voids forming in the necking region as shown in Figure 5-19 (B2), where the region of high void density is highlighted in yellow. Fracture is also found to

be mainly inter-granular as shown in (B2-1) as crack path follows around the outside of boundary of martensite islands.

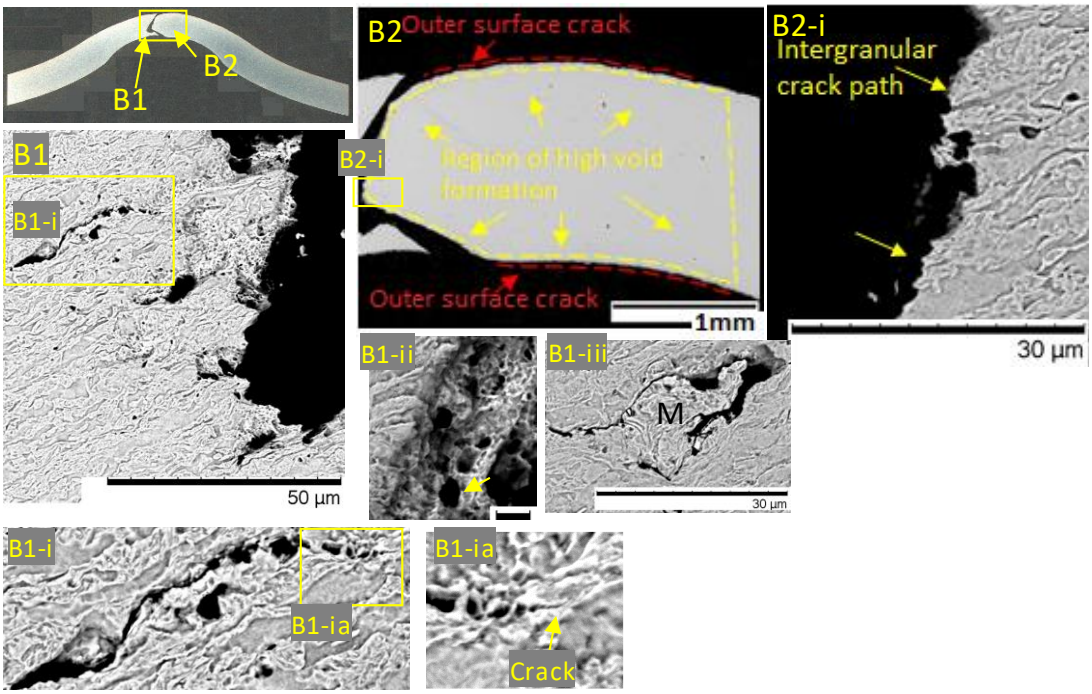

Figure 5-19 Microstructure damage inspection of specimen 185°C in the though-thickness cross-section.

In (B1), several formations on secondary cracks are observed near the fracture surface. The longest crack in the magnified image (B1-i) is orientated perpendicular to the main fracture path and reveals the long crack formed adjacent to martensite island boundaries. The crack tip is magnified and shown in image (B1-ia) when the crack tip propagates into the martensite island before the propagation is impeded. Void formation near the crack tip are in spherical shape and have not coalesce to form larger crack. (B1-iii) shows another secondary crack which formed around a large martensite island; which in this case is due to the incompatibility of plastic deformation between the large martensite island and the large deformation in the surrounding microstructure. Ductile shear dimples are also observed in this sample with the formation of large spherical voids in the fracture surface, shown in image (B1-ii).

Another type of damage is also observed in the 185°C, where damage is found to form at the outer surface of punch specimens, as indicated in Figure 5-19 (B2), previously. The types of damage formation identified on the top surface of the punch test specimen is as shown in Figure 5-20, where (B1a) shows large voids forming near the surface and in (B2a) is a shear crack formed on the surface orientated at 45°. An image of the surface microstructure taken at the furthest distance from the fracture surface is also shown in Figure 5-20, showing there is no sign of damage near the surface.

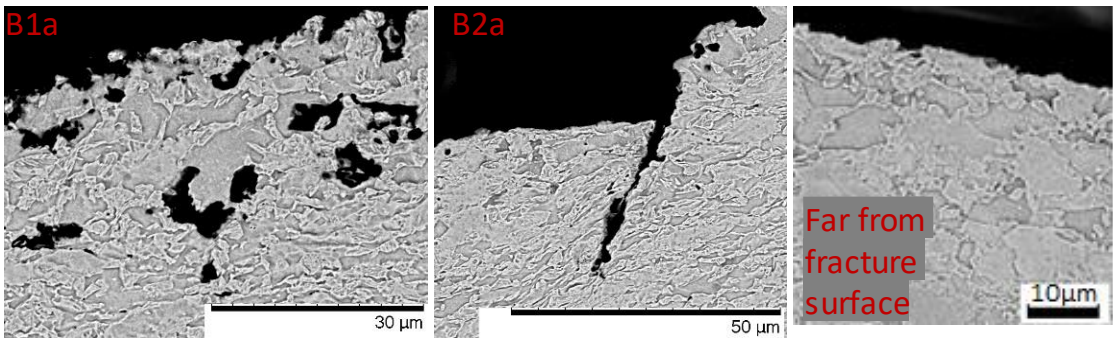

Figure 5-20 Damage sites found at the top surface of punch test specimen, 185°C

Specimen 290°C

It is found that the fracture surface at the centre through thickness cross-section of specimen 290°C it still connected. The large main shear fracture is not fully developed leaving the centre region still in contact. In the enlarged image region D in Figure 5-21, it is found that the middle region is not in contact as there is a fine fully developed crack which passed through it from point (D1) to (D3). In (D1), crack tip of the main crack leads into a region of with broken microstructures and cracked into many parts. Presence of secondary cracks are seen in these samples, especially near the main crack. In (D2 and D3), it is found that the fine crack that is separating the connected region is mainly inter-granular and propagates mainly around the outside of martensite islands. In another region of the specimens 290°C, a similar void which is seen at the surface of DP185°C is

also observed in specimen 290°C, with a large void developed beneath the specimen surface as shown in (Da).

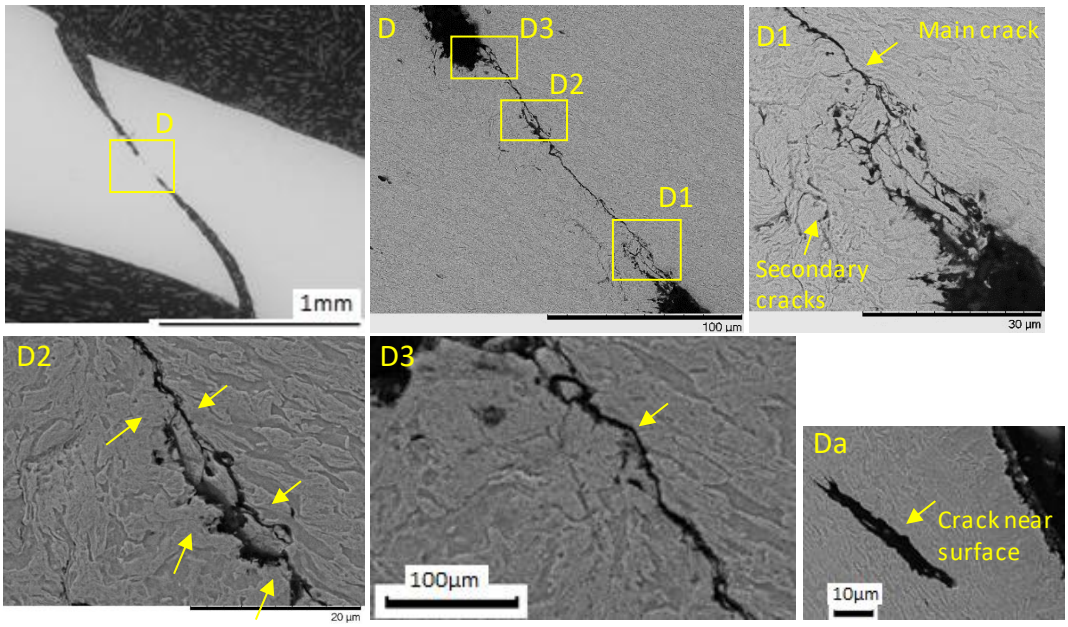

Figure 5-21 Damage in punch test specimen 290°C. At the middle of the though thickness, formation of fine crack is revealed within the connected region providing insight on the crack propagation path.

Specimen 340°C

Cross-section analysis of specimen 340°C shows a large shear fracture happening only at one side of the necking region as shown in Figure 5-22 (E1). On the opposite side of the sample at the localised necking region, a similar type of damage which was previously seen in specimen 185°C where there are two large cracks forming form the surface and grow towards the subsurface as shown in location (E2) and (E3).

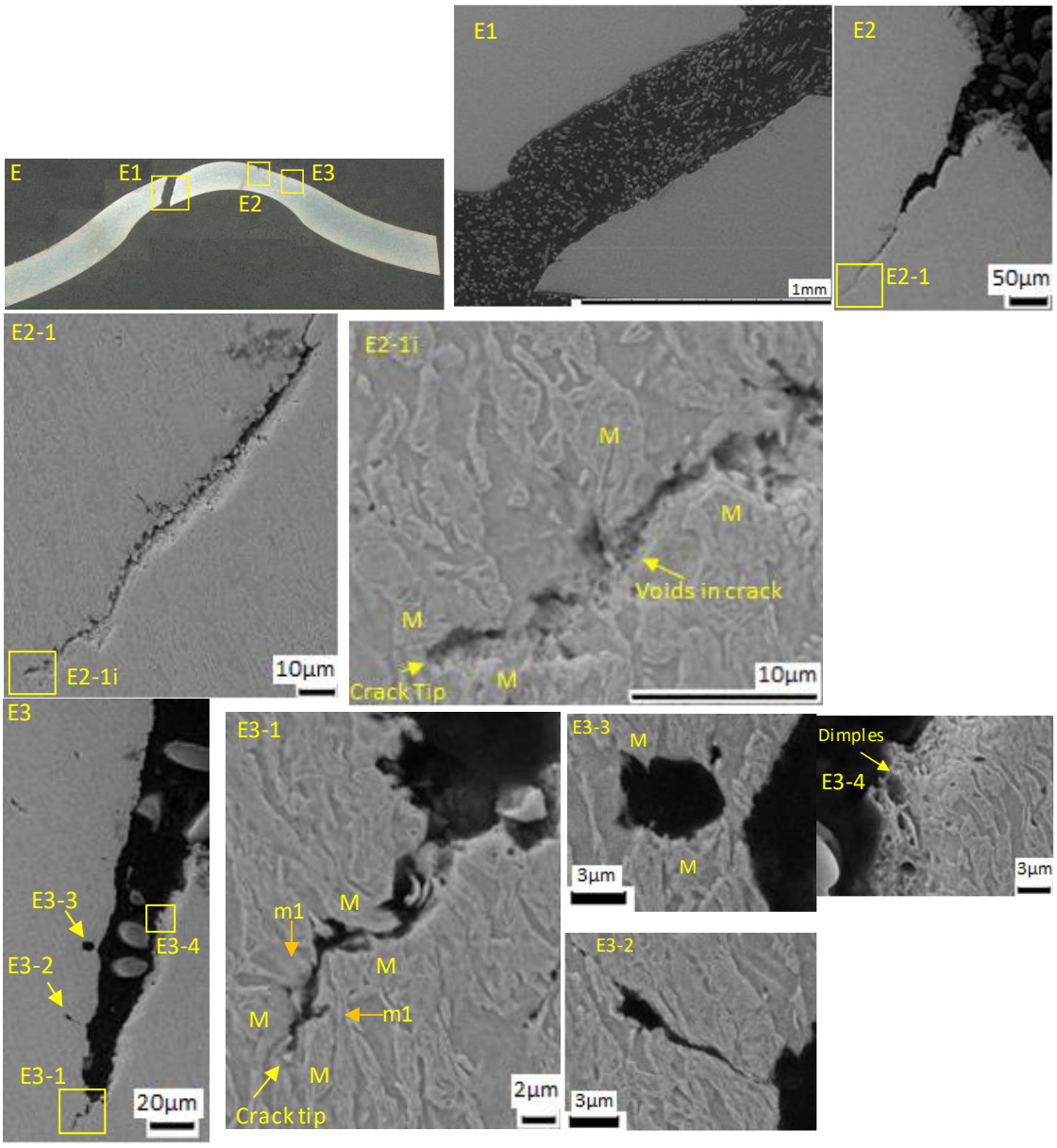

Figure 5-22 Damage in punch test specimen 340°C. Two large cracks are observed at the surface in (E2) and (E3).

The large surface crack in (E2) shows a fibrous fracture surface profile when it is near the outer surface and as the fracture grows deep towards the sub-surface, the crack seems to propagate in a straight line. The crack tip of crack in (E2) is closely inspected in (E2-1i) which reveals that before the crack propagation stops as the crack tip crosses into a martensite island, the prior crack propagation path was inter-granular and was following along the outside of martensite island boundaries. Region at the tip of the crack is also shallow revealing void formation underneath the crack. Another crack found in (E3),

however shows the region at the crack tip is deep and through the material (not shallow like in (E2). Similar in (E2), crack tip stops propagating as it crosses halfway through the martensite island, as shown in (E3-1). Image (E3-1) shows that the crack propagation (before reaching crack tip), the path seems to follow at the outside of martensite boundaries, in ferrite; the intact, unbroken martensite phase are labelled with "M". In the same image (E3-1), after that, the crack propagates through a thin martensite island (labelled as "m1" for both martensite islands broken halves) which is in the way of the crack path and is orientated perpendicular to propagating crack.

A few other types of damage are observed at the surface crack (E3), such as formation large spherical void near the fracture surface in (E3-3) which develops in between martensite islands, formation of long crack perpendicular towards the direction of surface crack in (E3-2) which follows along the exterior martensite islands. Formation of ductile shear dimples with spherical voids are also observed at the crack cross-section in image (E3-4).

Specimen 240°C and 365°C

Both specimen 240°C and 365°C shows a shear fracture angled at 45°. However, it is observed that near the main fracture in specimen 240°C, there are fine cracks developing parallel to the orientation of the main crack, which grew outside the martensite boundaries as shown in Figure 5-23 (C1-a) and (C1-b). These fine long cracks are only found in sample 240°C and is not observed in other materials. In (C1-b), the formation of the fine long cracks that developed from the surface towards the interior is also observed.

At (C2-1), voids which form around the exterior of martensite island, near the interface have coalesced with the nearby nucleating voids in the ferrite, leaving the hard martensite islands remained unbroken but highly plastically deformed due to increased global deformation.

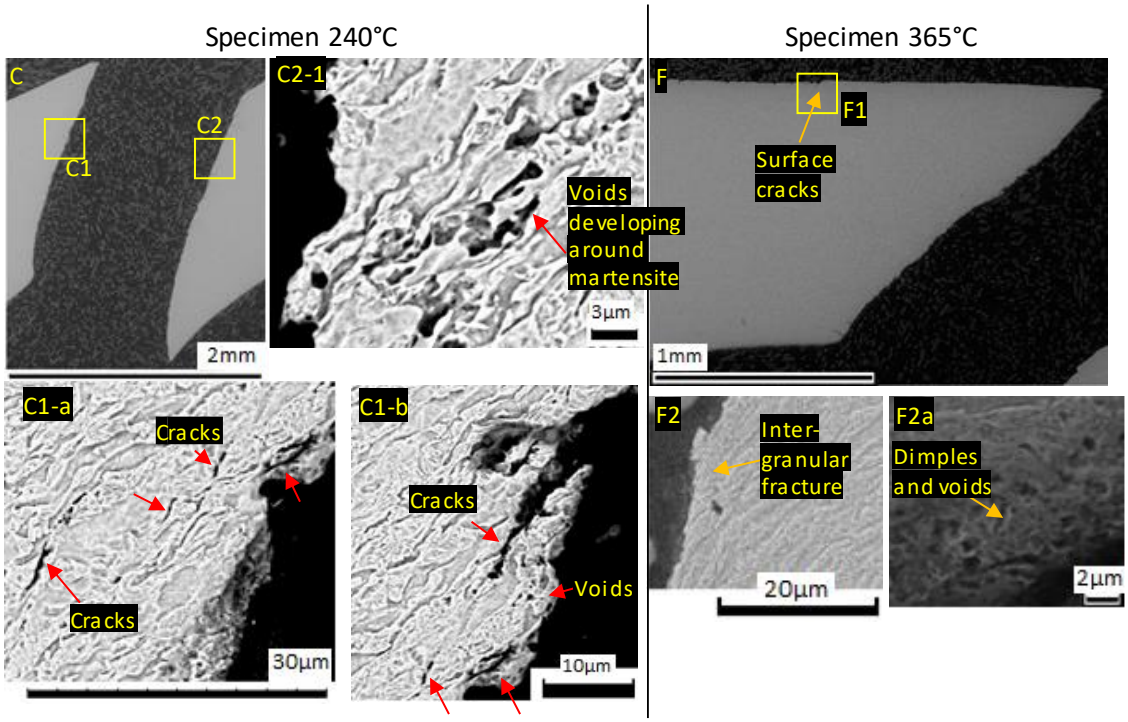

Figure 5-23 Damage observed in specimen 240°C (C) and specimen 365°C (F).

Damage observed in specimen 365°C is observed to be similar as reported in specimen 340°C; with a large shear fracture as shown in Figure 5-23 (F) and also a presence of surface cracking. Crack path of the main fracture is mainly inter-granular as shown in (F2) and fracture surface has shear dimples and spherical void formati

Chapter 6

Discussions

6.1. Local Plastic Deformation Analysed using µ-scale DIC

6.1.1. Strain Heterogeneity at the Scale of Microstructure

The first part of the study is focused on the local plastic deformation happening at the scale of microstructure of DP1000 steels; where the strain fields in both ferrite and martensite phase are closely analysed using µ-scale DIC. Results are collected at both high and low magnifications to allow a large amount of data to be collected at the area of interest as well as the surrounding microstructure thus enabling a statistically-meaningful analysis to be done on deformation and damage of the studied DP steels as shown in Figure 4-11. The key finding from this study provide an insight on the strain distribution of ferrite and martensite, where Figure 4-13 shows that a strain map obtained from running the in-situ tensile test reveal that strain distribution in the DP steels microstructure is highly heterogeneous as specimen reaches its UTS. Localization of high plastic deformation is preferentially in the region with large ferrite phase in the form of bands orientated at 45° with respect to the tensile direction. These obtained results are in line with the reports by (H Ghadbeigi et al., 2010; Joo et al., 2013; Marteau et al., 2013) as shown in Figure 6-1. Strain maps presented show the same pattern of strain distribution with differences in the hot spot values. These values may be affected by the different grades of DP steels being used, the global strain state of specimen when strain maps are extracted, as well as the size and dispersion of martensite in each investigated specimen. Strain heterogeneities in DP steels are highly affected by the microstructural factors, especially the local surrounding microstructures where the grain size and distribution of

martensite has a critical effect on the strain partitioning. (Han et al., 2013; Marteau et al., 2013; Tasan et al., 2014). Hence, explain the importance of capturing large field SEM images that cover large areas of the inspected microstructure as obtained in the work shown in Figure 6-1 (A).

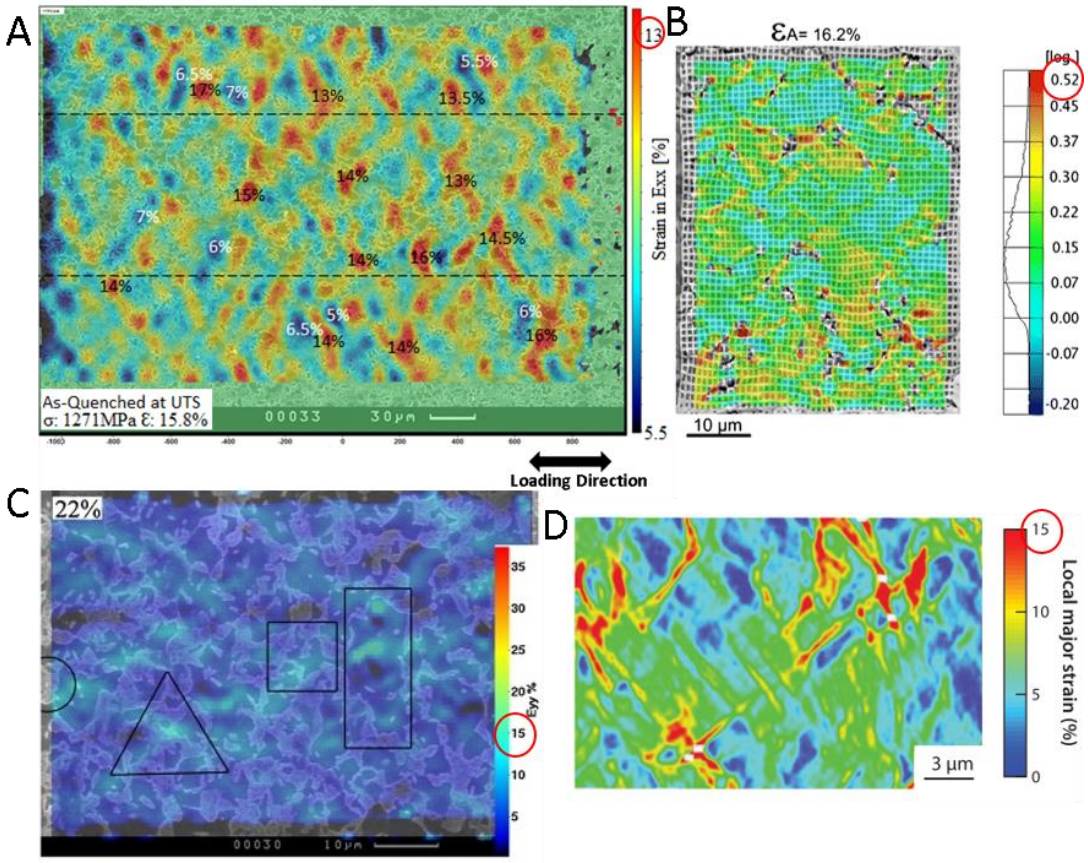

Figure 6-1 Strain distribution obtained from this work shown in (A) compared with the results obtained by (B)(Marteau et al., 2013)*, (C)*(H Ghadbeigi et al., 2010) *and (D)*(Joo et al., 2013)*. Strain measurements for hot spots or highest strain localization in the presented strain maps are circled in red.*

6.1.2. Strain Development in Microstructure up to Failure

The process of strain accommodation in the microstructure of DP1000 steels happening throughout a tensile test is shown in Figure 6-2. The figure presents a series of strain maps that shows the evolution of strain development in an as-quenched specimen. The behaviour of strain development (strain distribution pattern) obtained in this result are also similar to those found in the rest of the heat-treated samples. The figure is explained as follows:

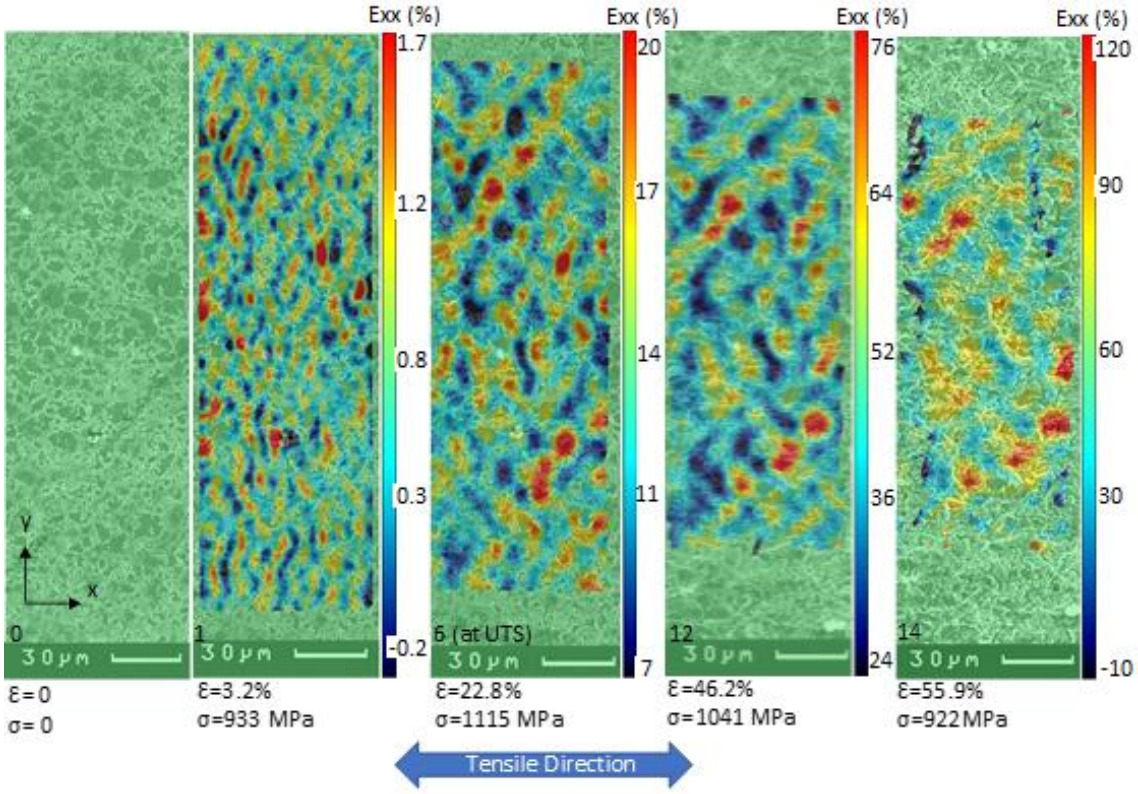

Figure 6-2 Evolution of strain distribution in a deforming microstructure of the as-quenched specimen taken at low magnification to capture the banded region and large ferrite grain region. From left (Step 0), is the undeformed microstructure, then (Step 1) is during the state when specimen just begin to yield, then (Step 6) is the stage where specimen reaches UTS, and later (Step 12) and finally (Step 14) which shows the strain distribution during the onset of specimen fracture.

At the beginning of the test (ε=0%), strain map is shows a uniform 0% strain for an undeformed microstructure. With increasing global strain from ε=0 to ε=3.2%, strain localisation begin to take place but at a very low local strain Exx values of -0.2% to 1.7%.

When specimen reaches its UTS, at ε=22.8%, strain heterogeneity can be observed more clearly with hot spots measuring at 20% of local strain values. At this stage during UTS, the amount of earliest initiation of martensite cracking is found to be highest. This will be further discussed in the next section. Finally, near the onset of specimen fracture (ε=55.9%), a severe strain heterogeneity is observed with very high localized deformation measuring at more than 120% local strain value. In this study, the local strain values of over 120% measured at the onset of fracture is also in agreement with the finding obtained by (H Ghadbeigi et al., 2010) of which their strain maps result for strain developments were shown in the literature review section, in Figure 2-7. The observation on strain development with increasing strain heterogeneity is also coherent with the finding by Kapp, Hebesberger and Kolednik, 2011, where the authors have investigated DP1000 and reported that with extremely high global deformation level, the severity of heterogeneity in strain distribution will also increases.

Results in Figure 6-2 is useful to understand the deformation mechanisms happening over a large area the investigated DP1000 microstructure before moving on to investigating local areas at higher strain resolution. It is important to analyse the local microstructural neighbourhood whether there is any presence of banded microstructure which may affect the strain distribution of a more localised region. These analysed regions over a large area however limits the observation on the grain boundaries of the microstructure. Therefore, another analysis has been carried out at a higher magnification which allow the study of strain accommodation within each phases at a higher resolution. Figure 6-3 shows a strain map obtained at a highly magnified area of DP1000 steels.

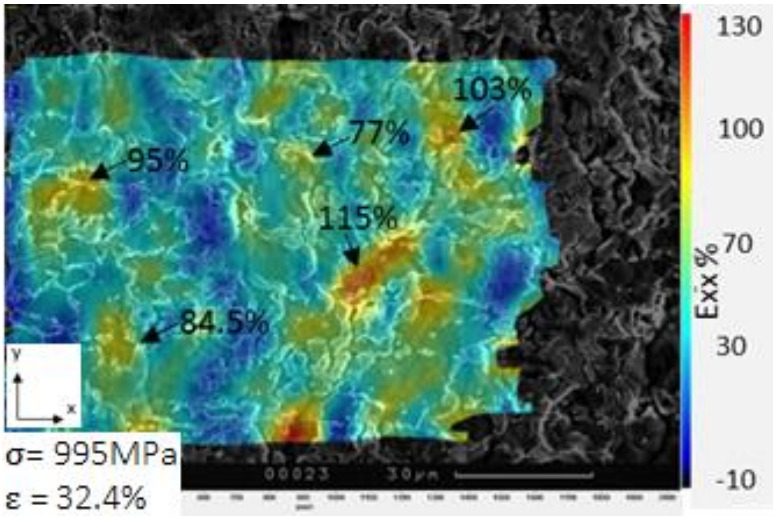

Figure 6-3 Maximum strain distribution at the onset of fracture in specimen as-quenched taken at a higher magnification revealing strain in the ferrite and martensite. Highest strain localization in the ferrite phase measuring at 115% and average strain in martensite can range from a minimum 20% strain up to 80% depending on the neighbouring microstructure.

This strain map shows the strain distribution of the DP steels specimen which is at the onset of fracture, where the maximum deformation has been successfully measured using μ-scale DIC. Usually due to large plastic deformation in microstructure, DIC correlation will fail at this point. However, this DIC analysis works successfully until the final stage and revealed the strain distribution in microstructure at the final stage of the test.

In the result, largest strain is found to localize in the ferrite phase and is measured as high as 115%. Martensite islands show high ductility with plastic deformation ranging from 20% to 80%, of which the values depend on the neighbouring microstructures. The extremely high local strain value at around 115% as the strain map is obtained at the last stage of the test, just before the onset of specimen failure. This result is in agreement with H Ghadbeigi *et al.*, 2010 where in their study, dual phase steels can accommodate very high strain values up to 120% in the ferrite phase; which is shown in the literature review section in Figure 2-7(d). These high strain heterogeneities observed are also reported by Kapp et al. 2011; Han et al. 2013 and Tasan et al. 2014.

6.1.3. The Effect of Martensite Distribution in Microstructure and the Strain Accommodation in Ferrite and Martensite Separately.

It is understood from the literature that the morphology and distribution of martensite affect the damage accumulation and the overall mechanical properties of DP microstructure (Avramovic-Cingara et al., 2009b; Bag et al., 1999; Kang et al., 2007; Tasan et al., 2010). This is because, the distribution of martensite increase can increase the heterogeneity of deformation in microstructure.

6.2.3.1 Representative image for all specimens

Representative images of the microstructure from specimens studied are shown in Figure 4-10. Martensite dispersion of the six analysed microstructures are found to be almost similar regardless the heat treatments applied. The calculated V_M (martensite phase volume fraction) from the representative image captured for every specimens are shown in Table 4-3 with an average of 63% with +/- 2% difference among the different tempering condition specimens. Despite the heat treatments applied, there are no changes in microstructure distribution because the range of temperatures used for heat treatments between 185°C to 365°C are too low to initiate the phase transformation in the microstructure. As shown in Figure 2-2, the intercritical annealing temperature for DP steels is at $\approx 700°C$ in order to initiate phase transformation. For the purpose of tempering process, the microstructure of DP steels is not meant to be changed however it is fundamentally meant for increasing the ductility (softening) of DP steels to allow the diffusion of carbon and making the martensite phase to soften and harden the ferrite phase (Baltazar Hernandez et al., 2011; Olson and Owen, 1992).

6.2.3.2 Martensite banding found in representative microstructures

The dispersion of martensite are found to be similar in all tempered specimens to the as-quenched ones as observed from the captured representative images. In the representative microstructures shown in Figure 4-10, two types of martensite distribution are observed where some areas are dense with large martensite islands with fine ferrite phase (banded martensite region) and some areas are dense with large ferrite phase with fine martensite islands (fine martensite/large ferrite region). These two types of distribution is shown in Figure 6-4 where banded region showing large martensite islands with fine ferrite (left), while large ferrite region has smaller – well-dispersed martensite (right) and transition region is when banded region meets large ferrite region.

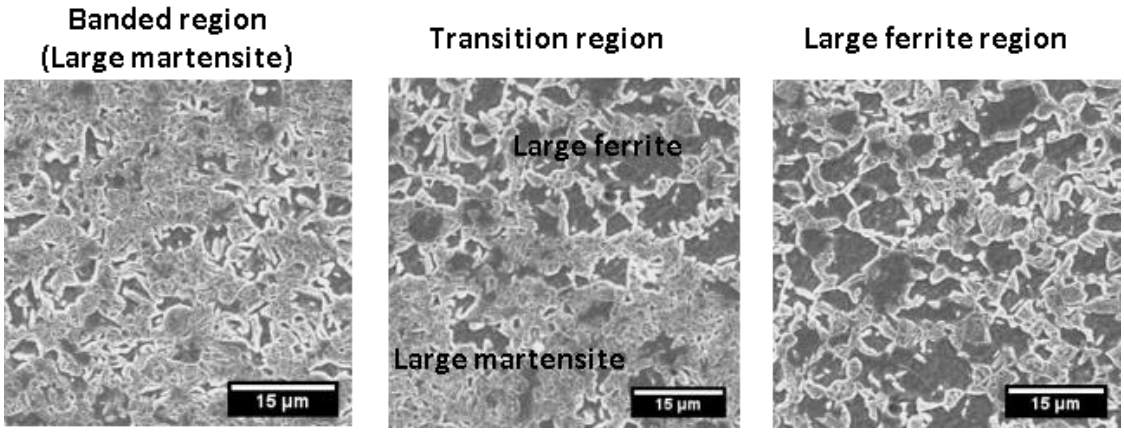

Figure 6-4 Two types of martensite morphologies found in the studied DP specimens.

Figure 4-13 shows an example of the microstructure labelled with sections of banded martensite region and large ferrite region. If the microstructure is observed using a much lower magnification in SEM, it is found that these banded regions are in alternate layer with the large ferrite regions, parallel to the rolling direction of the DP steels. The banded martensite distribution is uniform in a way that they are presence along the entire specimen width as presented in a schematic diagram in Figure 6-5. The thickness of these

martensite bands found in the representative images are measured to be around 70µm to 145µm. While regions of large ferrite have thickness of 40µm to 85µm.

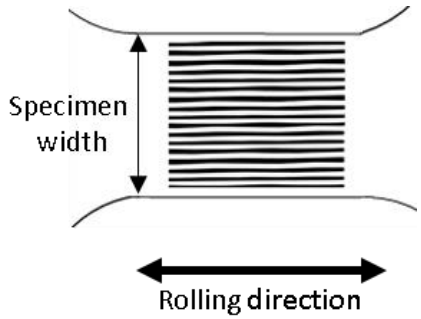

Figure 6-5 Schematic diagram showing the presence of martensite bands observed along the width of in-situ tensile specimen (not to scale).

The effect of martensite banding can be analysed using the strain maps obtained from running a tensile test inside SEM. In this study, it is found that strain concentration (hot spots) is the highest at the transition region; where the banded martensite region meets the large ferrite region. This is shown in Figure 6-6, hot spots can be clearly observed from the UTS stage ($\sigma_{Global} = 1115MPa$) where the highest strain values are found at the transition region measuring above 20%. During the onset of specimen fracture($\sigma_{Global} = 922MPa$), the strain values measured at the hot spot regions are well above 120%.

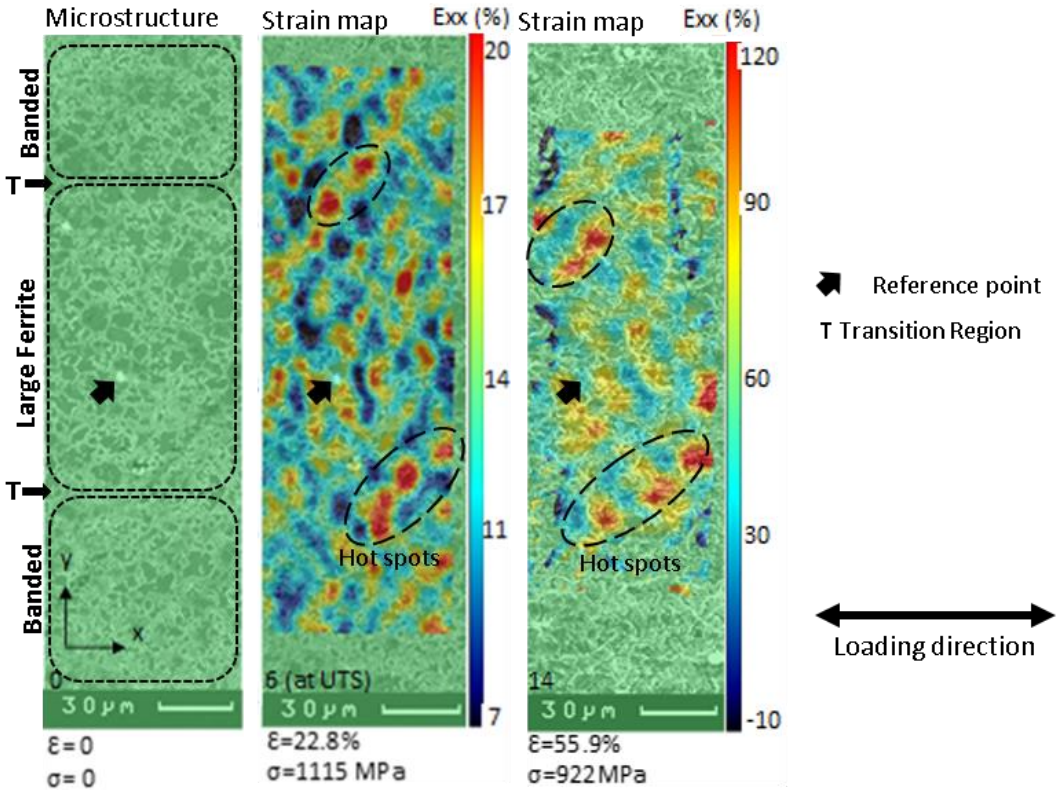

Figure 6-6 High strain values (hot spots) near happening at the transition region.

Tasan et al., 2010 reported that microstructural banding could cause a detrimental influence especially for continuous hard bands. The authors reported the hot spots within the continuous pealitic band studied in Figure 6-7 (a) develop in the narrowest section of the band which inevitably lead to the nucleation of voids. While Figure 6-7 (b) shows the formation of shear bands forming at a 45° to the direction of loading where the white arrow is indicating the shear band formed though the narrowest section of the banded region.

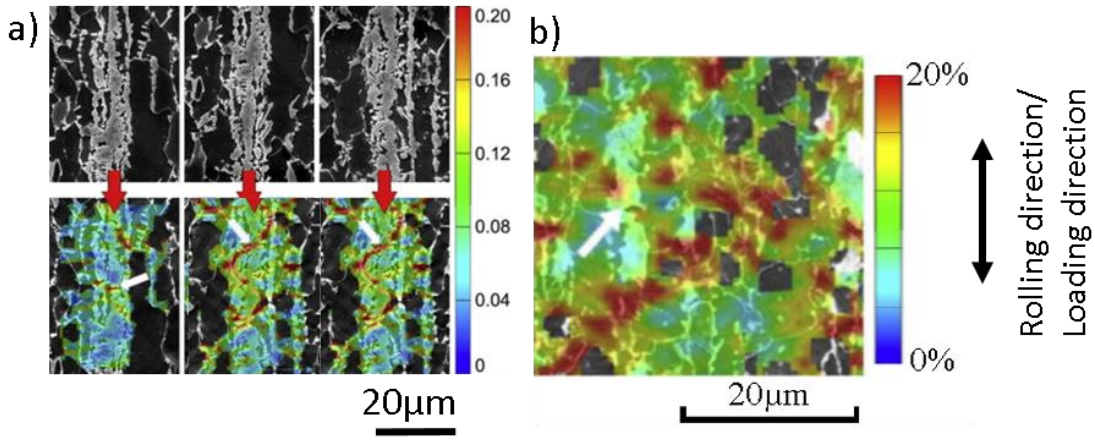

Figure 6-7 (a)Three martensitic bands of different morphologies showing the sites of void nucleation indicated with white arrows and (b) shows that shear band crossing through the banded region which is indicated using white arrow (Tasan et al., 2010).

Several differences can be highlighted in comparison to Tasan's work. First of all, the banded region observed in this study is martensitic compared to the pearlitic bands reported by Tasan. The martensitic bands found in this work is not a solid continuous band as shown by Tasan (hard continuous band), these martensitic bands are made up of a cluster of large separate martensite islands and densely packed to each other with fine/narrow ferrite phase in between. In this work, it is expected that hot spot formation will concentrate in the large ferrite phase compared to the banded region. However, report clearly shows that hot spots found in the transition region happening preferentially in the larger ferrite phase as highlighted in Figure 6-6. This can be explained by the high mismatch) of strain accommodation (strain partitioning in large ferrite in vicinity of the banded martensite. This is in agreement with report by Tasan where they mentioned that the strain partitioning between ferrite and martensite phase is clearly more noticeable compared to pearlite and ferrite (Tasan et al., 2010).

6.2. Earliest Initiation of Damage in DP1000 at the Scale of Microstructure

Various studies have reported on the damage initiation of DP steels but the presented results are analysed from a relatively small, local area of analysis. In this study, damage initiation sites are identified froma large area-of-analysis as shown in the representative microstructure image in Figure 4-10. Large area-of-analysis allows more damage initiation sites to be captured as well as to understand the effect of neighbouring microstructures. Earliest damage initation found are in the form of martensite cracking (or also known as micro-cracks). These 37 investigated damage sites collected are shown in APPENDIX 1 – Martensite Phase Crack Initiation

6.2.1. Effect of Tempering on Damage Initiation

There are at least five to seven damage initiation sites that are captured from each tested specimen after running the in-situ tensile tests. Figure 4-8 presents the captured damage initiation sites annotated to their respective loading states. In this study, is expected that specimens with higher tempering may delay the formation of damage as tempering reduces the hardness difference between ferrite and martensite (Han et al., 2013; Nakada et al., 2014). However, effects of tempering are not observed from these results as damage initiation for all specimens tend to appear at the UTS stage. The tempering temperatures used in this study may be too low and too close to each other, to be able to show a significant difference. It may be possible to observe the effects of tempering on the earliest initiation of damage, if the deeper tempering is applied. As tempering process conducted close or lower than the transformation temperatures (A_{C1}) can facilitate carbon diffusion (Baltazar Hernandez et al., 2011; Olson and Owen, 1992); hence altering the ferrite-martensite phase morphology .

6.2.2. Global Stress Required for the Earliest Damage Initiation

From the previous section, it is found that the effect of tempering is not observed on delaying the initiation of damage of the studied DP1000 specimens. Since there are no large differences when comparing the damage initiation to the tempering conditions, the collected data on damage initiation are grouped together to provide a statistical result.

The 37 earliest damage nucleation sites are plotted to their stress-strain values in a single chart as shown in Figure 4-9. What can be clearly seen in this figure is that, damage initiation takes place when the stress (global stress) state of the tensile specimen reached above 1000MPa. This finding is consistent with that of H Ghadbeigi et al., 2010 and Kang et al., 2007 as both papers show evidence of initiation of local damage happening at above 1000MPa. Most research on damage initiation in DP steels reported a very limited numbers to draw a conclusive finding. However, the large number of data collected for this study provide confidence for the obtained experimental results and it is possible to infer that damage for the martensite phase begin as specimen is at tensile loading (global stress) of 1000MPa.

6.2.3. Local Strain Values Required to Initiate Crack in Martensite

By considering the overall stress-strain curves in Figure 4-8, the damage initiation in martensite seems to be triggered at similar microscopic stress-strain values regardless the heat treatment applied. From the figure for all materials, it is indicated that damage in martensite happens during the elongation-to-fracture regime of the curve with higher frequency near the UTS. At this regime of the elongation to fracture, stress values maintain at around the UTS (above 1000MPa) however the local strain values measured

at the onset of fracture in martensite islands are found to concentrated at 20% for all materials.

The local strain values during the onset of damage in martensite for all six materials are gathered and plotted in Figure 6-8. From a total of 37 earliest local damage initiation identified in the six materials, it is found that the earliest martensite cracking took place at a local strain values ranging from 11% to 21%. In addition to that, the majority damage mechanisms which takes place in the studied local damage regions happens through martensite cracking for all the investigated DP materials with martensite volume fraction of around 60%. This finding is also aligned with the result by Tasan et al., 2015 as shown in the literature, in Figure 2-12 .

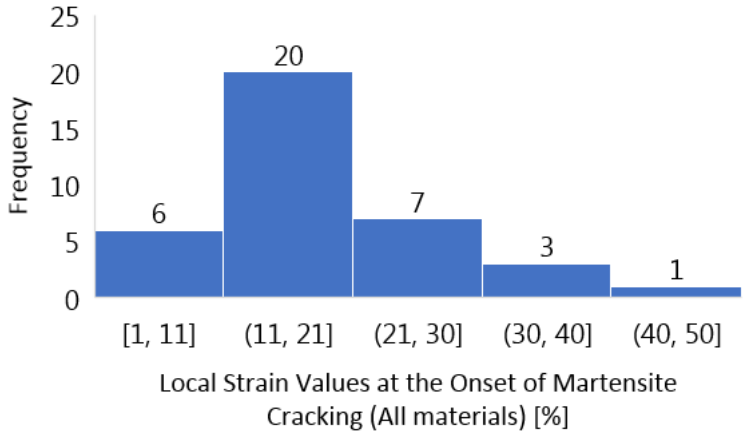

Figure 6-8 The local strain values measured during the onset of damage initiating in the martensite phase during micro-tensile testing collected from all materials. Histogram reveals the range of strain values where damage takes place in martensite with the highest frequency.

6.2.4. Critical Local Strain Values Required to Initiate Crack in Martensite

From the previous section, findings suggest that for damage to initiation to take place in DP1000 the conditions required are the global tensile specimen stress state should be at least 1000MPa and the local strain values at damage initiation sites should be between 11% - 21%. In addition to that, it is also discussed that the earliest damage initiation are most frequently observed the when specimens reached the UTS stage. Attention is drawn to the deformation behaviour happening in the microstructure during UTS by understanding strain accumulation between ferrite and martensite using statistical analysis method shown in Section 3.6.3 - Procedure to Obtain Average Strain for Ferrite and Martensite from DIC Strain Map.

The statistical data obtained are presented in Figure 4-14 where the deformation of ferrite and martensite phase during UTS are presented in a frequency distribution plot. Result shows that martensite phase in the studied DP1000 steels is very ductile because at UTS, the deformation taking place in hard martensite phase is similar to the ductile, ferrite phase. This can be observed in the distribution plots where both peaks of ferrite and martensite curves fall at around 10% mean strain value. With such large strain values measured inside the martensite phase, this finding is unexpected and suggests that damage initiation of the martensite in a DP1000 is not through brittle fracture and is not controlled by a critical stress value. Instead, the statistical results of strain values at the onset of damage in martensite seems to show that the fracture of martensite is indeed controlled by a critical strain value. It is mentioned in the literature that the initiation of crack in martensite requires a critical maximum principle stress (local stress at damage site) values of about 1700MPa based on the microstructure simulation carried out by Alharbi et al.,

2015. From the current study, it is found that the initiation of martensite cracking requires the global stress of tested sample should be least 1000MPa and is controlled with a critical local strain values of around 20% at the damage site. Alharbi et al., 2015 has carried out a microstructure simulation on a relatively small local area, while this current study produced a statistical analysis over a much larger area of representative microstructure which in returns allow many damage sites to be captured and analysed. Statistical analysis is therefore essential in understanding the behaviour of microstructures to ensure the obtained results are representative to the studied microstructure (e.g data represents the effect of microstructure distribution, neighbouring phase dispersion and morphology, etc.).

6.2.5. Identified Mechanisms for Martensite Cracking

From inspecting the surface of in-situ tensile test specimens, there are two main damage mechanisms identified for the initiation of earliest damage. The 37 collected damaged sites are categorized into the identified damage mechanisms and are shown in Table 4-5. There are two main damage mechanisms identified are: i) crack initiating from the centre of martensite phase and ii) cracks initiating near the ferrite-martensite interface. Out of the 37 damages sites, the majority of the damage sites initiated through cracking within the martensite phase with 26 counts. Cracking within the phase is when crack initiate from the centre of a martensite island and grow outwards, perpendicular to the loading direction as shown in example Figure 4-15. This finding is in line with the result presented in the literature, in Figure 2-12 where Tasan et al., 2015 has produced a detailed compilation of damage observation from various related studies on DP steels damage mechanisms. From Figure 2-12, it is observed that DP steels with martensite volume fraction higher than 50% are prone to martensite cracking. This is similar to the finding in this work where that the studied DP1000 steels contains around 63% with a +/- 6.5%

difference as shown in Table 4-3 ; and the majority damage mechanism found happen through martensite cracking. These findings are supported by Tasan et al., 2015 report, where martensite cracking are found to be the prominent mechanism in this material due to high martensite volume fraction that martensite islands are close/ connected together; which causes martensite phase to reach plasticity earlier. Meanwhile, for the near interface ferrite-martensite damage mechanism observed happens in the areas of larger ferrite grains with finer martensite islands. As previously discussed in **Section 6.2.3.2 Martensite banding found in representative microstructures**, the studied DP1000 steels consists of two microstructural distribution which could lead to the two types of damage mechanisms observed.

6.3. Novel Procedure to Study Damage Propagation in DP1000

6.3.1. Crack Propagation

This newly developed experimental procedure allows the investigation of propagating cracks at the scale of microstructure which also closely simulating the real crack propagation happening in the industrial forming process e.g. stamping process. The visualisation of crack propagation through the thickness is enabled through a post-mortem (micro-scale metallographic observation) analysis around the necking regions

The main crack in a punch test specimen is observed and the results confirms that the formation of large voids grow preferentially in the ferrite phase. Voids are found to initiate close to martensite-ferrite interface, with increase of loading these voids grow and coalesce to the nearest voids and thus forming a long crack that follows closely along the outer interface of martensite islands. Evidence are shown in Figure 5-19 (B1-i), Figure 5-21 (D2) and Figure 5-23 (C2-1). This type of damage formation is also observed from fractography analysis of tensile test specimens that are shown in Figure 4-25 (b2-ii),

Figure 4-26 and Figure 4-28 (d1). This ductile failure mechanism due to the coalescence of growing voids initiated at close proximities to each other; has also been observed in the work by Ghadbeigi et al., 2013. The nature of voids nucleation in the ferrite phase – close to martensite boundary can be explained by the high dislocation density and local hardness that facilitate void formation at high plastic deformation (Calcagnotto et al., 2010; Ghadbeigi et al., 2013). Fractography results from both punch test and in-situ tensile test in this study shows that the DP1000 steels failed through mainly ductile fractures where the observed dimples are finer in diameter and has shallower depth (Figure 5-18 [A1a-iii]). This is in agreement with the finding by Wang and Wei, 2013.

From the inspected punch test specimens, it is found that necking happens at both sides of the dome. One side of necking may already have a fully developed crack (main crack) while the other side of necking which is not fractured, may contain with more extensive amount of damage and possibly consist of larger propagating crack. The two sides of necking in punch test specimens are shown in Figure 5-17, where A is the main crack and B is the unbroken necking side. By observing the shape of the main crack, it is possible to say that the main cracks are likely to begin "close" from the surface and grew towards the mid thickness. Referring to the first image in Figure 5-21, image of the main crack is showing that both ends of the main crack have wider opening and the main crack is still "connected" in the mid thickness as highlighted in box D. Same observation are captured in Figure 5-18 (A1) and Figure 5-19 (B2). It is not clear to conclude the start/end of a main crack for specimens with 45° plane, shear fracture surface as shown in Figure 5-23 (C) and (F). It is stated previously that, these main cracks are initially developed "close" to the surface at the necking region. This potential theory can be supported by two further evidence regarding the nucleation of large voids (> 10μm) near outer surface of specimens; Figure 5-20 (B1a) and the formation of large cracks at around 45° to the

sruface plane (at around 145µm to 335µm) as shown in Figure 6-9. Similar observation is also reported by Luk'yanov et al., 1971 who investigated crack formation after performing a hot stamping process. They have reported on periodically recur formation of cracks of a depth up to 3mm near the outside surface located near the spherical part of punch as shown in Figure 6-10.

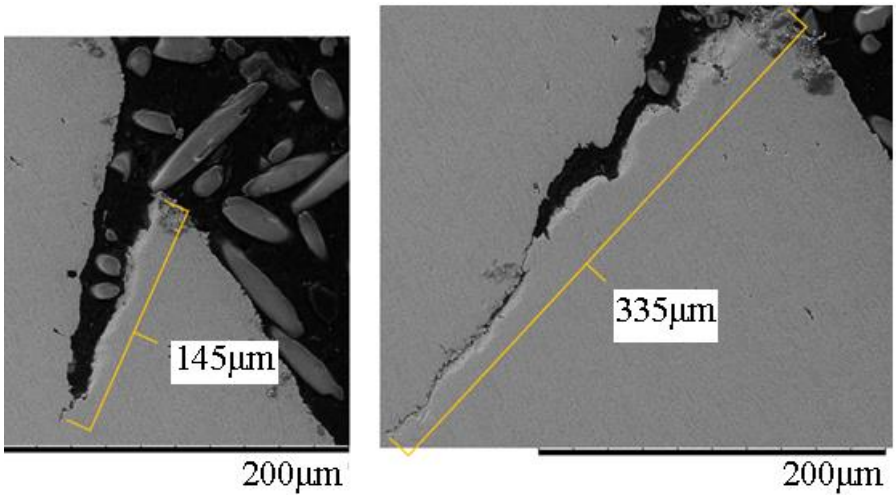

Figure 6-9 Large cracks found at the top surface of specimen 340°C where both cracks are propagating towards the centre thickness of specimen.

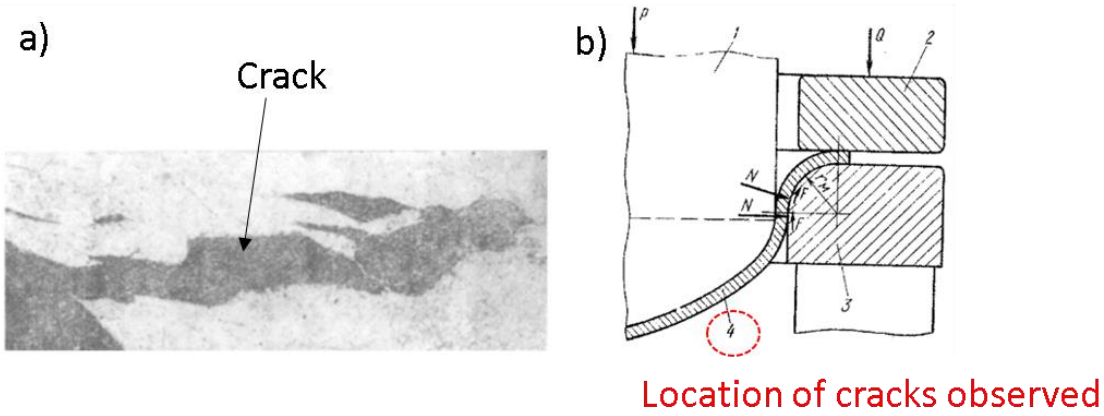

Figure 6-10 Magnified image of crack formation near the outside surface of punch specimen (a) and cracks are located at the outside surface of the spherical part of punch (b) (Luk'yanov et al., 1971).

The reported result on hot stamping provide good confidence for the designed punch test used in this study, but the material used in their investigation is stainless steel. In another study, shear fracture propagation has been investigated on a range DP steel

grades using a deep drawing process (Wang and Wei, 2013). In their study, they have also reported a similar fracture morphology where the tested DP steels with grades of 600-100MPa has underwent shear fracture at 45° plane through thickness. Wang and Wei, 2013 has reported two propagation modes such as (i) propagation along the ferrite-martensite interface and (ii) propagation across martensite island. These identified fracture propagation mechanisms are similar to the crack propagation observed in this study as shown in Figure 6-11 (Right); where crack path is preferentially in the ferrite region but following closely to the adjacent martensite phase (this can also be explained by the crack path following the shape of martensite boundary). This finding is also in agreement with Ghadbeigi et al., 2013; in which the authours stressed that crack formations are in the ferrite phase and is neither due to ferrite-martensite interfacial decohesion nor phase boundary delamination.

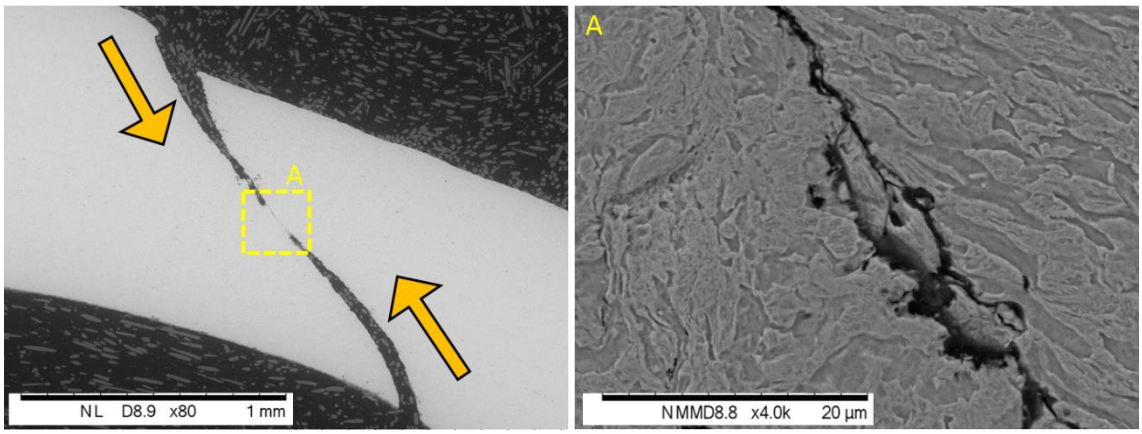

Figure 6-11 (Left) Direction of crack formation from the outer region towards the centre, mid-thickness denoted by A. (Right) Enlarged image of region A showing the crack path along the martensite grains.

Figure 6-11 (left) shows a fully developed crack with the middle section (A) is almost connected. From this image, it is safe to say that crack first developed near both of the outer surfaces, then these two main cracks propagated towards the mid-thickness.

If the two main cracks meets in the middle with increasing load, the two main cracks will merge into one main crack. In result, this one main crack will form a shear type 45° plane fracture surface as reported in most studies.This is an interesting finding that has not yet been reported in other papers. For the moment, this would remain as a theory for the crack development happening in a punch test. It is encouraged that in the future that this punch test will be repeated to prove this theory.

6.3.2. Feasibility of Punch Test

Punch test is capable to exert out-of-plane deformation with strain values above 50% on the studied DP1000 steels. The deformation development is shown in Figure 5-7. The deformation achieved using punch test is higher compared to the maximum deformation achieved from running a standard tensile test. Figure 4-4 shows that maximum strain (elongation to fracture) obtained from doing tensile test is only at around 14%. Post-mortem analysis reveals that there are more damage found in failed punch test specimens compared to the damage observed in in-situ tensile test specimens. The large plastic deformation applied on punch test specimen has generated more damage, especially at the necking (thinning) region of the dome as shown in Figure 5-17.

The 3D DIC technique prove to be very useful in providing information as necking begins in punch specimens during testing as shown in Figure 5-11. At the onset of specimen to failure, strain components in the Exx and Eyy directions shows that strain localisation at the “hot-spot” region in the strain distribution is measured up to 44%. The use of 3D DIC technique when running the punch test allow strain to be measured at the instance of crack propagating in the punch test.

After performing the punch test and examining the punch specimens in the through thickness cross-section, it is found that this designed punch test does not require any real-time result to study crack propagation. This is because necking happens at both sides of the inspected specimens, as shown in Figure 5-17. In the figure, at one side of the specimen shows a fully developed fracture and at another side is the unbroken necking region; with a very high plastic deformation which allows crack propagation to be studied.

The designed punch test is reliable in simulating the forming process happening in the automotive industry. The test proves to maintain good repeatability after many testing and results are found to be consistent in every tests. Figure 6-12 shows a satisfactory validation that the punch test exerts biaxial loading to punch blanks. This supported that the designed punch test resembles the industrial forming procedures that are performed on the AHSS steels.

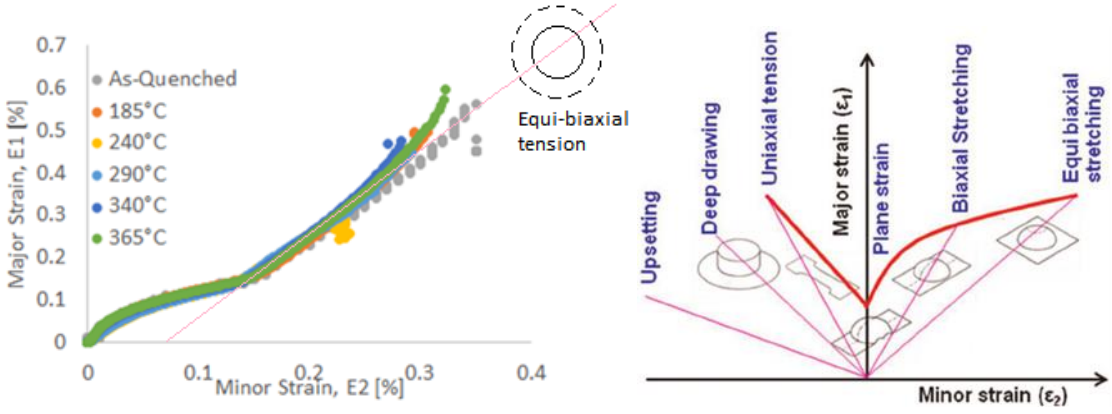

Figure 6-12 Comparing the result obtained from maximum principal strain, e_1 against min, principal strain e_2 of all materials (left). Pink trend line shows similar slope for biaxial stretching mode in the schematics FLD diagram, (right) (Paul, 2013).

6.4. Tempering Effect on DP1000 Steels

6.4.1. Standard Tensile test

Effects of tempering on the DP1000 are analysed from the response obtained by performing tensile tests and punch test. The results are shown in Table 6-1. Results from each tests showed small changes among the different tempering conditions of each specimens. Although the effect of tempering is small, there is still a clear trend on the reduction of the UTS with increasing tempering. Effect of tempering on the tensile response of the tempered DP1000 has been presented in Figure 4-5 previously. In the results, it showed that specimen 240°C has the best performance compared to other specimens as it has the largest elongation to fracture with a slight drop in UTS. From Table 4-1, it is observed that tempering at 185°C reduces the elongation to fracture, however there is a reversal effect for specimen 240°C where the elongation to fracture shows improvement at which the properties are close to AQ specimen. Overall, the effect of tempering on tensile response of DP1000 is aligned with the finding by Kamp et al, 2012 where tensile elongation dropped as DP steels are tempered between 200°C and 450°C.

The reduction of elongation to failure for heat treatment at 290°C might suggest the possibilities of optimal heat treatments in between 240°C and 290°C in order to improve the elongation to failure of the AQ material while maintaining the same UTS level. Although no significant improvement of the mechanical properties could be observed in this work for the heat treatments used for the supplied material, it is suggested that for future work, it is worth to consider applying heat treatments in between 240°C and 290°C to check these suggestions.

Table 6-1 Effect of tempering on the mechanical response of DP1000 steels.

	Standard Tensile Test		Phase Strain Difference (%)			Punch test	
	UTS (MPa)	**Strain (%)**	**Ferrite, F (%)**	**Martensite, M (%)**	**Δ (%)**	**Force F_{msx} [kN]**	**Out-of-plane displacement**
AQ	1061.77	13.85	10	9	1	32.91	13.03
185°C	1066.60	13.01	11.5	8	3.5	30.36	12.05
240°C	1060.33	14.18	8	7.5	0.5	31.99	13.68
290°C	1023.37	13.32	12.5	11.5	1	31.36	12.05
340°C	953.87	12.40	10.5	9.5	1	29.65	12.01
365°C	940.80	12.65	6.5	6	0.5	30.87	12.28

6.4.2. Strain Distribution at the Scale of Microstructure

It is expected in this study that through tempering, the strain partitioning between ferrite and martensite phase can be reduced as observed in the study by Kang *et al.*, 2007. However, in this study it is found that the tempering of DP1000 resulted in very small difference as shown in Table 6-1. For all specimens apart from specimen 185°C, the rest of the tempered specimens shows that strain accommodation in both ferrite and martensite phases are at around 0.5 to 1%. Kang *et al.*, 2007 performed tempering at 450°C and another one at intercritical temperature of 750°C that the temperature range is larger than the temperature range being used in this study, therefore effective on the microscopic strain distribution.

The tempering temperature range being used for this study, between 185°C-365°C is smaller compared to Kang's. These temperatures are also below the critical temperature and does not cause microstructure to change. Furthermore, the chosen temperatures are very close to each other to observe big difference of the deformation

behaviour. Specimen 240°C and specimen 365°C have the smallest strain difference of ferrite and martensite of 0.5%.

Specimen 185°C somehow has a sudden high value in the strain difference of 3.5%. This is due to a problem the failure when running a DIC analysis on the low magnification images for specimen 185°C. There were two sets of images taken, which are low magnification and high magnification. Thus, to overcome the problem, strain values for ferrite and martensite have to be extracted from the result processed using the high magnification image which caused the result to deviate from other specimens.

6.4.3. Punch Test

Tempering effect on deformation of punch test is analysed by assessing the maximum out-of-plane deformation before specimen fracture. Results obtained from punch test are found to be relatively close to each other. However, from the force-displacement result obtained from punch test suggested that specimen 240°C to have better formability. Response from punch test are shown in Figure 6-13 with included error bars. According to 3D strain analysis conducted on the deformed surface of punch test specimens, Table 5-6 also showed that specimen 240°C accommodates strain better compared to other specimens.

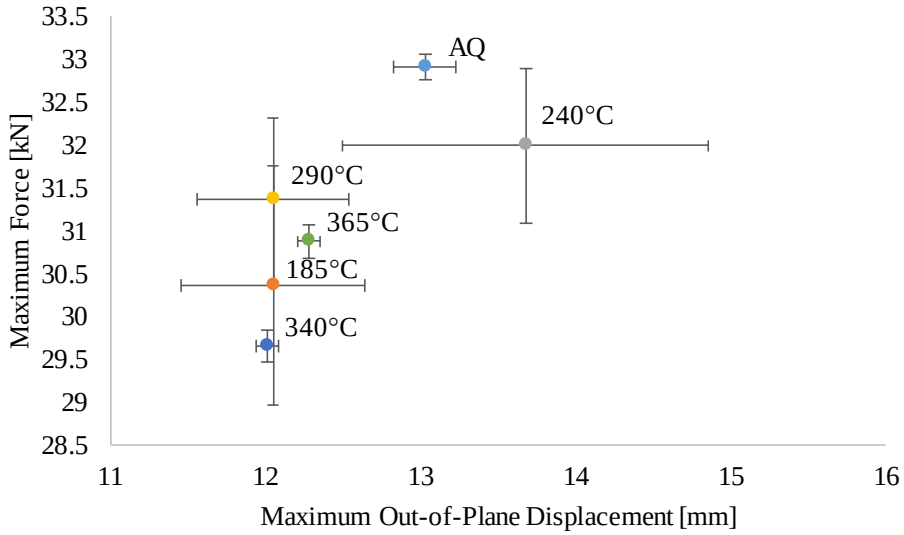

Figure 6-13 Punch test response obtained before fracture.

The range of temperatures for tempering being used in this study is not large enough to see a clear difference due to the tempering effect. Despite the effects observed on the mechanical properties of DP1000 are small, the changes found in the statistical data collected showed that the tempering process is effective. Overall, it is observed that DP1000 steels tempered at 240°C has been found to provide the best tensile elongation, better strain accommodation with very low strain difference between ferrite and martensite and last but not least; good formability in punch test.

Chapter 7

Conclusion

In this thesis, a thorough investigation has been carried out on DP1000 steels with a range of tempering conditions to generate statistically meaningful results specifically for the understanding of the damage development and deformation behaviour. Along with this study, an attempt to investigate crack propagation in DP1000 steels under conditions representative of industrial stamping operations has been successful through a newly developed experimental procedure that combines a laboratory-scale punch test with the use of 3D DIC.

For the DP1000 deformation behaviour, this study support the current finding that strain heterogeneity in DP steels is highly heterogenous with high plastic deformation localized preferentially in the region of large ferrite phase and the formation of strain bands orientated at 45° with respect to tensile loading. Strain heterogeneities in DP steels are highly affected by the microstructural factors, especially the local surrounding microstructures where the grain size and distribution of martensite has a critical effect on the strain partitioning. At extreme deformation level, strain heterogeneity becomes severe with the highest local strain recorded in the ferrite phase measuring at 115% and hard martensite phase that can undergo relatively high plastic deformation up to 80% (of which the values range depend on the neighbouring microstructures). Two types of martensite distribution has been observed in the studied DP1000, where some areas are dense with large martensite islands with fine ferrite phase (banded martensite region) and some areas are dense with large ferrite phase with fine martensite islands (fine martensite/large ferrite region). Research shown that strain concentration (hot spots) are found the highest at the transition region between the two identified distributions.

One of the more significant findings to emerge from this study is from the finding obtained on the damage developments of DP1000 steels. This study has identified that the earliest form of damage developed through martensite cracking. The formation of martensite cracking are found to be the highest during the UTS stage of tensile specimen. Experimental results confirmed that for the earliest initiation of martensite cracking of the studied DP1000 steels, the global stress should be above 1000MPa. Large amount of data on micro-scale deformation and damage has been collected over large representative microstructures for generating statistically meaningful result. From this procedure, experimental data obtained confirms that martensite phase are likely to fail when local strain values reaches around 11% to 21%. However, martensite cracking developing on the surface does not lead to final fracture of specimen.

A new procedure has been developed to characterise plastic deformation at the scale of microstructure and damage development in a statistically meaningful way by performing a DIC procedure at two different scales simultaneously. Plastic deformation in both ferrite and martensite phase analysed over a large representative microstructure are statistically measured up to the UTS point revealing that the martensite phase in the DP1000 is deforms plastically at very large strain values and showing a very similar strain heterogeneity as shown in the ferrite. From this, it can be said that martensite failed through ductile failure and is controlled by a critical strain value, instead of being defined as brittle failure where it is controlled by a critical stress values.

Prior to this study, it was difficult to capture crack propagation happening at the scale of microstructure. To overcome this problem, a new experimental procedure has been designed to study crack propagation through the newly designed laboratory-scale punch test. From the punch test, damage formation in DP steels can be assessed at both main fracture region and at the necking region. 3D DIC technique being used also provide strain

measurement as crack begin to propagate in the specimen observed at necking region. Necking region shows a very high formation of voids. In certain specimens, cracks are observed to form from the top surface and propagating towards the mid thickness. Punch test specimen 290°C shows large cracks from the outer and inner surface while middle region is still "attached". Upon closer look at the connected region, a very fine crack seems to have propagated through the connected region proving insight on crack propagation path with is mainly in the ferrite phase but along the boundaries of martensite.

Regardless the heat treatments applied, microstructure behave similarly as far as plastic deformation and damage initiation are concerned. Material 240°C tend to show an improved behaviour in both tensile test and punch test, however the differences are not huge which is probably due to the applied heat treatments which are being used in this study may not be optimal. To better conclude the optimal heat treatment to improve the properties of DP1000 steels, additional heat treatments has to be carried out, preferably between temperature 240°C and 290°C for a definitive conclusion on the heat treatments.

Overall, the main objectives especially in producing statistically meaningful results on the damage development and deformation behaviour has been achieved. A novel procedure to investigate crack propagation in DP1000 steels under biaxial loading similar to the forming test in industry has been developed and combined with the use of 3D DIC to allow strain analysis at necking which in turns provide strain measurement at crack propagation sites. It is however hard to conclude critically on the effect of heat treatments on DP steels, but specimen 240°C does show small improvements. Hopefully, this investigation will benefit modellers towards the development of physically based-multi-scale models to predict the overall macroscopic stress-strain curves using statistical experimental information about micro-scale deformation and damage generated in this work.

7.1. Recommendations for Future work

Effect of heat treatment on the improvement of AQ material does not show improvements after considering the error. However, from the trend observed in the stress-strain curves, there is a potential in DP1000 steels to be heat treated in between the temperature 240°C to 290°C. It is recommended that in the future work, that investigation is carried out on the DP1000 steels with heat treatment between the said recommended temperatures. Furthermore, result from the stress-strain curve should be repeated more than three times to have better confidence in the error in result.

Punch test proves to be very promising in the study of damage. However, the evolution of strain development at microstructure scale of the DP steels under biaxial loading cannot be studied except for post-mortem analysis after specimen has failed. It would beneficial in the future work to develop a micro-scale punch test inside SEM to observe the damage development mechanism at the scale of microstructure.

It is also recommended to conduct a finite element modelling of punch test to compute stress distribution to better understand the crack path though the though thickness

It is also suggested for the development of physically based-multi-scale models to predict the overall macroscopic stress-strain curves using statistical experimental information about micro-scale deformation and damage generate in this work.

References

Ahmad, E., Manzoor, T., Ali, K.L., Akhter, J.I., 2000. Effect of microvoid formation on the tensile properties of dual-phase steel. J. Mater. Eng. Perform. 9, 306–310. https://doi.org/10.1361/105994900770345962

Alharbi, K., Ghadbeigi, H., Efthymiadis, P., Zanganeh, M., Celotto, S., Dashwood, R., Pinna, C., 2015. Damage in dual phase steel DP1000 investigated using digital image correlation and microstructure simulation. Model. Simul. Mater. Sci. Eng. 23, 085005. https://doi.org/10.1088/0965-0393/23/8/085005

Avramovic-Cingara, G., Ososkov, Y., Jain, M.K., Wilkinson, D.S., 2009a. Effect of martensite distribution on damage behaviour in DP600 dual phase steels. Mater. Sci. Eng. A 516, 7–16. https://doi.org/https://doi.org/10.1016/j.msea.2009.03.055

Avramovic-Cingara, G., Ososkov, Y., Jain, M.K., Wilkinson, D.S., 2009b. Effect of martensite distribution on damage behaviour in DP600 dual phase steels. Mater. Sci. Eng. A 516, 7–16.

Bag, A., Ray, K.K., Dwarakadasa, E.S., 1999. Influence of martensite content and morphology on tensile and impact properties of high-martensite dual-phase steels. Metall. Mater. Trans. A 30, 1193–1202.

Bagheriasl, R., Worswick, M.J., 2015. Formability of AA3003 brazing sheet at elevated temperatures: limiting dome height experiments and determination of forming limit diagrams. Int. J. Mater. Form. 8, 229–244.

Balliger, N.K., Gladman, T., 1981. Work hardening of dual-phase steels. Met. Sci. 15, 95–108.

Baltazar Hernandez, V.H., Nayak, S.S., Zhou, Y., 2011. Tempering of martensite in dual-phase steels and its effects on softening behavior. Metall. Mater. Trans. A Phys. Metall. Mater. Sci. 42, 3115–3129. https://doi.org/10.1007/s11661-011-0739-3

Bariani, P.F., Bruschi, S., Ghiotti, A., Turetta, A., 2008. Testing formability in the hot stamping of HSS. CIRP Ann. 57, 265–268. https://doi.org/https://doi.org/10.1016/j.cirp.2008.03.049

Bruck, H.A., McNeill, S.R., Sutton, M.A., Peters, W.H., 1989. Digital image correlation using Newton-Raphson method of partial differential correction. Exp. Mech. 29, 261–267. https://doi.org/10.1007/BF02321405

Calcagnotto, M., Ponge, D., Raabe, D., 2010. Effect of grain refinement to 1 μm on strength and toughness of dual-phase steels. Mater. Sci. Eng. A 527, 7832–7840.

Davies, R.G., 1981. Tempering of dual-phase steels. Fundam. Dual-phase steels 265–277.

Davies, R.G., 1978. Influence of martensite composition and content on the properties of dual phase steels. Metall. Trans. A 9, 671–679. https://doi.org/10.1007/BF02659924

Davis, L.S., 2004. 7.0 User Manual.

Dieter, G.E., Bacon, D.J., 1986. Mechanical metallurgy. McGraw-hill New York.

Euro NCAP, 2011. Official Safety Assessment of the VW UP [WWW Document]. URL http://www.euroncap.com/de/results/vw/up!/11001

Ghadbeigi, H., Pinna, C., Celotto, S., 2013. Failure mechanisms in DP600 steel: Initiation, evolution and fracture. Mater. Sci. Eng. A 588, 420–431. https://doi.org/10.1016/J.MSEA.2013.09.048

Ghadbeigi, H., Pinna, C., Celotto, S., 2012. Quantitative strain analysis of the large deformation at the scale of microstructure: comparison between digital image correlation and microgrid techniques. Exp. Mech. 52, 1483–1492.

Ghadbeigi, H., Pinna, C., Celotto, S., Yates, J.R., 2010. Local plastic strain evolution in a high strength dual-phase steel. Mater. Sci. Eng. A 527, 5026–5032. https://doi.org/https://doi.org/10.1016/j.msea.2010.04.052

Ghadbeigi, H., Pinna, C., Celotto, S., Yates, J.R., 2010. Strain Evolution Measurement at the Microscale of a Dual Phase Steel Using Digital Image Correlation. Appl. Mech. Mater. 24–25, 201–206. https://doi.org/10.4028/www.scientific.net/AMM.24-25.201

Ghassemi-Armaki, H., Maaß, R., Bhat, S.P.P., Sriram, S., Greer, J.R.R., Kumar, K.S.S., 2014. Deformation response of ferrite and martensite in a dual-phase steel. Acta Mater. 62, 197–211. https://doi.org/10.1016/j.actamat.2013.10.001

Haddadi, H., Belhabib, S., 2008. Use of rigid-body motion for the investigation and estimation of the measurement errors related to digital image correlation technique. Opt. Lasers Eng. 46, 185–196. https://doi.org/10.1016/j.optlaseng.2007.05.008

Han, Q., Kang, Y., Hodgson, P.D., Stanford, N., 2013. Quantitative measurement of strain partitioning and slip systems in a dual-phase steel. Scr. Mater. 69, 13–16.

Hayashi, K., Miyata, K., Katsuki, F., Ishimoto, T., Nakano, T., 2013. Individual mechanical properties of ferrite and martensite in Fe-0.16 mass% C-1.0 mass% Si-1.5 mass% Mn steel. J. Alloys Compd. 577, 593–596. https://doi.org/10.1016/j.jallcom.2012.02.035

He, X.J., Terao, N., Berghezan, A., 1984. Influence of martensite morphology and its dispersion on mechanical properties and fracture mechanisms of Fe-Mn-C dual phase steels. Met. Sci. 18, 367–373. https://doi.org/10.1179/030634584790419953

Hockett, J.E., Gillis, P.P., 1971. Mechanical testing machine stiffness: Part I—Theory and calculations. Int. J. Mech. Sci. 13, 251–264.

Hosford, W.F., Caddell, R.M., 2011. Metal forming: mechanics and metallurgy. Cambridge University Press.

Instron, 2015. Introduction to Digital Image Correlation (DIC) [WWW Document]. LinkedIn Corp. URL https://www.slideshare.net/Instron/digitalmage-correlation-2015 (accessed 7.17.18).

Joo, S.-H., Lee, J.K., Koo, J.-M., Lee, S., Suh, D.-W., Kim, H.S., 2013. Method for measuring nanoscale local strain in a dual phase steel using digital image correlation with nanodot patterns. Scr. Mater. 68, 245–248.

Jordan, J., Bodnar, R., Dorricott, J., 2009. Use of the Holloman-Jaffe Tempering Parameter in the Development of High Strength Steel Plate. Can. Metall. Q. 48, 285–292. https://doi.org/10.1179/000844309794238955

Kadkhodapour, J., Butz, A., Ziaei Rad, S., Rad, S.Z., 2011. Mechanisms of void formation during tensile testing in a commercial, dual-phase steel. Acta Mater. 59, 2575–2588. https://doi.org/10.1016/j.actamat.2010.12.039

Kamp, A., Celotto, S., Hanlon, D.N., 2012. Effects of tempering on the mechanical properties of high strength dual-phase steels. Mater. Sci. Eng. A 538, 35–41. https://doi.org/10.1016/j.msea.2012.01.008

Kang, J., Jain, M., Wilkinson, D.S., Embury, J.D., 2005. Microscopic strain mapping using scanning electron microscopy topography image correlation at large strain. J. Strain Anal. Eng. Des. 40, 559–570. https://doi.org/10.1243/030932405X16151

Kang, J., Ososkov, Y., Embury, J.D., Wilkinson, D.S., 2007. Digital image correlation studies for microscopic strain distribution and damage in dual phase steels. Scr. Mater. 56, 999–1002. https://doi.org/10.1016/j.scriptamat.2007.01.031

Kapp, M., Hebesberger, T., Kolednik, O., 2011. A micro-level strain analysis of a high-strength dual-phase steel. Int. J. Mater. Res. 102, 687–691.

Karlsson, B., Sundström, B.O., 1974. Inhomogeneity in plastic deformation of two-phase

steels. Mater. Sci. Eng. 16, 161–168.
Keeler, S., Kimchi, M., 2015. Advanced high-strength steels application guidelines V5. WorldAutoSteel.
Korzekwa, D. a., Matlock, D.K., Krauss, G., 1984. Dislocation substructure as a function of strain in a dual-phase steel. Metall. Trans. A 15, 1221–1228. https://doi.org/10.1007/BF02644716
Luk'yanov, V.P., Gorokhov, E.D., Snezhkovskii, V.A., 1971. Analysis of causes of crack formation during stamping of stainless-steel bottoms. Chem. Pet. Eng. 7, 57–59.
Maire, E., Bouaziz, O., Di Michiel, M., Verdu, C., 2008. Initiation and growth of damage in a dual-phase steel observed by X-ray microtomography. Acta Mater. 56, 4954–4964. https://doi.org/10.1016/j.actamat.2008.06.015
Marteau, J., Haddadi, H., Bouvier, S., 2013. Investigation of strain heterogeneities between grains in ferritic and ferritic-martensitic steels. Exp. Mech. 53, 427–439.
Nakada, N., Nishiyama, M., Koga, N., Tsuchiyama, T., Takaki, S., 2014. Hierarchical strain distribution analysis formed in DP steel using a combination of metallographic image and digital image correlation method. Tetsu-To-Hagane/Journal Iron Steel Inst. Japan 100, 1238–1245.
Olsen, G.B., Cohen, M., 1972. A mechanism for the strain-induced nucleation of martensitic transformation. J. Less-Common Met. 28, 107–118.
Olson, G.B., Owen, W.S., 1992. Martensite; ASM International: Materials Park.
Pan, B., Qian, K., Xie, H., Asundi, A., 2009. Two-dimensional digital image correlation for in-plane displacement and strain measurement: a review. Meas. Sci. Technol. 20, 062001. https://doi.org/10.1088/0957-0233/20/6/062001
Panda, S.K., Kumar, D.R., 2010. Experimental and numerical studies on the forming behavior of tailor welded steel sheets in biaxial stretch forming. Mater. Des. 31, 1365–1383.
Paul, S., 2013. Theoretical analysis of strain- and stress-based forming limit diagrams, The Journal of Strain Analysis for Engineering Design. https://doi.org/10.1177/0309324712468524
Porter, D.A., Easterling, K.E., 1992. Phase Transformations in Metals and Alloys, Third Edition (Revised Reprint). Taylor & Francis.
Rashid, M.S., 1981. Dual phase steels. Annu. Rev. Mater. Sci. 11Rashid, 245–266.
Rashid, M.S., Cprek, E.R., 1978. Formability Topics-Metallic Materials, in: ASTM. p. 174.
Sarwar, M., Priestner, R., 1996. Influence of ferrite-martensite microstructural morphology on tensile properties of dual-phase steel. J. Mater. Sci. 31, 2091–2095.
Shen, H.P.P., Lei, T.C.C., Liu, J.Z.Z., 1986. Microscopic deformation behaviour of martensitic–ferritic dual-phase steels. Mater. Sci. Technol. 2, 28–33. https://doi.org/10.1179/mst.1986.2.1.28
Siebert, T., Becker, T., Spiltthof, K., Neumann, I., Krupka, R., 2007. Error estimations in digital image correlation technique, in: Applied Mechanics and Materials. Trans Tech Publ, pp. 265–270.
Simonsen, M., 2017. Strain Tensors and Criteria in Vic [WWW Document]. Correl. Solut. URL http://correlatedsolutions.com/support/index.php?/Knowledgebase/Article/View/2/0/strain-tensors-in-vic (accessed 8.22.18).
Speich, G.R., Schwoeble, A.J., Huffman, G.P., 1983. Tempering of Mn and Mn-Si-V dual-phase steels. Metall. Trans. A 14, 1079–1087.
Standard, A., 2011. E8/E8M. Stand. test methods Tens. Test. Met. Mater. 3, 66.
Steinbrunner, D.L., Matlock, D.K., Krauss, G., 1988. Void formation during tensile

testing of dual phase steels. Metall. Trans. A 19, 579–589.
Su, Y., Zhang, Q., Xu, X., Gao, Z., 2016. Quality assessment of speckle patterns for DIC by consideration of both systematic errors and random errors Quality assessment of speckle patterns for DIC by consideration of both systematic errors and random errors. Opt. Lasers Eng. 86, 132–142. https://doi.org/10.1016/j.optlaseng.2016.05.019
Sun, X., Choi, K.S., Liu, W.N., Khaleel, M.A., 2009. Predicting failure modes and ductility of dual phase steels using plastic strain localization. Int. J. Plast. 25, 1888–1909.
Sutton, M.A., Orteu, J.J., Schreier, H., 2009. Image correlation for shape, motion and deformation measurements: basic concepts, theory and applications. Springer Science & Business Media.
Tasan, C.C., Hoefnagels, J.P.M., Diehl, M., Yan, D., Roters, F., Raabe, D., 2014. Strain localization and damage in dual phase steels investigated by coupled in-situ deformation experiments and crystal plasticity simulations. Int. J. Plast. 63, 198–210. https://doi.org/10.1016/j.ijplas.2014.06.004
Tasan, C.C., Hoefnagels, J.P.M., Geers, M.G.D., 2010. Microstructural banding effects clarified through micrographic digital image correlation. Scr. Mater. 62, 835–838. https://doi.org/10.1016/j.scriptamat.2010.02.014
Tasan, C.C.C.C., Diehl, M., Yan, D., Bechtold, M., Roters, F., Schemmann, L., Zheng, C., Peranio, N., Ponge, D., Koyama, M., Tsuzaki, K., Raabe, D., 2015. An Overview of Dual-Phase Steels: Advances in Microstructure-Oriented Processing and Micromechanically Guided Design. Annu. Rev. Mater. Res. 45, 391–431. https://doi.org/10.1146/annurev-matsci-070214-021103
Voort, G. Vander, 2018. Microstructure of Isothermally-Treated Steels [WWW Document]. VAC AERO Int. INC. URL https://vacaero.com/information-resources/metallography-with-george-vander-voort/1123-microstructure-of-isothermally-treated-steels.html (accessed 8.2.18).
Wagner, M., Jahn, A., Beyer, E., Balzani, D., 2016. Design and Optimization of Steel Car Body Structures via Local Laser-Strengthening. Engineering 8, 276.
Wagoner, R.H., Wang, W., Sriram, S., 1994. Development of OSU formability test and OSU friction test. J. Mater. Process. Technol. 45, 13–18. https://doi.org/https://doi.org/10.1016/0924-0136(94)90311-5
Wang, W., Wei, X., 2013. The effect of martensite volume and distribution on shear fracture propagation of 600–1000 MPa dual phase sheet steels in the process of deep drawing. Int. J. Mech. Sci. 67, 100–107.
Wang, Y.Q., Sutton, M.A., Bruck, H.A., Schreier, H.W., 2009. Quantitative error assessment in pattern matching: effects of intensity pattern noise, interpolation, strain and image contrast on motion measurements. Strain 45, 160–178.
Yoneyama, S., 2016. Basic principle of digital image correlation for in-plane displacement and strain measurement. Adv. Compos. Mater. 25, 105–123.
Yoneyama, S., Murasawa, G., 2009. Digital Image Correlation, in Experimental Mechanics. Encycl. Life Support Syst. 7–10.
Yoon, J.-H., Cazacu, O., Yoon, J.W., Dick, R.E., 2010. Earing predictions for strongly textured aluminum sheets. Int. J. Mech. Sci. 52, 1563–1578.

Appendices

APPENDIX 1 – Martensite Phase Crack Initiation

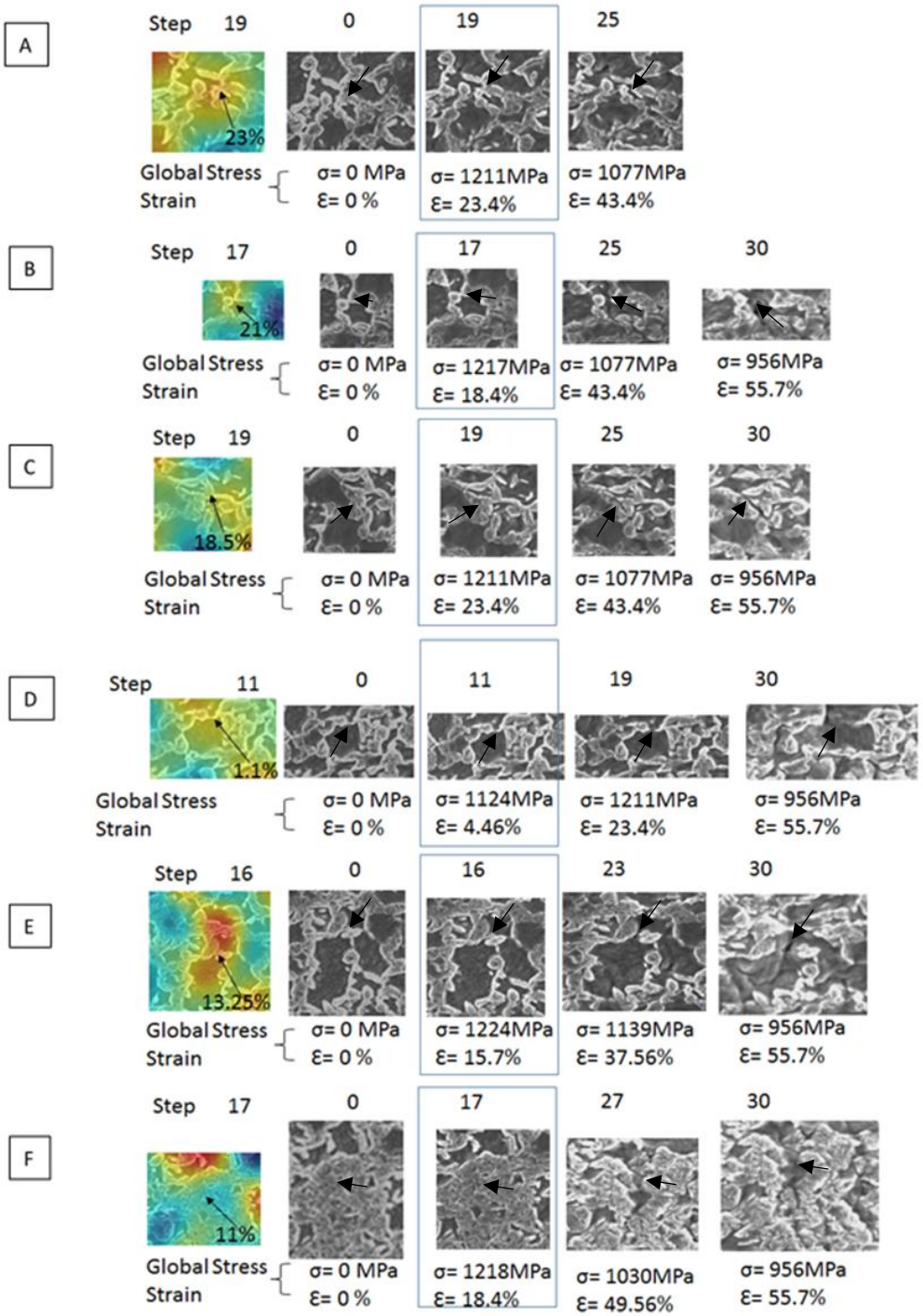

Figure 0-1 As-Quenched

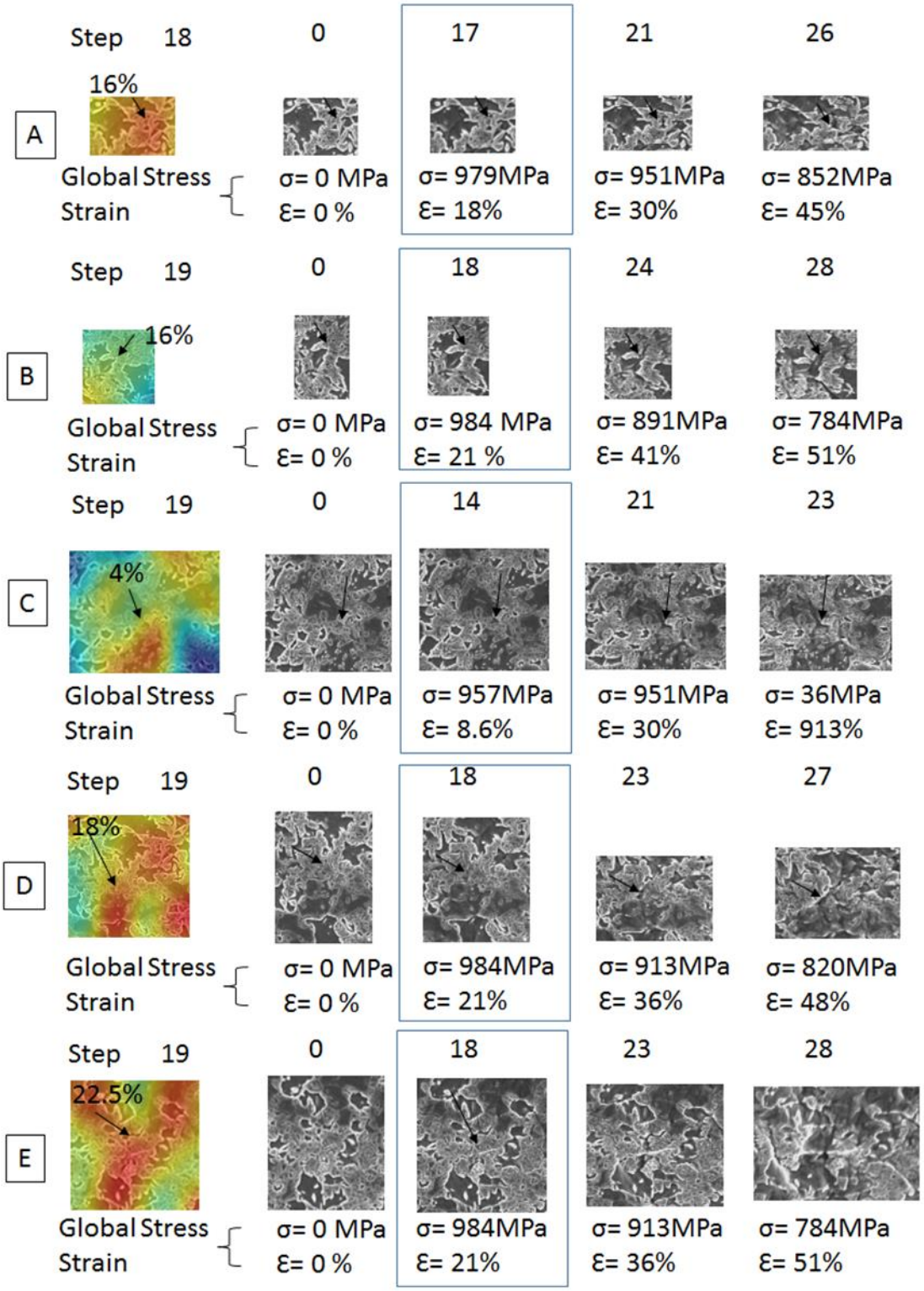

Figure 0-2 185°C

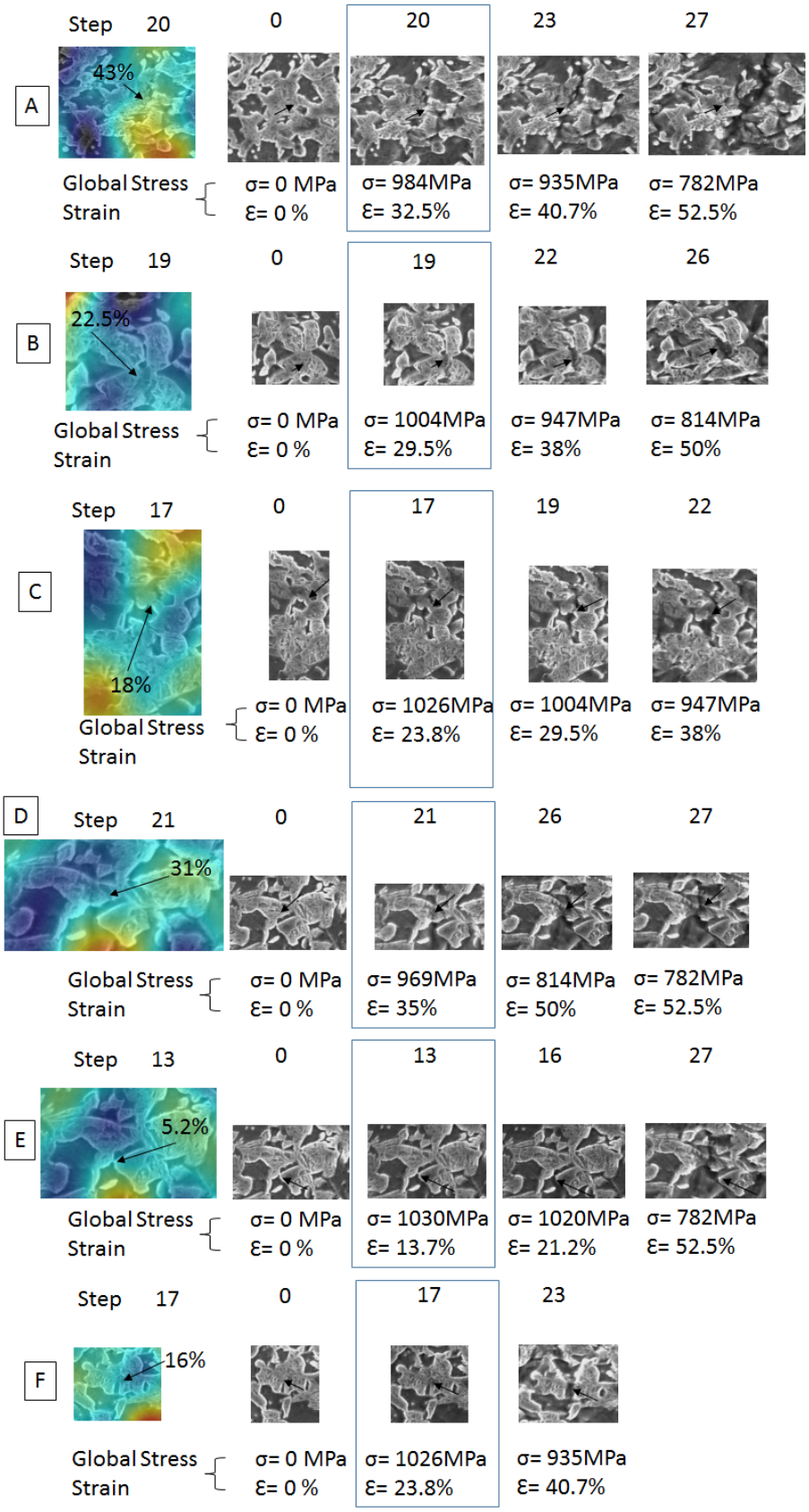

Figure 0-3 240°C

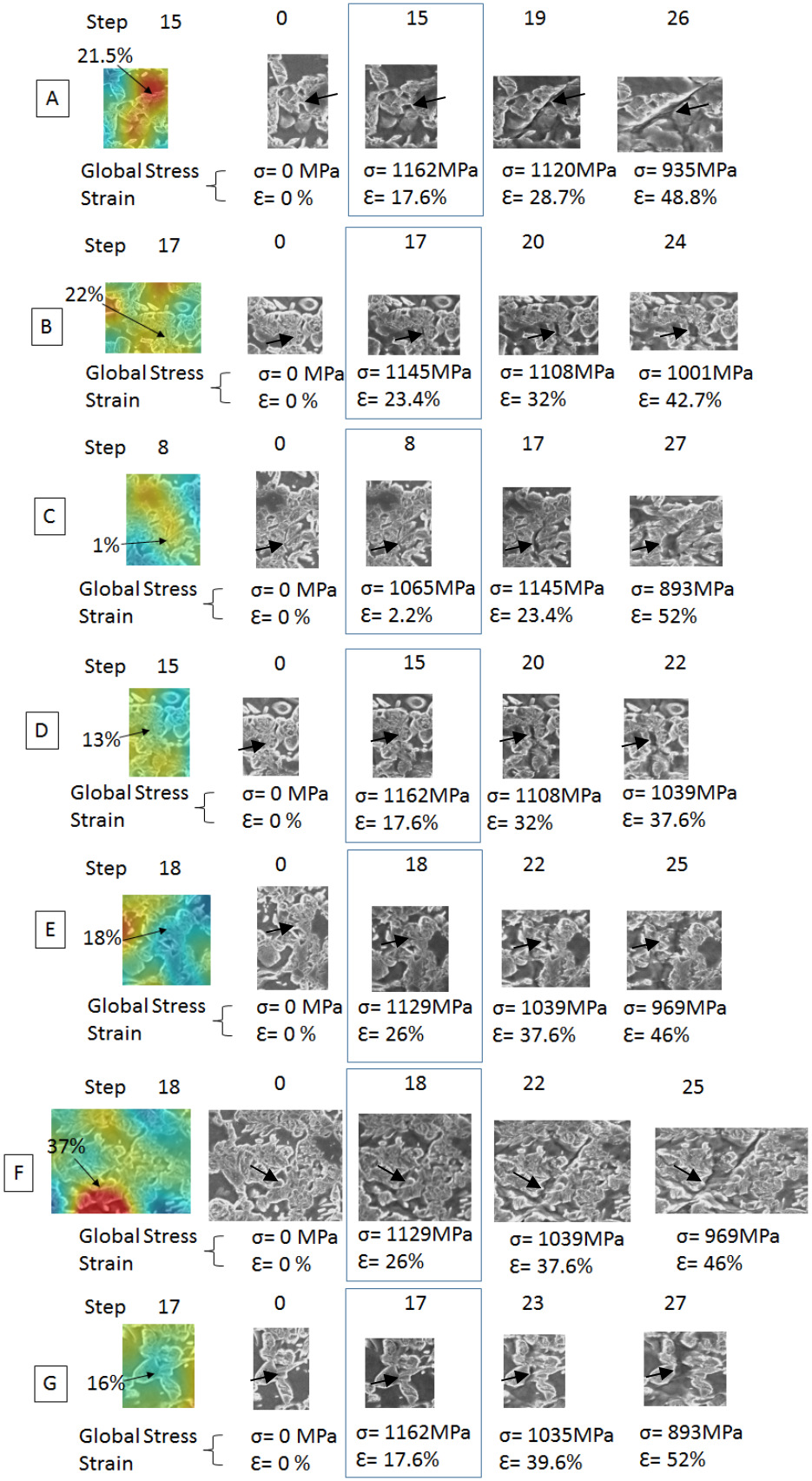

Figure 0-4 290°C

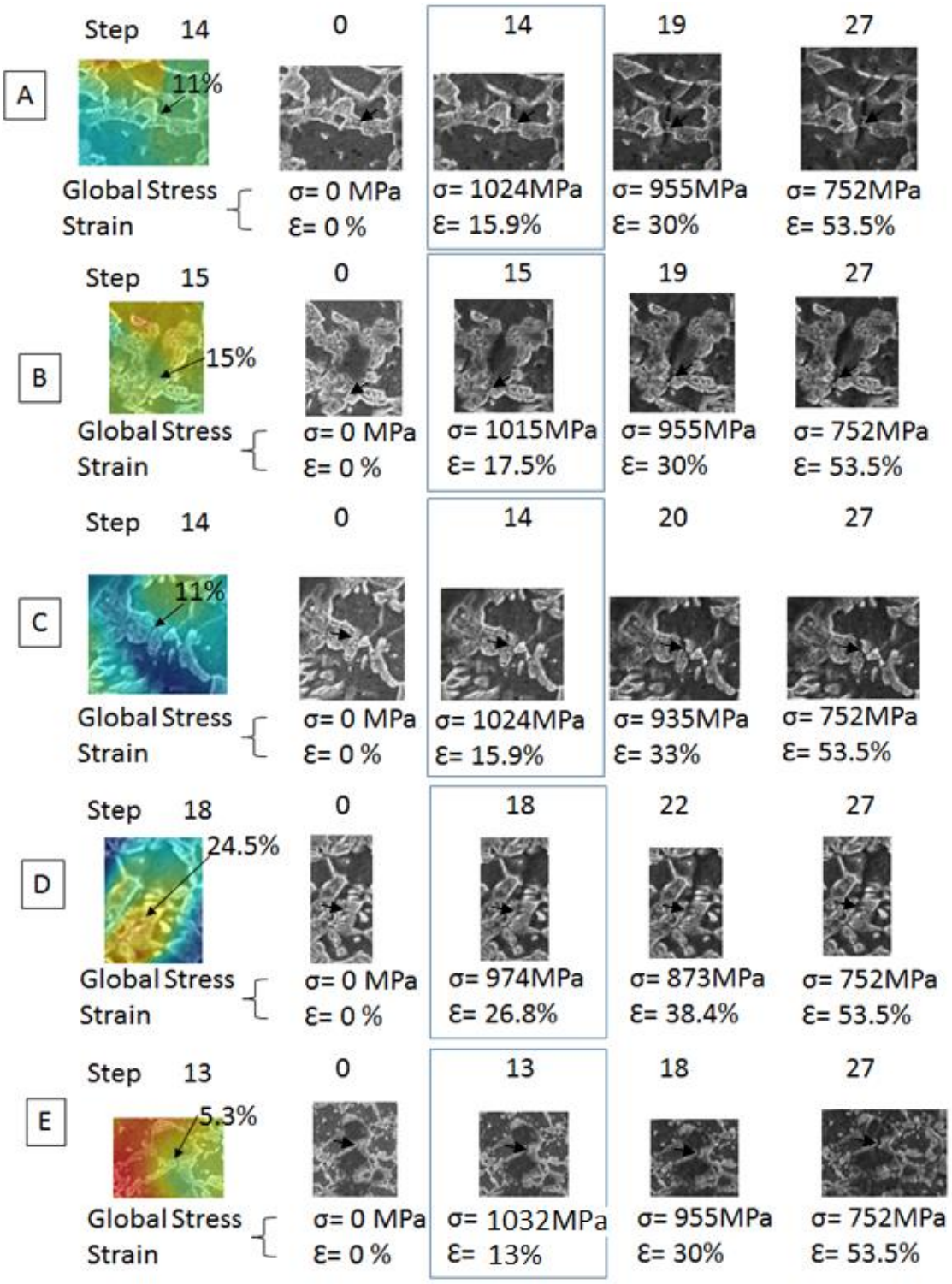

Figure 0-5 340°C

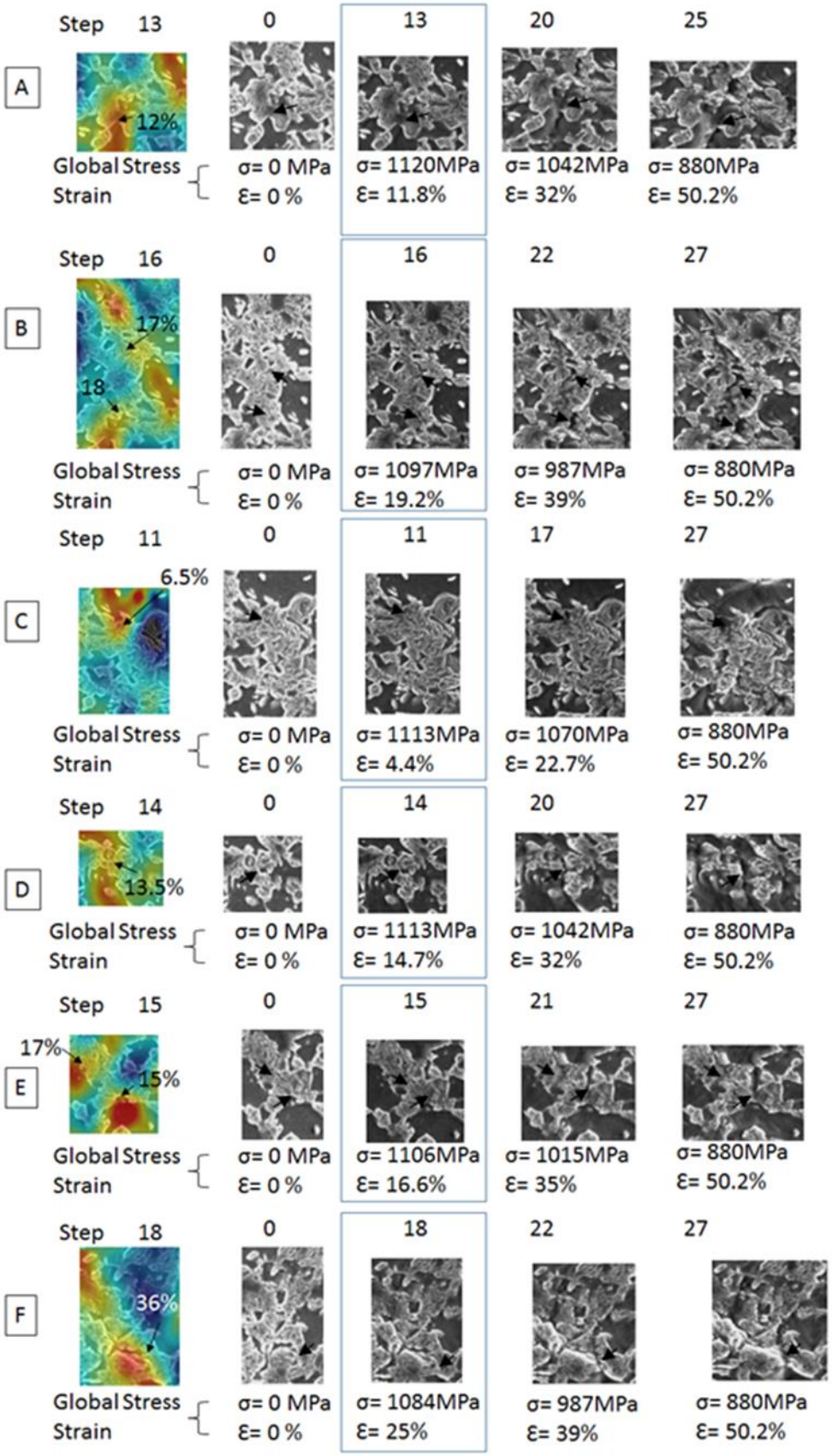
Step 13
0
13
20
25
A
12%
Global Stress
Strain
σ= 0 MPa
ε= 0 %
σ= 1120MPa
ε= 11.8%
σ= 1042MPa
ε= 32%
σ= 880MPa
ε= 50.2%
Step 16
0
16
22
27
B
17%
18
Global Stress
Strain
σ= 0 MPa
ε= 0 %
σ= 1097MPa
ε= 19.2%
σ= 987MPa
ε= 39%
σ= 880MPa
ε= 50.2%
Step 11
0
11
17
27
C
6.5%
Global Stress
Strain
σ= 0 MPa
ε= 0 %
σ= 1113MPa
ε= 4.4%
σ= 1070MPa
ε= 22.7%
σ= 880MPa
ε= 50.2%
Step 14
0
14
20
27
D
13.5%
Global Stress
Strain
σ= 0 MPa
ε= 0 %
σ= 1113MPa
ε= 14.7%
σ= 1042MPa
ε= 32%
σ= 880MPa
ε= 50.2%
Step 15
0
15
21
27
17%
E
15%
Global Stress
Strain
σ= 0 MPa
ε= 0 %
σ= 1106MPa
ε= 16.6%
σ= 1015MPa
ε= 35%
σ= 880MPa
ε= 50.2%
Step 18
0
18
22
27
F
36%
Global Stress
Strain
σ= 0 MPa
ε= 0 %
σ= 1084MPa
ε= 25%
σ= 987MPa
ε= 39%
σ= 880MPa
ε= 50.2%

365°C

APPENDIX 2 – Force-Displacement Data, Punch Test